Current and projected changes in the southern hemisphere UTLS ozone and effects of bushfire smoke aerosols

Submitted by

Jason Michael Siddaway, B.Sc (Hons.)

A thesis submitted in total fulfilment

of the requirements for the degree of

Doctor of Philosophy

School of Molecular Science

College of Science, Health and Engineering

La Trobe University

Bundoora, Victoria, 3086

April 1, 2015

Contents

List of Figures

List of Tables

Abstract

An analysis of future projections of ozone levels over Antarctica from coupled chemistry climate models (CCMVal-2) using multi-model median (MMM) trends found that the Antarctic Total Ozone Column (TOC) will not return to 1965 values during the September-November months by the end of the 21st century and that December TOC will not return to that baseline until 2080. The rate of TOC recovery during December was slower than for austral spring, due to a delayed increase of ozone at 50-100 hPa. At these altitudes, MMM temperature trends were projected to stop increasing by 2060 due to the combined radiative effect of a projected increase in greenhouse gases (GHG) and a decrease in ozone depleting substances. A persisting polar vortex was projected until the middle of the 21st century during December in the lower stratosphere.

Seasonal TOC zonal asymmetry patterns are analysed, with MMM seasonal trends during the observation period (1979-2005) showing reduced amplitudes and smaller eastward phase trends in TOC compared with satellite observations during austral spring. Fourier decomposition of MMM TOC trends show that the QSW-wave 1 harmonic is dominant during austral spring at Antarctic latitudes, indicating reduced tropospheric planetary wave forcing. There is qualitative agreement between eastward phase trends over Antarctica and model simulations during the ozone depletion period which then reverses with increasing ozone during the 21st century. A residual eastward phase trend towards the end of the century in both seasons is observed, suggesting a long-term phase shift in TOC distribution due to changes in GHGs and ozone depletion.

Limb-scattered radiance data was used to monitor the pyrocb event from the 2009 Black Saturday bushfire as it was transported into the lower stratosphere, reaching altitudes of

at least 21 km. The smoke plume dispersed over time and circled the globe in about 6 weeks, with smoke aerosols present in the lower stratosphere for approximately 3 months. Water vapour was entrained with the smoke plume from the upper troposphere, hydrating the dry lower stratosphere over latitudes of approximately 10-40°S. Water vapour perturbations were observed for at least 3 weeks after bushfire ignition from two sets of satellite measurements. Additionally, the smoke plume also transported ozone-poor air from the troposphere into the lower stratosphere, providing localised ozone depletion for at least 4 weeks up to the lower boundary of the Brewer Dobson Circulation. Such chemical perturbations have not been observed previously in relation to a pyrocb event.

Statement of Authorship

This thesis consists partly of work by the author that has been published or accepted for publication as described in the text. Except where reference is made in the text of the thesis, this thesis contains no other material published elsewhere or extracted in whole or in part from a thesis submitted for the award of any other degree or diploma. No other person's work has been used without due acknowledgment in the main text of the thesis. This thesis has not been submitted for the award of any degree or diploma in any other tertiary institution.

Jason Michael Siddaway, 1st April 2015

Acknowledgements

This thesis would not have been possible if it were not for the inspiration, dedication and encouragement of my initial primary PhD supervisor, Dr Svetlana Petelina. I would like to thank my other primary supervisor, Dr Andrew McDonald for the guidance and patience during those vital end days of my candidature, along with the support of my co-supervisor, Professor Peter Dyson. During my PhD studies, I had the fortunate opportunity to collaborate with some wonderful scientists, particularly Dr Andrew Klekociuk, who was generous with his ideas and time. I also need to thank Dr David Karoly, Dr Simon Alexander, Dr Artem Feofilov, Dr Mike Fromm and Dr Roger Dargaville for their assistance in aspects of my research and professional development.

I would like to acknowledge all the model teams that contributed to the CCMVal-2 model validation activity, along with the principal science teams associated with the OSIRIS instrument.

Within the La Trobe University Physics department, I would like to acknowledge Dr David Hoxley, Dr Grant Van Riessen and Dr Chris Pakes for their support throughout my studies. To fellow post-graduate students, both past and present, for discussions, programming assistance and friendship, Dr Shaun Cooper, Dr Adam Kellerman, Dr Brett Carter, Dr Alex Fink, Tom Kane, Chris Down and Emma Bland.

To all my family and friends for their unwavering belief and support, thanks for all that you have provided. Lastly, from the bottom of my heart, to my partner Bahar, who has supported me more than I can ever repay, in all possible ways, words are not enough. This just simply would not have happened without your love and support.

1 Introduction

The Upper Troposphere and Lower Stratosphere (UTLS) region is a transition layer that exhibits dynamic, chemical and radiative processes that can affect both the troposphere and stratosphere through bi-directional exchange, known as stratosphere-troposphere exchange (STE) [*Holton et al.*, 1995]. What occurs in this region is vital to our understanding and prediction of global climate change.

Downward transport of ozone due to STE has ramifications for surface air quality with increasing tropospheric ozone concentrations. This downward transport from the stratosphere is an important method by which stratospheric species, such as aerosols, are removed from that part of the atmosphere. Anthropogenic emissions, such as halogens and greenhouse gases are transported upwards to the stratosphere, initiating chemical reactions there that lead to stratospheric ozone depletion.

The UTLS is a region of relatively cold temperatures and plays an important role in thermal radiation escaping the troposphere into space, therefore affecting surface climate and climate feedback [*Gettelman et al.*, 2011].

The focus of this thesis lies within this UTLS region. We have analysed smoke aerosols from the unique 2009 Black Saturday bushfires penetrating the summer stratosphere at mid-latitudes and perturbing local chemistry. These aerosols provide an enhancement in water vapour and a local depletion of ozone. Chemistry-Climate Model (CCM) analyses of Antarctic ozone during the spring-summer months with both current and projected changes, are also presented.

1.1 Stratospheric ozone

Ozone is perhaps the most important constituent of the stratosphere with approximately 90% of the atmospheric ozone residing in what is referred to as the *Ozone Layer*. At tropical latitudes, this layer is situated at an altitude range of 20-30 km, with up to 60% of the global total column ozone in the lower stratosphere, at heights of 10-23 km. Stratospheric ozone concentrations vary with latitude and height depending on sunlight intensity, air density, temperature and transport mechanisms. It is produced naturally via photolytic decomposition of O_2 through a process known as the Chapman reactions, first proposed by *Chapman* [1930]. This dissociation occurs via solar ultraviolet radiation at wavelengths less than 242.4 nm [*Chapman*, 1930] via the chemical scheme shown below

$$O_2 + h\nu \longrightarrow 2O \tag{1.1}$$

$$O + O_2 + M \longrightarrow O_3 + M \tag{1.2}$$

$$O_3 + h\nu \longrightarrow O_2 + O(^1D) \tag{1.3}$$

$$O(^1D) + O_3 \longrightarrow 2O_2 \tag{1.4}$$

These temperature-dependent reactions describe formation and destruction of stratospheric ozone leading to a steady-state abundance of ozone in an oxygen-only chemical scheme. Reaction 1.1 produces atomic oxygen and reaction 1.2 describes the reaction of atomic oxygen with molecular oxygen and a third body M, which represents O_2 or N_2. Reaction 1.2 is the dominant natural mechanism in the stratosphere that leads to ozone molecule formation. As the concentration of M decreases with increasing altitude, the time constant for converting atomic and molecular oxygen to ozone increases with atmospheric height.

Ozone can then undergo photolysis as shown in reaction 1.3 producing oxygen atoms in its first excited state ($O(^1D)$) at wavelengths less than 320 nm [*Brasseur and Solomon*, 2005]. The quantum yield of production of $O(^1D)$ via photolysis is a function of wavelength, with increasing yield at decreasing wavelengths [*Sander et al.*, 2011]. At wave-

lengths greater than 310 nm, the photolysis reaction of 1.3 can also produce molecular atoms in their ground state ($O(^3P)$, not shown).

These reactions are rapid and continuously cycle ozone and atomic oxygen between one another in the stratosphere. Ozone can then recombine with atomic oxygen as shown in reaction 1.4. This reaction occurs with only a small fraction of atomic oxygen, therefore as concentrations of atomic oxygen increase with increasing altitude, the time constant for this reaction occurs at a slower rate at lower altitudes. Due to the interconversion between atomic oxygen and ozone they are often called the *odd oxygen* family, denoted as O_x. However, these reactions are for a pure oxygen atmosphere and other chemical species are also important in the budget of stratospheric ozone. The measured global concentrations of stratospheric ozone depletion cannot be explained by these Chapman reactions alone [*Solomon*, 1999], therefore additional catalytic cycles must also be involved, as described in the next section.

1.1.1 Halogens and ozone destruction

Following the publication of Chapman's paper, it was found that stratospheric ozone could be chemically destroyed via catalytic cycles involving hydrogen compounds [*Bates and Nicolet*, 1950] and nitrogen oxides [*Crutzen*, 1970]. Details of the chemical reactions involved with ozone and these species are summarised well in *Solomon* [1999]. Each of these chemical families can also be considered as the *odd hydrogen* and *odd nitrogen* families which destroy *odd oxygen* catalytically. Active species such as OH and NO are regenerated in these catalytic cycles, so increasingly small amounts of these gases still affect ozone abundances and provide important sinks of odd oxygen in the stratosphere. Natural abundances of odd hydrogen and nitrogen are perturbed through anthropogenic mechanisms via source gases such as CH_4 and N_2O. However, the majority of observed global ozone depletion is due to other processes, such as reactive chlorine catalytic cycles as first reported by *Molina and Rowland* [1974] and *Crutzen* [1974]. These reactions were found to be a far more efficient photochemistry scheme, along with reactive bromine catalytic cycles, leading to ozone destruction.

Natural stratospheric sources of these halogens originate from the destruction of methyl chloride (CH_3Cl) and methyl bromide (CH_3Br), which themselves originate from oceanic and plant emission processes [*Seinfeld and Pandis*, 2006]. These halogens then react as the catalyst species in the following general catalytic reactions which remove stratospheric odd oxygen:

$$X + O_3 \longrightarrow XO + O_2 \tag{1.5}$$

$$XO + O \longrightarrow X + O_2 \tag{1.6}$$

$$Net : O + O_3 \longrightarrow 2O_2 \tag{1.7}$$

X represents the catalyst and XO is an intermediate species. X is destroyed in reaction 1.5 and regenerated in 1.6. As long there is no sink for X present, only a few molecules of X are required to consume odd oxygen species. On coupling bromine and chlorine together with their intermediate species the following cycle occurs:

$$BrO + ClO \longrightarrow Br + Cl + O_2 \tag{1.8}$$

$$Cl + O_3 \longrightarrow ClO + O_2 \tag{1.9}$$

$$Br + O_3 \longrightarrow BrO + O_2 \tag{1.10}$$

$$Net : 2O_3 \longrightarrow 2O_2 \tag{1.11}$$

This set of reactions is more dominant in the lower stratosphere where the concentration of O_3 is far greater than atomic oxygen. Apart from such natural processes, it has also been identified that man-made chlorofluorocarbons (CFCs) are a major source of ozone-destroying stratospheric chlorine [*Molina and Rowland*, 1974]. These CFCs do not react with chemical species present at the surface, nor with constituents in the troposphere, but undergo chemical destruction from solar UV radiation in the stratosphere. This further promotes the catalytic cycles previously discussed. With increasing anthropogenic emissions from industrial areas predominantly located in the Northern Hemisphere (NH),

concentrations of CFCs from Antarctic surface stations were observed to be increasing, with a temporal lag allowing for hemispheric transport [*Montzka et al.*, 1996]) pointing to little or no destruction of CFCs in the troposphere.

This lead to the negotiation of the Montreal Protocol agreement in 1987 [*Sarma and Bankobeza*, 2000] to regulate production of CFCs and other Ozone Depleting Substances (ODSs). All 196 nations have signed the treaty since 1987. This has led to a major reduction in anthropogenic ODS production resulting in a decrease in cumulative concentrations of chlorine and bromine present in the stratosphere [*Froidevaux et al.*, 2006]). The regulation of these ODSs was based on the assumption that if ozone depletion wasn't curtailed, there would be severe consequences on the biosphere with increased surface UV radiation levels at the earth's surface. Model studies have simulated what would have happened to the global ozone layer if ODSs had continued to increase in the 21st century, pointing to a drastic decrease in the Total Ozone Column (TOC) at all latitudes [*Garcia et al.*, 2012]. Year-round ozone depletion at polar regions and increased surface warming due to the radiative impact of ODSs, leading to regional climate change was also predicted [*Morgenstern et al.*, 2008], [*Newman et al.*, 2009] and [*Garcia et al.*, 2012].

There has been a decline in the growth rates of major ODSs covered under the Montreal Protocol, such as CFC-11 and CFC-12 [*WMO*, 2011], which were highlighted as major ODSs by *Molina and Rowland* [1974]. There has also been a significant decline in methyl chloroform CH_3CCl_3. These anthropogenic ODSs have a long atmospheric lifetime, with CH_3CCl_3 having one of the shorter lifetimes of approximately 4.8 years [*Montzka et al.*, 1996]. *Lary et al.* [2007] found that total inorganic stratospheric concentrations were increasing until the late 1990's with a subsequent slow decline. A more comprehensive study involving 18 chlorine-containing species across 4 large latitude bands between 70°N-70°S from 2004-2009, found a global average decrease of approximately 0.5% per year [*Brown et al.*, 2014].

However, the effect of other halogen compounds whose contribution to ozone depletion is still increasing are being assessed, with increases in CFC's substitutes such as hydrochlorofluorocarbons (HCFCs) having a positive trend between 1995-2009 [*Saikawa*

et al., 2012]. HCFCs are regulated under the Montreal Protocol as a temporary replacement of CFCs. There has also been some revision of the atmospheric lifetimes of the more well known CFCs [*Ko et al.*, 2013]. For example, CFC-113 now has an estimated lifetime of around 109 years based on long-term satellite observation trends [*Rigby et al.*, 2013], an increase from the 85 year estimate previously stated in *WMO* [2007].

Vertical advection of very short-lived substances (VSLS) involving bromine species with a lifetime of less than 6 months, have been observed entering the tropical stratosphere [*Gettelman et al.*, 2009] providing continuing uncertainty of stratospheric anthropogenic ODS concentrations. The Montreal Protocol also covers emissions of bromine species. Even though the observed abundance in the atmosphere is significantly less (some 150 times less [*Seinfeld and Pandis*, 2006]) than chlorine species, they are similarly important as ODS's in the atmosphere. A long-term study on halon trends was conducted by *Newland et al.* [2013] which found that 3 out of the 4 halons considered (H-1211,H-1301,H-2402, H-1202) over the period of 1978-2011, had begun to decline in the mid-2000's, however H-1301 was continuing to increase as of mid-2011 and it's production is not currently controlled under the Montreal Protocol. All of these halons are wholly anthropogenic in origin with concentrations at near-zero in the early 1960's (*Newland et al.* [2013] and references therein).

Rapid tropospheric horizontal mixing and large scale ascent in the tropics as part of global circulation patterns, described in detail in *Holton et al.* [1995], means that regardless of the geographic location of industrial sources, atmospheric loading of CFCs is a global phenomenon with a global effect on ozone concentrations.

1.2 Stratospheric transport mechanisms associated with ozone and aerosols

1.2.1 Rossby waves

Rossby waves are planetary-scale waves that exist due to potential vorticity (PV) gradients. Parcels of air are displaced along PV gradients, inducing a velocity perturbation in order to conserve PV. This results in a wave pattern in the PV field that propagates westward relative to the mean atmospheric flow. Rossby waves with the largest amplitudes are quasi-stationary waves (QSW) and are produced from surface anchored sources such as continental scale orography and land-sea boundaries, which provide spatially inhomogeneous heating contrasts. They propagate up from the troposphere and equatorward, providing the mean zonal wind is eastward with a velocity that is smaller than some threshold [*Charney and Drazin*, 1961]. This threshold value is part of the Charney-Drazin theorem, and can be expressed as the following relationship:

$$0 < \bar{u} - c < \bar{u_c} \tag{1.12}$$

where c is the phase speed of the wave, and $\bar{u}$ - c is the phase speed of the wave relative to the zonal wind, u. Stationary waves ($c = 0$) can only vertically propagate into regions where the zonal winds are less than the threshold velocity, $\bar{u_c}$. For QSW propagation into the stratosphere, the zonal stratospheric wind must be eastward ($\bar{u_c}$ is positive), and is a function of the horizontal wavenumber of the Rossby wave. For the QSW wave-1 component, the threshold velocity is typically 100 ms^{-1} [*Brasseur and Solomon*, 2005].

These waves propagate into the middle stratosphere and deposit energy, which is known as wave breaking. Wave breaking, mixes the air isentropically across vast distances of the winter stratosphere within a region known as the 'surf zone' [*McIntyre and Palmer*, 1983], which is bounded by sharp gradients of PV in the winter subtropics and the polar vortex. This results in the stirring of tracers such as water vapour and ozone, and by stirring of PV, has an indirect effect on meridional circulation. For an adiabatic flow and

assuming steady state, a non-zero PV flux due to wave breaking requires a non-zero mean circulation via the zonal mean momentum budget, resulting in a poleward circulation [*Plumb*, 2002]. Thus wave breaking of Rossby waves drives a stratospheric poleward flow in the winter stratosphere, known as the 'Rossby wave pump'. For a detailed discussion of this mechanism see *Holton et al.* [1995].

Large amplitudes Rossby waves dominate the winter stratosphere outside the tropics where the zonal mean zonal wind is eastward, and more so in the NH where there are more geographical features than the Southern Hemisphere (SH). Planetary wave propagation is much reduced in the summer stratosphere resulting in a more symmetric pattern in dynamical fields such as geopotential height and temperature. *Wagner and Bowman* [2000] observed zonal ozone asymmetries during the NH summer due to Rossby waves with smaller amplitudes, penetrating through to the stratosphere causing substantial mixing at high latitudes.

In reality, only the longest Rossby waves penetrate into the extratropical stratosphere, and the Charney-Drazin criterion shown previously is satisfied only for wavenumbers 1-3 [*Brasseur and Solomon*, 2005]. Higher wavenumbers are associated with tropospheric weather systems but can sometimes be observed in the lowermost stratosphere.

Also present throughout the year in the lowermost stratosphere are synoptic-scale perturbations due to baroclinic instabilities [*Holton et al.*, 1995]. These disturbances increase in size due to the release of potential energy in the atmospheric flow associated with mid-latitude meridional temperature gradients. These temperature gradients can be due to land-sea contrasts, or caused by alternating high and low pressure systems in the troposphere prevalent in storm regions.

The summer stratosphere is dynamically quiescent with both weak large-scale mixing and downward transport at mid-high latitudes in the lower stratosphere. In the summer UTLS, year-round synoptic-scale tropospheric disturbances are considered responsible for the driving circulation forced by Rossby waves.

1.2.2 Brewer-Dobson circulation

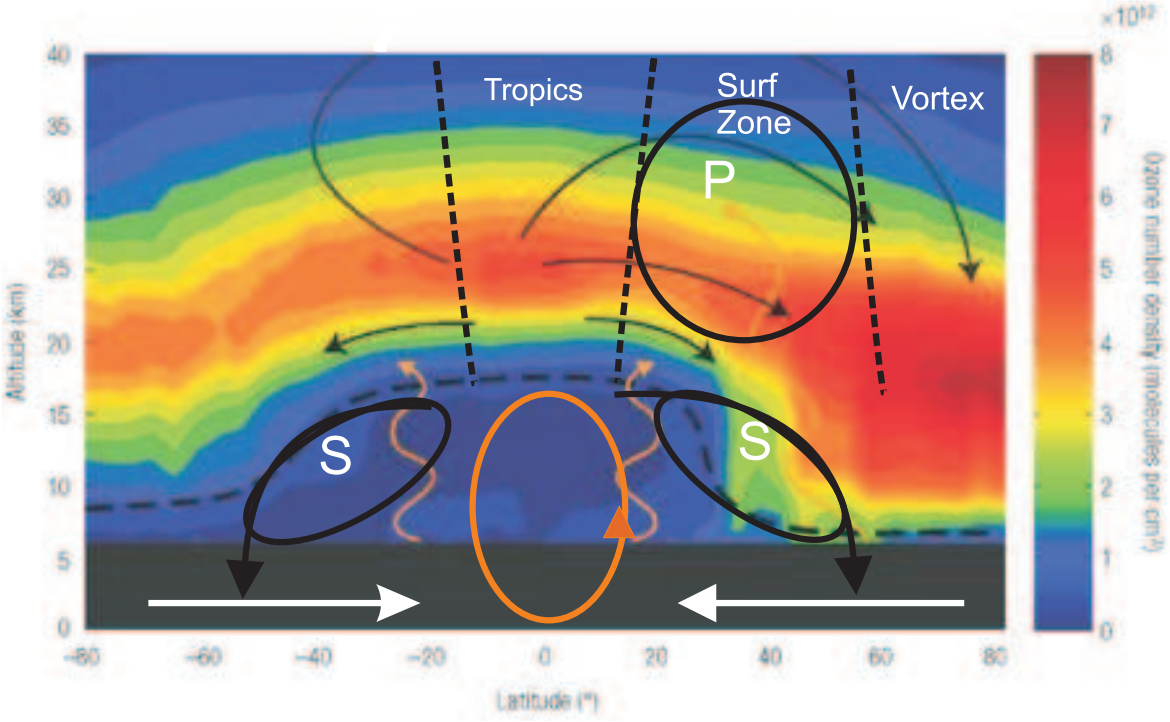

Figure 1.1: Adapted from Figure 1 in *Shaw and Shepherd* [2008] and Figure 2 in *Plumb* [2002]. Zonally averaged cross-section of ozone concentrations as measured by OSIRIS during March 2004. The black arrows indicates the Brewer-Dobson circulation being forced by waves propagating from the troposphere (orange wiggly arrows), particularly in the winter (northern) hemisphere. Dashed curved lines represent the tropopause and the straight dashed lines indicate the important latitudinal regions of the stratosphere. The black ellipses (P and S) indicate the regions of wave breaking in the stratosphere (planetary scale: P and synoptic scale: S). The orange ellipse represents the temperature driven Hadley circulation. The white arrows represent the conserving surface circulation branches.

Ozone concentrations in the stratosphere can be considered as a net balance of photochemical production and loss processes, catalytic destruction and transport mechanisms. Large scale meridional transport in the stratosphere is known as the Brewer-Dobson circulation (BDC), which was inferred through analysis of chemical abundances from ozone [*Dobson et al.*, 1930]; [*Dobson*, 1956], water vapour [*Brewer*, 1949] and later seen in monthly mean distribution trends of tracers based on satellite observations [*Randel et al.*, 1998]. Within the lower-middle stratosphere, the BDC transports ozone through tropical

upwelling, where most ozone is formed, and shifts it poleward with subsidence in the middle-high latitudes where higher concentrations are found. A schematic of the BDC circulation is shown in Figure 1.1.

This hemispheric meridional overturning is dominant in the winter hemisphere as it is driven by planetary waves at mid-high latitudes propagating upwards from the troposphere and breaking in the stratosphere [*Haynes et al.*, 1991]. However, some studies suggest that the tropical upwelling in the lower stratosphere is a combination of 'surf zone' wave breaking and forcing from equatorial planetary waves [*Garny et al.*, 2011]. Global mass conservation means that stratospheric air then returns to the troposphere at higher latitudes [*Seinfeld and Pandis*, 2006].

Air parcels traveling in the stratosphere also lose angular momentum as they move towards the pole. Where macroscale direct effects of friction are negligible in the stratosphere, this loss of angular momentum is ascribed to the effect of wave breaking. Within the polar vortex, stratospheric ozone undergoes large-scale descent with little mixing [*Plumb*, 2002]. Once within the vortex, air remains there for long periods undergoing diabatic cooling with ozone accumulating due to minimal photochemical processes during the polar night. The influence of the BDC in a given winter impacts on the ozone variability during the following spring and summer months [*Fioletov and Shepherd*, 2003]. The intensity of the diabatic circulation governs the strength of meridional mixing and diabatic descent, and hence, the amount of accumulated lower stratospheric ozone.

It is important to interpret the BDC as a 'residual' mean meridional circulation rather than an Eulerian mean, as it is the residual mean that is relevant to the transport of chemical tracers such as ozone. The BDC is driven by vertically propagating planetary waves from the troposphere that transport momentum to the stratosphere. This momentum is usually measured by upward Eliassen-Palm (EP) flux at the tropopause. Perturbations in this upward flux show an interannual variability in momentum transfer of approximately 10% [*Salby and Callaghan*, 2006]. Therefore, the upward momentum is absorbed in the stratosphere, forcing anomalous residual mean motion. The structure of this troposphere-stratosphere transfer at equatorial latitudes can also be modulated by a quasi-biennial

oscillation of stratospheric equatorial winds.

1.2.3 Quasi-Biennial oscillation

The Quasi-Biennial oscillation (QBO) of the equatorial zonal winds in the stratosphere [*Baldwin et al.*, 2001], and also the solar cycle [*Kuroda and Yamazaki*, 2010], are established mechanisms that affect interannual variations of lower stratospheric ozone. With the current solar cycle commencing in 2008, minimal solar activity has been observed in the first two years of the cycle [*Kamide and Kusano*, 2013]. It is suggested that the solar cycle effects on the interannual background zonal mean ozone values are minimal between 2008-2010. This will be discussed in relation to the results presented in Chapter 6.

The QBO is characterised by alternating patterns of westerly and easterly mean zonal winds between 5-100 hPa with an irregular periodicity of approximately 28 months [*Baldwin et al.*, 2001]. *Holton and Tan* [1982] found zonally symmetric oscillations in geopotential height and temperatures across a range of UTLS altitudes with positive (negative) anomalies in polar regions and negative (positive) anomalies at mid-latitudes during the westerly (easterly) phase of the QBO, over a 16 year period. This suggested an extratropical effect from the QBO.

The phase of the QBO influences vertical and meridional propagation of planetary waves in the stratosphere since the background zonal wind field refract the waves, acting as a waveguide. Hence, the QBO phase influences the position of the boundary between mid-latitude prevailing westerly (eastward moving) winds and easterlies in the subtropics [*Gray*, 2010]. This modulation of wave activity in the winter hemisphere at mid to high latitudes affects the polar vortex, particularly the weaker NH vortex.

The influence of the lower stratospheric QBO on NH extratropical circulation is known as the Holton and Tan (HT) relationship, first proposed by *Holton and Tan* [1980]. In a study of decadal-scale changes in the HT relationship, a negative correlation between temperatures in the NH polar vortex and the equatorial wind fields was reported by *Lu et al.* [2008]. They found that the stratosphere is warmer (colder) under an easterly (westerly) QBO over most of the period of 1958-2006. However, they found that the correlation

breaks down somewhat during the period of 1977-1997 and suggested this could be due to climate change and an influence from stratospheric ozone depletion, affecting mid-latitude planetary wave activity.

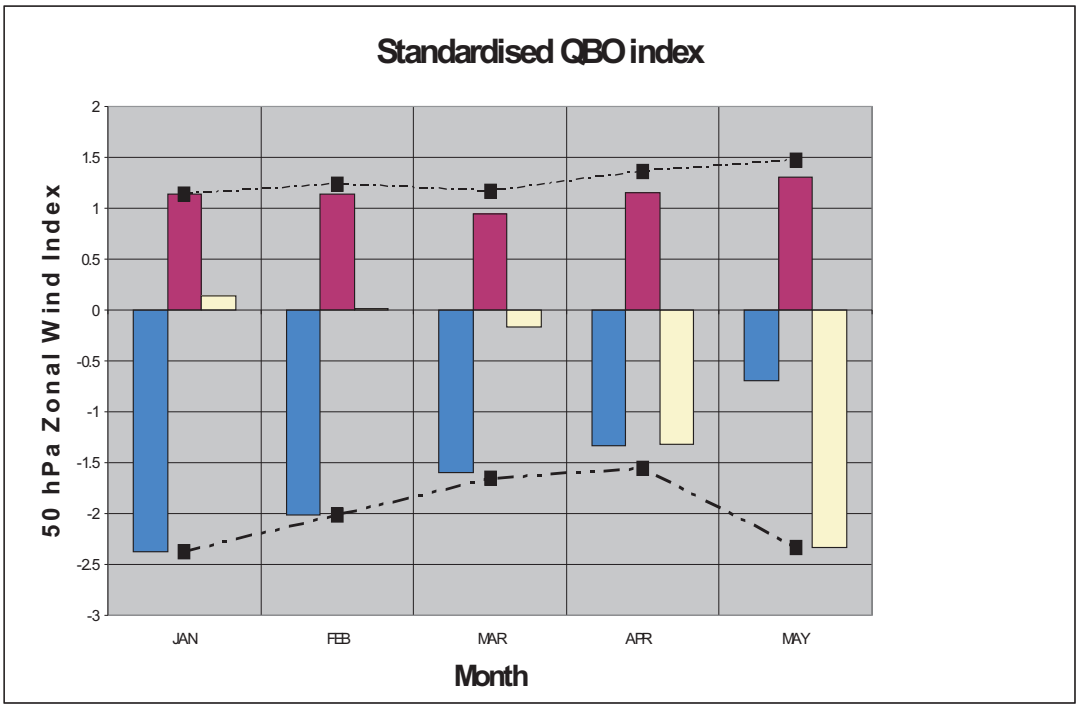

Figure 1.2: Adapted from standardized CDAS reanalysis data provided by NOAA (http://www.cpc.ncep.noaa.gov/data/indices/qbo.u50.index). Zonally averaged equatorial wind index at 50 hPa. Monthly averages are shown for 2008 (blue), 2009 (purple) and 2010 (yellow). Black dashed-dotted lines indicate monthly mean maximum and minimum values determined over 1979-2010.

This HT relationship is not as strong in the austral hemisphere, with SH mid-latitude wave activity not strong enough to affect the Antarctic vortex until the end of spring when the vortex starts breaking down. This leads to an interannual variation in ozone due to the QBO. At equatorial latitudes, the QBO dominates this variability, however the effect weakens at extra-tropical latitudes, where seasonal cycles are more important. For the month of February, the QBO at 50 hPa, was in an easterly phase during 2008, a westerly phase in 2009, and in a neutral phase in 2010. A plot of the monthly standardized 50 hPa index, from reanalysis data provided by the NOAA Climate Prediction Centre, is shown

in Figure 1.2.

The QBO can also affect the distribution of stratospheric aerosols, such as material from the El Chichon volcanic eruption as reported by *Trepte and Hitchman* [1992]. In the westerly QBO phase, global aerosol distribution is affected by meridional circulation, with more relative ascent of aerosols in the sub-tropics and relative descent at the equator, whilst during the easterly phase there is increased ascent over the equator. Ozone is also similarly affected by the phase of the QBO, with reduced ascent at the equator via meridional circulation during the westerly phase resulting in ozone accumulation in the lower stratosphere, due to reduced upwelling. Conversely during the eastward phase, increased upwelling transports O_3 to higher altitudes leading to negative anomalies in the lower stratosphere over the equator. The anomalies reverse sign at the sub-tropics according to satellite measurements of column ozone during each respective QBO phase due to meridional circulation [*Gray*, 2010]. This pattern at the sub-tropics extends out to higher latitudes. However, this mechanism is not well understood [*Baldwin et al.*, 2001].

1.3 Greenhouse gas emissions and ozone recovery

An important question in ozone science is what stratospheric ozone variation will occur in the 21st century with the expected continual decrease in ODS concentrations. It is unclear whether Antarctic stratospheric ozone will return to either a 1960 or 1980 baseline concentration by 2100 [*Eyring et al.*, 2010a]. In other words, the ozone concentration which existed prior to the formation of the Antarctic Ozone Hole.

Brasseur and Hitchman [1988] used a 2-D numerical model with interactive radiation, wave dynamics and a number of chemical trace species to show that a doubling of CO_2 towards the end of the century leads to an increase in TOC due to stratospheric cooling, particularly at polar latitudes in the upper stratosphere. This provided an offset to the CFC-induced polar ozone decrease. *Rosenfield et al.* [2002] found that due to a slowdown in catalytic ozone loss cycles, increasing CO_2 hastened the recovery of ozone in the middle to upper stratosphere at all latitudes (above 30 hPa in the tropics and above 50 hPa in

the extra-tropics). However, in the lower stratosphere there was a significant latitudinal variation in its effect on ozone recovery. At tropical latitudes there was a delay in ozone production and increased upward circulation leading to a slowdown in ozone recovery [*Rosenfield et al.*, 2002]. The effect on lower stratospheric ozone at SH mid-latitudes can depend on mixing of ozone-poor air from Antarctica and the effect of tropospheric forcing. However, *Rosenfield et al.* [2002] found that there was negligible impact on the ozone column from increased CO_2 over Antarctic latitudes.

One available method to investigate how a reduction in atmospheric halogen loading to natural 'background' levels will lead to stratospheric ozone recovery in the near future is to analyze simulations from coupled chemistry-climate models (CCMs). Such models are widely used to predict the future behavior of stratospheric ozone in response to different forcings [*Eyring et al.*, 2007]. CCMs provide simulations of various atmospheric parameters in three-dimensional space coupled with fully interactive stratospheric ozone chemistry. The degree of ozone recovery can also be affected by other changes in the atmospheric composition, such as current and future increases in concentrations of greenhouse gases (GHGs). GHGs affect ozone levels and complicate the attribution of ozone recovery to a decrease in halogens [*Eyring et al.*, 2010b].

A study using simulations from several CCMs [*Eyring et al.*, 2007] found that total ozone averaged over mid-latitudes will reach 1980 levels by the middle of the 21st century due to the combination of decreases in halogens and increases in GHGs. However, there was significant intermodel variation in the predicted recovery to a 1980 baseline for Antarctic TOC during the austral spring.

Focusing on the effect of polar lower stratospheric ozone due to increasing GHG concentrations, *Shindell et al.* [1998] found that temperature and wind changes altered planetary-wave propagation resulting in a more stable Arctic polar vortex, with colder temperatures leading to increased ozone depletion. The Antarctic ozone hole was also predicted to increase both in severity and duration due to GHG cooling of the lower stratosphere. If lower stratospheric temperatures decrease in the austral winter this increases the probability of polar stratospheric clouds forming and providing nucleation sites for ODSs.

1.4 Polar stratospheric clouds

During the polar winter, cold temperatures and the near-total isolation of air inside the polar vortex provide a good environment for the formation of clouds in the stratosphere. Even though the stratosphere is normally dry and cloudless, the temperature is so low (as low as 183 K [*Seinfeld and Pandis*, 2006]) that even trace amounts of water vapour condense to form clouds. These were noted by past explorers at both polar regions, as the clouds are optically thick and bright in color and were assumed to be composed of water ice. The term Polar Stratospheric Clouds (PSCs) was first used by *McCormick et al.* [1982], who presented the first satellite measurements of PSCs. These clouds were optically thin and occurred at altitudes up to 23 km, and where temperatures were $\leq$195K. Since then, there has been extensive research done on the PSC threshold temperature required for formation and growth using balloon measurements [*Hofmann and Deshler*, 1989], aircraft campaigns [*Del Negro et al.*, 1997] and laboratory measurements [*Peter*, 1997].

There are two types of PSCs, known as Type I and II. Type II PSCs are composed of water ice and have a typical particle diameter of 1-30 μm. Due to their relatively large size, these ice particles sediment out quickly leading to dehydration and nitrification (removal of reactive nitrogen) of the lower stratosphere within the polar vortex [*Brasseur and Solomon*, 2005]. The critical threshold temperature for these Type II PSCs is 188 K.

The composition of Type I PSCs is still an area of active research, but they have been reported via lidar observations [*Poole and McCormick*, 1988] as optically thin clouds with a diameter of approximately 1 μm, forming at temperatures higher than the frost point of Type II PSCs, of up to 195 K. *Toon et al.* [1986] proposed that Type 1 PSCs were due to uptake of nitric acid and water on pre-existing sulphate aerosols which formed nitric acid trihydrates (NAT). More recent observations, however, have shown that the Type I PSC formation temperature is inconsistent with the NAT equilibrium temperature. Despite definitive evidence of NAT particles within the winter polar stratosphere [*Voigt et al.*, 2000], current theories now suggest that other Type I PSC particles are also present. These particles, known as liquid tertiary solutions, are composed of a mixture of nitric

acid (HNO_3), water vapour and sulphuric acid (H_2SO_4), and are also present during the polar winter [*Brasseur and Solomon*, 2005].

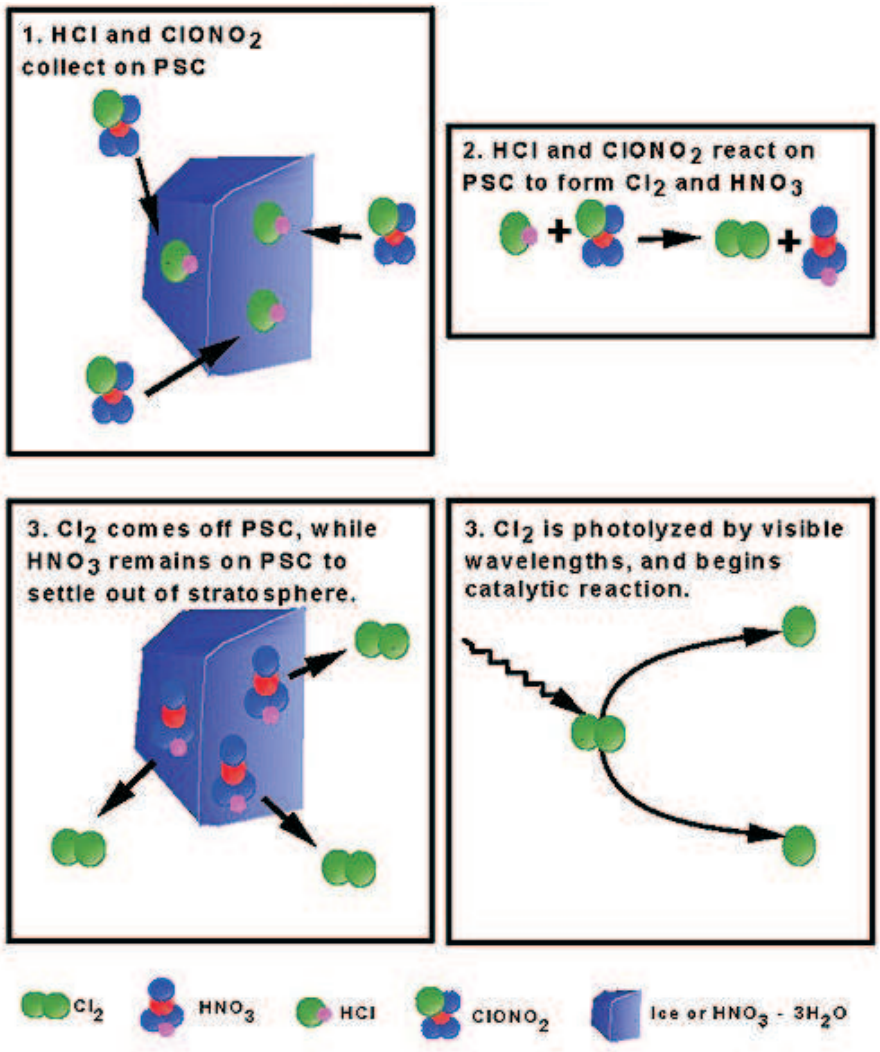

Figure 1.3: Schematic of the surface reaction on a PSC from *Cordero et al.* [2013].

Solomon et al. [1986] suggested that PSCs could provide a surface for heterogeneous (reactions between gaseous and solid chemical species) reactions involving HCl and $ClONO_2$ that would greatly accelerate ozone loss in the lower stratosphere. A schematic of this process is shown in Figure 1.3.

The photolysis of Cl_2 and other metastable compounds such as HOCl requires sunlight. Therefore, this ozone depletion mechanism would occur when the stratosphere was both

cold and sunlit; that is, during the austral spring over Antarctica. The photolysis of Cl_2 would rapidly form ClO. However, this process on PSCs could not deplete ozone early enough in the season to be consistent with observations [*Solomon et al.*, 1986]. *Solomon et al.* [1986] suggested that this and other heterogeneous reactions would suppress the NO_2 through formation of HNO_3 so that the ClO formed could not readily return to the $ClONO_2$ reservoir. If denitrification is also occurring as a result of larger PSCs, then this would lower the supply of nitrate and prevent ClO from forming $ClONO_2$ [*Seinfeld and Pandis*, 2006]. For a more detailed description of these heterogeneous reactions the reader is referred to *Solomon* [1999] and *Seinfeld and Pandis* [2006].

Another catalytic cycle was later found to cause very rapid ozone loss involving the formation and photolysis of a ClO dimer; Cl_2O_2 [*Molina and Molina*, 1987]. This process is now recognised as the primary catalytic process responsible for approximately 75% of the ozone depletion within the Antarctic Ozone Hole [*Brasseur and Solomon*, 2005]. When Cl_2 undergoes photolysis to form ClO, this can occur at larger wavelengths (280-420 nm) so only weak sunlight is required to break up Cl_2. Therefore, this can occur in the late winter as the sun starts to rise over Antarctica [*Cordero et al.*, 2013].

When a ClO molecule reacts with another, the ClO-ClO reaction proposed in *Molina and Molina* [1987] occurs as outlined in equations 1.13 to 1.15. Therefore measurements of ClO provide a direct measure of the rate of ozone loss.

$$ClO + ClO + M \longrightarrow Cl_2O_2 + M \tag{1.13}$$

$$Cl_2O_2 + h\nu \longrightarrow Cl + Cl + O_2 \tag{1.14}$$

$$2(Cl + O_3 \longrightarrow ClO + O_2) \tag{1.15}$$

$$Net : 2O_3 \longrightarrow 3O_2 \tag{1.16}$$

Strong evidence linking depletion of stratospheric ozone during austral spring with global emissions of halogens was reported by *Anderson et al.* [1991]. They looked at the temporal evolution of ClO and O_3 from in-situ aircraft observations as the ozone hole was forming, showing a significant anti-correlation across the Antarctic vortex boundary. Satellite observations of O_3 and ClO column abundances above 100 hPa (about 16 km) during September months, confirmed simultaneous increased ClO and depleted O_3 within the Antarctic vortex [*Waters et al.*, 1993].

Another important aspect to stratospheric chemistry is the BrO-ClO reaction as outlined in *McElroy et al.* [1986] which is now known to contribute approximately 20% of depletion within the Antarctic Ozone Hole [*Brasseur and Solomon*, 2005]. These two catalytic cycles don't require free oxygen atoms to destroy ozone unlike the conventional catalytic loss process outlined in equations 1.5 to 1.11, and account for the large majority of observed ozone loss.

Background stratospheric aerosols circulate down to the polar stratosphere and grow into Type I PSCs during winter, and if temperatures are cold enough, will further grow into Type II water ice clouds. Therefore any observed increase in aerosol surface area for such reactions are vital in the amount of ozone depletion that occurs through the processes outlined previously. The next section looks at the type of stratospheric aerosols being produced at lower latitudes and the variety of transport pathways that these aerosols take.

1.5 Stratospheric aerosols

Aerosols act as a key climate forcing agent and as an anthropogenic emission, are comparable with CO_2 in terms of net radiative forcing intensity, but with a larger variation on regional scales [*Yu et al.*, 2006]. They affect the Earth's energy budget directly via the scattering and absorbing of solar and thermal IR radiation and indirectly, by acting as cloud condensation nuclei (CCN). This indirect effect changes the cloud microphysics and therefore the radiative properties and lifetime of clouds. However, this has been difficult

to quantify in climate model simulations [*Haywood and Boucher*, 2000].

The large uncertainties in aerosol forcing are present due to incomplete knowledge of the physical and chemical properties of aerosols, as well as their distribution. Therefore, there has been a concerted effort in recent years to improving satellite measurements of aerosols [*Torres et al.*, 2007]. A review of the aerosol direct radiative effect found that anthropogenic aerosols over the global ocean account for approximately 21% of the atmospheric aerosol load [*Yu et al.*, 2006]. However, estimates of aerosol forcing over land are poorly constrained, due to the poor understanding of aerosol absorption and distribution.

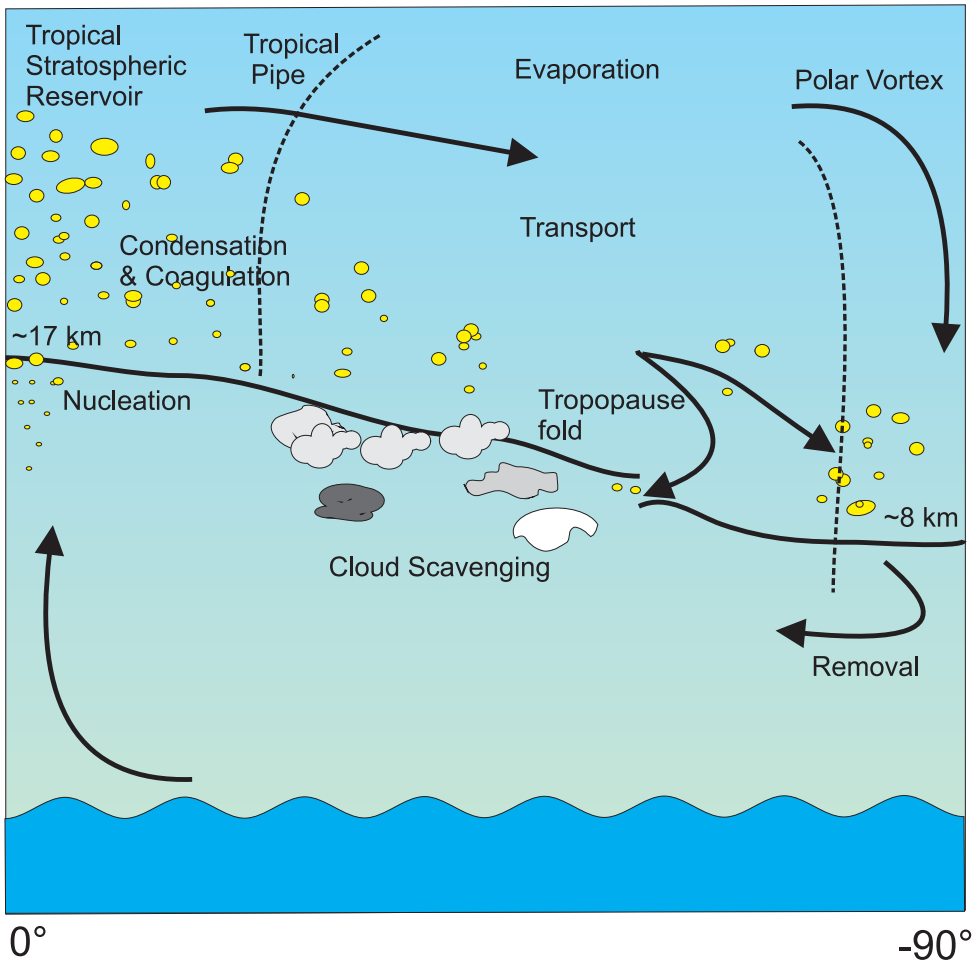

Figure 1.4: Adapted from *Hamill et al.* [1997] as a schematic of the life cycle of a typical stratospheric aerosol. This is described in the text below.

Atmospheric aerosols, both natural and anthropogenic, can have radii between 0.001 and 10 μm [*Haywood and Boucher*, 2000]. They can be directly emitted from a variety of sources, such as mineral dust or ash from industrial activities. Alternatively, they can be the result of secondary reactions from gas and aqueous phase oxidation, such as sulphate aerosols from marine phytoplankton or fossil fuel burning. These aerosols undergo mixing in the atmosphere and tropospheric aerosols are removed from the atmosphere through impact or precipitation. Tropospheric aerosols can have a lifetime anywhere from a minute to several weeks and are spatially very variable.

The life cycle of sulphate aerosols that form the unperturbed background lower stratospheric aerosol layer, as suggested by *Hamill et al.* [1997], is illustrated in Figure 1.4. Stratospheric aerosols are formed through nucleation in rising tropical air masses at the tropical tropopause or lower stratosphere, after which they coagulate and undergo growth by condensation and mixing with older aerosols. The aerosols then circle the earth continuously within the tropical stratospheric reservoir, first described by *Trepte and Hitchman* [1992]. That study found that aerosols particles situated a few kilometres above the tropopause are readily transported poleward, but aerosols above 21 km are confined to tropical latitudes, being controlled by the phase of the QBO.

When aerosols reach mid-latitudes they continue to circle the earth but slowly descend along isentropic surfaces to the lowermost stratosphere, as described by *Holton et al.* [1995]. Some particles will reach the polar stratosphere, becoming entrained in the polar winter vortex [*Hamill et al.*, 1997]. Once there, these aerosols provide potential nucleation sites for PSCs.

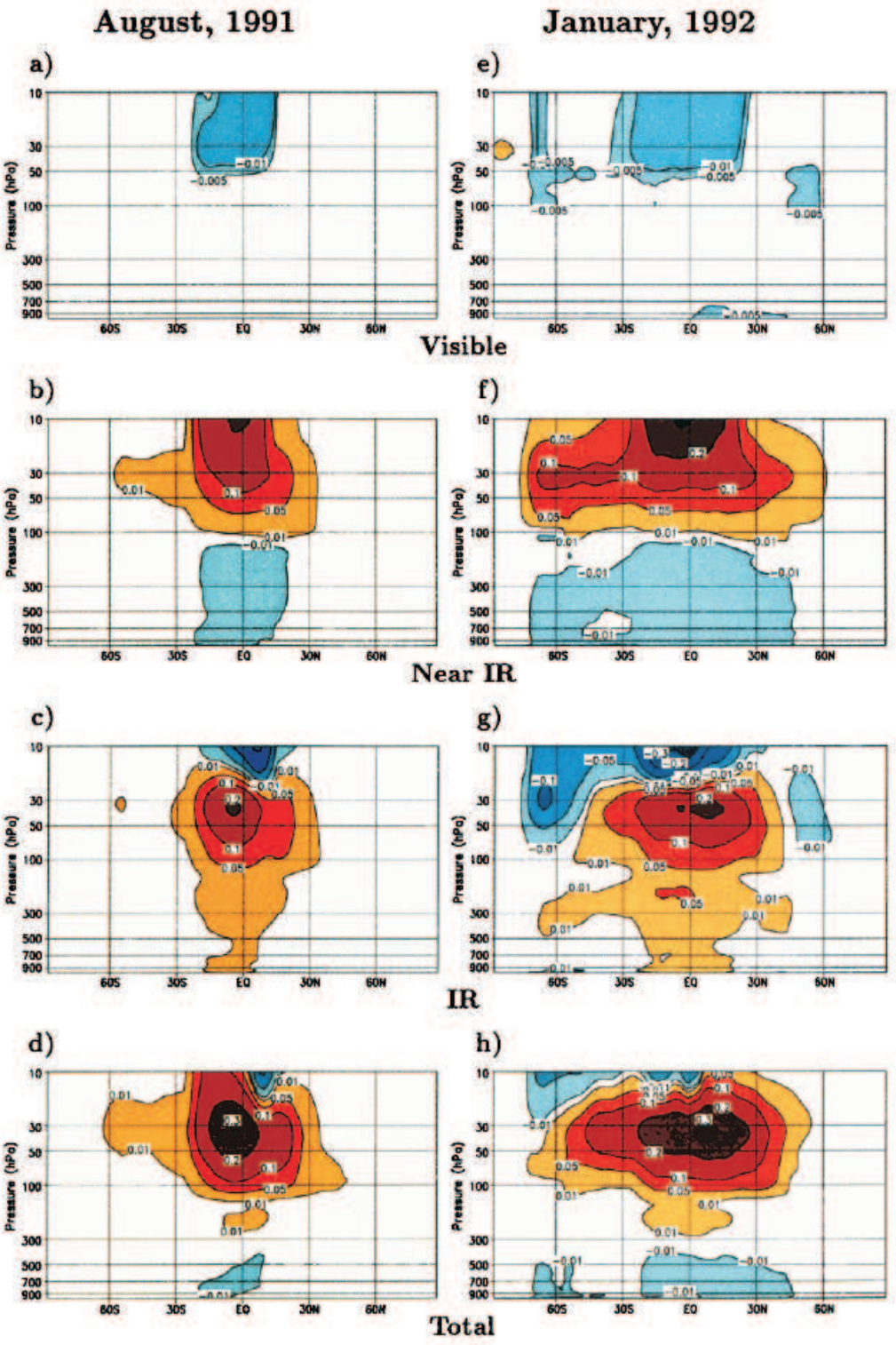

Figure 1.5: From *Robock* [2000] and references therein, showing vertical profiles of radiative monthly zonally averaged perturbations of radiative heating rate (K/day) in August, 1991 and January, 1992 caused by Mount Pinatubo aerosols following its eruption in June, 1991. Radiative heating shown for three different wavelength bands; visible (λ <0.68 μm, Figures a & e), near-IR (0.68 μm <λ <4μm, Figures b & f) , IR (λ >4 μm, Figures c & g) and total (Figures d & h).

Stratospheric aerosols were first quantified using balloon measurements, which found an increase in large particles (radii greater than 0.15 μm) as they ascended into the stratosphere [*Junge et al.*, 1961]. This was at a period of time when no major volcanic eruptions had occurred in many years [*Solomon et al.*, 2011]. These particles were later identified as being liquid aerosols composed of water and sulphuric acid [*Rosen*, 1971], forming an aerosol layer that extended from the tropopause up to approximately 30 km altitude [*Hamill et al.*, 1997]. It had been assumed that only these liquid sulphate aerosols were present in the stratosphere, undergoing seasonal variations and significant perturbations from major volcanic eruptions. However, above 30 km altitude, solid aerosols of dust and debris from meteoroid disintegration have been observed and could be transported to the lower stratosphere over polar regions from general circulation [*Renard et al.*, 2008]. That study also found soot particles present between 22-30 km at all latitudes, likely originating from biomass burning.

Large volcanic eruptions are powerful enough to directly inject sulphur dioxide into the stratosphere, where it oxidises to form sulphates, increasing the burden of stratospheric aerosols. There have been three major eruptions since 1980, two of them located in the tropics, which directly injected aerosols into the tropical stratosphere [*Robock*, 2000]. The last major eruption was Mount Pinatubo in the Philippines which injected water and sulphur dioxide into the stratosphere, forming sulphate aerosols with an e-folding time (a decrease of 1/e) of approximately 1 year [*Robock*, 2000], over a latitudinal extent from 30°N to 20°S within a few months after the eruption [*Young et al.*, 1994]. These volcanic aerosols circled the globe in 3 weeks [*Bluth et al.*, 1992], heating the stratosphere and resulting in surface cooling due to reduced direct radiation [*Robock*, 2000], as shown in Figure 1.5.

Aerosols can not only affect the radiative flux in the stratosphere, but also its chemistry by changing the temperature and providing surfaces for heterogeneous reactions. *Solomon et al.* [1996] found that variations in stratospheric aerosols at northern mid-latitudes (45-55°N) played an important role in ozone loss trends during the 1980's when considered in conjunction with anthropogenic halogen trends. Observed aerosol distributions, when

used in model calculations, enhanced ozone depletion due to halogen chemistry below 25 km. *Solomon et al.* [1996] suggested that aerosol-induced ozone changes could be statistically confused with the effect of the 11-year solar cycle, therefore overestimating trends ascribed to solar activity. Another study [*Portmann et al.*, 1996], using a climatology of satellite aerosol surface area measurements between 1979-1994 and poleward of 70°S, found that volcanic aerosols very likely modulated the severity of the Antarctic Ozone Hole. *Portmann et al.* [1996] found that a rapid deepening of the ozone hole in the early 1980's occurred following the El Chichon eruption in 1982, and again following the eruption of Mount Pinatubo in 1991, due to accelerated chlorine activation chemistry.

Figure 1.6 show MLS measurements of ClO and O_3 for 4 days during the austral winter-early spring period following the Mt Pinatubo eruption. This indicates increased ozone in the lower stratosphere during the polar winter (June & July) even though simultaneous observations show increasing density of ClO. This is possibly due to descending ozone-rich air from the upper stratosphere bringing in more ozone that can be destroyed by ODSs. Ozone depletion commences in August with further increase in ClO concentration providing large-scale O_3 destruction through the ClO catalytic cycle described previously. Greater ozone destruction by September leads to the formation of the Antarctic ozone hole.

Waters et al. [1993] reported increased chlorine dioxide (OClO) concentrations indicating increased chlorine activation by sulphate aerosol chemistry in 1992 (relative to 1991; *Sanders et al.* [1993]) at Antarctic high latitudes. But no links were established between Mt Pinatubo volcanic aerosols and ozone depletion over Antarctica. Similarly, *Solomon et al.* [1993] states that aerosol levels in 1991, just prior to the Pinatubo eruption, were at background levels, and that OClO was greatly increased in the austral autumn of 1992 when PSCs were unlikely to have formed. They suggested that Pinatubo aerosols contributed to an unprecedented depth and extent of Antarctic ozone depletion in the spring of 1992, which was supported by other studies, such as *Hofmann and Oltmans* [1993].

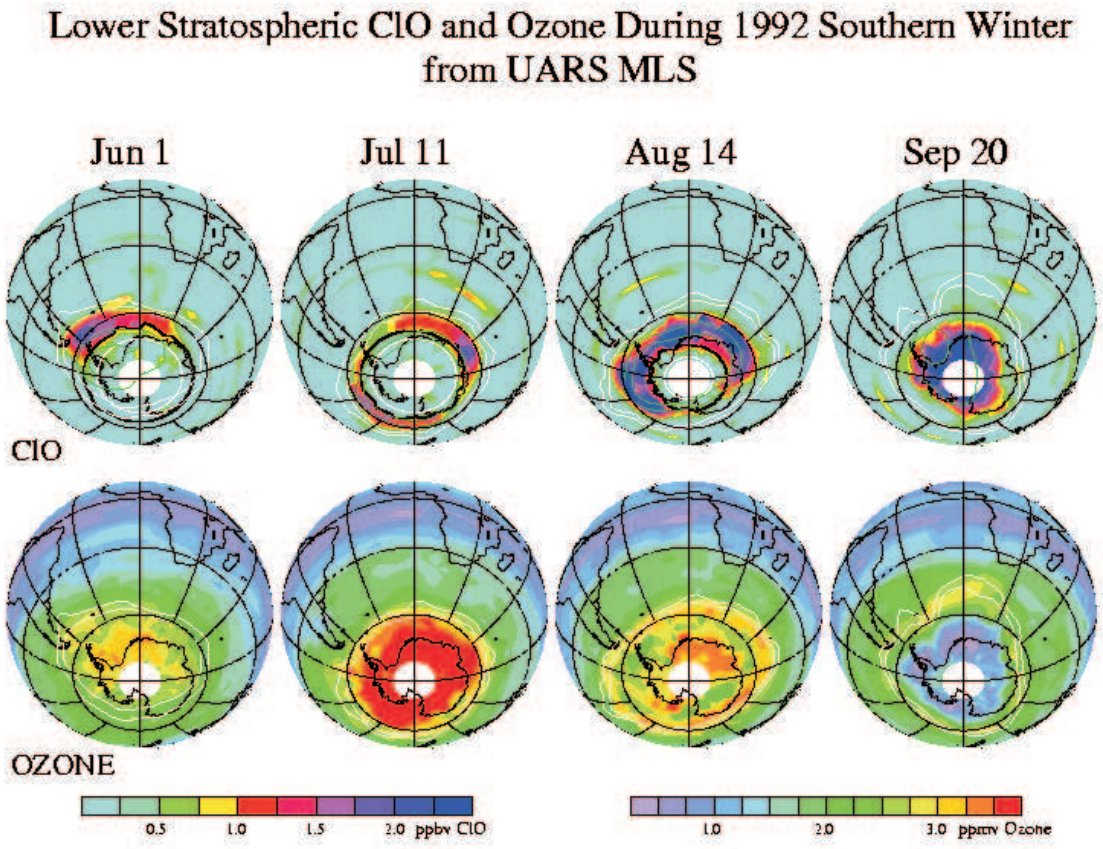

Figure 1.6: From the MLS scientific results website: http://mls.jpl.nasa.gov. This shows 4 selected days during the austral winter-early spring following the Mount Pinatubo eruption. Data was interpolated to a surface at approximately 20 km showing loss of O_3 within the polar vortex. Black contours surrounding the pole on the ClO maps show the daylight edge of MLS measurements.

A model study of the effect of the Pinatubo eruption found that at the edge of the ozone hole, where temperatures are not low enough for PSC formation, ozone depletion occurred due to volcanic aerosols, increasing the total ozone destruction [*Knight et al.*, 1998]. More recently *Robock et al.* [2007], examined SH circulation in the UTLS region and found no significant anomalies associated with the Mt Pinatubo eruption, or in fact any other major volcanic eruption of the past 50 years. During 1991, any anomalies in circulation patterns were associated with an El Nino event that took place that year.

The Mount Pinatubo eruption is the most recent major volcanic event that has occurred

to date. Since then, only minor volcanic activity has occurred [*Andersson et al.*, 2013]. However, a linear trend in satellite measurements of stratospheric aerosol optical depth between 2000-2010, was found to have an increase of approximately 5% per year at SH mid latitudes [*Vernier et al.*, 2011]. They concluded that this was due to moderate tropical volcanic eruptions between 2002 and 2008.

Aerosols have also been observed to penetrate the tropical tropopause via the Asian Monsoon system, an anticyclonic circulation system that is observed during the NH summer months[*Randel and Park*, 2006]. Satellite observations of hydrogen cyanide (HCN), a common biomass burning tracer, were observed in the lower stratosphere associated with the Asian Monsoon [*Randel et al.*, 2010]. It was concluded that as the upper troposphere is relatively depleted in HCN, these stratospheric enhancements of HCN were not associated with broad tropical upwelling. The Asian Monsoon is a particularly coherent and active circulation system [*Randel and Park*, 2006], and with tropospheric deep convection over Africa, combined to loft sulphur dioxide (SO_2) from a volcanic eruption in North Africa during 2011 into the lower stratosphere [*Bourassa et al.*, 2012].

Bourassa et al. [2012] reported that the volcano did not directly inject material into the stratosphere, but with the assistance of the Asian Monsoon, was able to pollute the lower stratosphere with SO_2 which formed sulphate aerosols. However, this was subsequently disputed in *Fromm et al.* [2013] and *Vernier et al.* [2013]. They presented satellite observations that suggested that this volcanic eruption did inject material directly into the lower stratosphere, so the Asian Monsoon mechanism was not required to explain volcanic aerosols from this event penetrating the stratosphere. Therefore, the pathway by which tropospheric aerosols are transported to the stratosphere is still a debated issue.

1.6 Biomass burning emissions

Biomass burning emissions are an important source of trace gases and aerosols in the atmosphere [*Crutzen and Andreae*, 1990]; [*Andreae and Merlet*, 2001]. Such emissions vary seasonally, depending on the time of the dry season, with intensive burning occurring

in the NH during December to March and in the SH during June to September [*Andreae*, 1991]. However, at tropical latitudes biomass burning can occur year round with fires in Africa, South America and parts of Asia due to agricultural, heating and cooking requirements, as well as natural ignition processes. Such burning primarily produces CO_2 and H_2O, which acts as a photosynthesis-respiration reaction, returning CO_2 to the atmosphere. On long enough time scales, this does not influence the atmospheric budget, unless the biomass that is burned is not replaced by regrowth [*Andreae*, 1991]. With large-scale deforestration, this does provide a net CO_2 release and contributes to global climate change as a feedback mechanism through the global carbon cycle [*Galanter et al.*, 2000].

Climate change can also be a driver for biomass burning with an analysis of paleo-fire data over the past 21,000 years showing an increase in fire occurrence with increasing surface temperature and a peak in intermediate moisture [*Daniau et al.*, 2012]. The interaction between fire emissions, vegetation and climate is complicated by anthropogenic influence with approximately 90% of biomass burning thought to be due to human activities [*Andreae*, 1991]. *Pechony and Shindell* [2010] in their model study found that the incidence of large wildfires in the future, driven by increasing temperatures in the 21st century, will outweigh anthropogenic biomass burning, in reversal of the situation over the last two centuries. However, likely regional impacts are more difficult to ascertain.

One analysis of a boreal forest fire in the NH which considered GHG gases, aerosols, black carbon deposition and surface albedo, reported that fire emissions provide a short-term increase in radiative forcing, but on a multidecadal scale, provide a decrease in radiative forcing due to the larger effect of surface albedo compared with emitted GHGs [*Randerson et al.*, 2006]. They concluded from this, that increases in boreal fire events may not necessarily accelerate climatic warming.

The composition and concentration of trace gases and aerosols released from a fire primarily depends on the combustion conditions and the fuel type, but the dominant fraction of emissions is released as carbon with CO_2 and CO (approximately 90% of total carbon emitted) [*Andreae and Merlet*, 2001]. CO_2 and H_2O are the main by-products of

any complete combustion of carbonaceous material [*Langmann et al.*, 2009] with incomplete combustion resulting in additional compounds emitted such as CO, CH_4 and other volatile organic carbon compounds (see *Andreae and Merlet* [2001] for a more complete list). Less than 5% of the emitted carbon is particulate matter [*Reid et al.*, 2005a]. However, smoke aerosols perturb the atmospheric radiation budget due to their light-scattering and absorption effects and their effects on cloud processes (see *Langmann et al.* [2009] and references therein). The emission of CO and other organic hydrocarbons in combination with nitrogen oxides leads to photochemical formation of ozone. Tropospheric ozone is detrimental to life and plants, and acts as a greenhouse gas within the lower atmosphere [*Langmann et al.*, 2009].

A large proportion of global smoke originates from burning in the tropics [*Andreae and Merlet*, 2001]. However, fires from extra-tropical latitudes also provide sources of smoke particles that undergo long-range transport and interact with the atmosphere on a global scale. Extra-tropical biomass burning events can significantly increase the atmospheric abundance of carbon monoxide (CO), sometimes by as much as a quarter of the global CO emissions from all surface fires [*Goode et al.*, 2000]; [*Lavoué et al.*, 2000].

CO is often used as an atmospheric tracer of smoke pollution transport from boreal forest fires [*Forster et al.*, 2001]. Ground-based and satellite-based techniques have confirmed that biomass burning emissions significantly perturb tropospheric levels of CO [*Galanter et al.*, 2000]. *Waibel et al.* [1999] observed high CO concentrations near the tropopause over Europe, due to smoke emitted from forest fires in Canada. If there is significant heat energy released from a powerful fire event leading to convection, then CO can be transported to the lower stratosphere [*Fromm et al.*, 2010];[*Siddaway and Petelina*, 2011]; [*Pumphrey et al.*, 2011].

1.7 Pyrocumulonimbus smoke plumes

The standard model for lower stratospheric aerosols, outside of the polar regions (i.e PSCs), is that they consist of material that originates from the troposphere due to slow

cross-tropopause ascent in the tropics, or by rapid injection via volcanic eruptions [*Thomason and Peter*, 2006]. As a result, models of the middle atmosphere often do not take into account any other process for troposphere-to-stratosphere transport [*Fromm et al.*, 2010]. Past studies of stratospheric aerosol loading on decadal time-scales have often supported this canonical model, with no reported observations of unusual local aerosols at mid-latitudes [*Deshler*, 2008], until observations of forest fire smoke in the stratosphere in 1998 were reported by *Fromm et al.* [2000].

The term pyrocumulonimbus (pyrocb) refers to large thunderstorms that are initiated or intensified by a large fire. Extreme pyrocb events provide enough energy through pyroconvection, that biomass burning emissions penetrate the extratropical tropopause and are injected into the lower stratosphere. Pyrocb events are particularly energetic events, in comparison with pyrocumulus convection events, which have been known about for decades [*Fromm et al.*, 2010]. *Fromm et al.* [2000] observed a significant increase in stratospheric aerosols in satellite solar occultation measurements between May-October 1998 at northern mid-latitudes, in the absence of any reported volcanic eruptions. Aerosol perturbations were observed at 3-5 km above the tropopause, originating from several fires in Canada and Russia, based on isentropic trajectories. A zonal mean increase in stratospheric aerosols persisted for 3 months according to *Fromm et al.* [2000].

Following on from the *Fromm et al.* [2000] paper, one study found enhancement of stratospheric methyl cyanide (CH_3CN), a known biomass burning product, due to fire activity over the U.S in 1992 [*Livesey et al.*, 2004]. That study observed CH_3CN enhancements at 100-68 hPa. *Jost et al.* [2004] presented observations of a 2002 northern mid-latitude forest fire smoke plume that was transported from the planetary boundary layer to the lower stratosphere (up to 15.8 km in altitude), containing aerosols and enhanced CO within the plume. It was speculated that this plume could affect stratospheric O_3. A two part study of a pyrocb event over Alberta, Canada looked in depth at characterising the impact of this injection into the stratosphere [*Fromm et al.*, 2008a]; [*Fromm et al.*, 2008b]. *Fromm et al.* [2008a] used satellite instruments to study the convective phase and short-term aftermath (from approximately 3 hours after ignition to 1 week af-

ter), considering the initial transport of the smoke plume from North America to Western Europe, its plume mass and particle size distribution. The second study [*Fromm et al.*, 2008b] synthesised a range of profile measurements to resolve particle radii, and found that the smoke pollution had extended from 20°N to 79°N within a month of ignition. This doubled the zonal average aerosol optical depth in the lower stratosphere.

Firestorms in southeast Australia during January 2003 resulted in a pyrocb event that produced a stratospheric injection [*Fromm et al.*, 2006], the first pyrocb event reported in the SH. This pyrocb was small, both temporally (approximately 3 hours) and spatially (approximately 10 km) in scale but of sufficient power to pollute the austral stratosphere with sunlight absorbing aerosols.

It has been established that biomass burning smoke plumes from well-known tropical regions such as the Amazon Basin [*Crutzen and Andreae*, 1990]; [*Lin et al.*, 2006] and Indonesia [*Folkins et al.*, 1997] are often quite large in horizontal extent and optically thick, thus strongly absorbing. The Total Ozone Monitoring Spectrometer (TOMS) satellite produces profiles of absorbing aerosol index (AI). For most of the TOMS satellite era, optically thick smoke plumes from biomass burning had previously never exceeded an AI value of 12 [*Fromm et al.*, 2010]. However, recent studies [*Fromm et al.*, 2008a] found that smoke plumes associated with these pyrocb events exceeded an AI value of 12. A table of the greatest TOMS AI values, between 1978 and 2005 can be found in *Fromm et al.* [2010]. Of the top 20 AI plumes, 13 of them are the result of documented or otherwise determined pyrocb events [*Fromm et al.*, 2010]. The Chisholm fire [*Fromm and Servranckx*, 2003] of 2001 tops the list of day-old smoke values with an AI of 29.9. The 2009 Black Saturday bushfire also reached a maximum AI value of 29.9, ranking it as one of the most optically thick smoke plumes ever observed. The pollution from this bushfire is central to this thesis. An outline of this study is given below.

Chapter 2 presents a month-by-month statistical analysis of Antarctic ozone from September-December during the 21st century as predicted by CCMVal-2 model simulations. It covers the period of time during the late spring-early summer when the polar vortex breaks up and therefore ozone-poor air is transported to lower latitudes in the

southern hemisphere. The later the breakup of the polar vortex, the greater the possible effect on mid-latitude ozone concentrations during the summer months.

Chapter 3 is also an analysis of CCMVal-2 model simulations, considering the effect of ozone zonal asymmetry from quasi-stationary planetary waves (QSW) using seasonal data of both spring and summer, and can be considered an extension of the *Grytsai et al.* [2007] study. This chapter considers model results during the observation period of 1979-2005 and compares with TOMS observations over the same time period. Fourier decomposition of the TOC field over 5 degree latitude bands allowed an investigation into the effect of QSWs on the longitudinal ozone distribution. The analysis also extends to the 21st century with future model simulations of TOC zonal asymmetry due to anthropogenic forcings alone, using projected GHG emissions and ODS concentrations.

In Chapter 4 the initial investigation into the transport of the smoke plume from the Australian Black Saturday bushfires from February 2009 is presented. This event provided a unique case study of the effect of biomass burning pollution on the lower stratosphere in the Southern Hemisphere. To our knowledge, this is the first time that bushfire aerosols have polluted the stratosphere for months after the bushfire in the Southern Hemisphere.

Chapter 5 introduces a novel method of using satellite limb radiance spectra, to show qualitatively that the smoke pollution from Black Saturday provided local enhancement of water vapour to the dry lower stratosphere in the weeks following ignition. This suggests, via a pyroconvection event, an atypical pathway for water vapour to be entrained into the mid-latitude stratosphere.

Finally, Chapter 6 investigates the impact of bushfire smoke aerosols on ozone concentrations within the austral summer stratosphere, using satellite measurements of carbon monoxide as a tracer, to identify the smoke plume in the Southern Hemisphere.

2 Evolution of Antarctic ozone from September-December predicted by CCMVal-2 model simulations

2.1 Introduction

It has been almost 30 years since the first measurements of significant stratospheric ozone depletion over Antarctica [*Farman et al.*, 1985] were linked to increasing anthropogenic halogen loading [*Solomon et al.*, 1986]. A peak in total combined chlorine compounds in the troposphere was observed in the mid-1990s, and the level of these substances are now mostly either zero or in decline [*WMO*, 2007]. In the stratosphere, the potential of ozone depleting substances (ODSs) is often measured by Equivalent Effective Stratospheric Chlorine (EESC) levels. EESC combines Cl_y and Br_y into a single quantity that leads to ozone depletion. Following on from the decline in surface emissions of ODSs, global mean concentrations of EESC are now decreasing as well [*Newman et al.*, 2007].

Establishing if the ozone layer over Antarctica has begun to recover and how long the recovery to pre-ozone hole levels might take is important, as this information can inform future policy on halogen compound production. The subject of when the ozone will recover and at what rate has many other important implications, such as possible effects on surface climate in Antarctica [*Perlwitz et al.*, 2008]) and over the Southern Hemisphere (SH) in general [*Son et al.*, 2010]. Antarctic ozone increase may also affect lower stratospheric circulation and mean age of air [*Deushi and Shibata*, 2011].

Numerous results on regional and global ozone and climate applications have already been derived from CCMVal-2 model simulations [*Eyring et al.*, 2010c]. These simulations are outlined in detail in Section 2.3. CCMVal-2 model studies that consider future projections of total ozone column (TOC) often use annual globally averaged TOC over extra-polar latitudes and mean October monthly zonal mean TOC values to represent Antarctic spring ozone trends [*Austin et al.*, 2010a]). Differing from other studies, the present analysis focuses on unique aspects of future Antarctic ozone increase, in particular monthly rates and speeds of TOC increase in austral spring and early summer (September-December).

Several studies have investigated the predicted relationship between stratospheric chlorine loading and TOC from CCMVal-2 model output [*Eyring et al.*, 2010c]; [*Oman et al.*, 2010]. *Austin et al.* [2010a] considered the decline and recovery of Antarctic October multi-model mean TOC using CCMVal-2 future simulations with respect to both a 1960 and a 1980 baseline. A direct comparison of October mean Cl_y at 50 hPa and TOC found a very similar trend between the two, when a 1980 baseline is selected, with both quantities returning to baseline values in 2055. When a 1960 baseline is chosen, the October mean Cl_y at 50 hPa does not return to baseline before the end of the century, and the October TOC returns shortly before 2100. *Oman et al.* [2010] found a similar result, relative to a 1960 baseline, when considering the partial column ozone at 500-20 hPa. These model studies indicate that EESC levels will greatly influence the return pattern of increasing ozone subsequent to peak depletion. The effect of increasing GHG emissions on climate change will also affect the ozone return date to a 1960 value, especially towards the end of the 21st century.

In this thesis, projections of Antarctic ozone increase due to both decreasing ODSs and climate change are considered, rather than a relationship between stratospheric chlorine levels and ozone. Ozone recovery is usually expressed in terms of the ozone increase that is related to removal of anthropogenically produced ODSs [*WMO*, 2007]. Ozone return date refers to ozone recovery to a pre-defined level (or reference year such as 1980 or 1960) prior to the depletion period. As a result, return of stratospheric ozone to a certain

pre-defined value and a full ozone recovery can be reached at different times [*Waugh et al.*, 2009a];[*Eyring et al.*, 2010c]).

Newman et al. [2006] found that full ozone recovery to 1980 levels, based purely on future ODS levels, will occur around 2068. *Oman et al.* [2010] considered evolution of partial columns in the 21st century and found that for the lower stratosphere (integrated over the 500-20 hPa range), peak spring ozone (October) returned to 1960 levels in 2090. That study included a similar selection of future model simulations as were used in this study, as shown later in the chapter. *Oman et al.* [2010] also calculated a multi-model trend in EESC at 50hPa and found a decrease to 85% of 1960 levels by 2100 (see Figure 10 in *Oman et al.* [2010]), attributing much of the trend in the lower stratosphere October ozone to the trend in EESC. *Eyring et al.* [2010b] considered different GHG sensitivity simulations for CCMVal-2 models and found that the SRES A2 scenario (more GHGs by 2100 than in the A1B scenario) resulted in a decrease of ozone in the lower stratosphere during the 21st century. The B1 scenario (less GHGs by 2100 than in the A1B scenario, *Nakićenović and Swart* [2000]) leads to an increase in ozone by the end of the century. However, the overall differences resulting from different GHG scenarios were minor. Alternatively, *Waugh et al.* [2009a] found that when the effect of climate change alone was considered, there were minimal decadal-scale variations in Antarctic spring ozone from 1960 until 2100. In that study, mean October ozone volume mixing ratio (VMR) at 50 hPa, as well as October TOC, were predicted to recover to a 1960 value by 2100 due to the combined forcing effect of GHG and ODS. Using a single CCM, *Perlwitz et al.* [2008] found that with chlorine fixed at 1960 values and using the A1B GHG scenario, October ozone at 70 hPa did not fluctuate significantly in 2000-2099. However, it is possible that 1960 levels of chlorine were not sufficient to exert enough influence on ozone, compared to the amount that was observed in the mid 1990s.

The aim of this study is to analyze Antarctic ozone evolution and return dates with respect to a historical baseline of 1960-1969 values using the model output from the most comprehensive collection of CCM data available. This baseline level is an averaged value of TOC that has not yet been significantly perturbed by ODS. There are differing opinions

on what time period to select as a baseline for ozone recovery estimations. It is common to use the 1980 value [*WMO*, 2007];[*WMO*, 2011]), which is an average of 1975-1984 values, as Antarctic ozone depletion was relatively small at that time. On the other hand, *Newman et al.* [2007] reported that EESC have been increasing rapidly before 1985, and thus the 1975-1984 baseline period may not correspond to the unperturbed ozone state.

In this work, a baseline derived from a mean of 1960-1969 values is used, hereafter referred to as a 1965 baseline, as stratospheric ozone was not yet significantly affected by anthropogenic halogen emissions at that time [*Farman et al.*, 1985]. This is further supported by the *Jones and Shanklin* [1995] results, who found that a decline in the ozone concentration during October was apparent in the early 1970s, while *Hofmann et al.* [1997] looked at 10 years of ozonesonde data from the South Pole and found that there was no ozone depletion before 1970. The results presented here were published in *Siddaway et al.* [2013].

2.2 Data analysis

In this chapter, the projected evolution of Antarctic ozone is investigated using monthly mean simulated TOC data in September-December, zonally averaged poleward of 60°S and variations of TOC with respect to the corresponding pre-ozone hole baseline levels. While many studies that focus on the ozone hole employ multi-model mean TOC values, the multi-model median (MMM) TOC and ozone VMR are used here. As the spread in individual model outputs can be large, especially for ozone concentrations at various pressure levels, using the median function gives an advantage of assigning a lower weight to the most deviating data. To quantify the uncertainty associated with the MMM trends to a 95% confidence limit, a bootstrapping technique was used. In order to generate the statistical uncertainty, a subsample of individual model median values was randomly sampled with replacement 1000 times to produce a normal distribution of medians. From this distribution, a confidence limit was calculated.

Previous CCMVal-2 model studies [*Eyring et al.*, 2010c]; [*Austin et al.*, 2010a], analysed

a multi-model mean with associated uncertainties using a Time-Series Additive Model (TSAM), as described in Chapter 9 of *Eyring et al.* [2010a] and in *Scinocca et al.* [2010]. The advantage of using this technique, is that model simulations of various time lengths can still be used to produce a robust mean trend over the full reference period of 1960-2100. In this study, only the model simulations that provided output over the entire study period were selected. It was also found that using a 1960 value as a baseline in the TSAM analysis resulted in a larger inter-model spread in TOC, compared to a 1980 baseline value [*Eyring et al.*, 2010a]. Investigating MMM TOC and ozone VMR from model time series of equal lengths relative to a 1965 baseline, as is done here, is considered advantageous as a lower weight is assigned to individual models that deviate mostly from the median.

In addition to TOC, effects of a projected ozone increase in the 21st century on the polar vortex is also analyzed by assessing monthly temperature and zonal mean zonal wind variations over the September-December period. This is in contrast to previous CCMVal-2 model studies which consider seasonally averaged values of temperature and zonal wind [*Eyring et al.*, 2010a]; [*Son et al.*, 2010], rather than on a month-by-month basis. This chapter expands on results presented in *Siddaway et al.* [2013].

2.3 Model simulations

Stratospheric Processes and their Role in Climate Project (SPARC) Chemistry-Climate Model Validation phase 2 (CCMVal-2) activity [*Eyring et al.*, 2010a] is a coordinated model intercomparison that included results from up to 17 CCMs, with some models providing a wider variety of simulations than others. Sixteen of these models provide future reference simulations (REF-B2), up to the end of the 21st century [*Eyring et al.*, 2010c]. REF-B2 simulations are transient simulations from 1960 to 2100 that contain time series of surface hydrocarbon halogens based on the adjusted World Meteorological Organization (WMO) A1 scenario [*WMO*, 2007] and surface GHG concentrations based on the Special Report on Emissions Scenario A1B [*Nakićenović and Swart*, 2000]. These REF-B2 simulations of the future atmospheric state include anthropogenic forcings only,

such as varying GHG surface concentrations and prescribed halogen emissions, with natural forcings due to solar variability and volcanic activity excluded. This is different from REF-B1 simulations that include both natural and anthropogenic forcings [*Eyring et al.*, 2007].

Austin et al. [2010b] analyzed metrics of the Antarctic ozone hole, such as minimum ozone and ozone mass deficit, from CCMVal-2 model output by comparing both REF-B1 and REF-B2 simulations. Such an approach is not considered in this study, as it is preferential to work with a continuous and homogenous dataset, whereas these two sets of simulations have different sources of uncertainty in their model integrations. REF-B1 simulations address internal uncertainties within each model with external forcings being based on observations, whereas REF-B2 simulations have external uncertainty associated with biases from climate models that provide prescribed forcings. Of all models used in this study, a quasi-biennial oscillation (QBO) signal is only included in those models that internally simulate QBO; namely MRI, UMSLIMCAT and the UKUCMA [*Eyring et al.*, 2010a]. All models except CMAM have prescribed sea surface temperature (SST) and sea ice cover (SIC) from coupled ocean model simulations [*Austin et al.*, 2010a]; [*Morgenstern et al.*, 2010]. A more detailed description of each model formulation is given by *Eyring et al.* [2010a] and by *Morgenstern et al.* [2010] and will not be repeated here.

Monthly mean TOC values were available for 14 models that participated in the REF-B2 simulations. Two out of these 14 models were excluded from the present analysis: GEOSCCM provided a future simulation only from 2000 and UMUKCA-METO only provided data until 2083. Monthly mean ozone VMR values were available for 11 models out of the 12 selected for TOC values. However, all 12 models were used for stratospheric temperatures and zonal mean wind metrics.

There were variations in the ensemble size for each model. Most models provided a single ensemble member, with the exception of MRI (2 ensemble members) and the CMAM, SOCOL, ULAQ and WACCM models (3 ensemble members). For each model with more than one ensemble member, their mean value was used. The analysis presented below of TOC was also repeated using the first ensemble member only, as was done in

Oman et al. [2010]. It was found that using multiple ensembles for the models listed above did not provide any noticeable differences compared to using the first ensemble member only.

2.4 Results

2.4.1 Trends in total column ozone

CCMVal-2 REF-B2 simulations of TOC from each CCM used in this study are shown in Figure 2.1. Model outputs, although widely spread, show a TOC minimum around the year 2000 for all months, which is in agreement with *Eyring et al.* [2010c]. The October MMM TOC trend in Figure 2.1 is in good qualitative agreement with other CCMVal-2 studies [*Austin et al.*, 2010a];[*Eyring et al.*, 2010c], based on the 1965 baseline, but quantitatively is approximately 50 DU lower then that found in *Eyring et al.* [2010c]. This is possibly due to differences in statistical analysis techniques (TSAM analysis) that was used in that study, and that only a subset of the models in *Eyring et al.* [2010c] are used in this study for reasons that have been previously explained. Note that TOC trends for the other months shown in Figure 2.1 are not directly compared to other studies due to the fact that other studies did not provide such results for September, November and December.

Figure 2.1 also shows that MMM TOC trends agrees well, within the 95% confidence interval, with satellite observations from 1979-2011. These observations are zonally averaged monthly mean TOC values measured by the Total Ozone Mapping Spectrometer (TOMS) Merged Ozone Dataset (MOD) [*Stolarski and Frith*, 2006]. While some individual model outputs show good agreement with observations, other models produce either too high, or too low TOC values. However, this bias is not consistent for all months considered, except UMUKCA-UCAM that has a consistently high bias for all months, which has been previously reported [*Eyring et al.*, 2010a], and UMSLIMCAT that has a generally low bias for each month, as seen in the initial model trend estimate in *Austin et al.* [2010b].

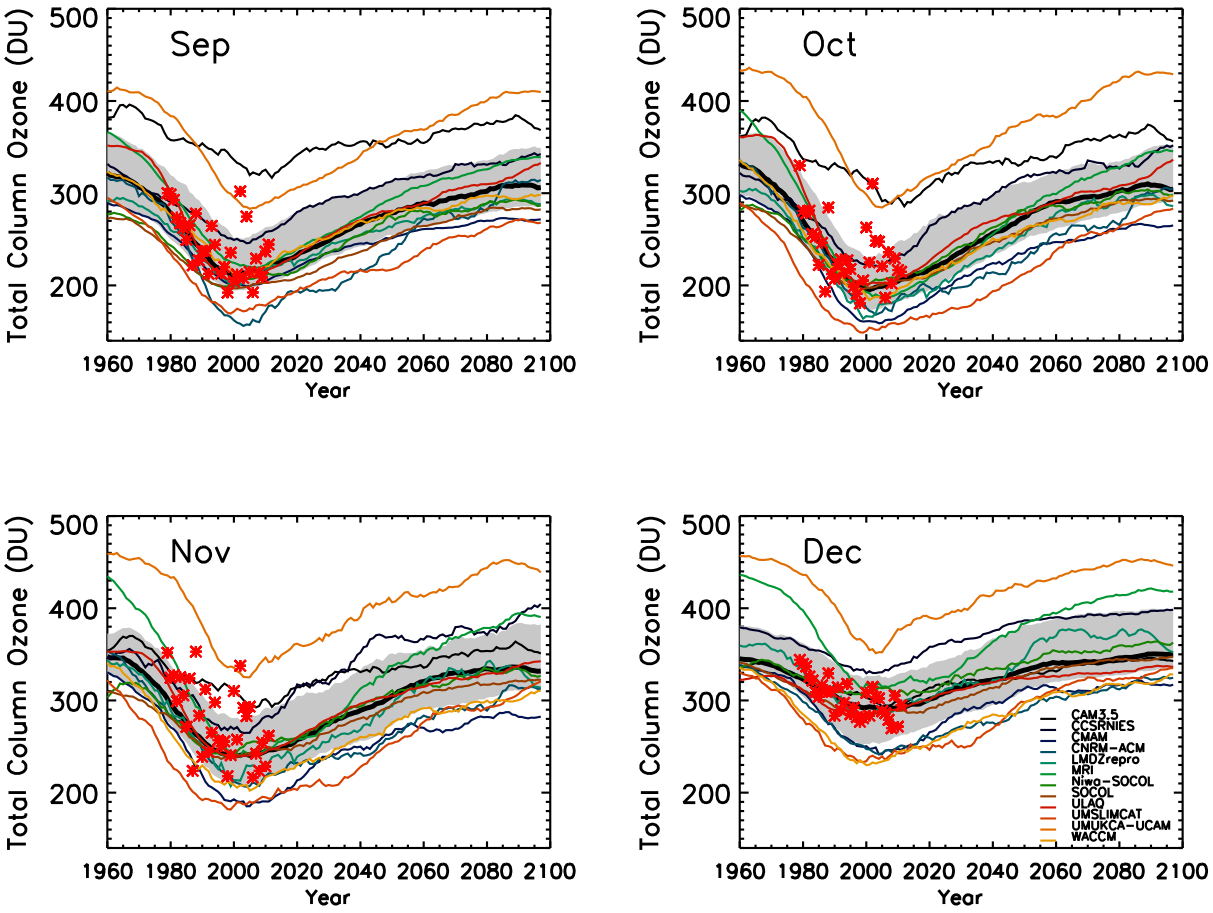

Figure 2.1: Total Column Ozone (TOC) time series zonally averaged poleward of 60°S from selected models as indicated on the bottom right panel. Thick black curve is the multi-model median (MMM), the grey area represents the 95% confidence limit of the median derived using a bootstrapping method. Data are smoothed with a 15-year uniformly weighted sliding mean filter. Red stars indicate zonally averaged unsmoothed TOC values poleward of 62.5°S from the TOMS version 8.5 merged ozone dataset (MOD) for 1979-2011.

As the individual model intercomparison and validation is not part of this work, no model was excluded based on their agreement with the TOMS TOC in Figure 2.1. Part of the reason for this is that some models are in good agreement with the measured TOC, but not in a good agreement, with one another, regarding zonal winds or temperature that are considered later in this study. Nevertheless, all steps of the analysis presented here, were repeated for only those 4 models that show a consistent agreement with TOMS TOC for each month considered in this study (not shown). These models are LMDZrepro, Niwa-SOCOL, SOCOL, and ULAQ. It was found that this narrow selection

of models did not significantly change the main results and conclusions of this work, including TOC return dates to the 1965 baseline, and speeds and rates of TOC increase. This could be, in part, due to the fact that the bootstrapping statistical analysis technique employed here minimises the effect of individual outliers when the MMM trend is calculated. Moreover, the interannual variability in TOMS data results from variability associated with combined natural and anthropogenic forcings, while CCMVal-2 models consider anthropogenic forcing only.

European Centre for Medium-Range Weather Forecasts (ECMWF) ERA-Interim reanalysis data [*Dee et al.*, 2011] in 1979-2010 were also compared (not shown) with CCMVal-2 TOC values and, similar to the TOMS data shown in 2.1, were within the 95% confidence interval of the MMM trends. Also CCMVal-2 models used here have a range of grid resolutions [*Morgenstern et al.*, 2010] that could possibly introduce a statistical bias with different sample populations contributing to individual model TOC trend values that are zonally averaged. In order to investigate this further, time series of ozone mass poleward of 60°S were produced. These results (not shown here) suggest that differences in model grid resolutions do not affect the analysis presented in this work.

Differing from CCMVal-2 model data, TOMS data in Figure 2.1 are not smoothed. To better illustrate how these datasets compare when treated in the same way, both datasets were smoothed with a 5-year uniformly weighted running filter over the 1979-2011 time period, shown in Figure 2.2. The MMM values do not fully capture the interannial variability seen in the observations. MMM trends seem to underestimate TOC values earlier in the observation period for most months, but overestimate the TOC peak depletion values in the beginning of the 21st century. As many previous studies used multi-model mean trends instead of median, both trends are shown in Figure 2.2. There is no significant advantage to using mean trends, particularly at the beginning of the simulation period. However, as was mentioned earlier, median values assign lower weight to the most deviating results that occur later in the simulation period.

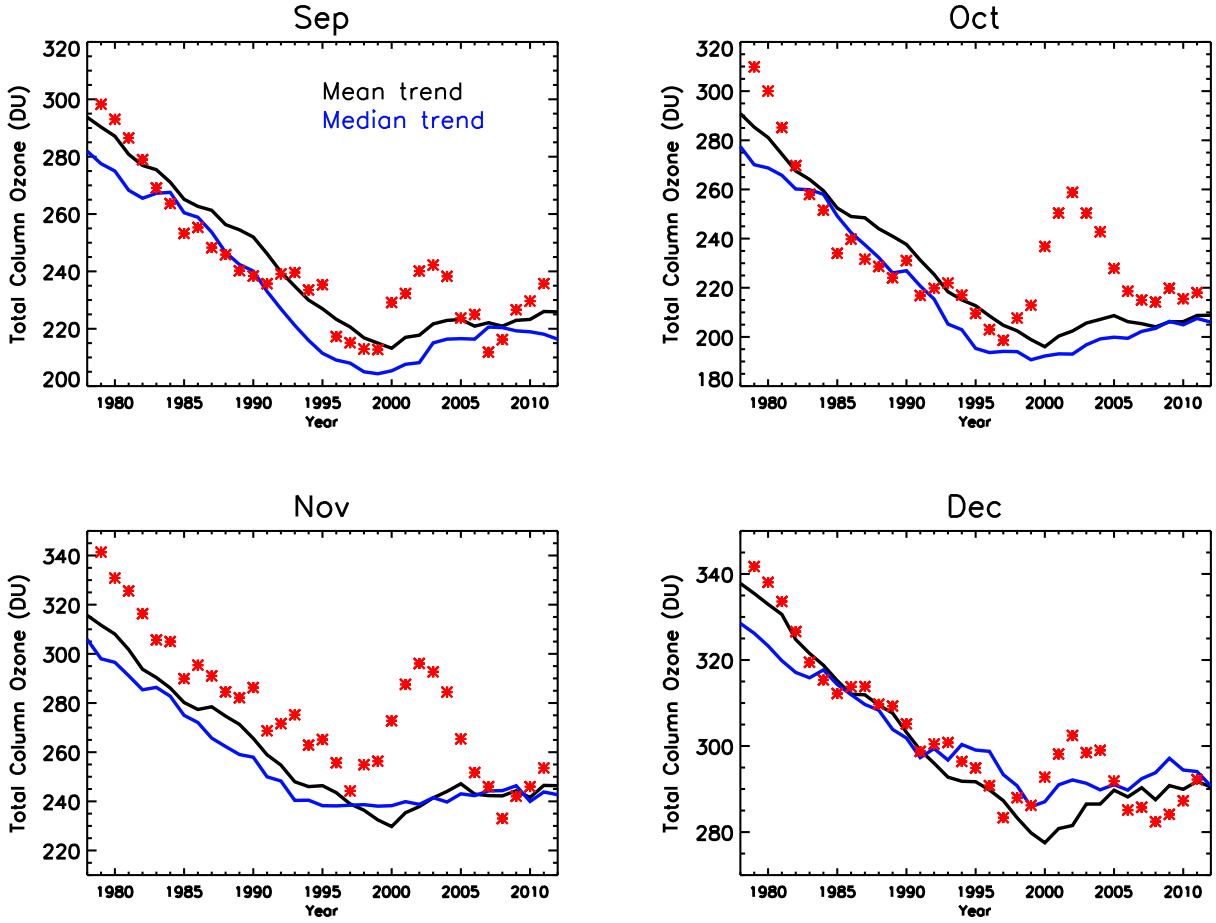

Figure 2.2: Multi-model median (blue) and mean (black) TOC time series in comparison with TOMS observations during the 1979-2011 period. Both datasets have been smoothed with a 5-year uniformly weighted sliding mean filter.

Multi-model monthly zonal median TOC deviation from the 1965 baseline for the period of 1960-2100, both as a percentage and an absolute deviation, are shown in Figures 2.3 and 2.4, respectively. These results suggest that September-November TOC does not return to its 1965 level by the end of the simulations (2098), but is within 1% (about 3 DU) of the 1965 baseline in 2090. A slight decrease again after 2090 may be a result of increasing influence of GHG cooling in the lower stratosphere towards the end of the 21st century. December TOC returns to the 1965 baseline in 2079 and continues to increase to approximately 2% (about 8 DU) above the baseline towards the end of the century. September - November TOC have an earliest return date in the 95% confidence interval between 2065-2075 (Figure 2.4). The lowest uncertainty range for the December TOC

return date is about 30 years. As all models in this study use the same REF-B2 scenario (same projected increase in GHGs and decrease in ODSs), the uncertainty associated with the scenario is common for all models. However, uncertainties amongst the individual model uncertainties will vary. *Charlton-Perez et al.* [2010] analyzed interannual variability, scenario and model uncertainties in four CCMVal-2 models for October and found that for Antarctic latitudes, the combined uncertainty due to the above mentioned factors, ranges between 15 and 30 DU during the 21st century.

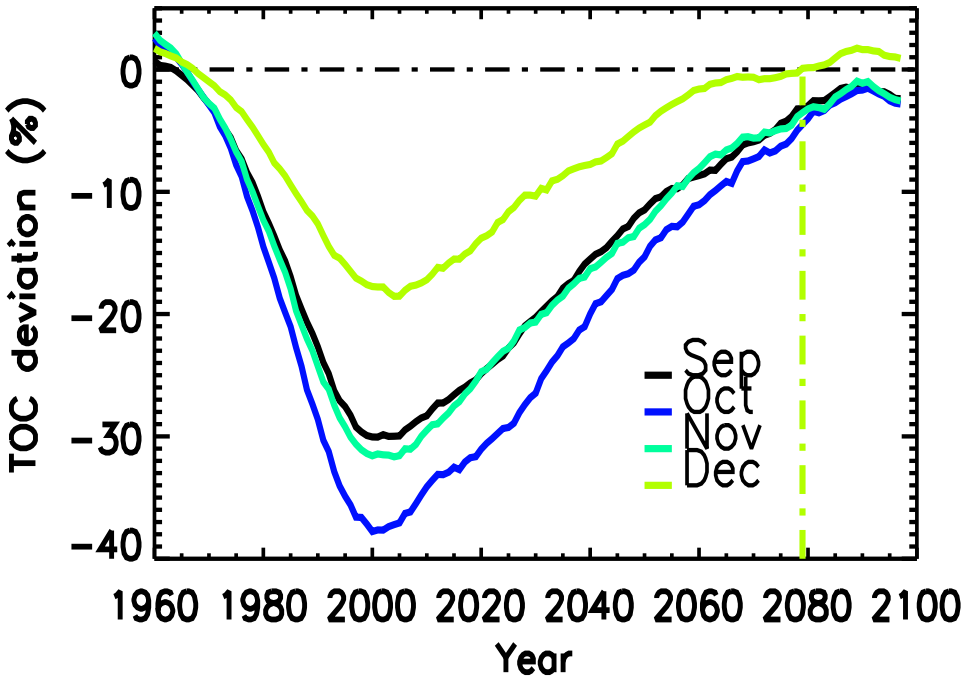

Figure 2.3: Time series of multi-model TOC median values for September-December as percent deviations from the 1965 baseline. Curves have been smoothed as described in Figure 2.1. TOC return dates to the 1965 baseline are shown by dashed-dotted lines and color-coded by the corresponding month.

The highest monthly ozone depletion of approximately 130 DU relative to the 1965 baseline, occurs in October as seen in Figure 2.4. This is about 50 DU larger than the ozone depletion relative to the 1980 baseline in REF-B2 simulations, but comparable to that for the 1960 baseline reported in previous CCMVal-2 model studies [*Austin et al.*, 2010b]; [*Eyring et al.*, 2010c]. Figure 2.4 also shows that the minimum TOC value for all

months is between 2000 and 2005. Assuming that the ozone hole is defined as a region where TOC values are less than 220 DU [*Newman et al.*, 2004], its size calculated from CCMVal-2 model outputs (not shown here), also reaches a maximum between 2000-2005.

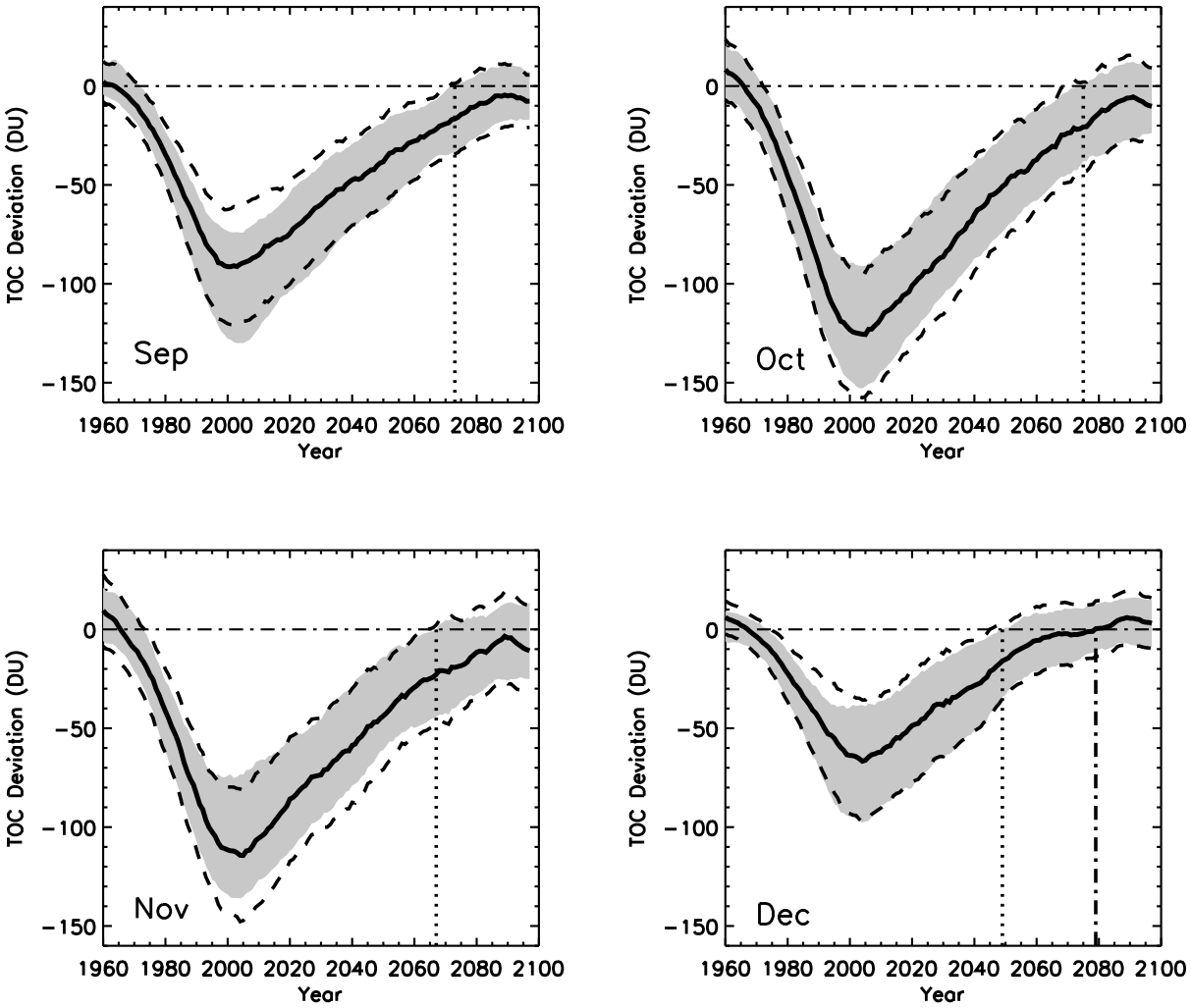

Figure 2.4: Time series of deviations for multi-model median TOC from the 1965 baseline for each month. The median TOC return date for December is shown by the vertical dot-dashed line. Shaded area is the 95% confidence limit of the median with the lower limits return dates shown by vertical dotted lines. Dashed curves show the median absolute deviation range.

Table 2.1: Decadal rates and speeds of TOC increase poleward of 60°S as a percentage of 1965 baseline (Case A), in DU/decade (Case B), and as a percentage relative to maximum depletion (baseline minus ∼ year 2000 conditions) (Case C). Bold italicized numbers indicate decades when December TOC has exceeded its 1965 baseline value.

Decades of 21st Century Decadal TOC rates										
Month	Case	2000-09	2010-19	2020-29	2030-39	2040-49	2050-59	2060-69	2070-79	2080-89
Sep	A	1.99	3.62	4.4	5.29	3.82	2.95	1.64	2.06	2.01
	B	6.45	11.69	14.2	17.07	12.32	9.51	5.3	6.65	6.49
	C	13.11	7.65	15.59	13.54	3.99	6.75	5.97	10.08	0.36
Oct	A	2.42	3.2	5.25	5.48	4.88	4.81	1.52	1.76	2.29
	B	7.97	10.53	17.27	18.01	16.04	15.82	4.98	5.8	7.53
	C	9.43	11.24	5.66	9.55	11.59	2.03	8.91	9.45	16.14
Nov	A	0.97	2.71	4.58	3.72	3.82	4.23	2.51	1.14	0.53
	B	3.42	9.5	16.07	13.04	13.41	14.84	8.82	3.99	1.85
	C	13.27	0.55	8.61	12.74	19.73	13.99	14.52	11.14	14.55
Dec	A	-0.17	2.13	3.52	2.21	2.66	2.29	0.5	***1.06***	***1.16***
	B	-0.57	7.62	12.58	7.9	9.53	8.21	1.78	***3.79***	***4.14***
	C	22.48	18.04	1.56	3.51	10.73	6.09	6.94	***5.12***	***6.89***

Figures 2.3 and 2.4 suggest that the rate of December TOC increase is slower than that for September-November months, even though the recovery of December TOC to baseline occurs earlier. This effect is quantified in Table 2.1, where the decadal TOC increase speeds (in DU/decade) and rates (in percent relative to baseline and in percent relative to the maximum depletion value) are presented.

2.4.2 Trends in ozone VMR at UTLS altitudes

Figure 2.5 shows vertical profiles for deviations of ozone VMR from baseline in the pressure range where the majority of atmospheric ozone over Antarctica is located and where most of the depletion takes place [*Solomon et al.*, 2005]. In September - October, the percentage (absolute) polar ozone loss is greatest at 70 (50) hPa, and in November - December at 100 (70) hPa. Thus, the region of the largest ozone loss moves from higher altitudes early in the ozone depletion season to lower altitudes later in the ozone depletion season.

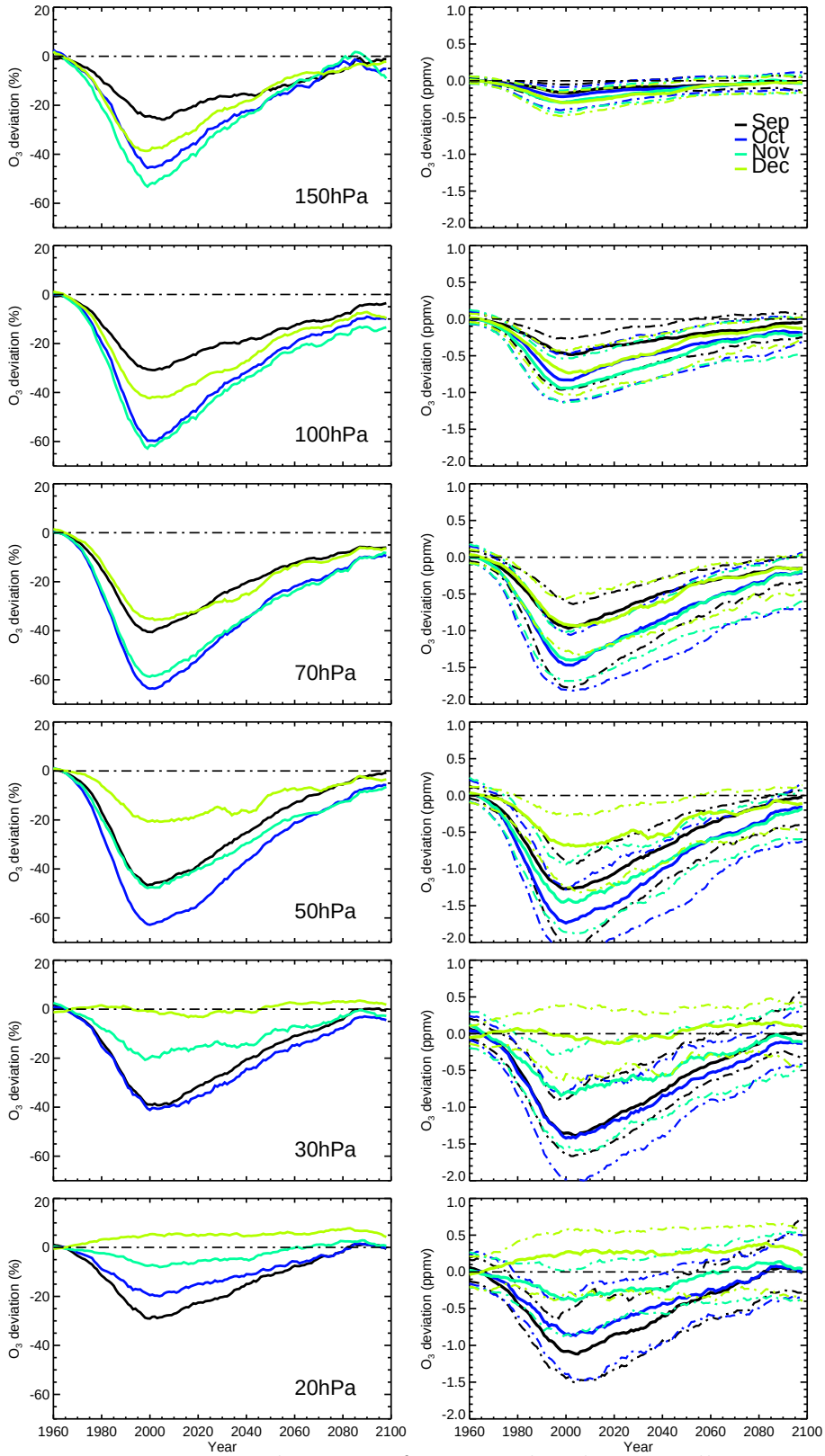

Figure 2.5: MMM ozone VMR deviations from 1965 baseline, zonally averaged poleward of 60°S for all available pressure levels in the range of 20-150 hPa. Left panels - percent deviation from baseline, right panels - absolute deviation from baseline. Dot-dashed lines indicate 95% confidence level of MMM. Trends have been smoothed with a 15-year boxcar filter.

This result is supported by observations of chemical tracers, which show that in spring, air transport within the Antarctic stratosphere is directed downwards [*Solomon*, 1999]. It is also supported by one of the conclusions in *Eyring et al.* [2010a], that by early summer, the breakdown of the polar vortex and the strengthening Brewer-Dobson circulation results in the transport of ozone-rich air to higher latitudes. A recent observational example of this effect was the time series of zonally averaged vertical ozone profiles poleward of 60°S in 2002-2009 reported in *Klekociuk et al.* [2011]. In that example, the upper edge of the ozone hole descends from about 19 km in early October to around 15 km in early December.

Based on 25 years of ozonesonde measurements at the South Pole and the Georg-Forster and Neumayer Antarctic stations, *Hassler et al.* [2011] investigated minimum daily ozone VMR at 50 hPa from late September until early October. Their data, as a vertical profile of percent ozone loss for 5 year averages between day 235 and 270 (see their Figure 5c) indicate that the loss rates increased at 150-50 hPa, but decreased at 40-20hPa. CCMVal-2 model projections for the same months show the maximum ozone loss occurring between 70 and 50 hPa, which agrees well with the measurements of *Hassler et al.* [2011].

At 150 hPa, the deviation of ozone VMR from baseline is smallest, and a return to near baseline values occurs by 2065 for all months. Above 150 hPa, as the pressure decreases (altitude increases), the December, and to a lesser extent November, ozone shows less depletion. December ozone VMR at 70 hPa, in comparison with the spring months, begins to show a noticeable slow down in the rate of its increase. This effect becomes even more pronounced at 50 hPa. At 30 hPa, the December ozone is not significantly depleted with its VMR deviating from the baseline by 0.2 ppmv, or less, which is about 5% of the baseline value. At 20 hPa, the December ozone VMR remains above the baseline, and the November ozone VMR is lower than the baseline by less than 0.4 ppmv, also about 5% of the baseline value. These are the likely reasons for the observed somewhat slower December TOC increase in 2010-2050 shown in Figures 2.3 and 2.4 and in Table 2.1.

2.4.3 Trends in stratospheric temperatures and winds

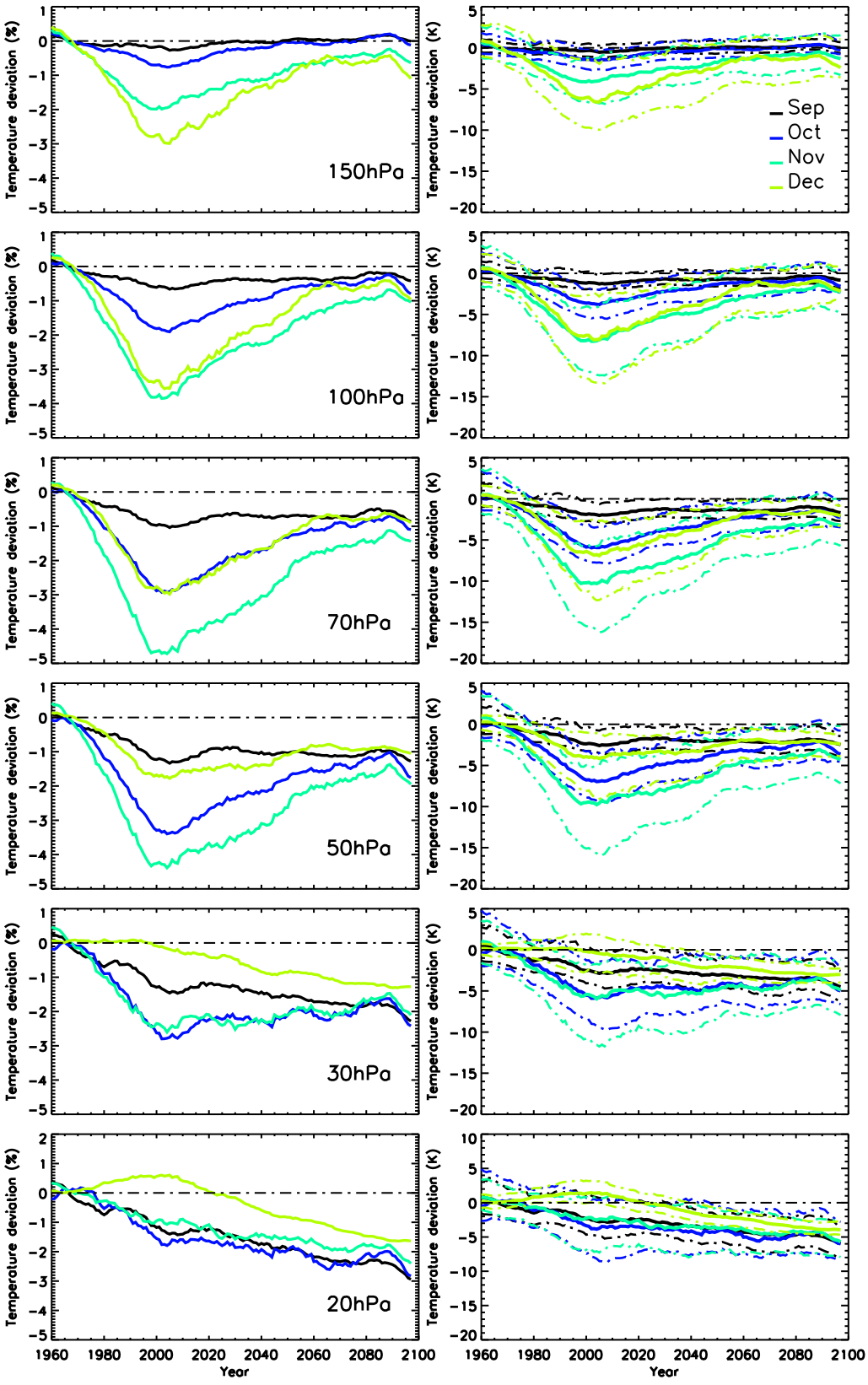

Figure 2.6: Same as in Figure 2.5, but for multi-model median temperatures.

In order to better understand projected Antarctic ozone recovery trends, particularly the slower TOC increase in December, trends in stratospheric temperature and winds have been investigated as shown in Figures 2.6 and 2.7, respectively. These parameters, also provided by CCMVal-2 model simulations, relate to changes in the size and strength of the polar vortex as ODSs concentration decrease and GHGs concentration increase [*Waugh and Polvani*, 2010]. Monthly zonal mean fields for these metrics were obtained at the same pressure levels as ozone VMR in Figure 2.5.

Zonal mean temperatures were calculated poleward of 60°S, whereas zonal mean zonal wind speeds were averaged over the 50-70°S range. This range covers latitudes where the edge of the polar vortex is expected to be located throughout the 21st century. Figure 2.6 suggests a general decrease in the lower stratospheric temperatures until 2000, a time when ozone was decreasing as well. Together, Figures 2.5 and 2.6 indicate a correlation between lower stratospheric temperatures and ozone levels. Such a correlation is likely to arise from temperature-dependent heterogeneous polar stratospheric chemistry including the production of gaseous Cl_2 and other metastable compounds on polar stratospheric clouds (PSCs) prior to photolysis, together with horizontal and vertical transport of air caused by planetary waves [*Wirth*, 1993]; [*Solomon et al.*, 2005].

At 150 hPa, CCMVal-2 multi-model temperatures return to a 1965 baseline by the end of the 21st century for September-October months. For all other altitudes and months examined in this study, stratospheric temperatures remain below the baseline value until the end of the 21st century, which can be attributed to the projected increase in GHG concentrations as stated in the A1B scenario [*Nakićenović and Swart*, 2000]. CCMVal-2 models in the REF-B2 simulations suggest that during the ozone decrease period of 1970-2000, temperature median trends at 100 hPa are approximately -0.3 K/decade for September, 0.9 K/decade for October and -1.8 K/decade for November, giving a spring average of around -1 K/decade. During December, the temperature trend is about -2 K/decade. These decadal trends are statistically significant to a 95% confidence interval with a 2-σ uncertainty range of around 30% for all months.

Randel et al. [2009] analyzed satellite, radiosonde and lidar temperature observations

in 1979-2007 at 100 hPa over the same latitude range and found a similar cooling trend of about -1 K/decade for spring months and -1.5 K/decade for summer months. The period of maximum temperature deviation from baseline in Figure 2.6 generally coincides with the period of maximum depletion in ozone VMR observed in Figure 2.5. December temperatures have the largest deviation from baseline at 100 hPa, November at 70 hPa, October at 50 hPa, and September at 20 hPa. These deviations in temperature appear to correlate with deviations in ozone at the same pressure levels for most months. September temperature is at its minimum at the end of the 21st century, rather than during the peak ozone depletion around the year 2000. December temperature also shows a slower increase at 50-70 hPa, in agreement with the slower December TOC recovery.

At 30 hPa, December temperatures show no significant trend during the period of ozone decrease until about 2000. At altitudes above 30 hPa, an initial increase in December temperature is followed by cooling towards the end of the 21st century. For this period, December ozone VMR in Figure 2.5 shows a small decrease, and then an increase at higher pressure levels. Both December ozone and December temperature time series indicate a reversal in the radiative effect of ozone. In the lowermost stratosphere, ozone and temperature correlate; a decrease in ozone levels leads to a decrease in temperature. But at higher altitudes they anti-correlate; an increase in ozone is associated with a radiative cooling observed after 2000 for all months. This anti-correlation is seen at 20 hPa for all months and also down to 30 hPa for December. As will be discussed later, such a decrease in temperature could be related to enhanced CO_2-induced cooling, which in turn leads to a slowdown in ozone destruction reactions [*Shepherd and Jonsson*, 2008].

During the period of 2000-2080, December lower stratospheric temperatures are influenced by increasing ozone with warming occurring at altitudes up to 50 hPa. However, temperatures at this altitude range also begin to plateau somewhat earlier than ozone VMR, around 2065 for 150-70 hPa. At altitudes corresponding to 50 hPa, December temperature increase is slow from 2000 onwards. Above these heights, stratospheric cooling increases with increasing altitude, with no temperature recovery to baseline due to effects of long-term CO_2 cooling. If lower stratospheric cooling associated with ozone depletion

could lead to a strengthening of the polar vortex, then warming associated with ozone recovery could decrease the stability of the vortex and affect future persistence of the vortex into early summer. To analyze this effect, monthly zonal mean zonal winds were considered at the same pressure levels as temperatures and ozone VMR in Figure 2.7. *Waugh et al.* [1999] found that similar to potential vorticity (PV), zonal wind is a useful diagnostic in assessing the breakup of the polar vortex, although not as highly derivative as PV. As noted earlier, zonal wind data is averaged across 50°-70°S, which encompasses the location of the edge of the polar vortex [*Lee et al.*, 2001]. Wind speeds across smaller 5° latitude bins were also analyzed in this work (not shown), and the resulting trends were similar to those averaged over the 50°-70°S region.

A minimum wind speed of 15 ms^{-1}, below which the vortex is considered to have broken down, is used in this study, similar to the method used in *Nash et al.* [1996]. For all pressure levels analyzed, spring month winds indicate that the polar vortex is present until the end of the 21st century. For December, model outputs suggest that at heights above 50 hPa, the polar vortex is broken-up. However, at altitudes below 50 hPa, the December wind speed of $\geq$15 ms^{-1} indicates that the vortex edge is present until the middle of the 21st century. As the polar vortex collapses in early summer, its edge could either disappear, or first shift poleward, and then disappear.

To analyze whether the December zonal mean wind speed exceeded the 15 ms^{-1} limit at higher latitudes, compared to what is shown in Figure 2.7, monthly zonal wind data were also considered at higher latitudes of 70-80°S. These results (not shown) revealed trends in zonal wind speeds at each pressure level very similar to those in Figure 2.7, suggesting that the stratospheric polar vortex quickly collapses in December.

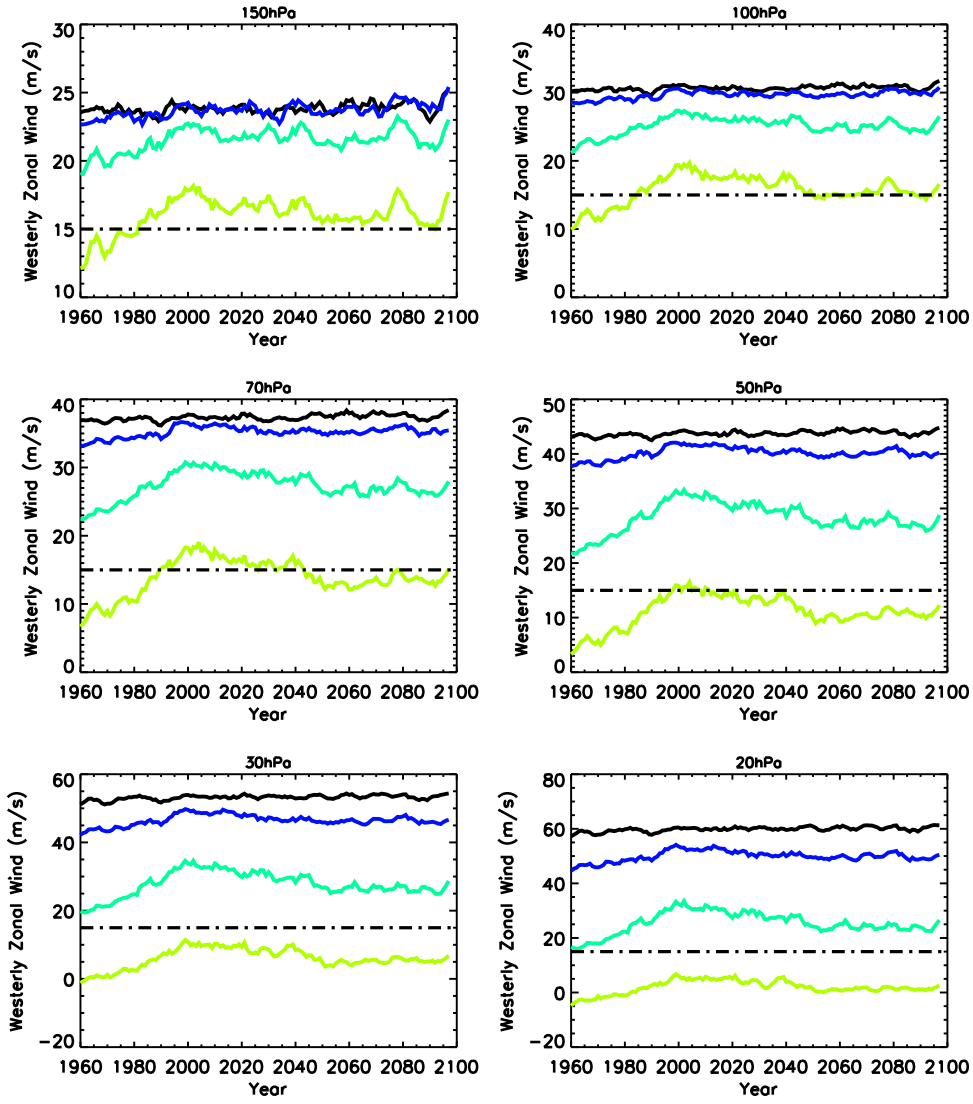

Figure 2.7: Time series of monthly zonal mean zonal wind speed averaged across 50°-70°S at 150-20 hPa. Dot-dashed lines indicate the minimum wind velocity of 15 ms^{-1} that identifies the polar vortex edge. Colours correspond to the same months as in Figure 2.5.

Figure 2.7 indicates that increasing polar westerly winds, associated with ozone depletion, are seen in the lower stratosphere during November and December until the year 2000. During the ozone recovery period, there is a corresponding decrease in polar westerly winds. When compared with results for TOC and ozone VMR in Figures 2.3, 2.4 and 2.5, there is about a one month time lag in zonal wind response to changes in ozone VMR. Overall, there is no significant trend in zonal winds for the months of September-October.

Monier and Weare [2011] found similar results with the ECMWF ERA-40 reanalysis data over the time period of 1980-2001, with a strengthening westerly wind associated with ozone depletion via the thermal wind balance.

Zonal winds were also considered with respect to trends seen in the monthly TOC values. The 1965 baseline wind value u_b and a mean peak value u_p between 2000-2005 are used to produce the time series for normalized zonal wind percentage deviation, δ, as shown in Figure 2.8. This normalized wind percentage deviation of annual wind speed values u(t) is calculated as:

$$\delta = \left[\frac{(u(t) - \bar{u_b})}{(u_p - \bar{u_b})} \right] \times 100\%, \tag{2.1}$$

As September wind data had high absolute wind values but small variability, in order to be shown together with other months, they were scaled by a factor of 10 at all altitudes. Figure 2.8 suggests that the percent increase in zonal wind speed during the ozone depletion period is very similar over all months. By 2100, model projections indicate a net increase in wind speeds for all months, compared to the 1965 baseline values, due to an indirect effect of increasing surface GHG concentrations via temperature changes. The increasing effect of GHGs is also seen in the secondary peak in zonal median wind at all pressure levels, for all months except September.

There is evidence that austral summer wind speeds increase significantly, both in the troposphere and in the stratosphere, due to decreasing ozone and increasing GHG concentrations [*Thompson and Solomon*, 2002]; [*Shindell and Schmidt*, 2004]; [*Perlwitz et al.*, 2008]; [*Son et al.*, 2010]. According to these studies, future changes in SH atmospheric circulation due to ozone recovery are expected to be opposed by increases in tropospheric GHGs. However, effects from increasing ozone concentrations and decreasing ozone hole size will still dominate at Antarctic latitudes until 2100.

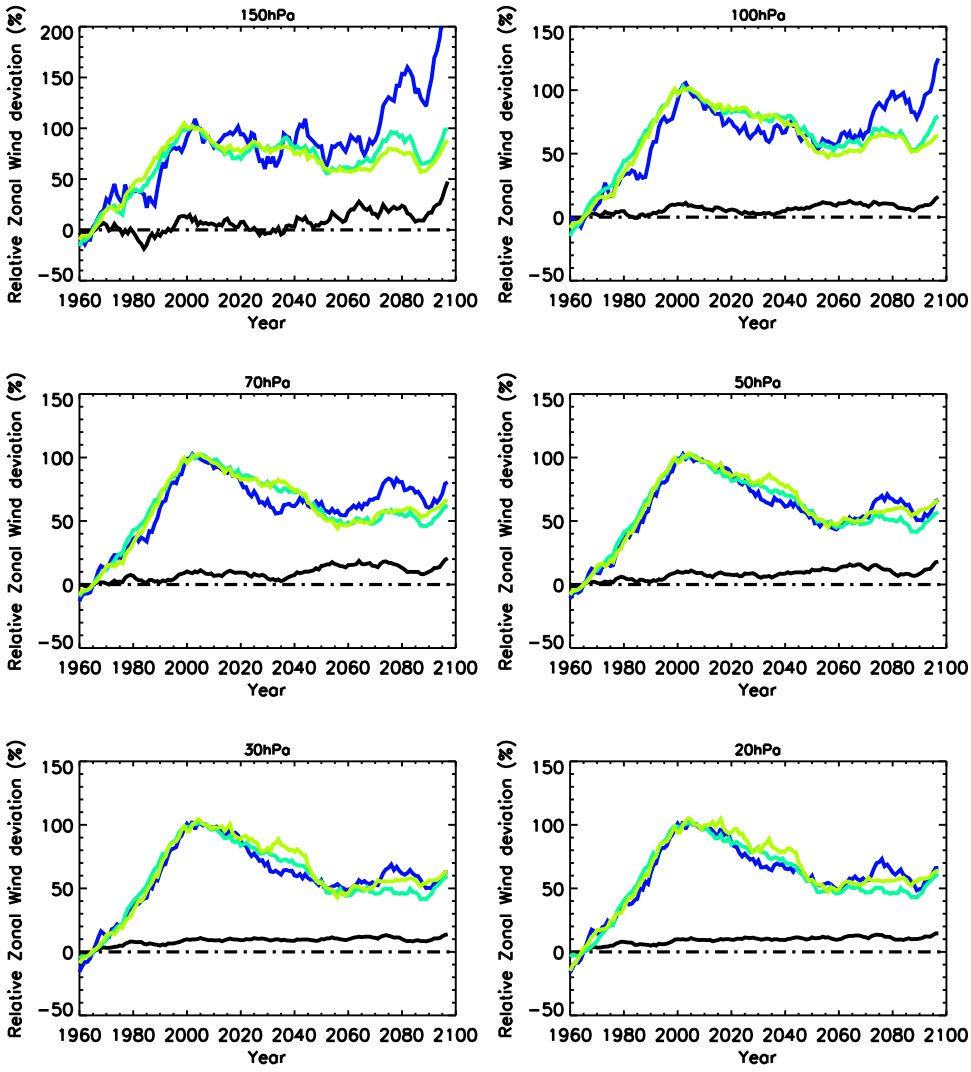

Figure 2.8: Normalized time series of percent deviation of zonal mean zonal wind speed averaged over 50°-70°S. The September wind data have been scaled by dividing by 10 at all altitudes. Colours correspond to the same months as in Figure 2.5.

2.5 Discussion and conclusions

This analysis of CCMVal-2 model simulations indicates that due to the combined effects of increasing GHGs and decreasing ODSs in the 21st century, Antarctic TOC will not return to a 1965 baseline during the September-November months, but will return to 1965 values for the month of December by 2080. The recovery of December TOC to this baseline has an uncertainty of around 30 years to a 95% confidence level. It is noted that the 1965

baseline is a somewhat arbitrary value, and thus the fact that September-November ozone will not return to its 1965 level by 2100 does not indicate that the ozone depletion due to ODSs will still be significant. As seen in Figures 2.3 and 2.4, by 2100, Antarctic ozone is still appreciably affected by ODSs (as dictated by the adjusted WMO A1 scenario), and the impact of increasing GHGs on ozone depletion is about as large as that of ODSs, but opposite in sign.

TOC increase rates and speeds in Table 2.1 (Cases A and B) are low for all months in 2000-2009, and those for December are often significantly lower, up to a factor of 10, compared to other months. Model simulations suggest that in early spring, the maximum contribution to decrease in TOC comes from ozone depletion at higher altitudes, and in early summer from ozone depletion at lower altitudes. This is in agreement with the independent observations discussed in Section 2.4.3. At 50-100 hPa, December ozone does not return to the 1965 baseline by 2100, in contrast to the return date for December TOC of 2080. Furthermore, slower rates of December TOC increase projected for certain decades, as shown in Table 2.1, originate from slower rates of December ozone VMR increase at 50-100 hPa. This slower increase is especially evident at 50-70 hPa, which are also the altitudes of highest December ozone depletion. At 20-30 hPa, December ozone VMR show minimal variation during the 21st century.

MMM trends in monthly temperatures correlate well with ozone within the lower-most stratosphere (70-150 hPa), particularly during October-November, as expected for temperature-dependent polar stratospheric chemistry, where temperatures rise with increased ozone. However, at altitudes corresponding to 20-30 hPa, there is a reversed radiative effect due to a combined effect of increased GHGs and decreased ODS concentrations. At 50-100 hPa, model simulations indicate that December temperatures stop increasing around 2060 and remain nearly constant until the end of the century. During this time period, December ozone VMR is still slowly increasing, indicating no apparent dependence on temperature and a weakening of the polar vortex as ozone-rich air from lower latitudes moves to these pressure levels.

A decrease in temperature in the lower polar stratosphere, particularly within the polar

vortex, results in an increase in the meridional temperature gradient at the vortex edge and thus enhances westerly zonal winds in this region. Circumpolar westerly zonal winds show an increase in magnitude during the period of ozone depletion with a corresponding decrease during ozone recovery for all months considered. Using a 15 ms^{-1} minimum in zonal wind speed as a proxy for the polar vortex edge, the polar vortex was found to be present for all spring months across all altitudes considered, but had broken up by December above 50 hPa. In the lowermost stratosphere, model simulations for December indicate a persistant polar vortex well into early summer, especially during the peak ozone depletion period, around the year 2000. At pressures $\geq$ 100 hPa, zonal winds suggest a presence of the vortex in December until the end of the model simulations. At 50-70 hPa, the December vortex lasts until 2045, and after that date the cooling rate starts to decrease, as shown in Figure 2.6.

At altitudes above 10 hPa, stratospheric cooling can lead to a decreased efficiency of chemical ozone destruction, and therefore to an increased ozone VMR, as observed in *Finger et al.* [1995]. At altitudes below 10 hPa, increased cooling promotes more heterogeneous reactions. However, the efficiency of such reactions also depends on water vapour concentrations as discussed by *Shindell* [2001]. Model results analyzed here show that such an anti-correlation (cooling temperatures leading to increased ozone) can be seen down to altitudes of 30 hPa. *Shepherd and Jonsson* [2008] suggested that global mean temperature variations should be considered in terms of changes in CO_2 and ODS, rather than ozone. They found that during 2010-2040, a period of rapid ODS decrease, up to 40% of the increase in mean global upper stratospheric ozone (between 50 and 0.5 hPa) is attributed to CO_2 cooling. However, during the depletion period of 1975-1995, only 10% of ozone loss is attributed to CO_2 cooling, which is much smaller compared with the effect of ODS increases alone [*Shepherd and Jonsson*, 2008]. However, these global effects of increasing CO_2 on ozone levels may not be the same on a regional scale. For example, it was found that lower stratospheric ozone averaged over the southern hemisphere mid-latitudes decreases with increasing GHG concentrations [*Waugh et al.*, 2009a]. Multi-model trends obtained in this study indicate that during spring months,

decreasing ODSs lead to increasing ozone. But as the end of the 21st century approaches, December ozone is predicted to be less influenced by halogens and more influenced by increasing GHGs, as evidenced by a decreased radiative heating that occurs in the lower stratosphere.

CCMVal-2 models indicate a response of zonal winds to recovering ozone, namely a decrease in wind speed with increasing ozone VMR. A wind response to changes in temperature, associated with ozone concentration, has about a one month time lag with maximal ozone gradients seen in October-November and maximum wind gradients seen a month later, in November-December. This pattern is also reported by *Akiyoshi et al.* [2009], based on observations and a CCM simulation (CCSRNIES). Persistence of the polar vortex into the summer months could also be linked to decreasing planetary wave activity, which was described in *Monier and Weare* [2011]. The breakdown of the polar westerly winds is induced by dynamical heating from breaking planetary waves, and the timing of this breakdown in early summer can influence the propagation of gravity waves into the mesosphere, thus potentially affecting the strength of the mesospheric branch of the Brewer-Dobson circulation [*Smith et al.*, 2010]. In this study, December westerly zonal winds over a 100 year period (between approximately 1990-2090) show a long term decrease with an earlier vortex breakup at the end of the model simulations compared to the peak ozone depletion period, particularly between 50 and 70 hPa. This is similar to the result of *Deushi and Shibata* [2011]. Using the MRI model, they found a maximum decrease in mean age of air at 50 hPa in December due to lower stratospheric wave forcing.

A delay in the vortex breakup, indicated by CCMVal-2 MMM wind time series, leads to a delay in TOC increase during December. Anthropogenic ODS emissions dominate in the lower stratosphere, while CO_2 cooling dominates at higher altitudes. However, an increase in GHG concentrations may start affecting ozone levels in the lower stratosphere towards the end of the 21st century, when ODSs no longer have a significant influence on atmospheric ozone over Antarctica.

This analysis of ozone recovery is based on zonal averages, and thus the previously reported zonal asymmetries in the TOC field (e.g.*Grytsai et al.* [2007]) may lead to some

local variations in ozone return dates. Zonal asymmetry in CCMVal-2 model output of TOC distribution, is explored in greater detail in the next chapter.

3 CCMVal-2 model trends in the zonal asymmetry of Antarctic stratospheric ozone

3.1 Introduction

This Chapter is focused on the further analysis of Antarctic ozone hole recovery during the 21st century using CCMVal-2 model simulations, and specifically on projected Antarctic ozone hole zonal asymmetry patterns resulting from the effects of quasi-stationary planetary waves. It has been shown that there is a significant spatial correlation between the total ozone column (TOC) wave structure and planetary wave propagation [*Wirth*, 1993]. In the Southern Hemisphere (SH), the QSW of zonal wave number 1 is a prominent feature in the spring TOC distribution [*Wirth*, 1993]. *Wirth* [1993] also demonstrated that during winter, SH wave activity at mid-latitudes influences polar stratospheric temperatures and thus the severity of ozone depletion.

Satellite measurements during the 1979-2005 period observed a longitudinal variation in TOC distribution at Antarctic latitudes that varies during the Spring ozone hole season [*Grytsai et al.*, 2007]. These longitudinal variations cause a zonal asymmetry in zonal ozone that can be indicative of planetary wave activity at mid-latitudes affecting meridional transport of ozone or ozone depleting substances.

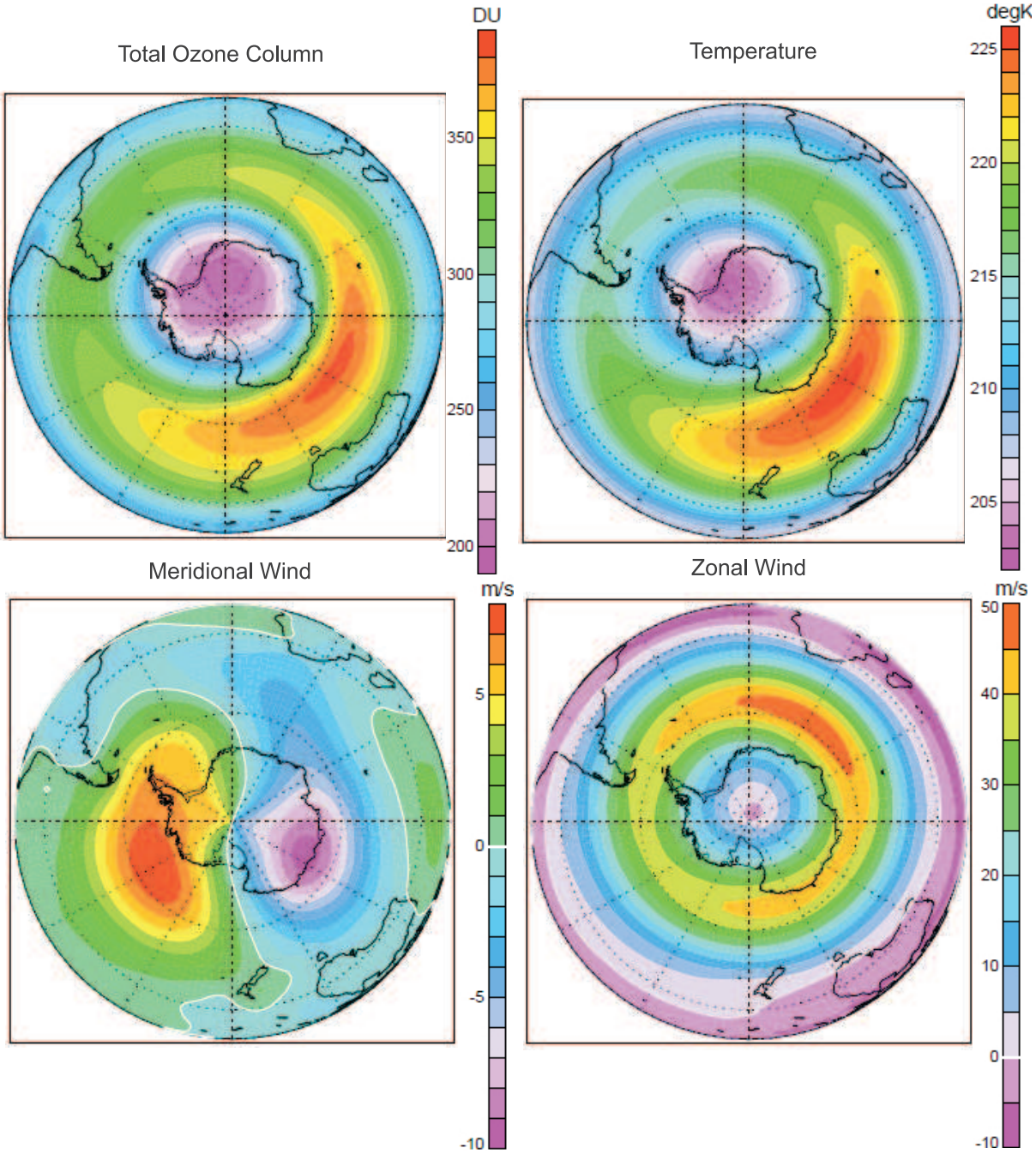

Figure 3.1: Southern Hemisphere metrics averaged over 1979-2013 for the austral spring. All metrics are obtained from NCAR/NCEP-2 reanalysis at the 50 hPa level except for TOC which is obtained from ERA-Interim. Plots provided by Andrew Klekociuk, Australian Antarctic Division.

In the austral spring months (SON), the zonal TOC distribution in the characteristic 'collar' region outside the ozone hole has a pronounced wave-1 pattern with a peak and

trough separated longitudinally by approximately 180°. This 'collar' region is due to poleward transport associated with the Brewer-Dobson circulation accumulating ozone around the dynamic barrier of the polar vortex [*Holton et al.*, 1995]. An example of this collar region is shown in the ERA-Interim reanalysis TOC data in Figure 3.1 which illustrates the band of high ozone around Antarctica, latitudinally centered around 60°S. QSW wave activity produces a region of ascending (cooling) air and descending (warming) air separated by 180° longitude. This temperature pattern sets up a pressure gradient, forcing eddies in the wind field and creating regions of poleward and equatorward air flow, approximately 90° east and west of the temperature maximum, respectively.

The TOC value at a particular geographic location also depends on the vertical location of the tropopause, which is influenced by the synoptic-scale processes in the tropopause at mid-latitudes. Therefore an elevated tropopause tends to thin out the ozone density leading to lower TOC values. Over Antarctica the zonal distribution of TOC correlates with the tropopause pressure mostly during the austral spring [*Evtushevsky et al.*, 2008], and the decrease in TOC is associated with the increased thermal tropopause height, providing a zonal asymmetry in the Antarctic tropopause height during spring. *Evtushevsky et al.* [2008] analyzed data from the Total Ozone Mapping Spectrometer (TOMS) and the Ozone Monitoring Instrument (OMI) in 2005-2006 and found a significant zonal asymmetry in the tropopause height with a maximum height over West Antarctica. That study suggested that TOC zonal asymmetry in the SON months were due to QSW activity, while winter zonal asymmetry was due to asymmetry in the surface temperature.

Zonal asymmetry in stratospheric ozone also influences the SH climate. *Gillett et al.* [2009] found that prescribing zonally asymmetric stratospheric ozone (instead of a fixed zonal mean value) into the radiative transfer scheme in a CCM resulted in a more accurate simulation of zonal mean stratospheric temperature trends in comparison with observations. This suggests that zonal ozone asymmetry is a robust climate component and should be included in climate models. An underestimation of temperature trends when using prescribed zonal-mean ozone in climate models was further demonstrated in *Waugh et al.* [2009b]. That study suggested that zonal asymmetry plays an important

role in the SH temperature and geopotential height (thus affecting the strength of the polar vortex), and that with the ozone hole recovery during the 21st century, the zonal asymmetry effects will decrease.

In the *Grytsai et al.* [2007] study, the longitudinal position of the spring TOC zonal minimum (λ_{min}) and maximum (λ_{max}) values in the collar region exhibited a general eastward shift from 1979 to 2005. They found that the trend shift was larger for the λ_{min} than for the λ_{max}. This was linked to the feedback of the Ozone Hole on excitation of the stratospheric QSW wave-1 component outside the polar vortex [*Grytsai et al.*, 2007]. However, a detailed assessment of the underlying physical mechanism, as well as the analysis of the future zonal patterns in the Antarctic ozone, are yet to be reported. Because the shift of λ_{min} is potentially exposing a larger area of the biologically productive Weddell Sea region to progressively higher levels of ultra-violet radiation during spring, it is important to understand the cause of the TOC asymmetry and its future regional trends. The analysis of *Ialongo et al.* [2012] extends the results of *Grytsai et al.* [2007] by assessing satellite observations of ozone zonal asymmetry in 2005-2010. Both studies agree on the spatial distribution of TOC and found that ozone asymmetry extends to the entire stratosphere with the amplitude of the QSW wave-1 component decreasing with increasing altitude.

3.2 Data Analysis and methodology

In this thesis, the seasonal mean TOC fields produced by the CCMVal-2 activity are examined. A review of the models used in CCMVal-2 can be found in *Eyring et al.* [2010c] and *Morgenstern et al.* [2010]. The CCMVal-2 models used here are different from those used in Chapter 2 due to the availability of model simulations that provide TOC values gridded in both latitude and longitude. Out of the 17 chemistry-climate models (CCMs) that provided data for CCMVal-2, 15 simulate relevant 3-dimensional atmospheric circulation parameters with fully interactive stratospheric chemistry where external forcing, such as greenhouse gases (GHGs), ozone-depleting substances (ODS),

and stratospheric aerosols are prescribed. This work focuses on the austral spring (SON) and summer (DJF) months for the 'modern era' (1979-2005, REF-B1 reference runs) and the 'prediction era' (2005-2100, REF-B2 reference runs). The analysis presented in *Grytsai et al.* [2007] is extended in this study, using observational data to include the DJF months.

REF-B1 simulations address internal model uncertainties, due to external forcings, both anthropogenic and natural, such as solar irradiance,volcanic eruptions and GHG concentrations [*Morgenstern et al.*, 2010]. Therefore to compare with modern satellite observations, REF-B1 model output was restricted to the 1979-2005 period. However, to consider the future trends of zonal asymmetry in ozone distribution, with specific assumptions on future anthropogenic GHG increases and halogen emissions decreasing under the SRES A1B scenario [*Eyring et al.*, 2007], the REF-B2 simulations are used. Not all model groups provided REF-B2 simulations with longitudinal variations in ozone (not zonal means). Therefore, only results from 10 models are presented here. As in Chapter 2, some models provided multiple ensemble simulations. However, in this study only a single model run from each model group is used.

To compare CCMVal-2 multi-model trends during the 'modern era' with observations, the TOMS version 8.5 dataset is used in this study. This dataset also includes data from the Ozone Monitoring Instrument (OMI), and thus is a different version of TOMS data than that used in Chapter 2, where the TOMS merged dataset (MOD) is considered. MOD version 8.5 ozone observations, gridded to 5° latitude and 10° longitude, are available and extend back to 1970 to include data from the Solar Backscatter Ultraviolet (SBUV) instrument. However, data exclusion is more stringent at polar latitudes in the MOD dataset and provides no significant advantage for comparison with CCMVal-2 models over the Antarctic latitudes. Our analysis of both TOMS/OMI and TOMS/MOD datasets showed no significant difference, and in order to compare our results with the analysis of *Grytsai et al.* [2007], which considered the TOMS/OMI observations, it was deemed appropriate to use the TOMS/OMI dataset. Note that the MOD version 8.6 ozone data is the latest version that has been released (http://acd-ext.gsfc.nasa.gov/Data_services/merged/), but

only zonally averaged ozone values have been supplied in that version at the time of this writing.

Monthly satellite and model TOC values have been used to obtain seasonal mean statistics in relation to QSW trends as such planetary waves, which have been shown to vary on timescales greater than 30 days [*Randel*, 1988]. Traveling planetary wave components vary on much smaller time scales. Therefore using monthly data, instead of daily mean data, provides a simple low frequency filter to consider QSW's alone.

Here we define some further terms referred to in this study that characterise zonal asymmetry. The longitudinal position of the TOC zonal extremes are given as λ_{min} and λ_{max}, therefore the amplitude of the TOC zonal distribution, A_{zw}, is defined as the half difference of the TOC at λ_{min} and λ_{max} for a particular latitude. In relation to QSW harmonics, the TOC maximum of the wave-1 and wave-2 components are referred to as λ_{W1} and λ_{W2} and the amplitudes of those components are A_{W1} and A_{W2}. In order to obtain characteristics (phase and amplitude) of these wave components, Fourier decomposition was performed on the TOC distribution as done in *Grytsai et al.* [2007].

3.3 Results

3.3.1 Seasonal trends in zonal asymmetry of TOC

In order to statistically examine the zonal TOC asymmetry for each model reference period, data was averaged into 5° latitude bands from 50-80°S, centered at each 5° step. For example, 60° represents the mean of TOC values between 57.5° and 62.5°. This allowed for a clearer comparison between CCMVal-2 models which have a variety of grid resolutions, and TOM observations. In fact, it was not possible to restrict the CMAM model to the 50°S as the model grid resolution at this latitude was too coarse, as TOC values were outside the 5° step, with no values between 47.5-52.5°S. The latitude range selected includes the ozone 'collar' region outside the ozone hole where wave perturbations are significant [*Grytsai et al.*, 2007]. Figure 3.2 shows an example of REF-B1 simulations for the WACCM model for the SON season. This model was selected as an example due

to its reasonable agreement with TOMS observations with respect to amplitude ratios (shown in Table 3.1).

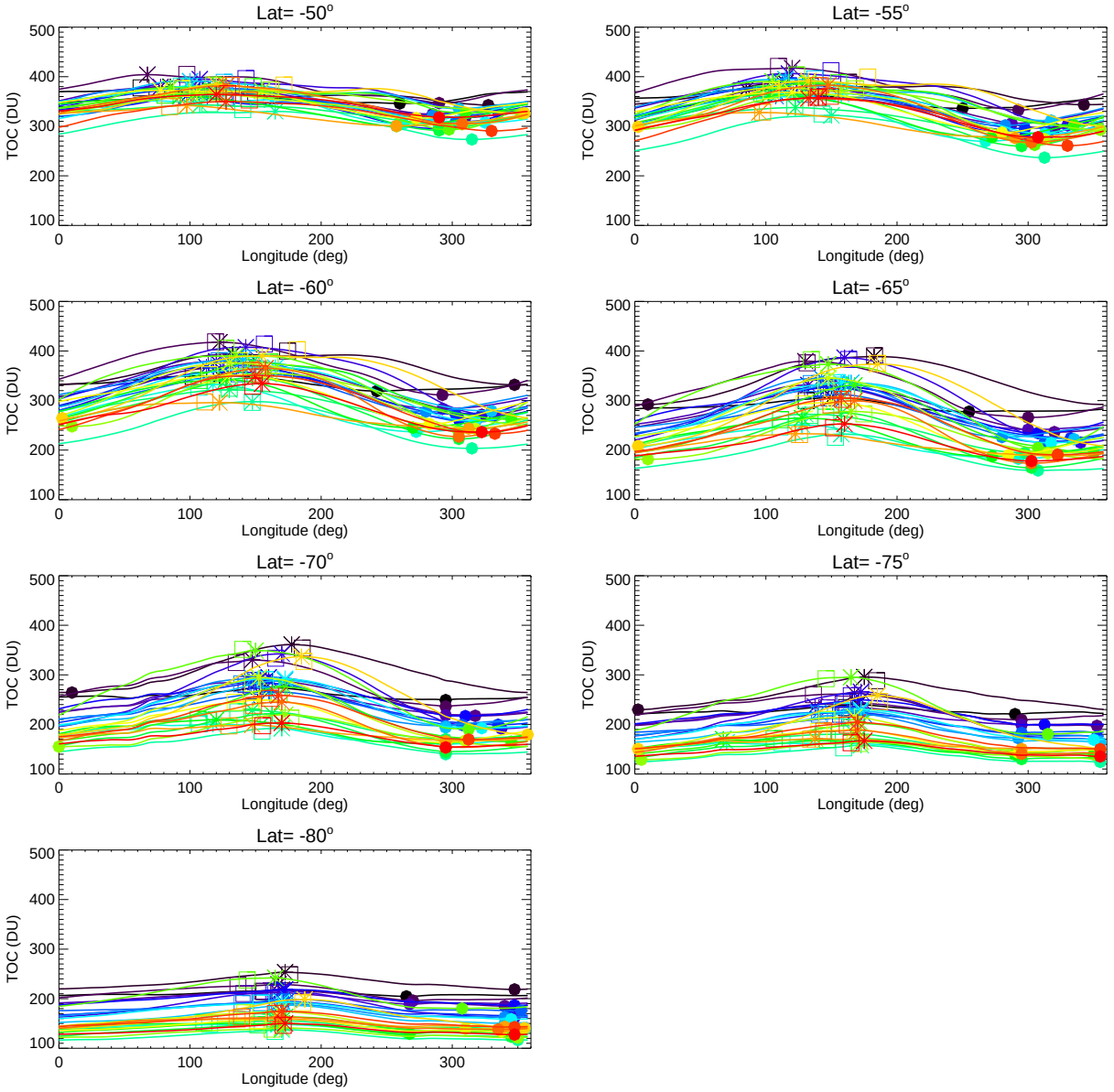

Figure 3.2: Interannual longitudinal variations in mean spring TOC for the WACCM model at 50-80°S for the years of 1979-2005. Colours from dark blue (1979) to red (2005) represent individual years. Circles show locations of λ_{min}, asterix show locations of λ_{max} and squares show the maximum λ_{W1} value.

The TOC distribution shows a generally wave-like structure with interannual variability. The lowest variability in the zonal wave is observed at 50°S, and the highest wave amplitude is observed at 65-70°S. TOMS observations were previously found to have a similar TOC pattern over this period with a maximum in the wave amplitude at latitudes near the edge of the ozone hole [*Grytsai et al.*, 2007].

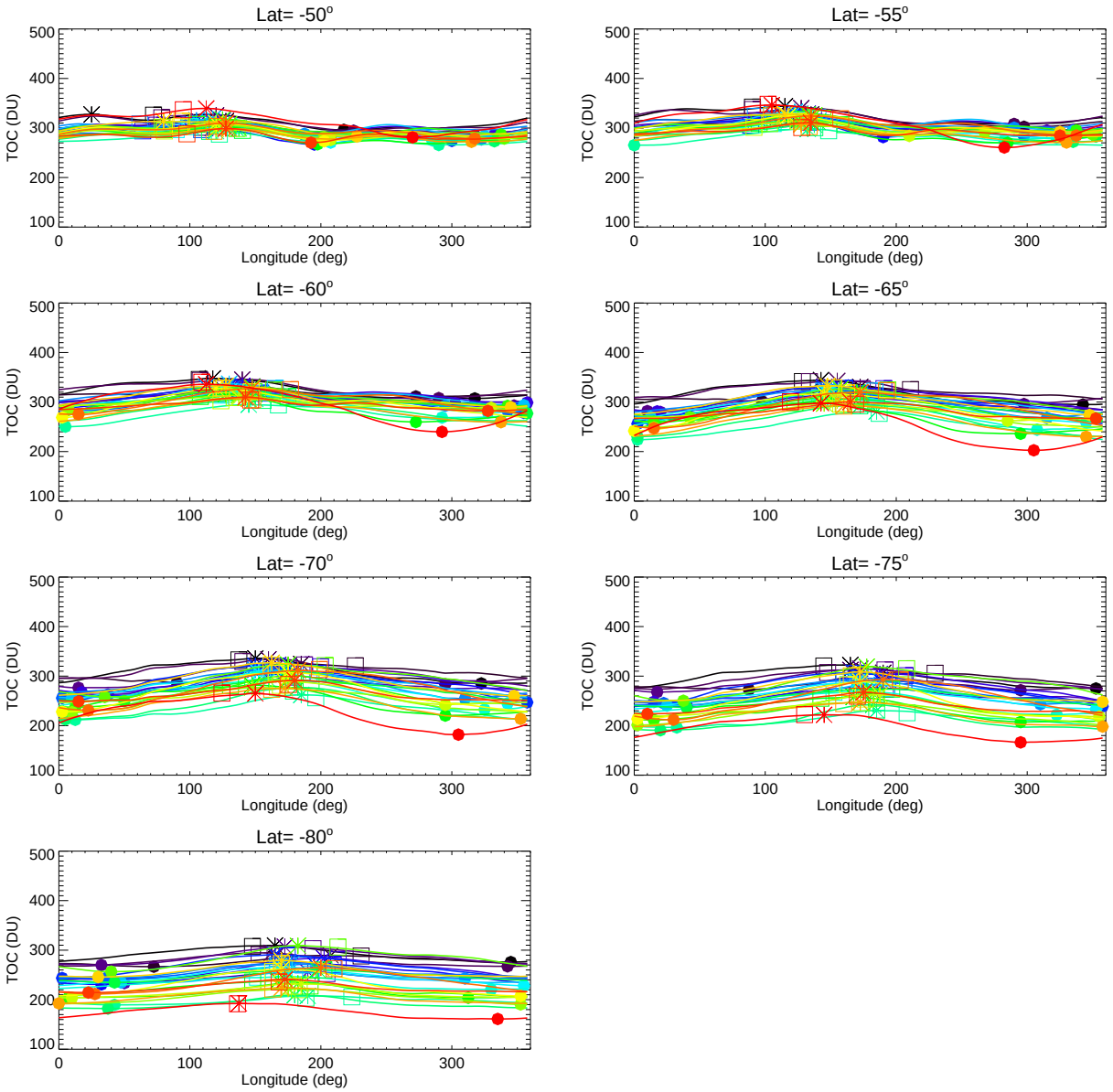

Figure 3.3: As in Figure 3.2 but for the mean summer TOC.

Figure 3.3 illustrates the interannual TOC distribution for the DJF months over the same latitude range and time period, as Figure 3.2. Compared to the SON months, the

DJF months show a much smaller wave-like structure in the TOC distribution with a weaker stationary wave pattern. This is reflected in the TOMS measurements over the 1979-2005 period, where at higher latitudes, the TOC zonal distribution during DJF has a decreased asymmetry compared with the SON months, resulting in less robust trends in the longitudinal locations (λ_{max} and λ_{min}). Figure 3.4 illustrates this with the spring amplitudes 2-3 times larger in magnitude than in the summer months. There is a clear maximum in amplitude at 65° during SON. However, there is no clear maximum in the summer months. Due to the polar night extending into September at 80°S latitude, there are measurement gaps each year at this time. Therefore, a seasonal SON value from TOMS data was not calculated for this latitude. A_{zw} values during SON months vary between 30-60 DU and during DJF months the zonal amplitude is between approximately 10-20 DU.

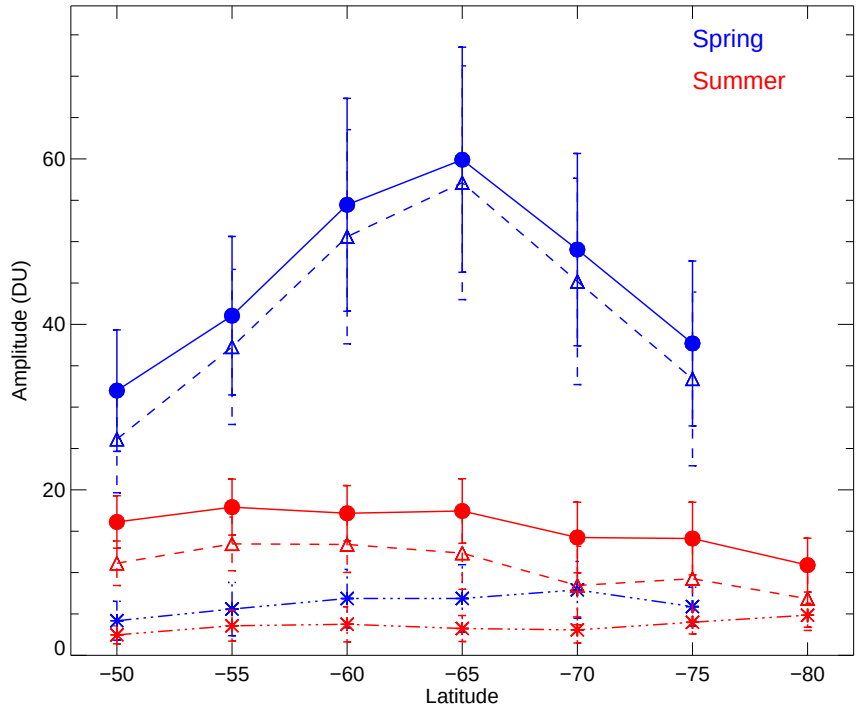

Figure 3.4: TOMS TOC zonal mean amplitudes for 1979-2005 for each latitude band; for A_{zw} (solid lines with circles), A_{W1} (dashed lines and triangles) and A_{W2} (dashed-dotted lines and asterisks). Seasons are colour-coded as shown and error bars denote the 1-σ deviation values.

Also shown in Figure 3.4 are the amplitudes of the wave-1 and wave-2 components of the TOMS TOC distribution for each season. The A_{W1} dominates the spring TOC distribution pattern at 80-95% of the A_{zw} value at each latitude. The wave-1 harmonic during summer is still reasonably dominant with an amplitude of at least 65% of A_{zw}. However, the wave-2 harmonic seems to play a slightly larger role in the TOC distribution for the austral summer compared with spring, poleward of 70°S.

Weak QSW patterns during DJF months have been observed in the geopotential height field [*Quintanar and Mechoso*, 1995] and in ozone measurements [*Miles et al.*, 1994]. *Evtushevsky et al.* [2008] observed a minimal zonal asymmetry in the tropopause height across east and west Antarctica at 65°S during DJF months with little variation in the ozone concentration. A study of zonal asymmetry in stratospheric ozone based on the Odin satellite observations from 2001-2010 found a similar weak pattern in the stationary wave structure [*Gabriel et al.*, 2011]. They suggested that such a mild planetary wave-like structure could be due to synoptic-scale baroclinic waves inducing asymmetries in the eddy mixing processes in the UTLS region, breaking down the QSW pattern. *Miles et al.* [1994] observed stationary and traveling wave-1 disturbances in the temperature field during DJF, with the stationary wave confined to the lowermost stratosphere with traveling waves prominent in the middle stratosphere.

To illustrate the extent of TOC zonal asymmetry present in CCMVal-2 simulations and to compare with TOMS observations, Figure 3.5 shows the A_{zw} values for the SON season. This illustrates the spread in amplitudes across the latitude range between models and the variance in shape, when compared with the TOMS observations in Figure 3.4. Amplitude maximum values reach approximately 40 DU for some models which is only 2/3 of that shown in TOMS measurements, with an overall range of between 10-40 DU. Some models show minimal latitudinal distribution in zonal asymmetry, with the E39CA model in particular showing minimal TOC zonal asymmetry with little variation in amplitude values across all latitudes. The multi-model median has a maximum zonal asymmetry between 60-65°S for the REF-B1 models, indicating the edge of the polar vortex, with individual models showing a wide range of latitudes for the location of this dynamic barrier during

SON months. All A_{zw} values and the median trends are statistically robust, but show a reduced zonal asymmetry in the TOC fields compared with those observed during the austral spring.

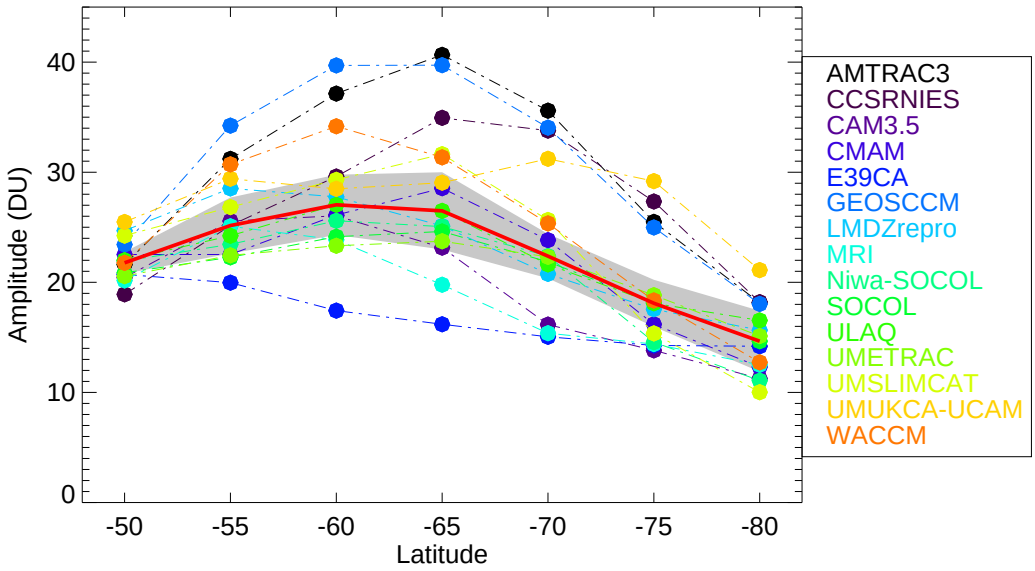

Figure 3.5: All REF-B1 model simulations of A_{zw} during SON for each latitude band, for the period of 1979-2005, colour-coded as shown to the right of the plot. The multi-model median trend is shown as a thick red line and the grey area represents the 95% confidence interval of the median.

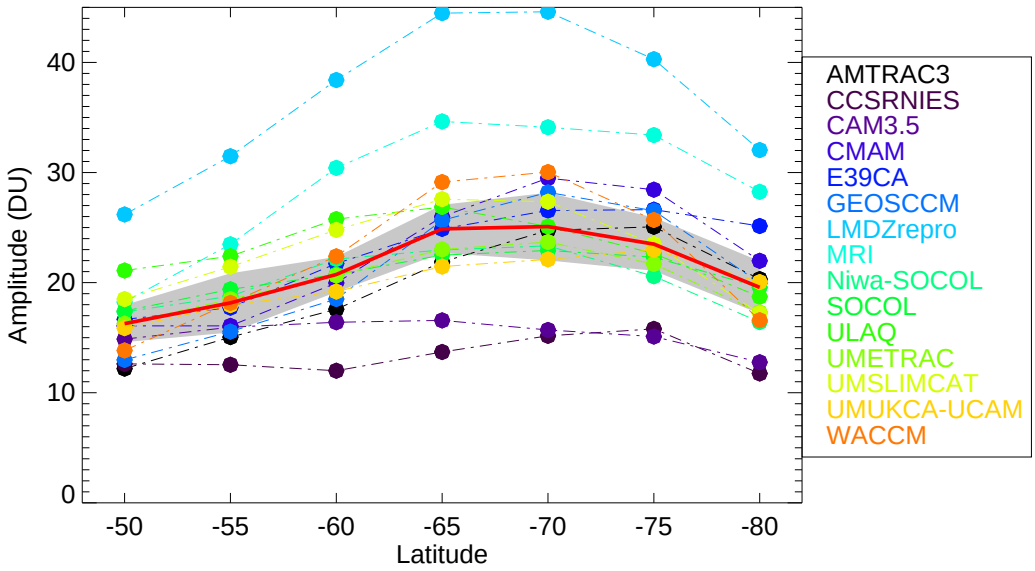

Figure 3.6: As in Figure 3.5 but for the mean DJF TOC.

Figure 3.6 shows the TOC zonal asymmetry from model simulations during the DJF season. Once again, there is a large spread of values in TOC amplitude between the models, with all models and the multi-model trend having statistically robust values up to a 95% confidence limit. When compared with TOMS observations for the same season, shown in Figure 3.4, there is a better agreement for TOC zonal asymmetry in the range of amplitude values of the median trend (between 15-25 DU). The range of amplitudes observed in the LMDZrepro and MRI models are greater than what is found during the SON months, contradicting satellite comparison of TOC asymmetry between the seasons. TOMS observations show a reasonably stable magnitude in A_{zw} during austral summer across polar latitudes with a general decrease in asymmetry towards the pole. The multi-model median trend in Figure 3.6 shows the opposite effect with an increasing poleward trend in TOC zonal asymmetry.

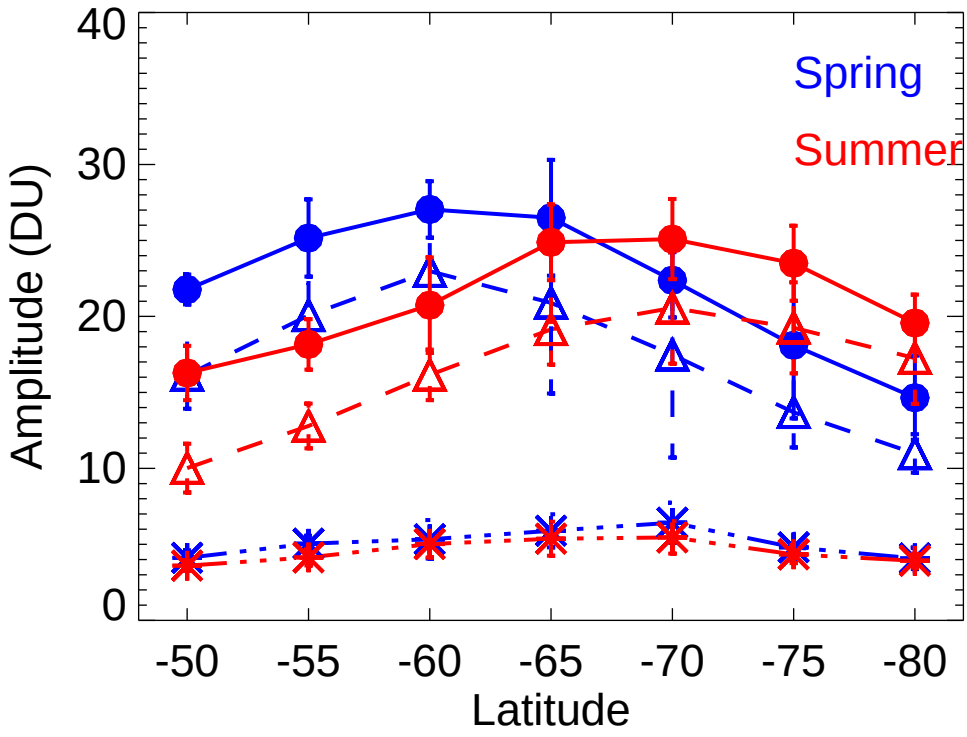

Figure 3.7: As in Figure 3.4 but for median values of all REF-B1 model simulations.

The REF-B1 wave-1 amplitudes, decomposed from the zonal wave amplitudes, also dominate the TOC signal during austral spring with a multi-model median trend of A_{w1}

at 75-85% of the A_{zw} values shown in Figure 3.5. This is illustrated in Figure 3.7. During summer, the model A_{w1} values at each season are more comparable with TOMS at latitudes up to 70°S(between 60-75% of A_{zw}). Poleward of this, the wave-1 amplitude reaches about 85% of the TOC A_{zw} and is twice the magnitude in model trends compared to TOMS. Median values of A_{W2} are much smaller at around 5 DU for most model simulations across both seasons as observed in the TOMS data. *Ialongo et al.* [2012] also used Fourier analysis to look at harmonics that contributed to the ozone values measured by the OMI instrument at 65°S, and found that 95% of ozone variability was due to wave numbers of 1 to 3, and those with numbers higher than 2 were somewhat unreliable. It would seem that the first two harmonics in model trends account for almost all the TOC A_{zw} values during spring and summer.

Table 3.1 lists the A_{W2}/A_{W1} amplitude ratios (as percentages) of all REF-B1 models used in this study, the multi-model median trend of these ratios and the TOMS/OMI amplitude ratios, all averaged over the observation period for each season. The uncertainty values listed are the standard errors in each ratio, also as a percentage, except for the median values which show the 95% confidence interval calculated from the bootstrapping method. The standard error values were calculated using an approximate solution to Fieller's Theorem as outlined in *Dunlap and Silver* [1986]. Model ratios which are statistically similar with overlapping uncertainty ranges to TOMS observations, are highlighted in bold.

During the SON season, these ratios provide a measure of the distortion of the polar vortex, with higher ratios indicating larger amplitudes of the wave-2 component. TOMS observations in Table 3.1 show small ratios (12-18%) indicating a dominant wave-1 component. REF-B1 models show a larger variability in the ratio values and more intra-model spread in ratios across the examined latitude ranges. This is in agreement with *Eyring et al.* [2010a] that considered climatological means of the stationary wave field in the geopotential height over the 'observation' period.

Table 3.1: Summary of A_{W1} and A_{W2} amplitude ratios (W_2/W_1) as percentages for all REF-B1 models and TOMS/OMI observations averaged over 1979-2005, together with individual model standard error in the ratios. Multi-model medians are given with a 95% confidence interval. Note, the CMAM model resolution did not allow for a value to be obtained for the 50° latitude bin. Model ratios shown in bold have overlapping uncertainty ranges to TOMS observations.

Model	*Season*	*Antarctic 5° latitude bins*						
		50	*55*	*60*	*65*	*70*	*75*	*80*
AMTRAC3	SON	25±3	20±2	**14±2**	**13±1**	23±2	25±2	33±2
	DJF	49±11	40±5	**33±4**	**25±3**	21±2	16±1	21±2
CAM3.5	SON	32±3	24±2	**16±2**	**11±2**	**15±2**	**17±2**	21±2
	DJF	42±10	44±10	41±9	30±4	27±4	23±3	30±5
CCSRNIES	SON	24±3	**18±2**	23±3	30±3	35±5	30±5	34±7
	DJF	28±5	**27±4**	**30±4**	**28±4**	26±4	24±3	25±3
CMAM	SON	-	19±2	**18±2**	23±2	27±2	26±3	35±5
	DJF	-	36±4	36±4	30±3	23±2	18±1	16±1
E39CA	SON	33±4	31±4	40±5	44±6	50±7	31±4	40±5
	DJF	40±6	36±5	**27±3**	23±2	23±2	17±2	19±2
GEOSCCM	SON	27±4	**19±3**	**14±3**	15±2	**21±2**	26±2	35±2
	DJF	39±8	36±5	**31±4**	22±3	18±2	16±2	22±2
LMDZrepro	SON	**19±2**	18±2	22±3	29±4	43±4	37±4	35±5
	DJF	**21±2**	22±2	**25±2**	**27±2**	27±2	21±2	17±2
MRI	SON	32±4	33±4	35±4	37±5	38±6	37±5	52±8
	DJF	**27±4**	**27±3**	**28±3**	**25±2**	18±2	14±2	13±1
Niwa-SOCOL	SON	22±3	24±3	36±4	39±4	41±4	34±4	36±7
	DJF	30±4	**28±4**	**32±3**	32±3	29±3	22±3	23±3
SOCOL	SON	26±3	30±3	41±4	44±5	43±4	40±4	37±4
	DJF	33±6	36±4	38±3	39±3	**36±3**	29±3	24±2
ULAQ	SON	29±3	27±3	27±3	29±3	36±3	42±4	50±6
	DJF	**23±3**	22±2	23±3	**24±3**	26±3	28±3	28±3
UMETRAC	SON	36±6	35±5	45±7	52±7	68±9	43±6	50±7
	DJF	**28±4**	**30±4**	**35±4**	39±5	45±6	**36±4**	35±4
UMSLIMCAT	SON	54±7	60±8	87±12	88±10	71±8	49±7	32±6
	DJF	40±8	36±4	40±5	41±4	**37±4**	33±3	28±3
UMUKCA-UCAM	SON	23±3	21±2	21±3	22±3	23±2	23±2	33±3
	DJF	49±8	41±5	**34±4**	**32±4**	**31±4**	25±3	24±2
WACCM	SON	**18±2**	**16±2**	**15±2**	**15±2**	**21±2**	24±2	27±4
	DJF	**27±6**	**25±3**	**22±2**	15±2	16±1	17±2	21±2
MM Median	SON	26±5	24±6	**23±10**	29±11	36±10	31±7	35±4
	DJF	33±6	**36±5**	**32±4**	**28±4**	**26±4**	22±6	23±2
TOMS/OMI	SON	16±2	15±2	14±2	12±2	18±2	18±2	-
	DJF	22±4	27±4	28±5	26±4	36±6	43±5	71±12

The AMTRAC3, CAM3.5, GEOSCCM and WACCM models give reasonable amplitude ratios in comparison with TOMS observations. However, the majority of models gives a ratio larger than TOMS by a factor of 2 or 3, showing poor agreement with observations, which deteriorates further approaching the pole. These large ratios are predominately due to a small A_{W1} magnitude, with the wave pattern in the TOC distribution generally having a much weaker amplitude than what is seen in TOMS observations. The multi-model median values are approximately twice the value of TOMS observations, indicating that the modelled wave-2 component is playing a larger role in the TOC asymmetry during the SON season than in observations, as the wave-2 components for each model are approximately the same as what is illustrated in Figure 3.4.

During the DJF months, the wave amplitude ratios are generally higher than for the SON season, with individual models continuing to show a large spread in values. However, some models show larger ratios during SON (E39CA, MRI, UMETRAC and UMSLIM-CAT). As shown by values highlighted in bold, the MRI, UMETRAC,UMUKCA-UCAMs models agree better with observations during summer (DJF), than they do during spring (SON). The multi-model median gives moderate agreement with TOMS observations at latitudes between 55-70°S. Model amplitude ratios poleward of 65°S tend to decrease in value towards the pole while TOMS observations show a sharp rise in ratio value during DJF.

Whilst in model simulations the wave-1 component dominates the TOC zonal asymmetry at Antarctic latitudes, the A_{zw} value in some model simulations do not seasonally vary significantly from austral spring to summer. This indicates that the model TOC zonal asymmetry is much less than what is observed in the SON season, but during DJF there is more of a definitive zonal asymmetry present in the REF-B1 TOC distribution.

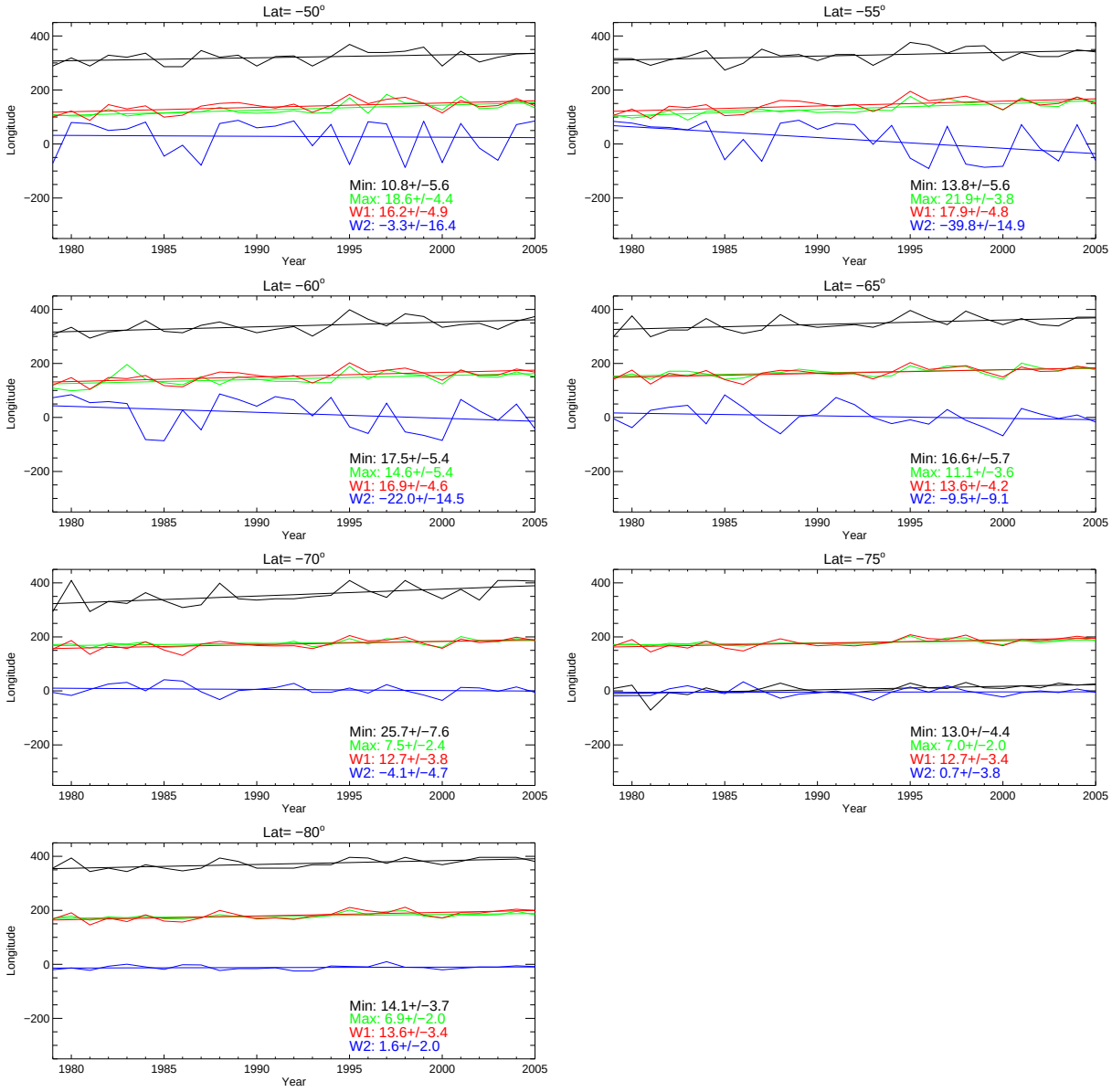

Figure 3.8: QSW wave parameters for the AMTRAC3 model during SON months for 1979-2005. Linear trends for λ_{min}, λ_{max}, as well as the longitudinal positions of λ_{W1} and λ_{W2}, are shown as straight lines. Decadal trend values, averaged for the SON months, are shown for each 5°S latitude range along with the 1-σ uncertainty associated with the linear trend. Each wave parameter is colour-coded as shown on the plots and trend values shown are in degrees/decade.

To consider the long-term behavior of Antarctic ozone zonal asymmetry, linear trends of wave parameters for each model over the observation period (1979-2005) were obtained, by minimising the chi-squared error statistic. In order to derive an accurate linear trend

for each parameter, longitudinal positions of wave extremes were occasionally adjusted by ±360°, to 'wrap' the phase of the QSW pattern, often resulting in a longitudinal range greater than 0-360°. For example, the longitudinal position of the zonal TOC maximum is at 330° for one year, the following year it is located at 20°, given as 380° to provide a clearer linear trend along the latitude circle.

Linear decadal trends of the locations of λ_{min}, λ_{max} and the QSW zonal wave-1 ridge (λ_{W1}) and wave-2 ridge (λ_{W2}) are shown for the AMTRAC3 model during austral spring in Figure 3.8. This suggests a statistically significant eastward (positive) phase shift in λ_{min} for the SON season at all latitude ranges, with a maximum phase trend at 70°S. The λ_{W1} trends are also statistically significant to 1 standard deviation, with an eastward trend in decadal phase shift over the observation period. λ_{W2} shows a much larger decadal trend at 55-60°S, in the westward (negative) direction, but this decreases poleward and becomes statistically insignificant.

Spring trends in zonal TOC λ_{min} and λ_{max} phase shift from 50° to 80°S for 15 REF-B1 models are shown in Figures 3.9 and 3.10, respectively. For comparison, TOMS/OMI observations are included as well. Most models suggest an eastward shift in the zonal TOC minimum position, with several models showing only a weak decadal trend poleward of 60°S in contrast to TOMS observations which show an increasing trend towards the pole. Some models show a reversed (westward) trend over Antarctica, in particular the E39CA, MRI and Niwa-SOCOL models, however these trends are not statistically significant. In fact, only the AMTRAC and GEOSCCM models are significant to 1-σ across all polar latitudes, and they show reasonable agreement with TOMS observations. The ULAQ, CCSRNIES and CAM3.5 models have robust trends across at least 3 latitude bins, but show poor agreement with observations.

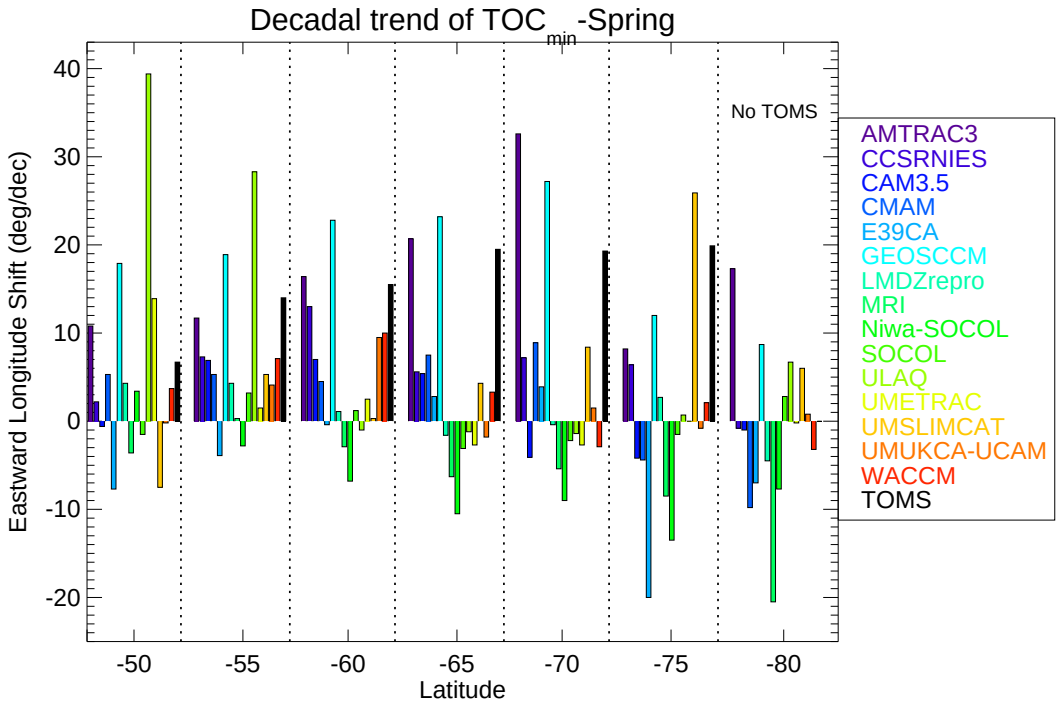

Figure 3.9: All REF-B1 CCMVal-2 model simulations for SON trends in TOC λ_{min} phase shift over the period 1979-2005 for the 7 latitude ranges. Colour-coding is shown to the right of the plot. TOMS observations are included as a black bar to the right of each latitude bin.

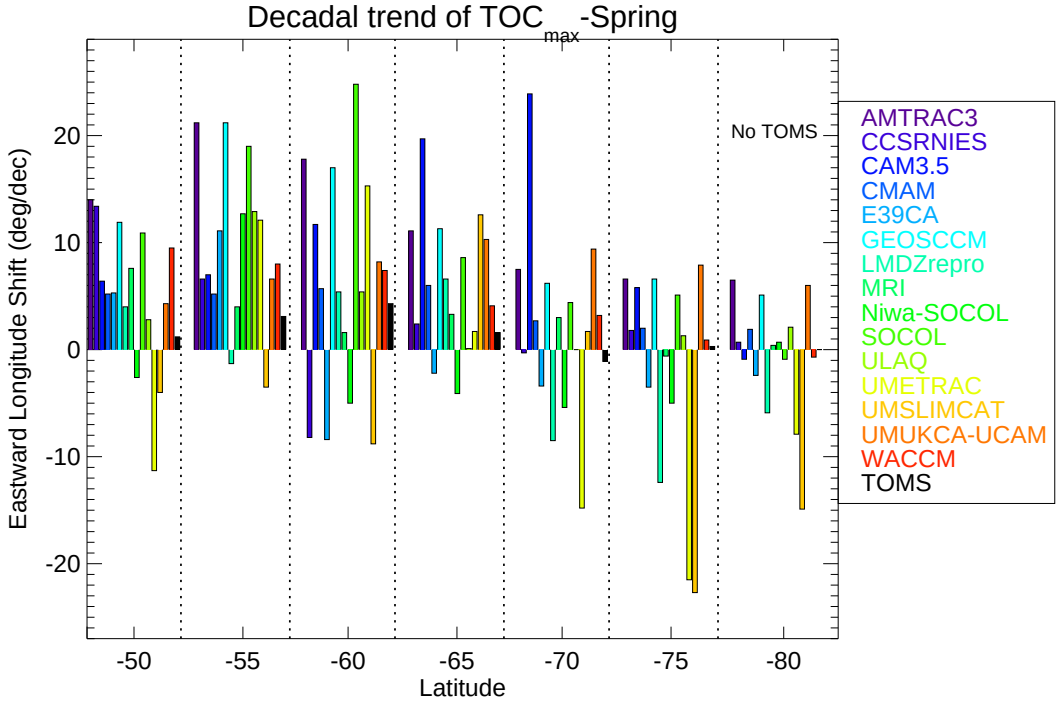

Figure 3.10: As in Figure 3.9, but for trends in zonal TOC maximum phase shift.

Decadel trends in zonal TOC λ_{max} during the SON season (Figure 3.10) also suggest a predominately eastward phase shift, which decreases poleward. Most models show a dominant eastward shift at lower latitudes, that weakens at higher latitudes for the zonal TOC λ_{max}. Some models show a westward trend across the latitude range, with some strong trends at higher latitudes found for the UMETRAC and UMSLIMCAT models. However, like the zonal λ_{min} trends, none of the negative (westward) trends are statistically robust during the observation period. AMTRAC and GEOSCCM models are robust across all latitudes again, with several others (CAM3.5,CMAM, MRI, SOCOL, ULAQ, UMUKCA-UCAM and WACCM) showing trends significant to at least 1-σ. In particular, equatorward of 65°S, a number of models suggest a significant eastward phase trend in λ_{max}. The λ_{max} at these latitudes would represent the 'collar' region around the ozone hole, where ozone from lower latitudes accumulates around the spring polar vortex. The λ_{min} trends poleward of 65°S would represent the long term behaviour of the ozone hole during the depletion period.

Figures 3.11 and 3.12 show the DJF trends in the TOC zonal minimum and maximum phase shift from REF-B1 simulations. Decadal patterns in these phase shifts show a generally larger eastward trend than for the SON season, as seen in TOMS/OMI data. Almost all models show a dominate eastward shift over the observation period across all latitudes for the λ_{min} trends.

Compared to the SON λ_{min} trends, there are more statistically significant model trends (to 1-σ) during the DJF season, with the E39CA, GEOSCCM, Niwa-SOCOL significant across all latitudes, and the MRI and UMUKCA-UCAM models robust across most latitudes. In TOMS observations, the λ_{max} trends during the DJF season, decrease towards 60°S and then reverse westward towards the pole. However, almost all model phase trends are eastward across the 7 selected latitude bands. E39CA model trends in λ_{max} during summer are significant across all latitudes, with UMSLIMCAT, UMUCKA-UCAM and GEOSCCM robust across most latitudes.

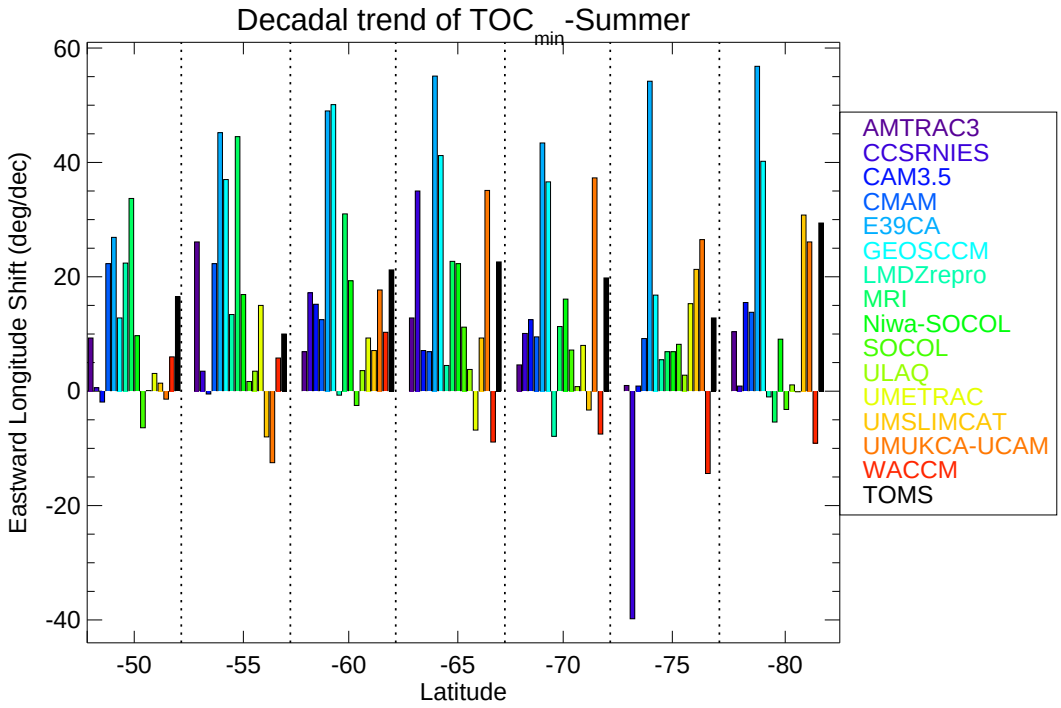

Figure 3.11: As in Figure 3.9, but for the DJF season.

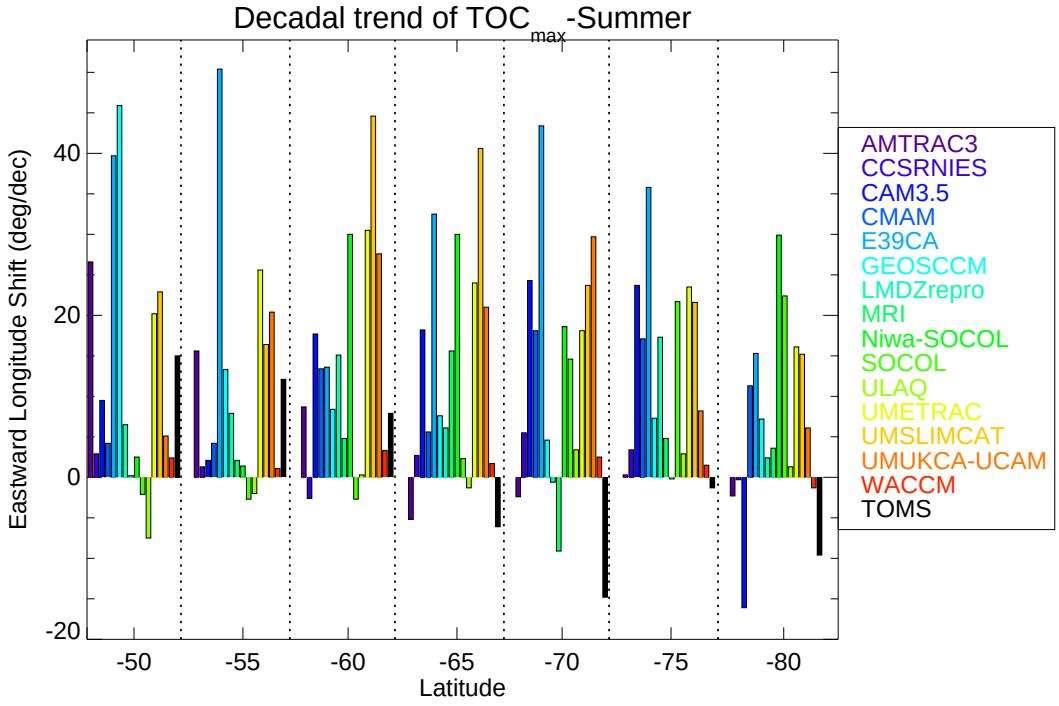

Figure 3.12: As in Figure 3.10, but for the DJF season.

When comparing between the two seasons, model linear trends during austral summer (DJF) were comparable with observations at the zonal extremes, although sometimes showing a larger phase trend at each latitude range, up to 40° per decade (4 times larger than TOMS). With the exception of GEOSCCM, no models have statistically significant phase trends across both seasons. Some models even seem to show strong trends in one season and very poor in the other season (e.g E39CA).

Both the amplitude and phase trends in model simulations suggest a strong zonal asymmetry in the TOC field that is present in the DJF season, but not quite as evident in the TOMS dataset. The REF-B1 model TOC zonal asymmetry during the SON season mostly shows small eastward decadel trends in both the λ_{min} and λ_{max} with only two models, AMTRAC3 and GEOSCCM, simulating a comparable TOC zonal asymmetry pattern with observations, during the ozone hole season. However, all models fail to simulate an increasing poleward trend in the λ_{min} during the SON season.

In Section 3.3.2, the multi-model median trends in each season are compared with TOMS/OMI observations, and the statistical significance of such trends in the zonal asymmetry of TOC distribution is evaluated. The multi-model phase shift trends in λ_{W1} and λ_{W2} are also analyzed in order to identify a dynamic cause of model trends for the zonal wave extremes. These trends are then projected into the 'prediction era' until 2100 using CCMVal-2 REF-B2 simulations. REF-B2 model runs begin from 1960 (see Chapter 2). However, in this study REF-B2 model data commencing in 2005 are used (REF-B2 model simulations were provided from 1960-2100) to provide continuity with REF-B1 model results. Therefore the year 2005 represents the boundary between the observation era and the prediction era.

3.3.2 Multi-model trends in TOC zonal asymmetry

Multi-model TOC trends were derived in the same manner as in Chapter 2, using a bootstrapping method to calculate a median value and a 95% confidence interval. Decadal trends of TOMS/OMI TOC observations and multi-model medians (MMM) in TOC phase shift for both seasons in the 'observation era' of 1979-2005 are shown in Figure 3.13 for

zonal minimum, maximum, wave-1, and wave-2 components, respectively. All components have a phase trend from REF-B1 models less than 10° per decade across all latitudes. For SON months, λ_{min} trends show a small eastward shift of 2-5°S per decade, equatorward of 70°S and within the spring polar vortex (poleward of 70°S) MMM trends suggest a stable longitudinal position. This implies no trend in the position of the ozone hole relative to the pole during spring over the 26 year period. This contradicts TOMS observations, which show an increasing eastward phase trend approaching the pole with a maximum of approximately 20° per decade, with all TOMS trends poleward of 50°S statistically significant to 2-σ. MMM λ_{min} trends are mostly significant to a 95% confidence level between 50-65°S latitudes, similar to the λ_{max} trends, which are a little less robust and show slightly bigger phase trends (5-8° per decade) over the 1979-2005 period. MMM λ_{max} trends also stabilise within the polar vortex during spring with no real phase trend observed.

The seasonal trends in λ_{max} (Figure 3.13; panel b) show that there is a MMM phase trend maximum at 55° in the SON season with no significant phase trends across all latitudes from 1979-2005. MMM TOC λ_{max} trends during SON are reasonably similar in magnitude to both TOMS λ_{max} and MMM λ_{min} trends. Model results suggest a symmetric small eastward phase shift of the zonal TOC distribution that decreases with increasing latitude. However, the TOMS SON distribution has a significant λ_{min} decadal trend that increases towards the pole, and a minimal λ_{max} trends at most latitudes.

TOMS and MMM summer trends in λ_{min} show a more dominant eastward phase shift across most latitudes than observed in SON months, with model trends showing a maximum shift of approximately 8° per decade at 55°S, whereas TOMS trends show a maximum trend at 80°S. Summer trends are generally less robust for both datasets, indicating much greater variability in the longitudinal position of λ_{min}.

Model λ_{max} trends for the DJF season show much poorer agreement with observations at all latitudes, with a maximum trend in phase shift at 70°. TOMS trends show a sharp decline in eastward phase shift that reverses at 65°S with a westward phase trend towards the pole. This is not seen in MMM trends which show a steady eastward decadal phase

shift in λ_{max} similar to what is observed in MMM trends in λ_{min}.

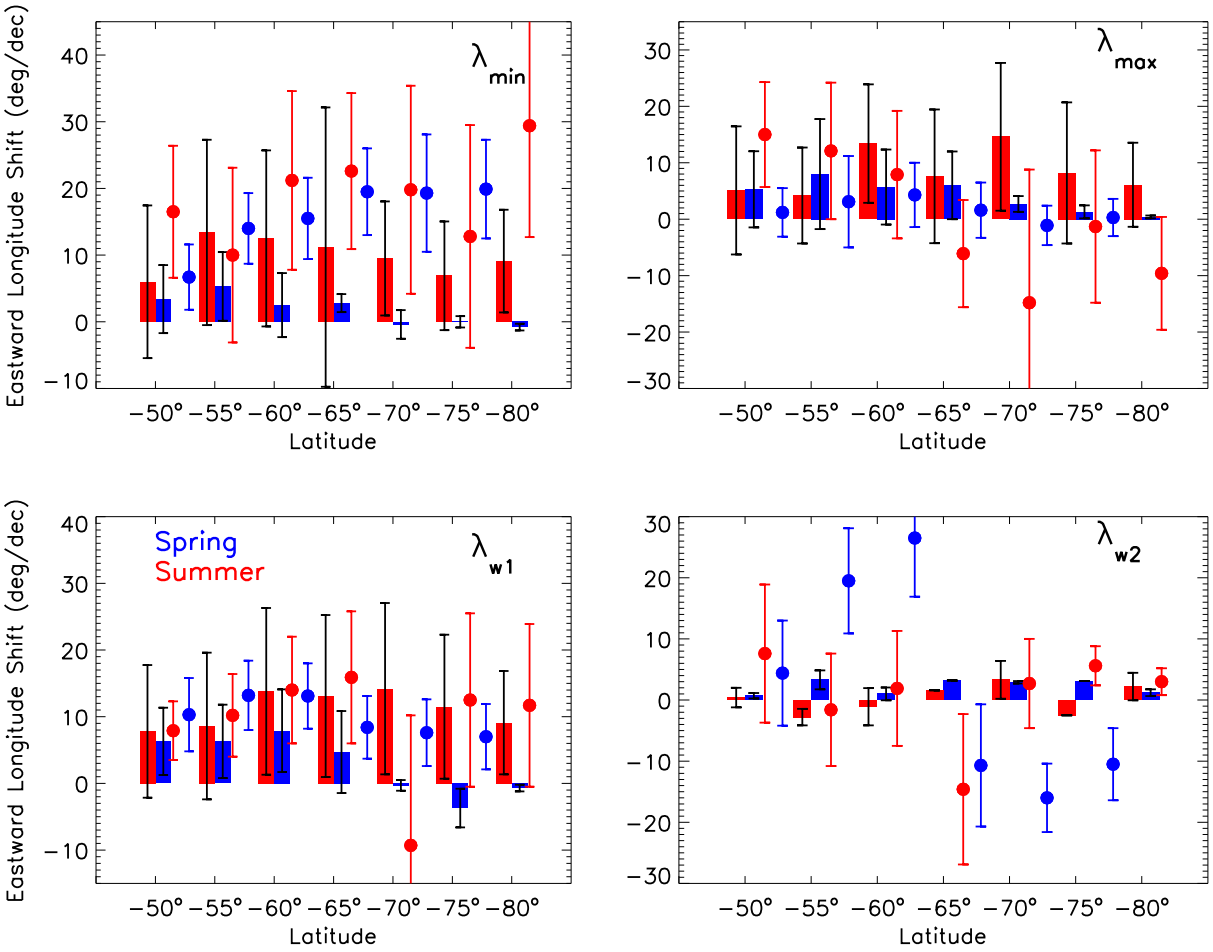

Figure 3.13: REF-B1 Multi-model medians of decadal phase shift over the SON months (blue) and DJF months(red), for the 7 latitude ranges over the period 1979-2005. Black error bars denote the 95% confidence interval for the model trends. Circles represent TOMS/OMI trends for the same latitude bins, plotted to the right of their respective latitudes with error bars representing 1-σ uncertainty values. Note the variation in the y-axis scaling between plots.

Panel (c) in Figure 3.13 illustrates the phase trends of the QSW-1 component of the zonal TOC distribution for the austral spring and summer. As shown in Figure 3.5, the amplitude of the model zonal TOC distributions is dominated by the QSW wave-1 component, in agreement with previous studies [*Ialongo et al.*, 2012]. In the MMM phase trends for the SON season, the wave-1 components are comparable to the λ_{max} and λ_{min} trends at latitudes up to 65°S, with a robust peak trend in λ_{w1} at 60°S. This implies a

dynamic influence from the QSW wave-1 component in the TOC distribution at latitudes outside the polar vortex. At this latitude range, the TOMS λ_{w1} trends are also statistically significant, at twice the magnitude of MMM trends. The DJF MMM λ_{w1} trends show a maximum TOC shift at 70°S, and are robust across most latitudes. Other than the large statistical uncertainty range of the TOMS/OMI data at 70°S, there is good qualitative and quantitative agreement between TOMS and MMM results for the DJF months.

Decadal phase trends in λ_{w2} are shown in panel (d) of Figure 3.13 for both austral seasons. This illustrates the spring TOMS westward phase trends poleward of 60°S in the TOMS data which act to oppose the dominant eastward wave-1 phase trend, resulting in a significant eastward trend in the λ_{min} but a stable position in the λ_{max}. The MMM trends in λ_{w2} are generally much smaller in magnitude than their TOMS counterparts for both seasons. Even though the MMM phase trends are small, they are generally statistically significant. Poleward of 65°S during the SON months, the small eastward wave-2 trends combine with the wave-1 trends to give no real phase shift in the overall TOC distribution at these latitudes. This indicates little or no QSW influence on the TOC distribution within the polar vortex for REF-B1 models, and that within the spring vortex, photochemical processes dominate TOC distribution.

MMM trends equatorward of 65°S for λ_{w1} during austral spring show a similar pattern to TOMS trends, with MMM trends approximately half or 2/3 of the magnitude of TOMS trends. The MMM trends are even closer to observation trends at these latitudes during the DJF months. This would suggest that the dynamic influence of SH mid-latitude planetary waves on model TOC distribution during SON is much less than what is observed, as found in *Wirth* [1993]. However, during the DJF months, a comparison of MMM and TOMS trends suggest a similar dynamic influence from these mid-latitude planetary waves. Whilst the wave-2 harmonic shows a similar amplitude to TOMS observations, as previously discussed, the model phase trends do not agree very well, particularly during the ozone hole season.

REF-B2 model simulations were used to derive MMM trends in the TOC phase shift during the 'prediction era' (2005-2100). As previously stated (Section 3.2), these REF-B2

MMM trends are derived from only 10 CCMs; the AMTRAC3, CAM3.5, E39CA, UME-TREC and WACCM models are not included in this part of the study. REF-B2 model simulations consider the effect of anthropogenic forcings only, as described in Chapter 2. For comparison with REF-B1 model trends, Figure 3.14 shows the MMM trends for the REF-B2 model simulations averaged from 1979-2005. This part of the REF-B2 model analysis did not include the GEOSCCM model, as the REF-B2 simulations provided from this model commenced in 2005.

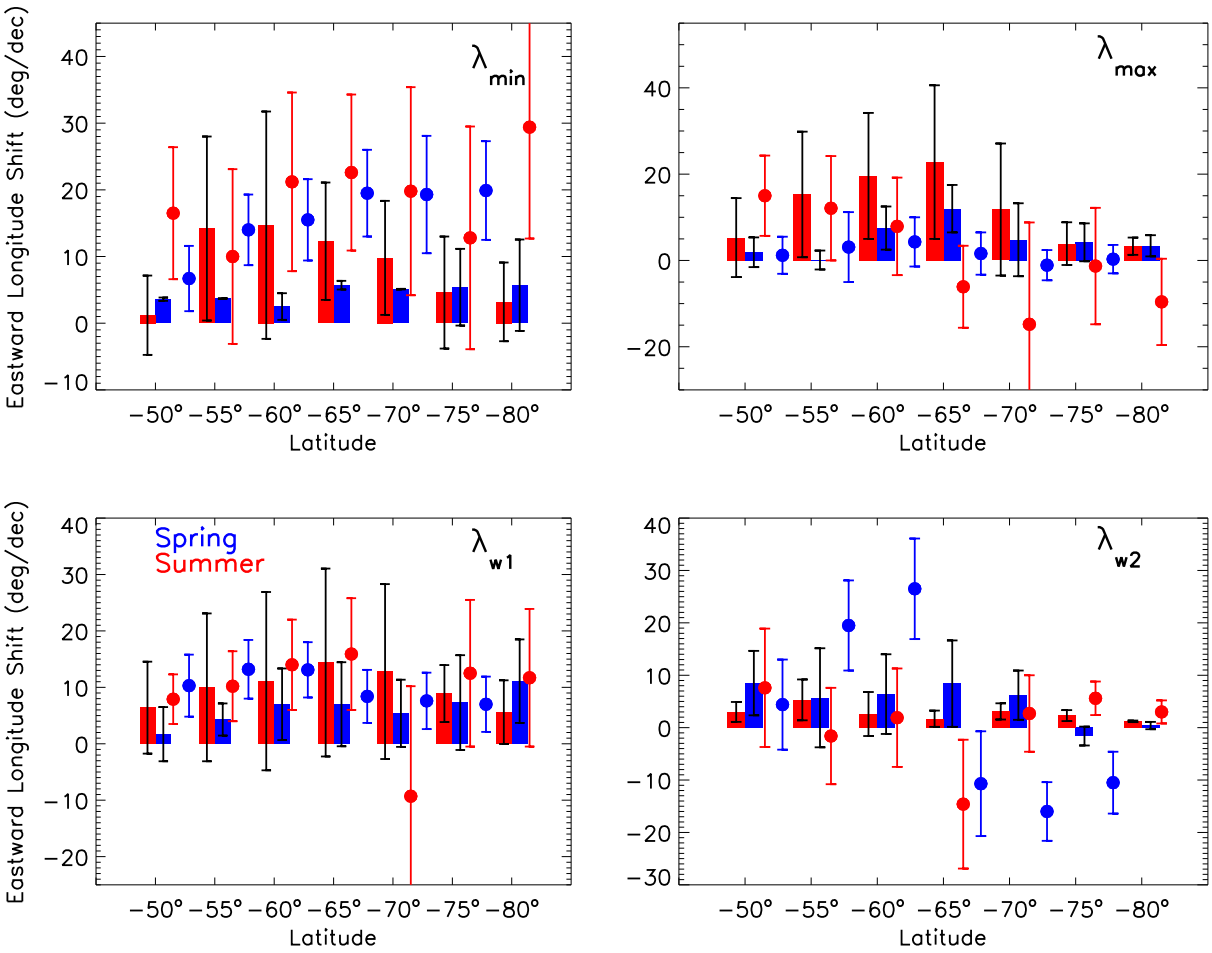

Figure 3.14: As in Figure 3.13 but for REF-B2 Multi-model medians from 1979-2005.

REF-B2 MMM spring (SON) trends in λ_{min} (Figure 3.14; panel a) show a reduced magnitude in decadal trends, in comparison with TOMS/OMI observations. However, unlike the REF-B1 trends, the REF-B2 SON decadal phase trends increase towards the

pole, up to almost 10° per decade. The λ_{min} SON trends are statistically significant across all latitudes to a 90% confidence limit. This is reflected in the SON λ_{w1} trends (Figure 3.14; panel c), which tend to increase with increasing latitude. Poleward of 50°S, these λ_{w1} trends are also statistically significant. The MMM λ_{max} trends are larger in magnitude than the TOMS trends with a maximum at 65°S, of 10° per decade.

REF-B2 MMM phase trends during DJF, are larger in magnitude than during the SON season, across most latitudes in all panels shown in Figure 3.14. Maximum phase trends for λ_{max} and λ_{w1}, are observed at 65°S, with a more equatorward peak trend for λ_{min} located at 55°S.

REF-B2 MMM trends, relative to REF-B1 MMM trends, have a better qualitative agreement with TOMS observations during SON months. The DJF MMM trends are very similar for REF-B1 and REF-B2 simulations, in their agreement with observations. There is a clearer maximum DJF phase shift trend at 65°S for λ_{max} in the REF-B2 simulations, as seen in the λ_{w1} trends in the same season. The Antarctic land-sea boundary is located at this latitude, suggesting a clearer QSW forcing in the TOC distribution for the REF-B2 model simulations. However, both REF-B1 and REF-B2 MMM λ_{max} phase trends during the DJF season, do not show a reversal to westward phase trends that is observed in the TOMS decadal trends.

Figure 3.15 shows the predicted phase trends for the first half of the 21st century, 2005-2050. Antarctic ozone is expected to increase during this time [*Eyring et al.*, 2010c]; [*Eyring et al.*, 2013] due to decreasing ODSs, prescribed by the adjusted World Meteorological Organization A1 scenario [*WMO*, 2007]. The decadel MMM phase trends for both austral seasons are much smaller, compared to the observation period, with no individual phase trend greater than 4° per decade. Poleward of 65°S there is a statistically significant, yet small residual eastward trend for λ_{w1}, with the TOC extremes (λ_{max}, λ_{min}) showing minimal decadal trends. At sub-polar regions, equatorward of 65°S there is a dominance of small westward phase trends, mostly significant to a 95% confidence limit during both seasons. The wave-1 component reflects this westward phase trend at sub-polar latitudes, a situation which is reversed eastward of 70°S. A minimal eastward phase

trend is observed during the SON season in the TOC distribution at latitudes poleward of 70°S, but is not statistically significant. The wave-1 component seems to greatly influence the phase trends in both seasons, with the wave-2 component only providing a counterpoint to the wave-1 harmonic during the DJF season between 60-70°S.

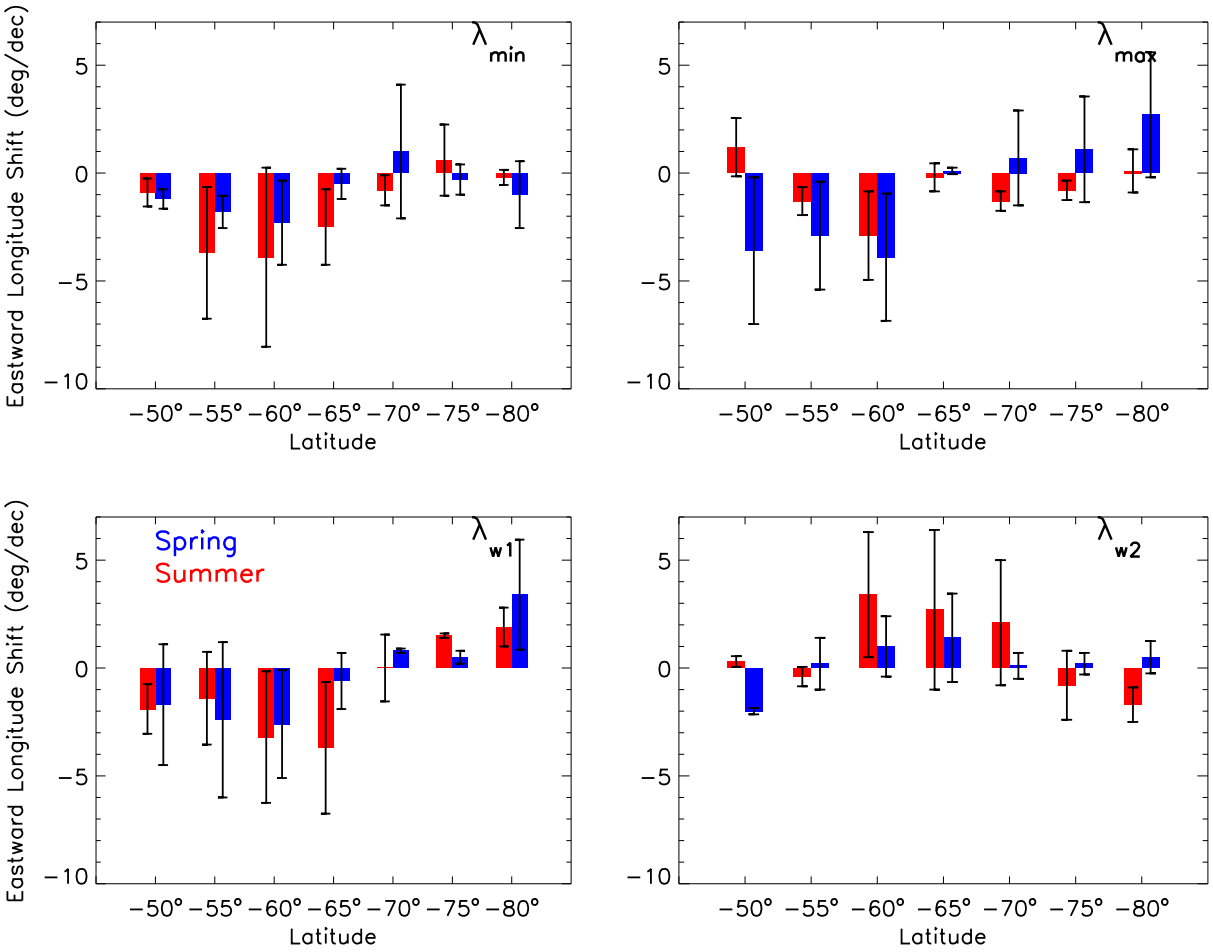

Figure 3.15: As in Figure 3.14 but for REF-B2 Multi-model medians from 2005-2050.

The reduction or reversal in TOC phase shift in the future period appears to be a response to future ozone recovery, particularly during the SON season. With projected anthropogenic forcings (decreasing ODSs and increasing GHG emissions) during the 21st century dictated by the scenarios used in the REF-B2 simulations, the residual eastward phase trend during the SON season reflects the projected decrease in ODSs at latitudes poleward of 65°S.

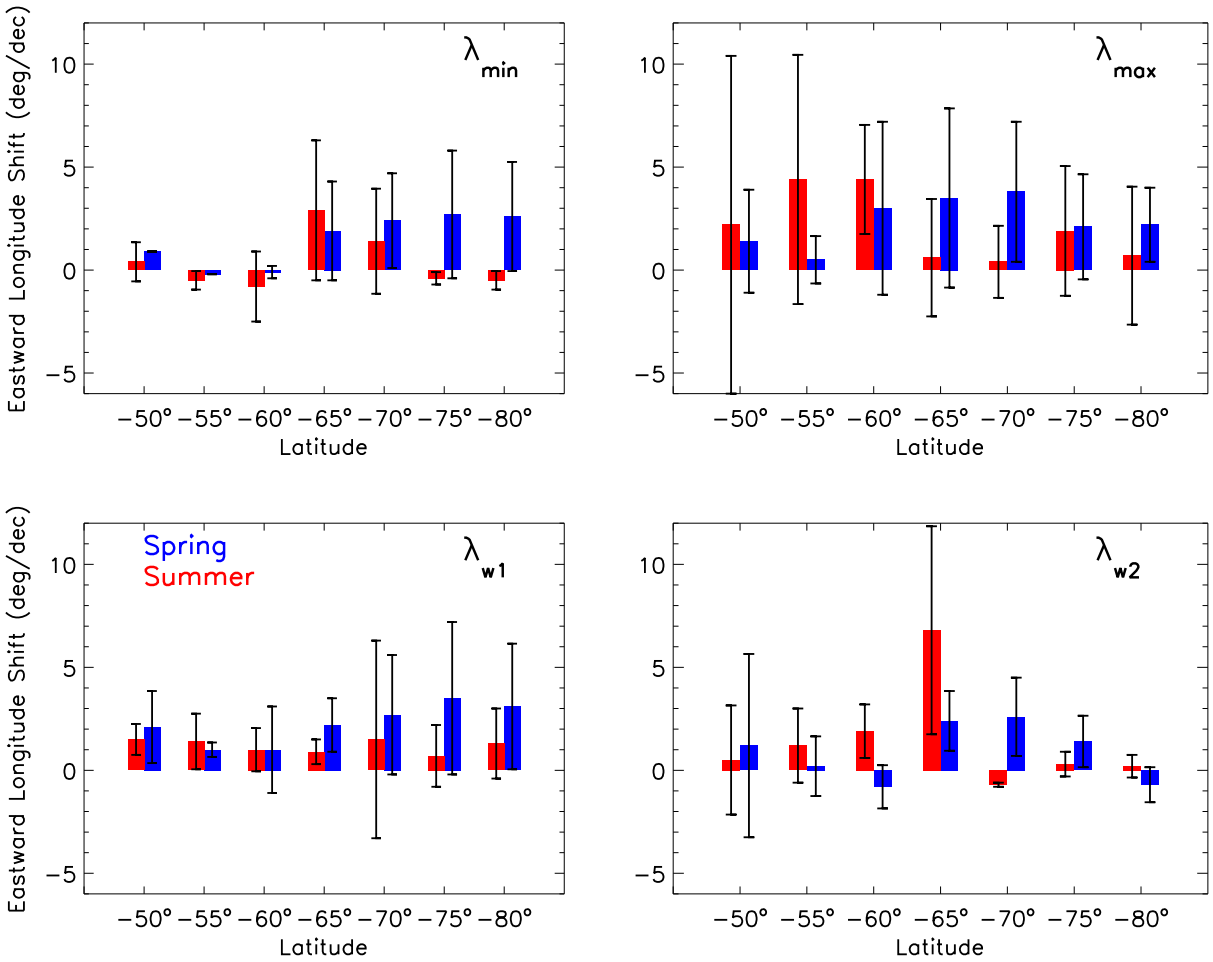

Figure 3.16: As in Figure 3.14 but for REF-B2 Multi-model medians from 2050-2100.

Figure 3.16 illustrates the seasonal decadal phase trends for the 2050-2100 period. The λ_{min} trends at sub-polar latitudes for both seasons are minimal, indicating a stable λ_{min} position on a decadal scale. At latitudes poleward of 60°S, for the SON season there is a small eastward trend of 2° per decade. The λ_{max} trends during austral spring months are similar to the λ_{min} trends, with the λ_{max} trends a little larger in magnitude. Most DJF MMM phase trends show a minimal eastward shift across all latitudes. The wave-1 component of the TOC distribution also shows an eastward phase trend across all latitudes, with the SON trends, both larger in magnitude and statistically more sound, than the corresponding DJF trends. These results suggest a residual eastward trend for both seasons, across most latitudes, but with only minimal confidence. This indicates significant variability between REF-B2 models towards the end of the 21st century.

3.3.3 Projected ozone recovery relative to zonal mean

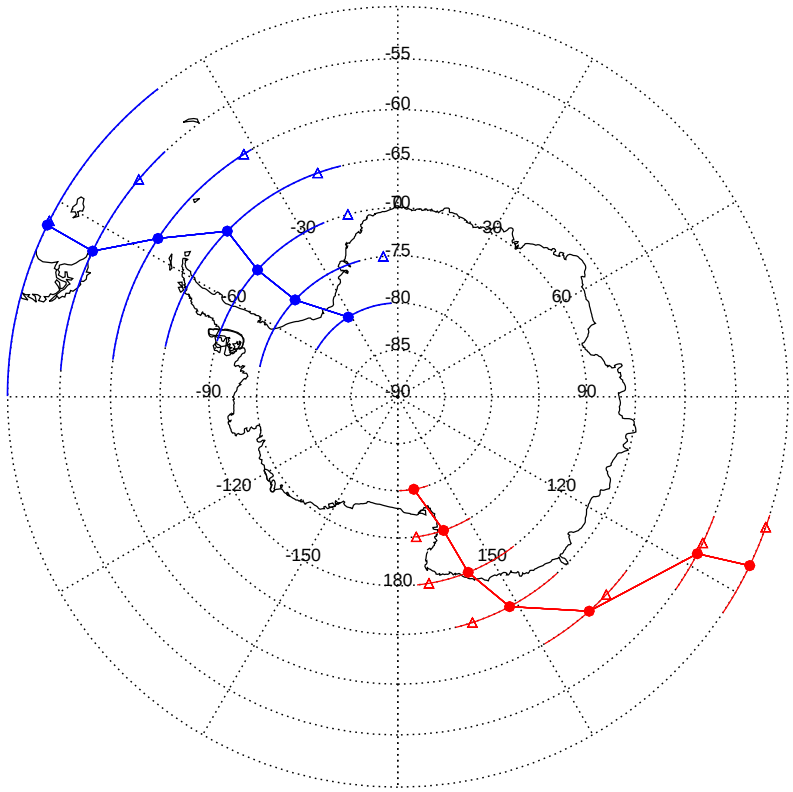

Figure 3.17: REF-B1 MMM longitudinal locations of the spring TOC extremes (λ_{max} and λ_{min}) averaged over 1979-2005. λ_{max} positions (red) and λ_{min} positions (blue) are shown for each 5° latitude band, with curves indicating the 95% confidence interval. Triangles denote mean zonal TOC extreme locations from TOMS observation up to 75°.

According to *Grytsai et al.* [2007], during the 1979-2005 period, the longitudinal positions of the zonal TOC minimum and maximum were located in the Atlantic (about 30°W) and Pacific (about 150°E) sectors, respectively. REF-B1 MMM values of zonal TOC minimum locations are shifted westward with respect to the TOMS observations by approximately 20° at each latitude band. The locations of the zonal TOC maximum, however, agree very well with TOMS observations, with all mean TOMS λ_{max} locations well within the MMM 95% confidence interval. REF-B2 MMM values in the 1979-2005 period, are very similar to what is shown in Figure 3.17 for the austral spring (SON) season. The longitudinal positions of λ_{max} and λ_{min}, equatorward of 70°S in the REF-B2 simulations, are a little more westward than their REF-B1 counterparts.

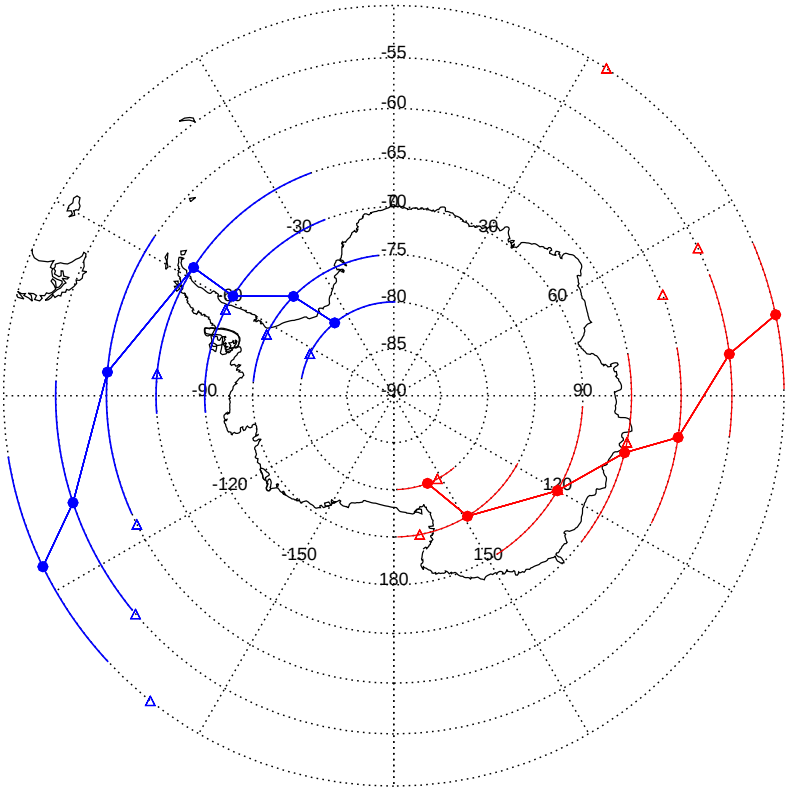

Figure 3.18: As in Figure 3.17, but for the DJF season. Note that TOMS observations at 80°S were available during this season and are included.

MMM longitudinal positions of the TOC extremes for the austral summer (DJF), averaged over 1979-2005, are shown in Figure 3.18. The mean position of the TOC extremes of both TOMS observations and REF-B1 simulations, have rotated westward with respect to their respective SON positions. This westward displacement increases with decreasing latitude (moving equatorward) in both TOMS and model trends. In fact, the REF-B1 MMM values do not quite capture the significant westward curl in the summer TOMS observations observed at latitudes between 50-60°S. The MMM λ_{min} positions during DJF are now eastward of the TOMS positions (between 10-30°). The MMM λ_{max} positions are also eastward (between 0-45°), with respect to TOMS positions. The REF-B2 MMM trends for the DJF season show similar λ_{max} positions to the REF-B1 models (shown in Figure 3.18). However, the REF-B2 λ_{min} zonal positions are still westward of TOMS λ_{min} averages poleward of 60°S.

As the TOC zonal asymmetry pattern has a smaller amplitude during the summer months (see Figure 3.3), this makes it difficult to determine annual maxima and minima in the TOC distribution for some years. TOMS TOC extreme locations during DJF months, are often outside the MMM 95% confidence interval equatorward of 65°S. However, model results do agree qualitatively with TOMS observations during both seasons, with MMM values having a westward curl in the positions of the TOC extremes, outwards from the pole. REF-B2 MMM positions of the zonal extremes, are in slightly better agreement with TOMS positions equatorward of 65°S.

Time series of longitudinal trends from REF-B2 model simulations over the entire model run time (1960-2100), for both seasons, are considered in the Hovmöller contour plots at 65°S shown in Figures 3.19 and 3.20. These Hovmöller plots show how the TOC distribution varies with respect to longitude and annual mean for the REF-B2 models used in this study. Each model was interpolated to a common grid resolution of 5° latitude bins and 2° longitude bins and a multi-model mean value within each grid box calculated. The 65°S latitude range is shown in the Hovmöller plots during the austral spring and summer months. The coloured dashed lines in each plot, represent the approximate MMM value of zonal λ_{max} and λ_{min} from the REF-B1 simulations as shown in Figures 3.17 and 3.18, and are shown to highlight the direction of TOC phase trends over time.

Figure 3.19 illustrates that there is an eastward shift in the TOC zonal asymmetry during the ozone depletion period until approximately 2010. The eastward shift trend stabilises during the ozone recovery period. There is a suggestion of a small secondary eastward shift towards the end of the century, which is seen in the TOC maximum location. As these model simulations consider anthropogenic forcings only, this result suggests a link between the decreasing TOC eastward phase shift and a decrease in ODS levels. In the observation period (Figure 3.13), an increasing eastward shift in the TOC zonal asymmetry is observed during the period of increasing halogen concentrations.

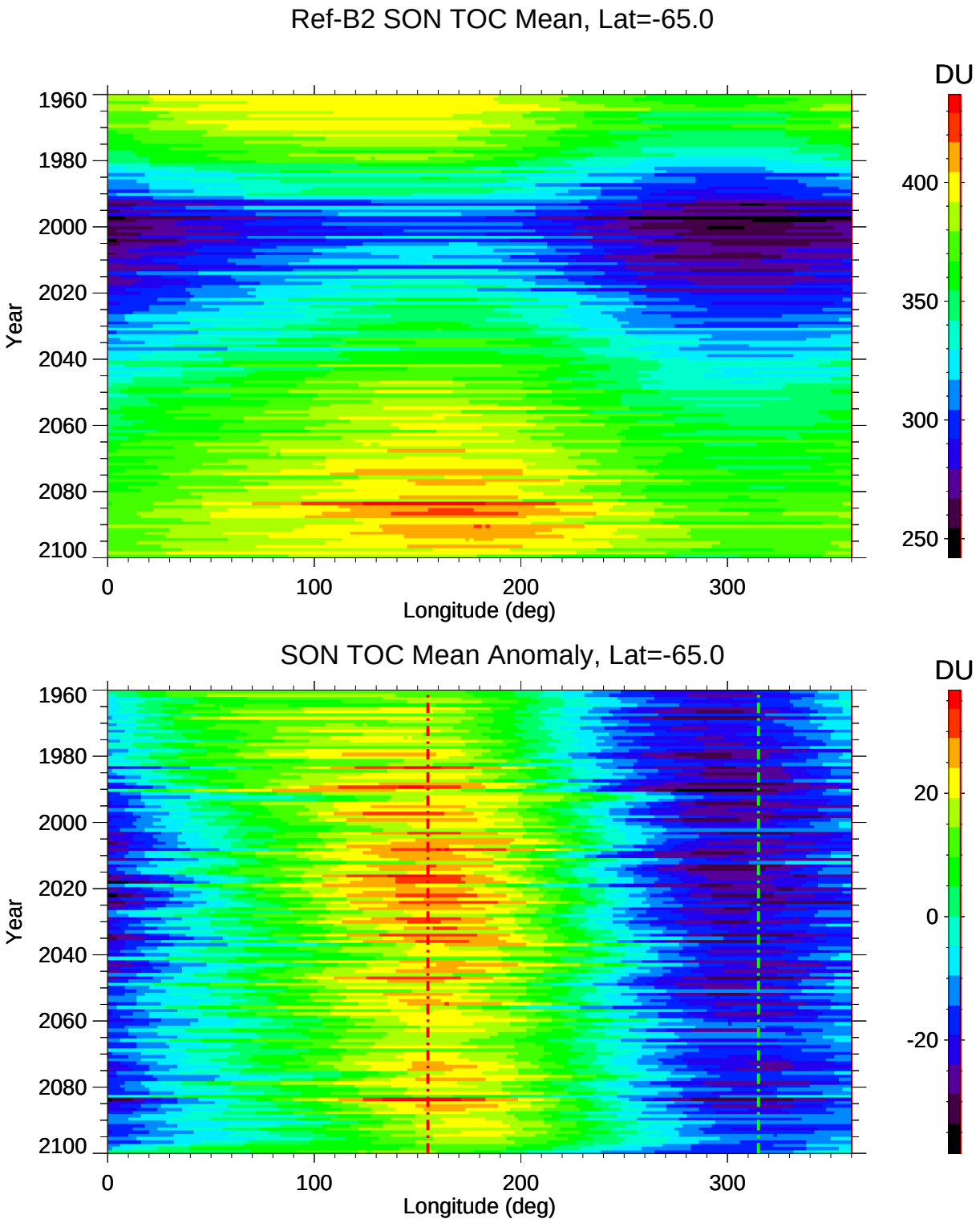

Figure 3.19: Temporal-longitudinal contour plot of all REF-B2 model simulations of the TOC seasonal mean (top) and the anomaly from the TOC zonal mean (bottom) at 65°S, during SON from 1960-2100. Dashed-dotted lines indicate 1979-2005 REF-B1 median values of the longitudinal position of λ_{max} (red) and λ_{min} (green) for this latitude.

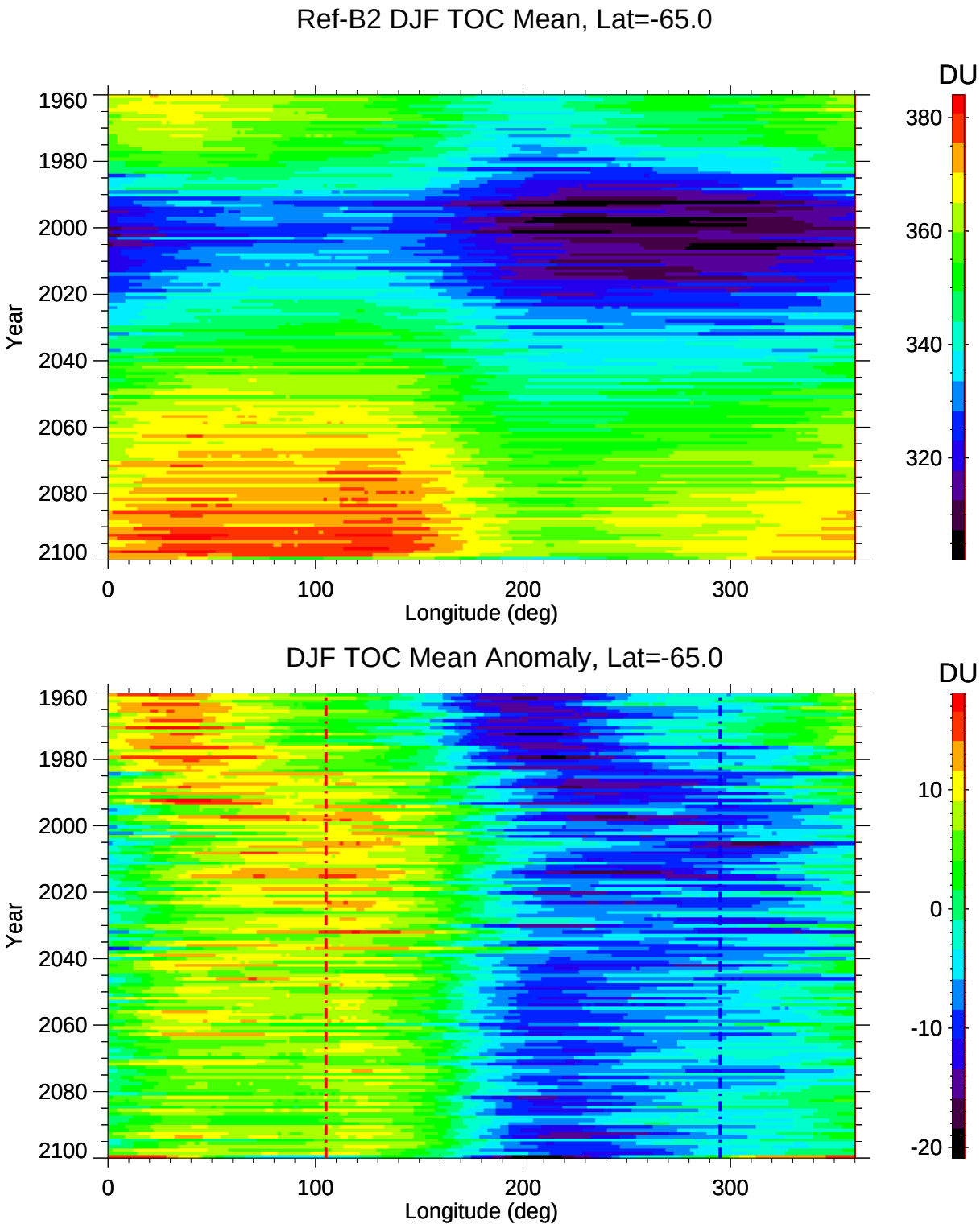

Figure 3.20: As in Figure 3.19, but for the DJF months. Note that the longitudinal position of λ_{min} from the 1979-2005 REF-B1 median is shown in blue here, for clarity.

The results indicate that towards the end of the 21st century, there is still a residual eastward shift in TOC zonal asymmetry. This shift occurs during a period of projected TOC increase, together with decreasing ODS levels and increasing GHG emissions set by the parameters of the REF-B2 simulations. This points to more dynamical effect from QSW activity affecting zonal TOC over Antarctica, once ODS levels decrease to lower concentrations. CCMVal-2 REF-B2 simulations in relation to halogen loading, predict a return to 1960 values towards the end of the 21st century [*Eyring et al.*, 2010c].

The projected evolution of the zonal asymmetry of TOC in the DJF season shown in Figure 3.20 indicates that the TOC wave-like distribution has a smaller amplitude than in the SON season, with a smaller range of values between λ_{max} and λ_{min} observed in the TOC anomaly plot. However, TOC zonal asymmetry is still observed over the period. A reduced eastward shift during the ozone recovery period (after year 2000) shows more interannual variability than during the SON months, which is particularly evident in the TOC anomaly minimum values from 2000-2040. In the period beyond 2050, the λ_{max} values seem to branch apart at around 40°E and 110°E, further breaking up the zonal asymmetry in the TOC distribution by 2100.

Figure 3.21 shows the TOC anomaly for both seasons relative to a 1965 baseline value, as used in Chapter 2. The zonal mean TOC values at 65°S from REF-B2 simulations, together with TOC variation at the approximate mean longitudes of λ_{max} and λ_{min}, return to 1965 values at the end of the century (around 2090) in the austral spring. During summer, the zonal mean returns to the 1965 baseline much earlier (approximately 2055), as expected with the break-up of the polar vortex. However, for both seasons at the λ_{max} and λ_{min} positions, the turning points of TOC recovery are delayed by around 20 years, even though the magnitudes of the anomalies themselves, are much less than the zonal mean. The summer λ_{max} and λ_{min} positions gradually approach 1965 baseline values by the end of the simulations. Although the magnitude of this TOC depletion is not as large as during spring, it is suggested that this may have a potential impact on the amount of sea ice present at some longitudes due to variation of UV radiation received at the surface.

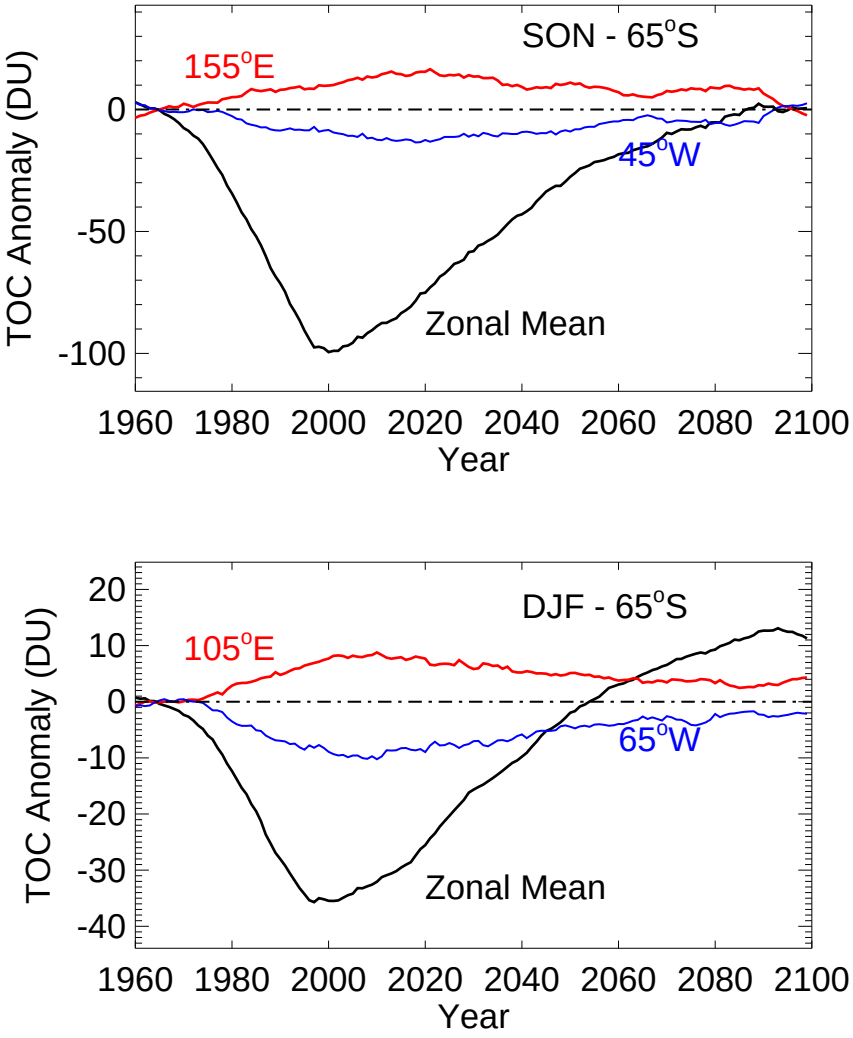

Figure 3.21: Time series of REF-B2 Multi-Model mean TOC zonal anomalies at 65°S relative to a 1965 baseline value for austral spring (top) and summer (bottom). Red (λ_{max} longitude) and blue (λ_{min} longitude) curves are the TOC residuals at the stated longitude, with the zonal mean value removed. A 11-year uniformly weighted sliding mean filter has been applied.

To further illustrate the dynamic influence on the TOC asymmetry, Figures 3.22 and 3.23 illustrate the multi-model mean 50 hPa geopotential height (GPH) fields from REF-B2 simulations for both seasons. Also shown, are the zonal anomalies over the time period as an indication of the GPH amplitudes present in the lower stratosphere.

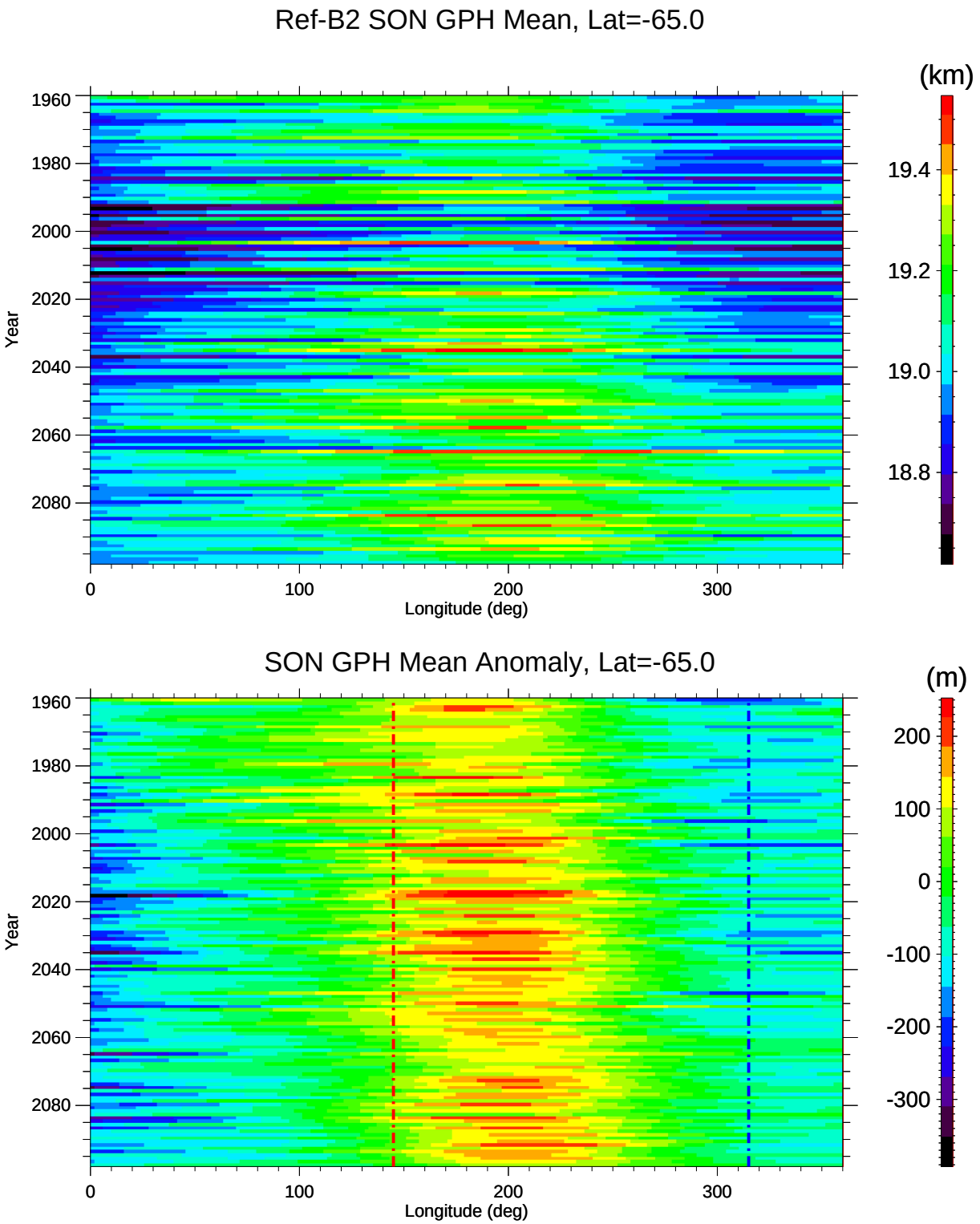

Figure 3.22: As in Figure 3.19 but for the 50 hPa geopotential height field. Dashed-dotted lines are the same as in Figure 3.19 for reference.

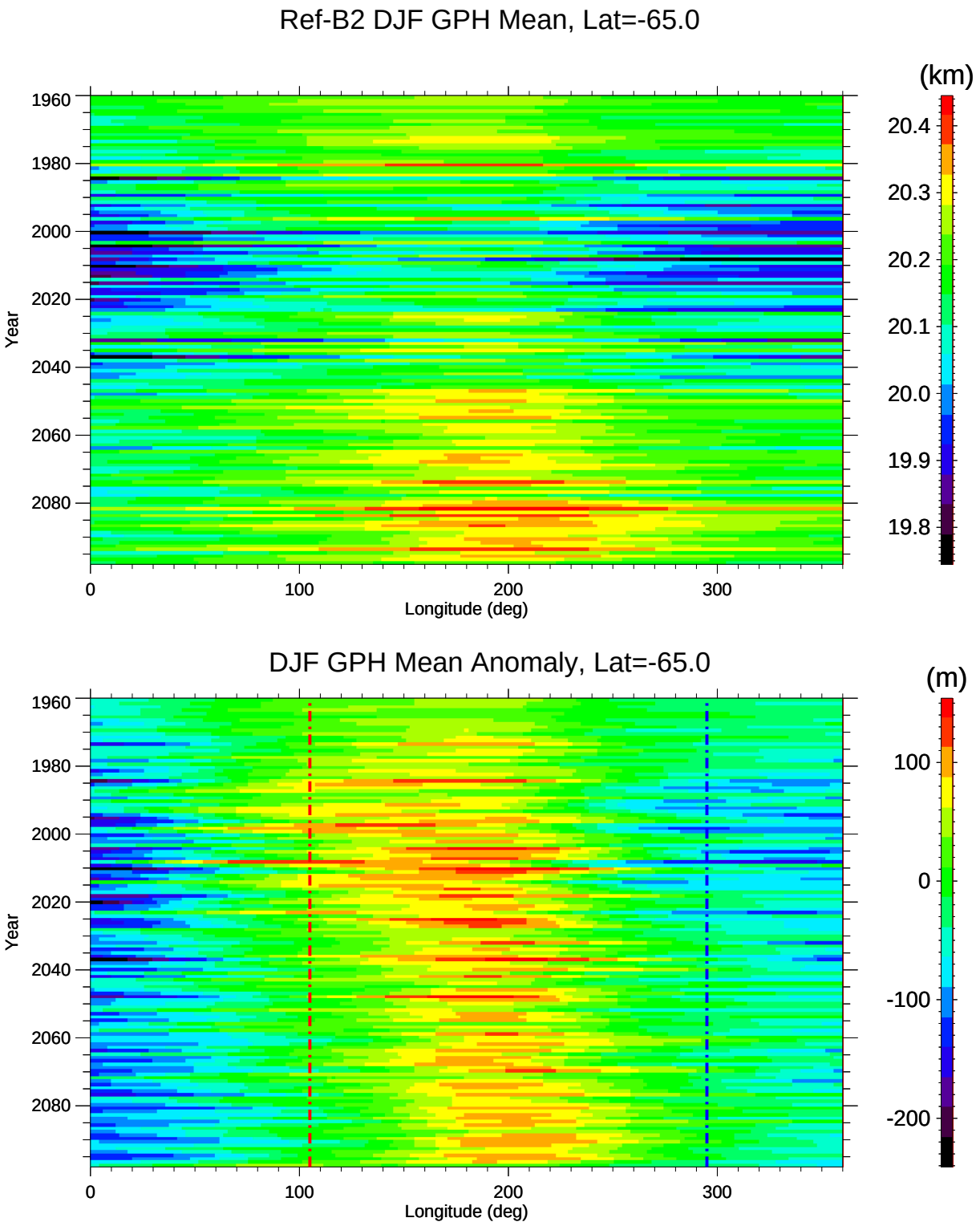

Figure 3.23: As in Figure 3.22 but for the DJF season.

During the SON season, there is a consistent eastward offset of 30-50° between maxima and minima of the TOC and GPH until the end of the simulations, with the GPH zonal anomaly having an eastward phase trend during the depletion period and stabilising during the recovery period. The offset during the DJF season increases with the GPH ridge at around 90° eastward of the TOC ridge at 65°S. The magnitude of the seasonal mean amplitudes at this latitude, are similar to the 30 year monthly linear trends of observations that were presented in *Thompson and Solomon* [2002]. Over a 30 year period (1970-2000), model GPH amplitudes show a decrease of approximately 200 metres during SON months, and about 170 metres during DJF months.

3.4 Discussion and conclusions

Decadal trends in the TOC zonal asymmetry during the observation period of 1979-2005 are derived from CCMVal-2 multi-model median values and compared with observations from the TOMS/OMI dataset. A wave-like structure in the zonal TOC distribution from REF-B1 model simulations is observed in the SON months, at latitudes of 50-80°S, in agreement with observations [*Grytsai et al.*, 2007]. A weaker stationary wave pattern from REF-B1 model simulations, is observed in the DJF months. Similar to Chapter 2, mult-model medians (MMM) were used to consider decadal trends in the TOC zonal asymmetry of CCMVal-2 models.

The MMM amplitudes of the TOC zonal asymmetry distribution over 5° latitude ranges are reduced by a factor of two compared to what was observed in TOMS trends, during SON months. MMM amplitudes peaked at less than 30 DU at the polar vortex edge (60-65°S), compared to a clear spring amplitude maximum of over 60 DU from satellite observations. Individual model amplitudes showed a large spread of values, but all of them underestimate spring TOC zonal asymmetry across all polar latitudes. This suggests a weaker tropospheric planetary wave forcing in model simulations, than what is observed. The amplitudes of the QSW wave-1 component dominate the zonal TOC distribution, often accounting for up to 90% of the zonal variation, similar to TOMS observations.

As expected, there was less zonal asymmetry in the MMM TOC distribution during the austral summer. However, a weak QSW pattern was still present, and as with the SON season, decomposition of model zonal TOC values during DJF months, shows a dominant QSW wave-1 component. The MMM DJF amplitudes are similar to TOMS observations, but slightly larger in magnitude. However, there was still quite a spread between individual models, with some models showing more TOC zonal asymmetry in DJF than in SON (LMDZrepro and MRI). This could be due to models simulating the SH polar vortex much later in the year (into early summer), than what is observed [*Eyring et al.*, 2010a].

The MMM wave-2/wave-1 amplitude ratios were between 0.22-0.36 during both seasons, which is consistently higher than TOMS observations during SON months across all latitudes considered. This suggests that either the wave-1 amplitudes are underestimated or the wave-2 amplitudes are overestimated during the ozone hole season. This distorts the polar vortex unrealistically in the model simulations, as found in the geopotential height field at 10 hPa for the REF-B1 simulations [*Eyring et al.*, 2010a]. These wave-2 components are often eastward travelling waves, prevalent in the stratosphere during the SON season, but confined to the lowermost stratosphere during DJF months [*Miles et al.*, 1994]. In both seasons, the amplitudes of the wave-2 components seem to be comparable to observations. However, the wave-1 components during SON months are much smaller, suggesting a reduced strength in QSW forcing across all models.

The main focus of this study was the temporal behavior of model TOC zonal asymmetry. Figures 3.9 to 3.12 show large intra-model variability in decadal phase trends, but overall a dominant eastward phase shift during the 'observation' period. Multi-model median TOC values suggest that the TOC zonal extremes (λ_{min} and λ_{max}) have an eastward shift across all latitudes during the ozone depletion period. This contradicts TOMS observations that show a statistically significant eastward phase shift of λ_{min}, but a stable longitudinal position of λ_{max} during the austral spring. Some model results are statistically significant to a 90%- 95% confidence limit, at latitudes equatorward of the polar vortex. However, magnitudes of the model phase trends are much smaller than those from TOMS/OMI

observations for λ_{min}, as was observed in the model amplitudes during spring.

During SON months, MMM trends indicate an eastward decadal shift in λ_{min} that is half the magnitude of that observed in TOMS trends at sub-polar latitudes (equatorward of 70°S). These small eastward phase trends were mostly significant outside, and at the edge of the polar vortex (50-65°S). Poleward of 65°S, REF-B1 MMM trends show no significant phase shift for either λ_{min} or λ_{max}.

Model trends in the TOC phase shift during the DJF season are much larger in magnitude than those during the SON season. Some of the model DJF decadal trends were statisically significant, particularly in λ_{w1} phase trends. In fact, there was better agreement between TOMS and MMM trends at most latitudes for the QSW wave-1 component than the TOC extreme trends. REF-B1 trends in λ_{min}, λ_{max} and λ_{w1} reveal a peak phase shift between 60-70°S during DJF months. TOMS trends show a decreasing eastward phase shift in λ_{max}, reversing westward at 65°S. TOMS λ_{min} have a statistically significant eastward phase trend at all latitudes, however the TOMS λ_{w1} seem to agree well with MMM trends at most latitudes. Summer observations show a wider range of interannual longitudinal positions of TOC extremes, possibly due to lower amplitudes of the zonal TOC distribution, that results in a lower asymmetry and thus lower wave-1 amplitudes.

In contrast to TOMS trends, CCMVal-2 model simulations show no clear, or statistically significant λ_{w2} trends over both seasons. Whilst the TOC amplitudes match well with observations during DJF, the phase trends show a reasonably stable location with no response to ozone depletion during the 1979-2005 period.

The difference in TOC phase shift trends between observations and models could be the effect from the wave-1 and wave-2 components on the TOC asymmetry pattern, with statistically significant phase shifts in opposing directions observed by TOMS, but not seen in the MMM trends. *Raphael* [1998] compared the QSW pattern in the geopotential height field from two models from the National Centre For Atmospheric Research (NCAR) with reanalysis data. The Climate System Model (CSM1) was run with an interactive ocean and the Community Climate Model version 3 (CCM3) was run without an interactive ocean. In comparison to reanalysis data, the wave-2 component was better simulated by

the CSM1 model due to thermal forcing from the interactive ocean. They suggested that sea-ice distributions (SIC) and sea-surface temperatures (SST) played an important role in the forcing caused by the wave-2 component. All CCMVal-2 models included in this study use prescribed monthly averaged parameters derived from observations (HadISST1 datasets) as boundary conditions in the REF-B1 simulations [*Eyring et al.*, 2010a].

For the same observation period of 1979-2005, MMM trends were found from REF-B2 model simulations as shown in Figure 3.14. The trends in λ_{max} for the SON months also show a small eastward phase shift across most Antarctic latitudes. However, the eastward trend in the λ_{min} shows a qualitatively improved agreement with TOMS observations with an increasing eastward phase shift towards the pole, with trends at all latitudes significant to a 90% confidence limit. The REF-B2 λ_{max} trends are similar to what is observed in the REF-B1 trends for the SON season. However, the decadal phase shifts are still half the magnitude of those seen in the TOMS trends. Summer trends in the REF-B2 simulations are very similar to those found in the REF-B1 simulations, with a statistically significant increase in λ_{max} trends found within the 'collar' region at sub-polar latitudes, reaching a peak of over 20° per decade at 65°S. Trends in the wave-2 component are also increased somewhat compared to REF-B1 trends for both seasons, however, they do not match the phase variability seen in the TOMS trends.

Therefore, during the SON months, there seems to be improved agreement with model results, when only anthropogenic forcings are considered. This is also seen in the wave-1 component, where over most latitude ranges, trends are significant within a 95% confidence limit, and are in reasonable agreement with the QSW phase trends in the TOMS observations within the polar vortex. The models that were not used for REF-B2 phase trends, but were used for REF-B1 trends (AMTRAC3, CAM3.5, E39CA, GEOSCCM, UMETRAC and WACCM), were not themselves, poor performing, in relation to decadal TOC phase trends. In fact, AMTRAC3 and GEOSCCM performed well, in comparison with TOMS phase shift trends during the observations period. Therefore, it was not merely the absence of these models in the derived MMM trends that improved qualitative agreement with TOMS observations.

Whilst dynamical influence from QSW forcing is still suggested to be reduced when compared to observations, it seems that model trends improved somewhat with the use of modelled SST and SIC trends as listed in *Eyring et al.* [2010a]. REF-B1 simulations use the HadISST1 observational dataset [*Rayner et al.*, 2006] to provide forcings, whereas the B2 models use a variety of GCM output, including the HadGEM1 climate model [*Johns et al.*, 2006], depending on the model. Interestingly, mean SSTs from the HadGEM1 over the observation period, were found to have a approximately 2K cold bias at Antarctic latitudes [*Johns et al.*, 2006]; [*Eyring et al.*, 2010a].

The effect of anthropogenic forcings alone (decreasing ODS levels and increasing GHG emissions) in the first half of the 21st century (2005-2050) show a somewhat reduced eastward phase shift in TOC distribution, with a maximum longitudinal shift of about 4° per decade. With the expected ozone recovery during the 21st century, the ozone hole extent is projected to decrease due to a shrinking polar vortex during austral spring. This is best reflected in the λ_{min} phase trends which show a longitudinally stable trend poleward of 65°S, and a reversed westward trend equatorward of this latitude, during SON months. The reversed trend is statistically significant for both TOC extremes at these sub-polar latitudes, and is reflected in the λ_{w1} trends for both seasons. During the DJF months there is an eastward trend at latitudes between 60 and 70°S. Overall, there is a reversed westward trend outside the polar vortex and a small residual eastward trend inside the polar vortex.

In the second half of the 21st century (2050-2100), there is a persisting residual eastward trend in the TOC distribution poleward of 60°S during austral spring. However, the trends are not statistically robust. Summer months show a stable or eastward trend at latitudes equatorward of this latitude. The residual trends are reflected in the wave-1 harmonic across all latitudes. The trends during this period of time are dominated by the TOC response to increasing GHG levels in the A1B scenario, as ODSs are at this time playing a more minor role according to the prescribed projection of halogen emissions. This suggests that there is a general eastward phase shift in TOC extremes due to both the GHG changes and the ozone depletion. GHG changes drive a basic long-term phase

shift, which is enhanced in SON and DJF by the ozone depletion. It is suggested that the model trends in the TOC asymmetry are caused by a general strengthening of the stratospheric zonal flow, which is interacting with the ocean-land boundary and orography of the Antarctic continent through QSW forcing and thus influencing the TOC pattern. However, this is a cautious suggestion, as the trends towards the end of the century are not robust for all latitudes. As previously stated, it was noted in *Eyring et al.* [2010a] that in comparison with observations, there is a late breakup of the Antarctic vortex. Recent satellite measurements suggest, similar to the CCMVal-2 model results, that from 2006-2010, the ozone hole is generally breaking up quite late in the season compared to the 1979-2005 mean [*Klekociuk et al.*, 2011]. Therefore, perhaps a persistent polar vortex is still likely to be present during December, thus affecting the seasonal summer trends.

The longitudinal locations of the zonal TOC extremes agree well with TOMS observations in 1979-2005 during the SON season, particularly for λ_{max}. However, MMM λ_{min} location are shifted westward, with respect to TOMS mean trends. Similarly, model results for the DJF season show a more consistent westward curl of the TOC extremes over the Antarctic continent. Hovmöller plots of the zonal mean anomalies at 65°S show a clear eastward trend in the TOC extreme positions during the ozone depletion period (austral spring) and a weaker, but still clear trend, during the summer months. During both seasons, there is a persistent residual eastward trend at the end of the century, which suggests that ozone recovery will remain asymmetric in the lower stratosphere due to QSW forcing. This asymmetric ozone recovery should, therefore, have an effect on stratospheric temperature trends over Antarctica. This is similar to the conclusions of *Gabriel et al.* [2011], that such an impact on stratospheric temperatures can lead to a variable offsetting of the impact of increasing GHG on the SH circulation. Prior studies highlighted the importance of ozone recovery on minimising, or even reversing, the effects of GHGs on the summertime atmospheric circulation projections [*Son et al.*, 2010].

Time series of median trends in TOC zonal anomalies from a 1965 baseline show only a minimal delay in the return of TOC to the 1965 baseline at seasonal longitude positions of λ_{min} and λ_{max}, in comparison with the return dates of the TOC zonal mean at 65°S.

However this does vary dramatically with latitude (not shown). TOC anomolies at 60 °S during SON months, are projected to return to baseline values 25 years after the zonal mean, where the zonal mean was projected to return by 2065. For DJF months, TOC remains slightly depleted at the end of the simulations, but the DJF zonal mean recovers to 1965 values by the middle of the century. The effect of such TOC zonal asymmetry has implications for surface UV radiation between the southern tip of South America and the Antarctic Peninsula. The influence of increasing GHGs on TOC asymmetry over Antarctic latitudes is also possible through a strengthening of the Brewer-Dobson circulation, as reported by *Butchart and Scaife* [2001], together with meridional ozone and temperature gradients. CCMVal-2 models do accurately reproduce the strength of the stratospheric circulation [*Eyring et al.*, 2010a]. Quantitatively, the models underestimate the contribution of orographic wave forcings. However, they seem to agree reasonably well qualitatively, with TOMS observations.

Due to anthropogenic forcings alone, MMM trends show a small decadal eastward phase shift in TOC zonal asymmetry during the ozone depletion period (1979-2005) which slows down within the polar vortex (poleward of 65°S), or reverses to a westward phase shift outside the vortex (equatorward of 65°S), during the ozone recovery phase (2005-2050). This phase shift seems to be dictated by ODS concentrations. There is a suggestion of a residual eastward trend from GHG cooling towards the end of the 21st century, when ODS emissions have decreased beyond a certain level. Such influence on the Antarctic TOC distribution is observed over both the austral spring and summer seasons.

The contribution of tropospheric chemistry on LS ozone within CCMs were not discussed in this study. Most CCMVal-2 models do not include tropospheric chemistry in their simulations, and as a result can have difficulties in simulating chemical processes within the extra-tropical Upper Troposphere and Lower Stratosphere (UTLS) region. For example, many CCMVAL-2 models perform poorly in UTLS vertical profiles of important chemical tracers, such as carbon monoxide (CO) and ozone (O_3 [*Eyring et al.*, 2010a]. The CCMVal-2 CCMs use height-resolved aerosol data based on satellite measurements of sulphate aerosols. These measurements are problematic, however, as it is often diffi-

cult to distinguish between sulphate aerosols and PSCs at Antarctic latitudes. Therefore, assumptions on aerosol density must be made [*Eyring et al.*, 2010a].

4 Transport and evolution of the 2009 Australian Black Saturday bushfire smoke in the lower stratosphere observed by OSIRIS on Odin

4.1 Introduction

On 7 February 2009 (known as Black Saturday), record high day and night-time temperatures, low humidity and high speed winds resulted in intense bushfires over large parts of south-eastern Victoria, Australia. 173 people died and over 4500 km^2 of bushland was burned. Most of the state of Victoria had experienced its driest start to a year on record with temperature records set in the state's north-west, where it reached 48.8°C, the highest ever recorded in the world, so far south (35.7°S) [National Climate Centre, 2009]. Even though forest fires are common in Australia's hot summer months, this fire was exceptional and is considered one of the worst natural disasters in Australian history.

As a result of this event, a significant amount of smoke aerosols was injected into the upper troposphere-lower stratosphere (UTLS) region. According to observational data presented in this work, the majority of biomass burning material reached 17-19 km altitudes within one week after the fire.

Biomass burning is common, particularly at tropical latitudes where it is either part of a natural vegetation cycle, or anthropogenic, due to agricultural needs. Such events produce

large varieties of gaseous and particulate emissions that are injected into the atmosphere and may globally affect its chemistry and radiative forcing (e.g. *Crutzen and Andreae* [1990]). There have been numerous studies on smoke chemistry from biomass burning (*Crutzen and Andreae* [1990]; *Andreae and Merlet* [2001]; *Reid et al.* [2005a]; *Reid et al.* [2005b]; *Alvarado and Prinn* [2009]), with a wide range of emission types determined by the fuel source, oxygen availability, and combustion processes. Understanding the impact of such emissions on the atmospheric radiative balance is especially important as the current surface temperature increase in many fire prone regions due to climate change [*Son et al.*, 2009] is likely to cause drier conditions in some areas and thus lead to more firestorm events. As smoke undergoes dispersion in the atmosphere, its properties can evolve quite rapidly. This introduces large uncertainties in aerosol radiative forcing calculations and the ability of smoke aerosols to act as cloud condensation nuclei. This can result in significant errors in the outputs from climate models [*Reid et al.*, 2005a]; [*Yu et al.*, 2006].

Penetration of biomass burning smoke material into the lower stratosphere became a focus of scientific study only recently [*Fromm et al.*, 2000]; [*Fromm and Servranckx*, 2003]; [*Livesey et al.*, 2004]; [*Jost et al.*, 2004]; [*Fromm et al.*, 2006]. Large volcanic eruptions were long considered the only process by which aerosols and gases are injected into the lower stratosphere region from the troposphere. The tropopause acts as a dynamic barrier to the upward transport of aerosols from the troposphere because of the steep gradient in temperature lapse rate. However, volcanic eruptions often have enough energy for particulates to penetrate this barrier. More recent studies have changed focus to explore troposphere-to-stratosphere aerosol transport caused by a combination of extreme heat-energy release and convection, known as pyro-cumulonimbus (pyroCb) eruptions [*Fromm and Servranckx*, 2003]; [*Fromm et al.*, 2005]. Very few such events have been reported, especially in the Southern Hemisphere. *Fromm et al.* [2006] analysed a pyroconvective storm that resulted from bushfires in south-eastern Australia in 2003. That storm injected smoke material into the lower stratosphere, and its plume had characteristics similar to those of a volcanic eruption [*Tupper et al.*, 2005].

In the past, major volcanic eruptions were considered the most suitable events for studying the transport and evolution of aerosols in the lower stratosphere. An example of this, is the Mount Pinatubo eruption in June 1991, which injected approximately 20 mega tonnes (Mt) of sulphur dioxide into the atmosphere, producing the largest stratospheric aerosol cloud in the 20th Century [*Bluth et al.*, 1992]. That eruption provided a clear view of the transport of aerosols in the tropical stratosphere, and was the first case that could be studied extensively by the use of satellite measurements.

The 2009 Australian BS bushfire was so strong and powerful, that the aerosol material injected into the lower stratosphere remained there for several months and was easily detectable by various remote sensing techniques. Events like this provide a valuable source of information on processes in the UTLS region that introduce significant amount of aerosols into the lower stratosphere, that were once thought to originate from volcanic eruptions only [*Fromm et al.*, 2010].

In this chapter, an analysis is presented of the evolution and transport of the Australian Black Saturday bushfire smoke plume (hereafter referred to as 'the plume') from February-June 2009. This is performed using the limb-scattered spectral solar radiances measured by the Optical Spectrograph and InfraRed Imager System (OSIRIS) instrument onboard the Odin satellite. Specifically, we investigate the temporal and spatial evolution of the plume density at peak, as well as its horizontal and vertical transport and dispersion at altitudes between 16 and 24 km. This is important for general atmospheric monitoring purposes, understanding various processes in the UTLS region, and improving atmospheric chemistry and climate models. The results from the OSIRIS analysis were published in *Siddaway and Petelina* [2011].

In comparison with many currently operating satellite instruments, OSIRIS has good geographic coverage, fine vertical and spectral resolution, and performs measurements in a spectral range suitable for aerosol studies. Of the other satellite instruments capable of detection of aerosols in the stratosphere, Cloud-Aerosol Lidar and Infrared PathFnder Satellite Observations (CALIPSO) was inoperative during the mid-February - mid-March, 2009 period, and Atmospheric Chemistry Experiment (ACE) did not have sufficient cov-

erage at the latitudes and time of interest. Ozone Monitoring Instrument (OMI) on Aura observed an enhancement in its aerosol index caused by the smoke particles, but is unable to resolve vertical structure and thus separate tropospheric and stratospheric aerosols. The SCanning Imaging Absorption SpectroMeter for Atmospheric CHartographY (SCIAMACHY) instrument on Envisat also measures the limb-scattered solar radiation, but with a lower (compared to OSIRIS) vertical resolution of approximately 3.5 km.

4.1.1 Observations of Black Saturday pyrocb plume

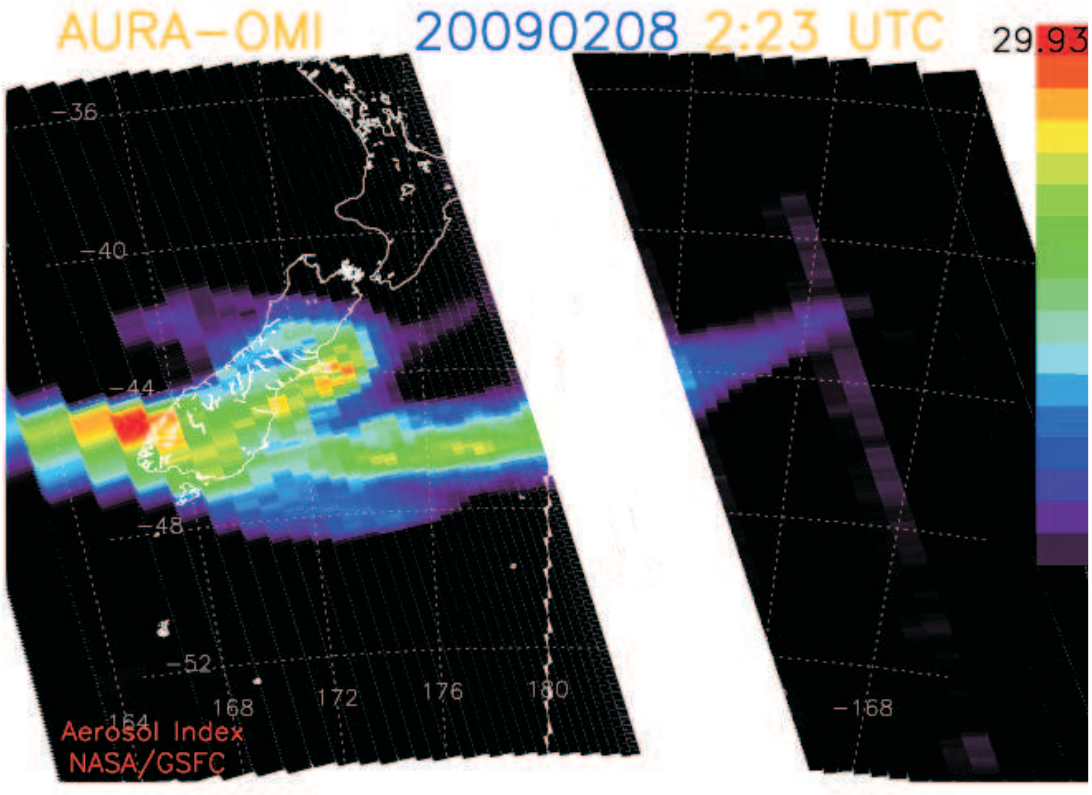

Figure 4.1: Partial map of the Black Saturday pyrocb smoke plume over New Zealand from 8 February 2009, the day after ignition of the bushfires. The white band represents corrupted OMI pixels due to a known instrument problem. Courtesy of Mike Fromm.

The pyrocb smoke plume resulting from the Black Saturday (BS) bushfires is comparable with the most intense firestorms reported in *Fromm et al.* [2010]. The analysis of the

smoke plume reported in this chapter uses OSIRIS measurements that commence some 4 days after ignition (11 February 2009), when OSIRIS first clearly observed the smoke plume. Prior to this date, other satellite instruments observed the smoke plume. For example, Figure 4.1 shows a significant enhancement of Aerosol Index (AI) taken from OMI on 8 February 2009, the day after ignition, with a maximum AI value of almost 30.

Figure 4.1 indicates that the BS smoke plume traveled eastward from southeastern Australia and within 24 hours of ignition was situated over New Zealand. This image shows a very concentrated plume of smoke aerosols that has already been vertically transported to the UTLS region, with AI being a strong function of plume altitude [*Fromm et al.*, 2005]. However, this observation does not constrain the height accurately. In order to do this, observations from the Cloud-Aerosol Lidar with Orthogonal Polarization (CALIOP) instrument onboard the Cloud-Aerosol Lidar and Infrared Pathfinder Satellite Observation (CALIPSO) satellite [*Winker et al.*, 2007] are considered. Results from CALIOP will be referred to as CALIPSO from this point onwards. The CALIPSO satellite is part of the A-train cluster of satellites [*Stephens et al.*, 2002] and is the first space-borne lidar instrument used for aerosol and cloud measurements [*Winker et al.*, 2007].

Figure 4.2 is the first clear stratospheric observation from CALIPSO of the BS smoke plume in a night-time scan, showing the plume located at an altitude of around 17 km with a total attenuated backscatter of between 1.5-4 $km^{-1}.sr^{-1}$, indicating weak cloud scattering and strong aerosol scattering [*Winker et al.*, 2007]. The vertical feature mask shows that the plume is represented as a stratospheric layer feature. The combination of such satellite observations over the following few days, found that the smoke plume was horizontally transported equatorward, and then remained quite stationary for a few days (Mike Fromm, private communication). The main plume then underwent dispersion as observed by OSIRIS.

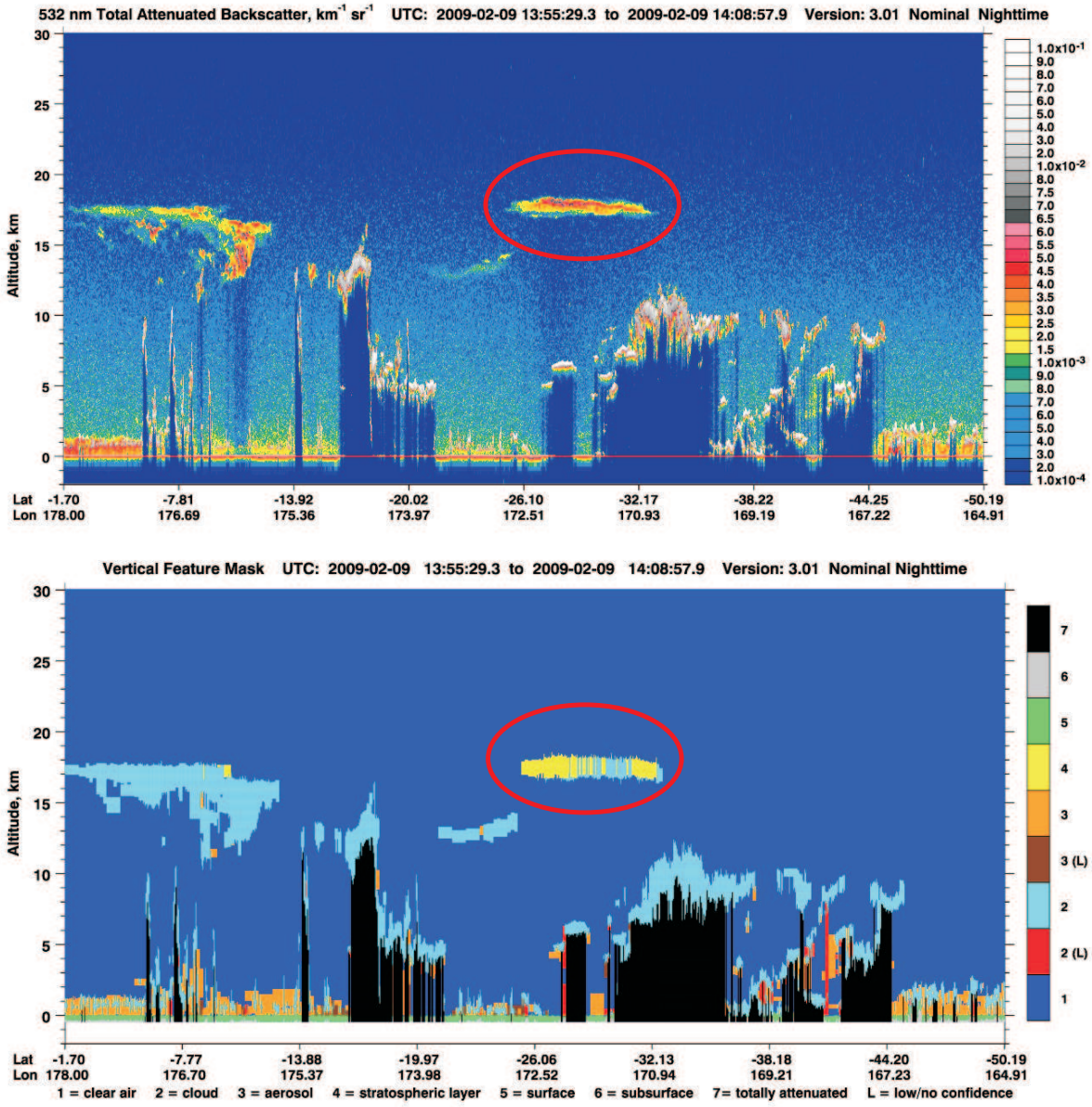

Figure 4.2: CALIPSO altitude-time images from 10 February 2009 at $\sim$ 02:00 local time of a) 532nm Total Attenuated Backscatter (1/km.sr) and b) Vertical Feature Mask. The smoke plume is circled in red.

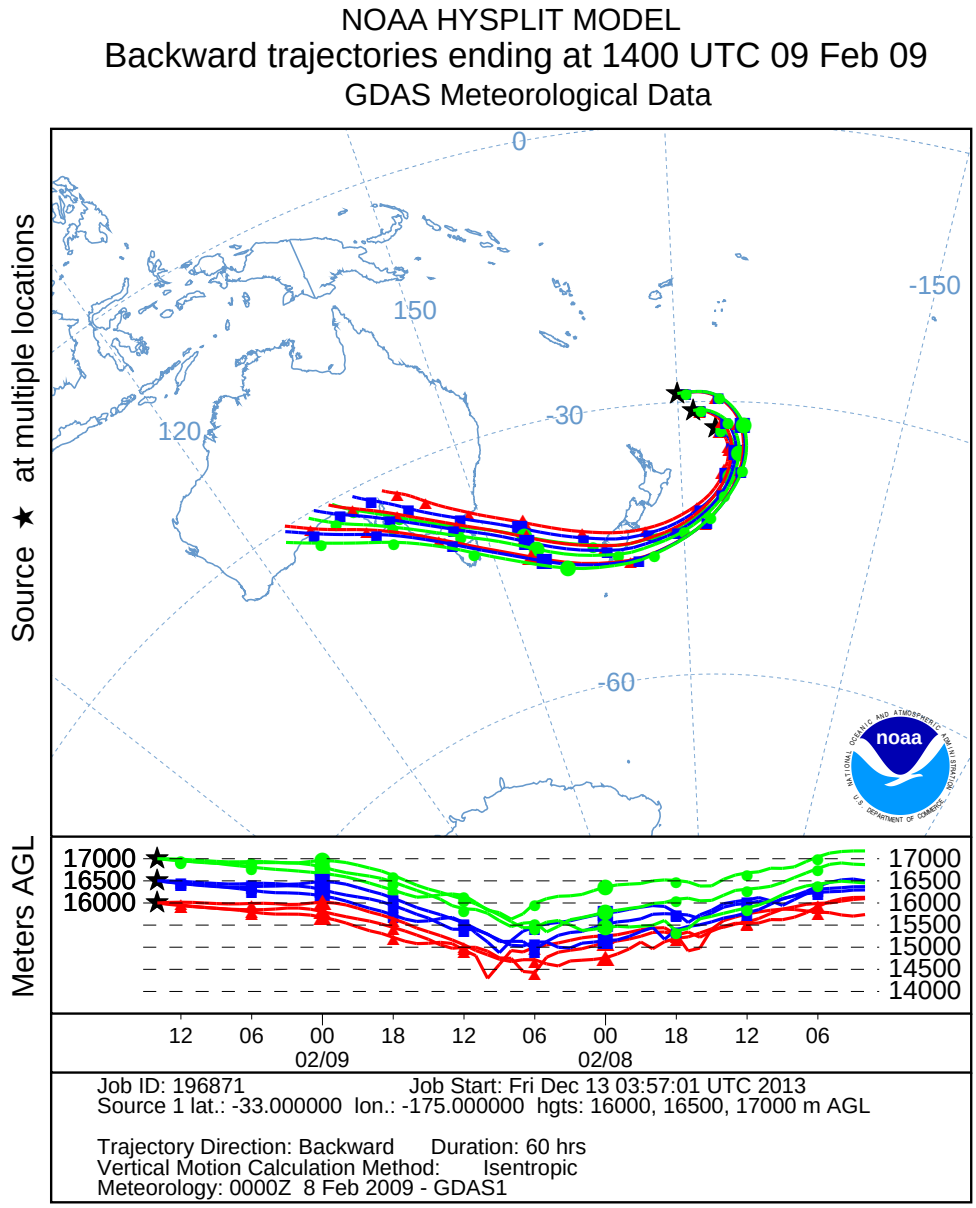

Figure 4.3: 60 hour backward trajectory analysis obtained from the HYSPLIT Model originating from 9 February 2009 at 1400 UTC. Trajectory paths are isotherms colour-coded by altitude of origin.

Using OMI AI to horizontally locate the plume and CALIPSO to provide a vertical range constraint, a backward trajectory analysis was done using the Hybrid Single Particle Lagrangian Integrated Trajectory Model (HYSPLIT) [*Draxler and Hess*, 1998]. This is shown in Figure 4.3. HYSPLIT trajectories are run interactively online (http://ready.arl.noaa.gov/HYSPLIT.php) using meteorological data from the Global

Data Assimilation System (GDAS) as input and isotherms to derive vertical motion. Each trajectory path originates from a range of altitudes centered around 17 km. The 3 spatial locations are based on OMI images (not shown), and the start time for the trajectory, on the time when the CALIPSO scan was taken (Figure 4.2). The backward trajectories support both the prior position of the smoke plume shown in Figure 4.1, and that the plume originated over south-eastern Australia.

Figure 4.4 shows the smoke plume on 16 February 2009 (8 days after ignition) now having a latitudinal extent of 22-34°S, with weaker scattering occurring (compared with Figure 4.2) as indicated by the yellow-green colour of the plume in the CALIPSO plot. The plume is observed to have reached an altitude top of approximately 19 km. This is one of the last clear CALIPSO observations of the smoke plume as the instrument underwent maintenance shortly after and was not operational until mid-March.

A 10-day HYSPLIT forward trajectory is shown in Figure 4.5 starting from the same location and time as the previous trajectory plot (Figure 4.3) in order to coincide with the CALIPSO profile shown in Figure 4.4. In addition, OMI AI measurements confirmed that the plume had AI values over 10 until 13 February, 2009 (Mike Fromm, private communication). The plume remained relatively stationary during this time due to anticyclonic circulation, supported in the trajectory analysis shown in Figure 4.5. Most trajectory paths show the plume eventually traveling westward at sub-equatorial latitudes as outlined later in this chapter. There also seems to be some indication of a possible smoke plume dispersion transported eastward and poleward towards the southern tip of South America. This introduces the possibility of BS smoke aerosols reaching sub-polar latitudes and interacting with the polar stratosphere. This eastward plume transport is considered in Chapter 6.

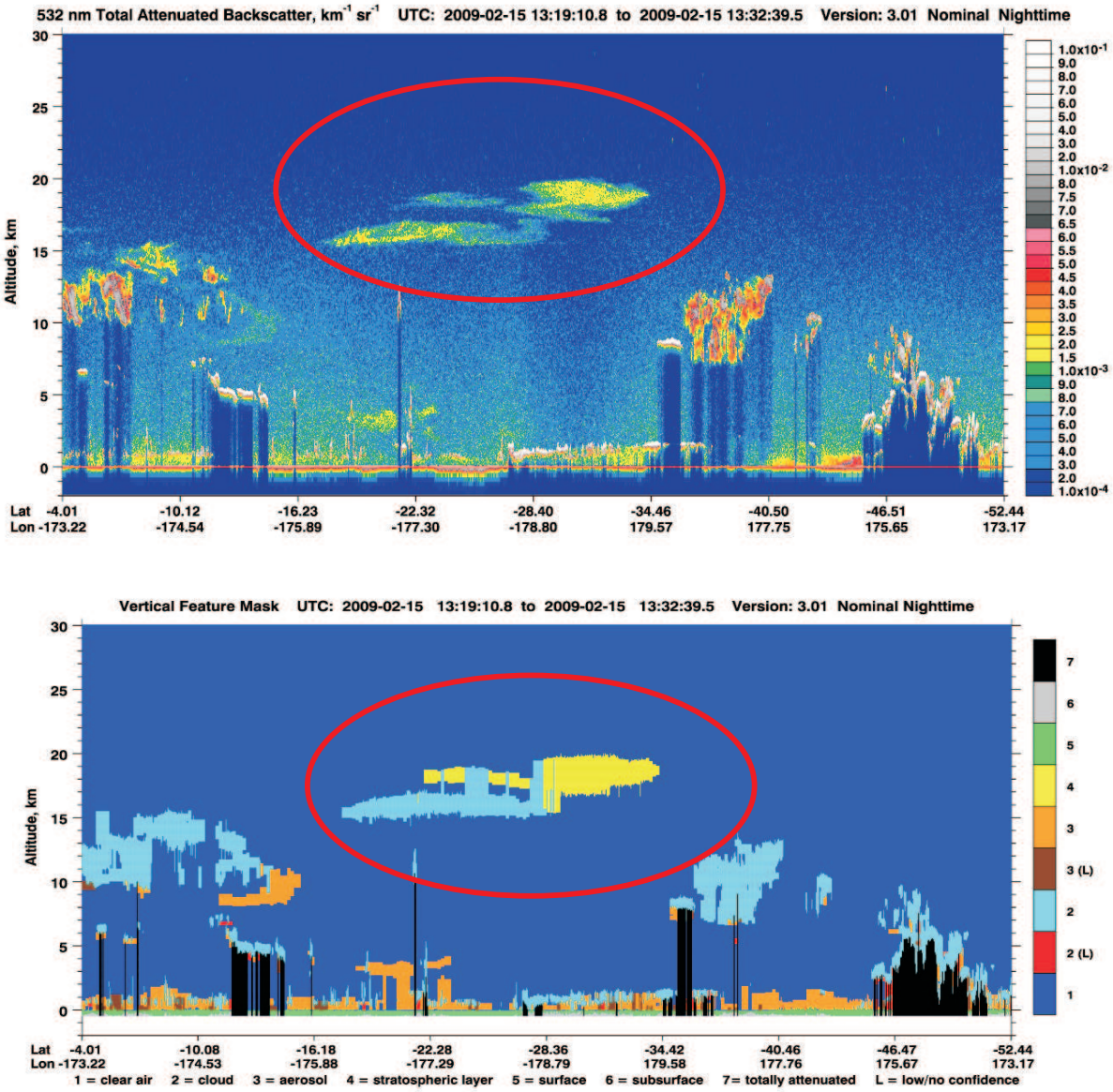

Figure 4.4: As for Figure 4.2 on 16 February 2009 at $\sim$ 01:00 local time.

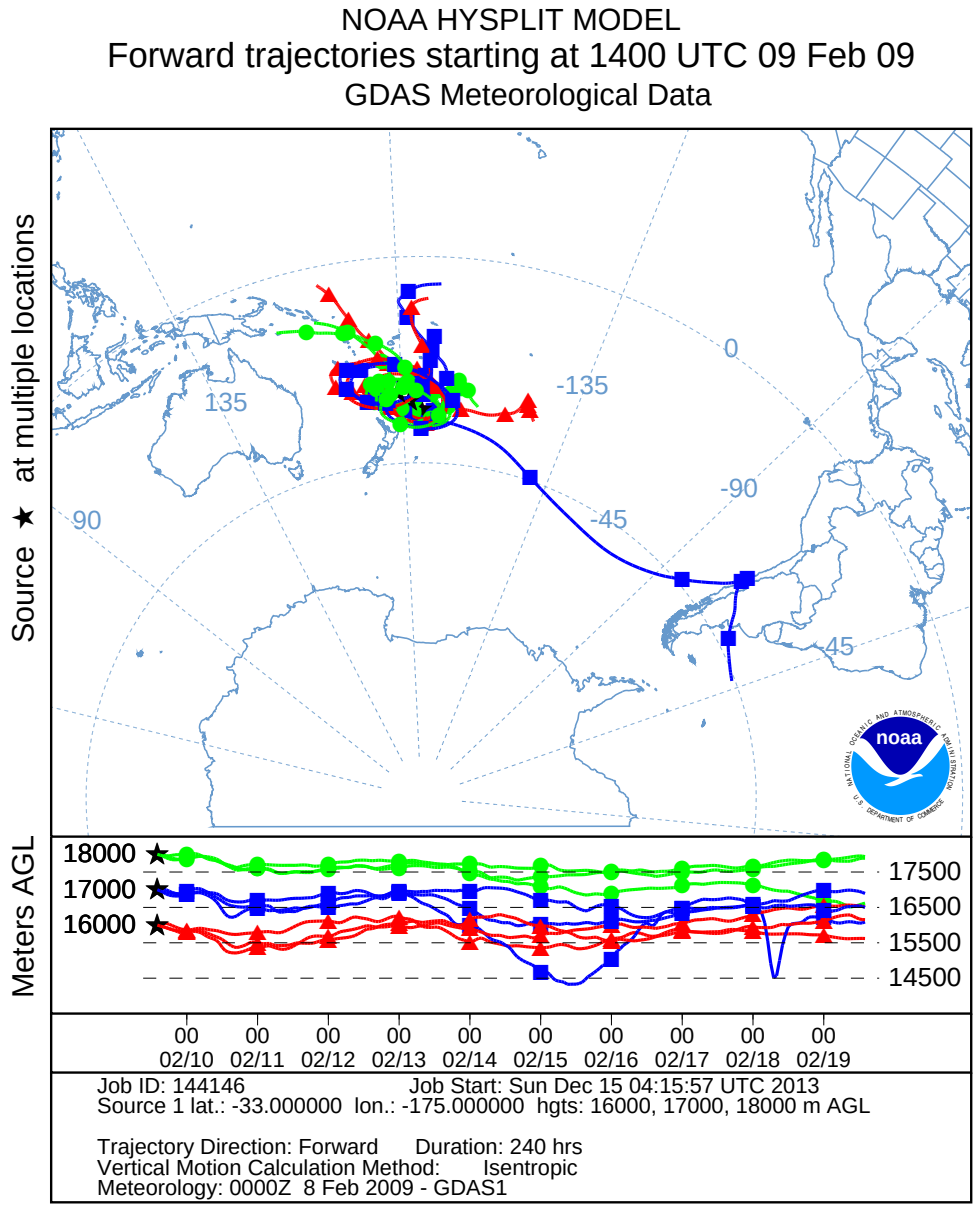

Figure 4.5: 10 day forward trajectory analysis obtained from the HYSPLIT Model originating from 9 February 2009 at 1400 UTC.

4.2 Instrument Description

Odin is an ongoing satellite mission that was launched in 2001 into a 600 km sun-synchronous, near-terminator orbit [*Murtagh et al.*, 2002]. Its latitudinal coverage in the orbit plane ranges from 82°S to 82°N, scanning the Earth's limb at a speed of 0.75

km/sec. OSIRIS, one of two instruments on Odin, measures the limb-scattered solar radiance in the wavelength range of 275-815 nm with a spectral resolution of approximately 1 nm. The instrument tangent point, always in the orbit plane for this study, crosses the equator at 18:00 local time on the ascending node. Due to its orbital geometry, OSIRIS does not observe mid to high latitudes in the winter hemisphere. This, however, does not affect the results of this study as the extra-tropical latitudes where the plume was located were sunlit during the February-June period.

The OSIRIS field-of-view covers an area 1 km high by 40 km across, along the instrument line-of-sight. OSIRIS measures scattered radiance spectra at tangent altitudes between 6 and 110 km at a vertical step of about 2 km. Further details on OSIRIS technical characteristics and performance are given by *Llewellyn et al.* [2004]. A single altitude scan is completed in 90 seconds providing nearly 60 scans per orbit. With 15 orbits per day, the Odin geographic coverage is nearly-global, making OSIRIS suitable for studying various atmospheric constituents, including stratospheric sulphate aerosols. We note that although OSIRIS stratospheric aerosol extinction profiles are produced on a regular basis, the retrieval algorithm uses microphysical parameters for volcanic sulphate particles [*Bourassa et al.*, 2007]. As the bushfire plume material has different microphysical properties compared to sulphate aerosols, it can not be accurately analysed with the current OSIRIS aerosol retrieval algorithm. In fact, the smoke presence affects the retrieval algorithm and has to be carefully accounted for in all OSIRIS Level 2 retrievals, including aerosols. Measurements contaminated by smoke are presently treated in the same way as those containing clouds: retrievals are performed only for altitudes above the cloud top (in this case above the smoke plume).

4.3 Methodology

In this section the approach to smoke plume analysis based on the characteristics of the OSIRIS data is outlined. Factors that could potentially reduce the accuracy of our results and measures we took to minimise the effects from such factors are also discussed.

4.3.1 Spectral range

Although the OSIRIS spectral range is broad, from 275 to 815 nm, the longest available wavelengths in the near infrared (NIR), around 800 nm, are more suitable for the plume detection. In this case, the contrast between molecular and aerosol scattering is higher due to the Rayleigh scattering cross-section being inversely proportional to the 4th power of wavelength (λ). For aerosol particles, the scattering cross-section is proportional to $\lambda^{-\alpha}$, where α is the Ångstrom exponent, which is always <4 [*Schuster et al.*, 2006]. Therefore, using NIR wavelengths takes advantage of the largest difference between molecular and aerosol contribution to the limb-scattered signal.

This effect is demonstrated in Figure 4.6, which shows an example of OSIRIS limb scattered spectral radiances between 10 and 30 km for a clean (Panel a) and a smoke-containing (Panel b) scan. The gap at 470-530 nm corresponds to the order sorter region in the OSIRIS CCD detector. Prominent spectral features present in both panels of Figure 4.6 are: Hartley-Huggins ozone absorption bands in the ultraviolet region, the Chappuis ozone absorption band centred at about 603 nm, and the Oxygen A-band and B-band centred at around 763 nm and 688 nm, respectively. The coloured curves in both panels indicate altitudes within the 15, 17 and 19 km vertical slices (2 km vertical steps), where the smoke plume was detected in scan 43591026 (Panel b).

The smoke presence has a clear effect on corresponding OSIRIS radiances in Figure 4.6 where these radiances are noticeably elevated due to additional single and multiple scattering caused by smoke particles. This is more evident at longer λ. The plume-containing spectra exhibit an increase in radiance with increasing λ to the right of the Chappuis absorption band at λ>670 nm. All spectra on Panel (a), as well as all spectra at plume-free altitudes on Panel (b), show the opposite trend; a decrease in radiance with increasing λ. At around 800 nm, the highest radiance values are observed in the 19 km vertical step indicating that the largest aerosol particles, with $\alpha \sim \lambda$, are present in the smoke plume at a height of approximately 18 km.

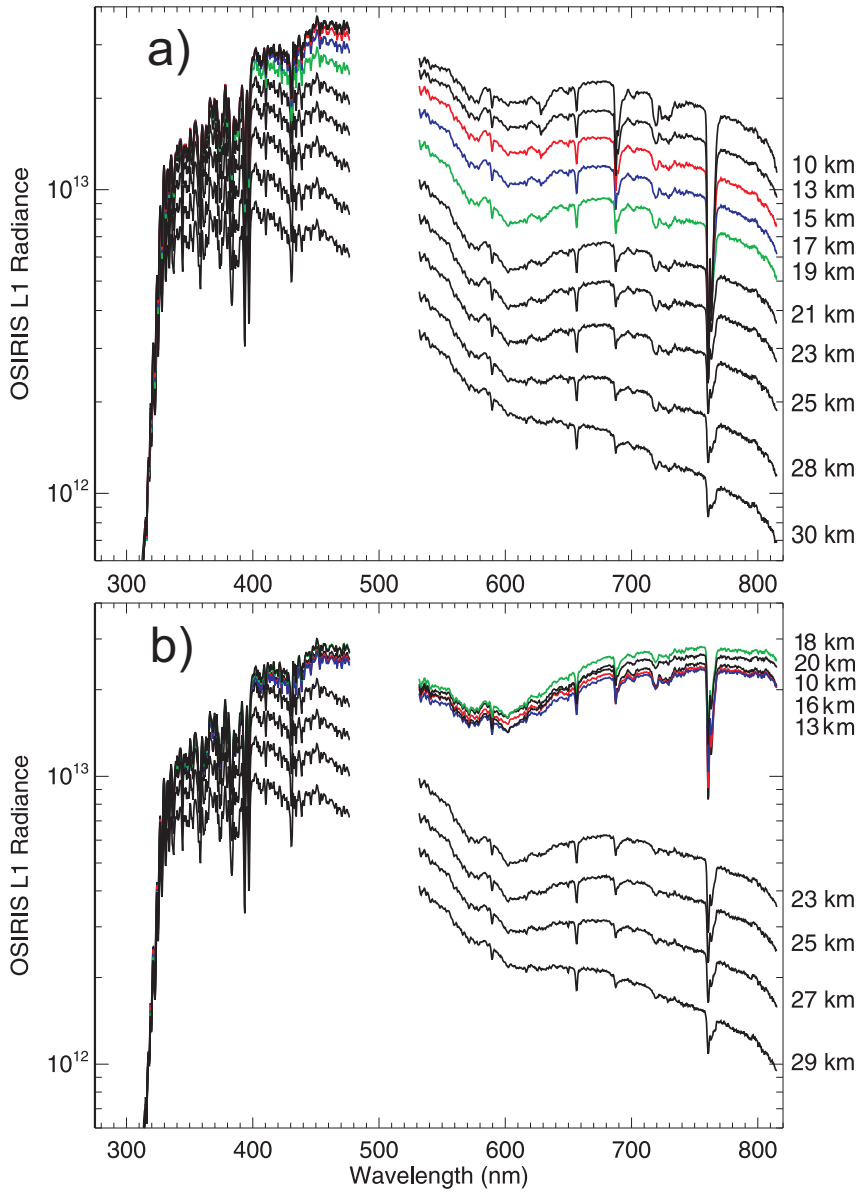

Figure 4.6: OSIRIS spectral radiances [photons/(sterad cm^2 nm sec)] in the altitude range of 10-30 km for (a) typical smoke-free scan 43311020 and (b) plume-containing scan 43591026. Note the left-hand y-axis is a logarithmic scale. The right-hand y-axis labels illustrate the rounded tangent altitudes of each individual spectrum. Red lines indicate spectrum taken in the 15 km vertical slice, blue indicates the 17 km slice, and green indicates the 19 km slice.

Energetic solar and cosmic particles, although rare at lower stratospheric altitudes, can slightly increase the signal in a particular CCD pixel. This effect can cause a temporary radiance spike in this pixel. This spike normally disappears by the time the next exposure is taken. To minimize this effect, the limb-scattered Level 1 radiances can be averaged

over several pixels before any Level 2 retrieval is performed. In this work, the averaging over several pixels in the emission- and absorption-free region from 796 to 802 nm is performed. It is also worth noting, that at UTLS altitudes, the OSIRIS signal-to-noise ratio at these wavelengths is higher than 10^4 and does not add to the uncertainty of this study.

4.3.2 Daily global radiance maps

With the instrument vertical resolution of about 2 km, OSIRIS Level 1 radiances were selected at a 2 km vertical step for tangent altitudes between 6 and 26 km. Global radiance maps were produced for each day from 7 February until mid-June, with the exception of the 28 March - 5 April period when no OSIRIS measurements were available. While each radiance map covers only a 2 km vertical layer, the smoke signature often extends vertically over 6 km. Plume positions in all vertical slices are considered, but only the altitude of maximum radiance enhancement is used for the analysis of the smoke horizontal transport in section 4.4. Examples of these global radiance maps are shown in Figure 4.8.

4.3.3 Smoke dispersion analysis

The retrieval of smoke aerosol concentrations (particle number density) requires knowledge of the smoke microphysical characteristics that are largely unknown for this bushfire, the determination of which is beyond the scope of this work. However, a related parameter - change in the limb-scattered radiance due to presence of bushfire smoke particles (and thus changes in the combined effect from particle chemical composition, number density and sizes), can be analysed. In this case, uncertainties associated with unknown particle microphysics can be avoided. However, uncertainties caused by variations in multiple scattering due to changes in smoke aerosol concentration and variable albedo are possible.

The signal observed by OSIRIS consists of a single scattering component and a multiple scattering component from molecules and aerosol particles along the instrument

line-of-sight. According to model simulations for this observation geometry, the relative contribution from single and multiple scattering to the limb signal at altitudes of 20 km (with no albedo effects) is about 80% and 20% respectively [*Griffioen and Oikarinen*, 2000]; [*Bourassa et al.*, 2007]. For an albedo equal to 1, these contributions change to about 50% for both single and multiple scattering components (D. Degenstein, private communication). Consequently, the unknown albedo may add to the uncertainties in the derived net plume radiances. At the same time, the plume is optically thick, and this reduces the albedo effects in comparison with the plume-free measurements. The total uncertainty in our analysis of the smoke dispersion is estimated at up to 20%. This is based on the results from *Griffioen and Oikarinen* [2000] and *Bourassa et al.* [2007], and takes into account that the albedo variability will be minimised when calculating the percentage difference between daily zonal mean radiances in 2008 and 2009 (this is described in detail in the next paragraph). This value is comparable to the uncertainties in the aerosol extinction retrieved from OSIRIS limb measurements at UTLS altitudes, even when the particle microphysics is well known [*Bourassa et al.*, 2007].

Daily zonal mean OSIRIS L1 radiances from 1st of February until mid-June 2009 (smoke radiances) have been compared with daily zonal mean radiances calculated for the same time period in 2008 (background radiances). The use of 2008 radiance data to represent the background radiances is justified by the fact that background aerosol concentrations in the stratosphere were very low during the several years prior to volcanic eruptions in mid-2008 [*Deshler et al.*, 2006]; [*Bourassa et al.*, 2010]. As will be shown later, addition of the first eleven days in February to the dispersion analysis confirms the agreement between the corresponding smoke-free radiances in 2008 and 2009. This also confirms the validity of representing the background 2009 radiances with the 2008 data for the corresponding time periods. The analysis was performed until June 8 due to the seasonal change in the Odin observation geometry. As the solar zenith angle (SZA) increases for measurements made further away from the equinox, the number of suitable day-time measurements (for SZA less than 87°) after June 8 became insufficient to make statistically representative calculations of daily zonal mean radiances.

When calculating daily zonal mean smoke and background radiances, the data were restricted to measurements for which all individual SZA and solar scattering angles (SSA) were within $\pm 1^\circ$ of each other. This minimised any possible bias between daily mean 2008 and 2009 limb-scattered radiances, due to variations in the observational geometry.

4.3.4 Smoke evolution analysis

To analyse the temporal evolution (gradual dissipation) of the main smoke plume material, the net plume radiance at peak was calculated. This peak plume radiance, governed by the number, size, and chemical composition of smoke particles, was derived by subtracting the background radiance from the smoke-containing radiance, all averaged over several pixels near 800 nm (as described in Section 4.3.1), at each 2 km altitude step. Background radiances, determined by a combination of Rayleigh scattering, aerosol scattering, and multiple scattering, were obtained by calculating zonal mean background radiances from all OSIRIS measurements of a clean atmosphere in 2008 for 2 week intervals, in each 10° latitude bin, and for narrow ranges of SSA that correspond to those of the observed plume. The narrow range of SSA is important, as SSA represents the angle of aerosol phase function, which depends on particle size and index of refraction, and determines the fraction of sunlight scattered in the instrument's direction.

A typical example of the smoke-containing radiance profile and smoke-free (background) radiance profile averaged over more than 30 measurements of clean atmosphere in 2008 is shown in Figure 4.7. An excellent match of the 2008 and 2009 radiances above the plume peak (above 22.5 km) supports the validity of this approach. The maximum variability range for the background radiance profiles is shown in Figure 4.7 by the dotted curves. This range, due to limited OSIRIS vertical resolution and changes in atmospheric density because of dynamics, varies from 10%, or less, at 14-16 km altitudes to up to 20% at the highest plume peak altitude of 24 km. It is noted that the plume is likely to be inhomogeneous horizontally and vertically, and that OSIRIS would not be able to resolve such detail due to limitations in vertical resolution and spatial coverage.

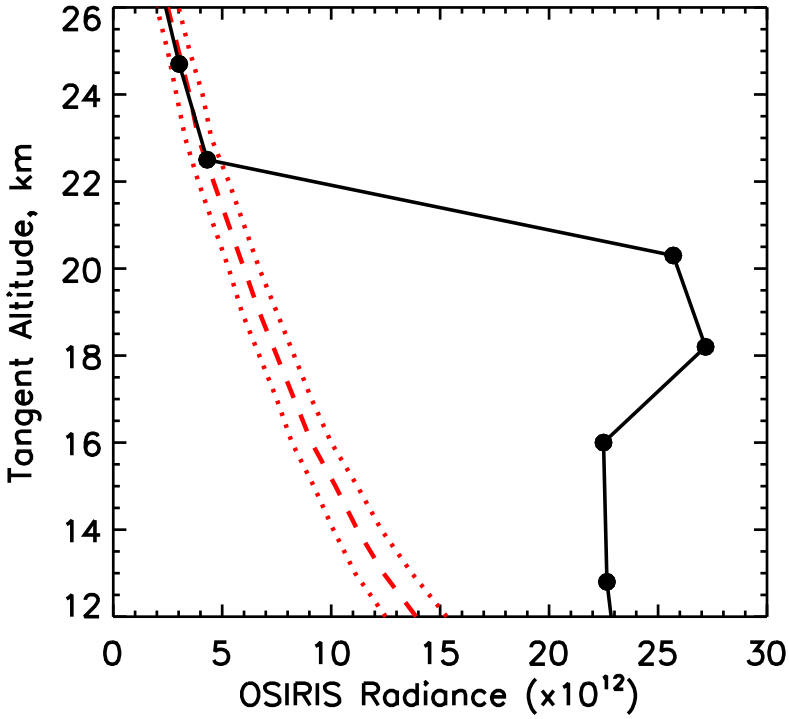

Figure 4.7: Black Saturday bushfire plume profile on 19 February 2009 for OSIRIS scan 43591026 (solid curve). OSIRIS spectral radiance are in units of photons s^{-1} cm^{-2} nm^{-1} sr^{-1}. Black circles indicate individual tangent altitudes within the scan. Mean background profile from measurements in 2008 is shown by the dashed curve, and its variability range is indicated by dotted curves.

4.4 Results and discussion

4.4.1 Smoke horizontal transport

The smoke plume, typically within the 5-25°S latitude range, was clearly seen as radiance enhancements on global daily maps. During the first week after the event, the plume was clearly identifiable between 14 and 18 km as the dominant feature in the region of interest (over the Tasman Sea). This plume location during the first week after ignition is confirmed by other satellite observations (see section 4.1.1). However, in addition to the enhancements caused by the smoke, other similar features were sometimes observed below 16 km (not shown). These features are normally caused by high altitude tropospheric clouds at tropical latitudes. Such enhancements were rarely seen above 16 km, and most

of the time the plume was the only visible feature above 18 km.

Subvisual cirrus clouds, which can be present at 17-19 km altitudes at subtropical latitudes, do not affect the results of our analysis. These clouds were extensively studied with OSIRIS in the past using the InfraRed Imager, another part of OSIRIS that operates at 1.27 and 1.53 μm [*Bourassa et al.*, 2005]. At that time, our extensive search for any signatures of subvisible cirrus clouds in the Optical Spectrograph radiances, already identified by the Infrared Imager, revealed no changes (all Optical Spectrograph wavelengths, including 800 nm).

The first clear observation of the main bushfire smoke plume above the tropopause, shown in Figure 4.8a, was made between 16 and 18 km on 11 February to the north-east of New Zealand. The main plume had moved eastward from south-east Australia and vertically advected above 14 km, four days after the fire. Its vertical extent was approximately 4 km, as it was observed in both the 15 km and 17 km altitude step. As can be seen in Figure 4.8, on this day (as well as the next few days not shown here) several other radiance enhancements were present over various locations. Whether these enhancements were caused by the presence of other biomass burning emissions or high-altitude clouds, can not be determined from OSIRIS observations alone. Generally speaking, February is a quiet time of the year in relation to Southern Hemisphere biomass burning, with the major source areas of Indonesia, Africa and South America becoming significant later in the year [*Edwards et al.*, 2006]. At the same time, isolated radiance enhancements below 18 km were sporadically seen by OSIRIS over these source areas during the period covered in this work. As noted earlier, such radiance enhancements due to other sources were not observed above 18 km, making the identification of the bushfire plume location quite clear. This is illustrated in Figure 4.8b where OSIRIS Level 1 radiances measured on 18 February 2009 in the 18-20 km vertical region are plotted.

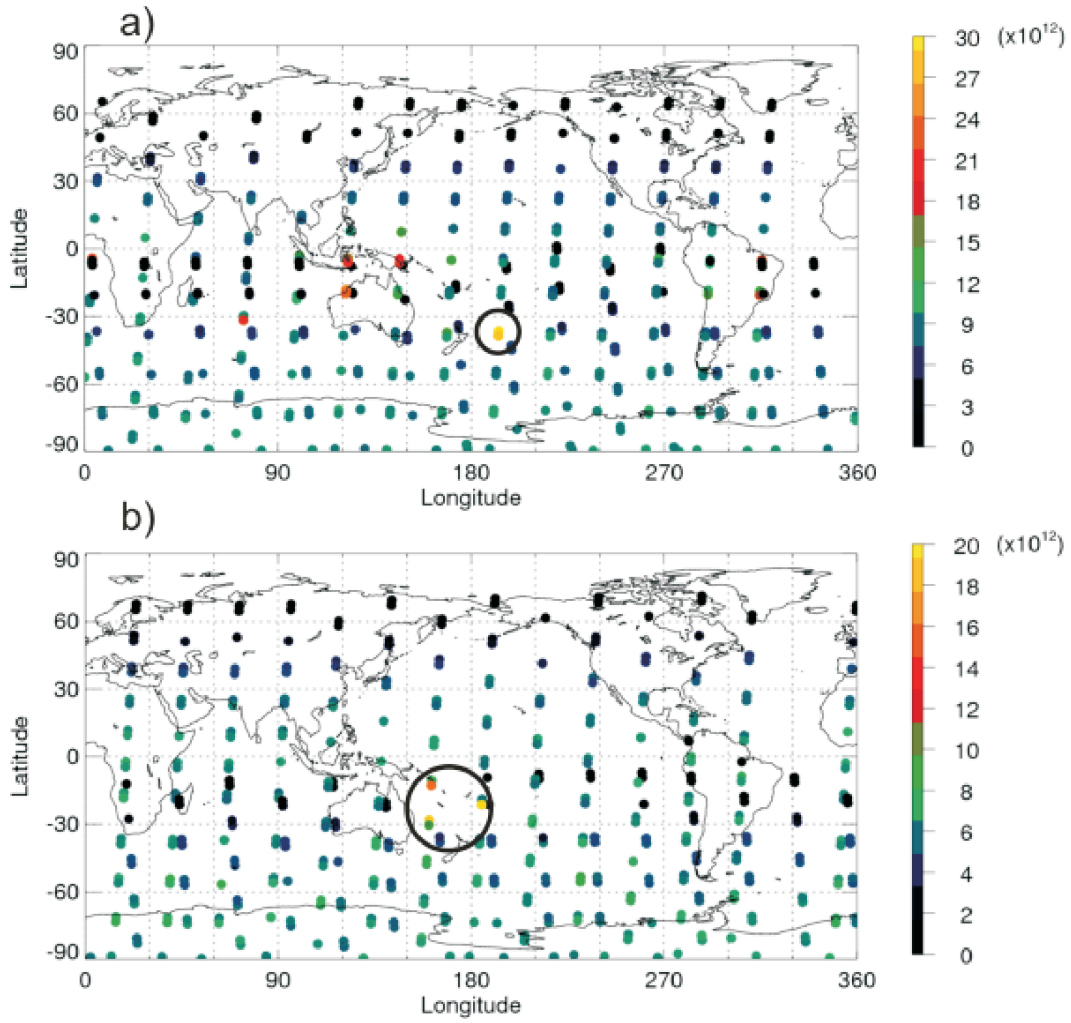

Figure 4.8: OSIRIS global radiance maps for (a) 11 February 2009 in the 17 km vertical slice and (b) 18 February 2009 in the 19 km vertical slice. Locations of the solid circles indicate ground projections of the instrument tangent point at a corresponding tangent altitude (17 and 19 km). The colour of the solid circles corresponds to radiance values with the colour scale being different for each vertical slice. Black circles highlight the observed plume locations.

Figure 4.9 shows the daily plume positions from February 11 until March 26. Green squares indicate the extended position of the plume peak when it dispersed over the Pacific Ocean on 26 March. By this time, the main plume had circled the globe, which took about 6 weeks from the time it was first detected in the UTLS region on February 11. We also note that from mid-February until June, it was mostly confined to 18-22 km altitudes. Figure 4.9 shows considerable 'jumps' in the day-to day locations of the

smoke plume. These jumps result from plume dispersion in combination with the limited measurement spatial resolution.

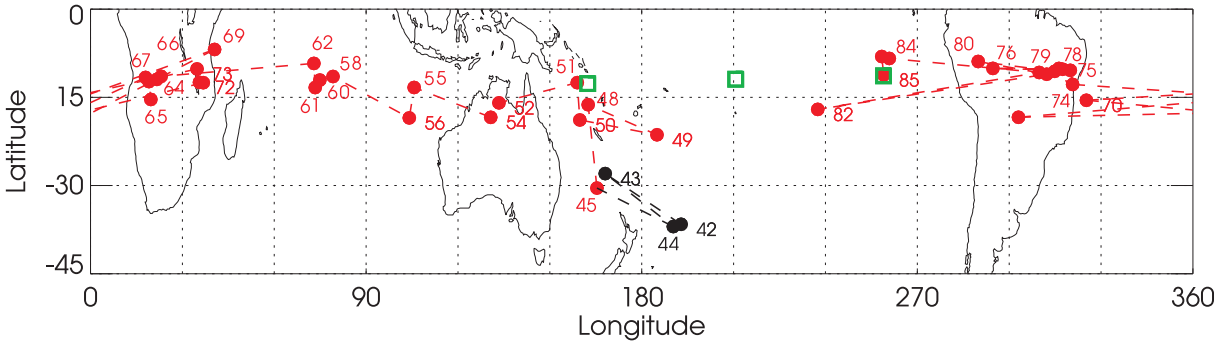

Figure 4.9: Plume locations from 11 February to 26 March 2009 at 15 km (black circles), 19 km (red circles), and 21 km (green squares). Measurements at 21 km (green squares) correspond to 26 March. The number against each point is the date in the form of 'day of year'(DOY).

As reported by *Bluth et al.* [1992], Pinatubo aerosols encircled the Earth within about 22 days after the event. Above 20 km, that aerosol cloud was mostly confined within the extra-tropical channel. *Lambert et al.* [1993] found that most Pinatubo aerosols remained in the tropical stratosphere for at least 6 months, with the largest particle concentrations above the equator. Such confinement of aerosols in this region, acting as a tropical reservoir, has been previously suggested by *Hitchman et al.* [1994] and *Grant et al.* [1996]. Similar to Pinatubo volcanic aerosols, the 2009 Australian plume remained within the extra-tropical channel, confined to latitudes of 5-25°S.

OSIRIS observed a predominant westward direction in the smoke plume transport, while the Pinatubo aerosols and the 2006 Australian bushfire smoke were transported eastward (*McCormick and Veiga* [1992]; *Dirksen et al.* [2009]). It is known that the lower stratospheric vertical and horizontal winds are greatly influenced by the QBO phase. The steeper sub-tropical aerosol gradients are expected in the easterly phase of the QBO, as was the case after the Mount Pinatubo eruption [*Choi*, 1998]. According to NOAA CDS reanalysis data, the 50 hPa (approximately 20 km altitude) zonal wind indices, in February-April 2009, ranged between 9.7 and 7.1. In May 2009, the 50 hPa index was 11.3. These values indicate that the QBO was in a westerly phase in February-May 2009.

The 2009 zonal wind indices are opposite in sign to those observed up to 14 months after the Mount Pinatubo eruption, where the QBO was in an easterly phase [*Thomas et al.*, 2009]. The wind index values given are original NOAA reanalysis wind indices, compared to the standardised indices shown in Figure 1.2.

Our analysis of zonal mean wind data from the European Centre for Medium-range Weather Forecasts (ECMWF) reanalysis (ERA-Interim) dataset for the February-March 2009 period showed a predominant westward wind direction at plume latitudes of 5-25°S at 30 and 50 hPa pressure levels with a mean velocity of approximately 10 ms^{-1} as shown in Figure 4.10.

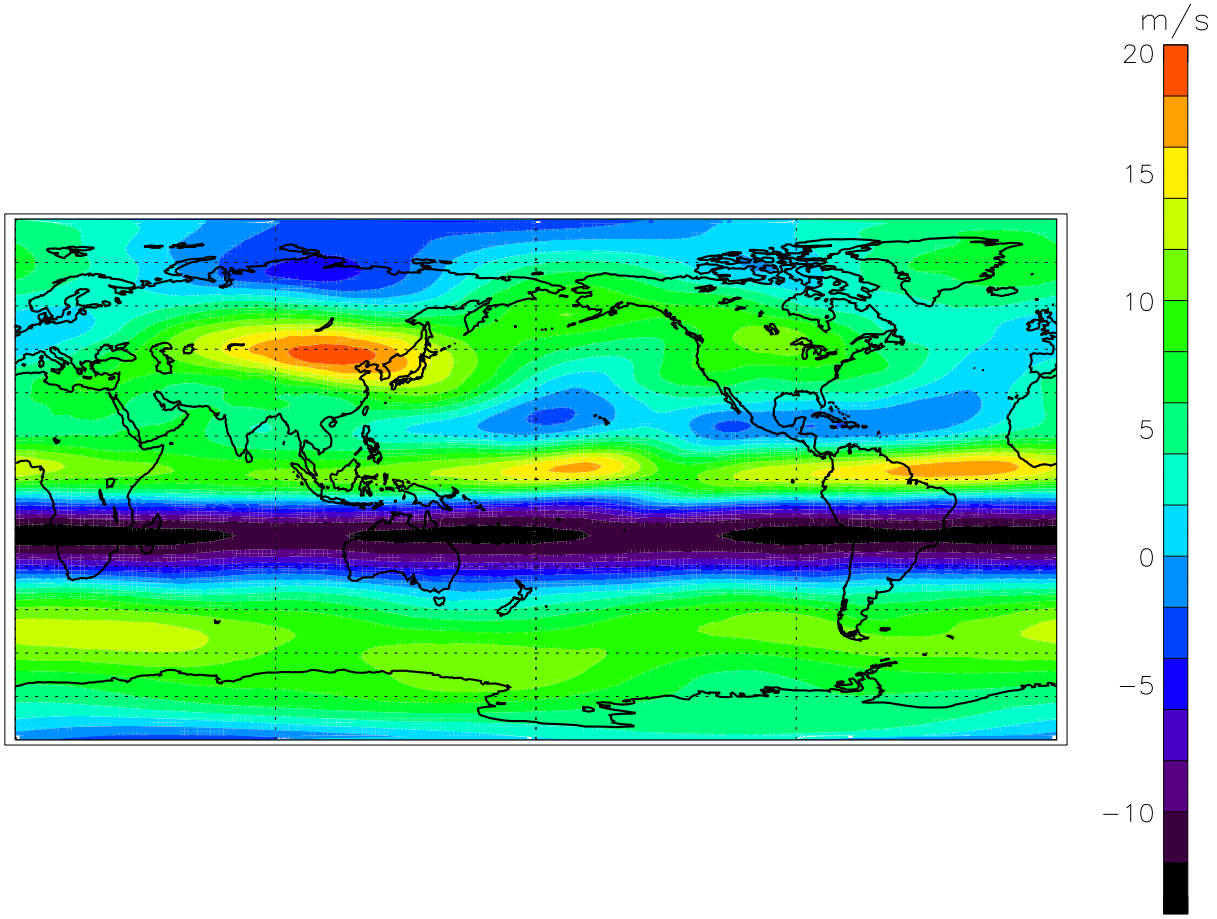

Figure 4.10: Global 50 hPa zonal mean zonal wind velocity from ECMWF reanalysis data averaged over February-March 2009. Note that wind velocity is positive in the eastward direction.

4.4.2 Smoke dispersion

The percentage difference in OSIRIS daily zonal mean smoke (2009) and background (2008) radiances at latitudes of 5-25°S is shown in Figure 4.11 for altitudes 18-20 km (upper panel) and 20-22 km (lower panel). OSIRIS did not perform continuous observations from March 29 to April 5 2009, which corresponds to days of year (DOY) 88-95, and on April 8-14 2008 (DOY 98-104). A 15-day boxcar filter, applied to these daily mean points, is shown in Figure 4.11 by the thick black line. Three distinct time periods that can be identified in Figure 4.11 are: 1) smoke-free period (DOY 32-41), 2) gradual dispersion of plume in the lower stratosphere (DOY 42-70), 3) gradual removal of smoke aerosols from the UTLS region (DOY 70-160).

For the first period in Figure 4.11, a 15-day running average yields a good (within 5%) agreement between 2009 and 2008 background radiances at 19 km, but up to an approximate 10% difference at 21 km. The actual difference for some individual points, however, may reach 20% at altitudes of 21 km. There are no significant differences in the OSIRIS observation geometry in 2008 and 2009 that might have caused this disparity. In addition, geometry-related effects would have been removed by the strict SSA and SZA coincidence criteria imposed on daily measurements used in the analysis.

Variations in atmospheric dynamics, particularly differences in local vertical winds during both years, may lead to variations in background molecular and aerosol concentrations and thus contribute to the disparity. As atmospheric density decreases exponentially with increasing altitude, such effects should be more pronounced at higher altitudes, which is precisely what OSIRIS has observed. A similar effect, possibly due to atmospheric dynamics, is also seen for days 95-110. Consequently, a -5% and -10% offset can be applied to a 0% horizontal baseline in Figure 4.11 (not plotted), in order to quantify the UTLS pollution caused by the smoke particles at 19 km and 21 km, respectively.

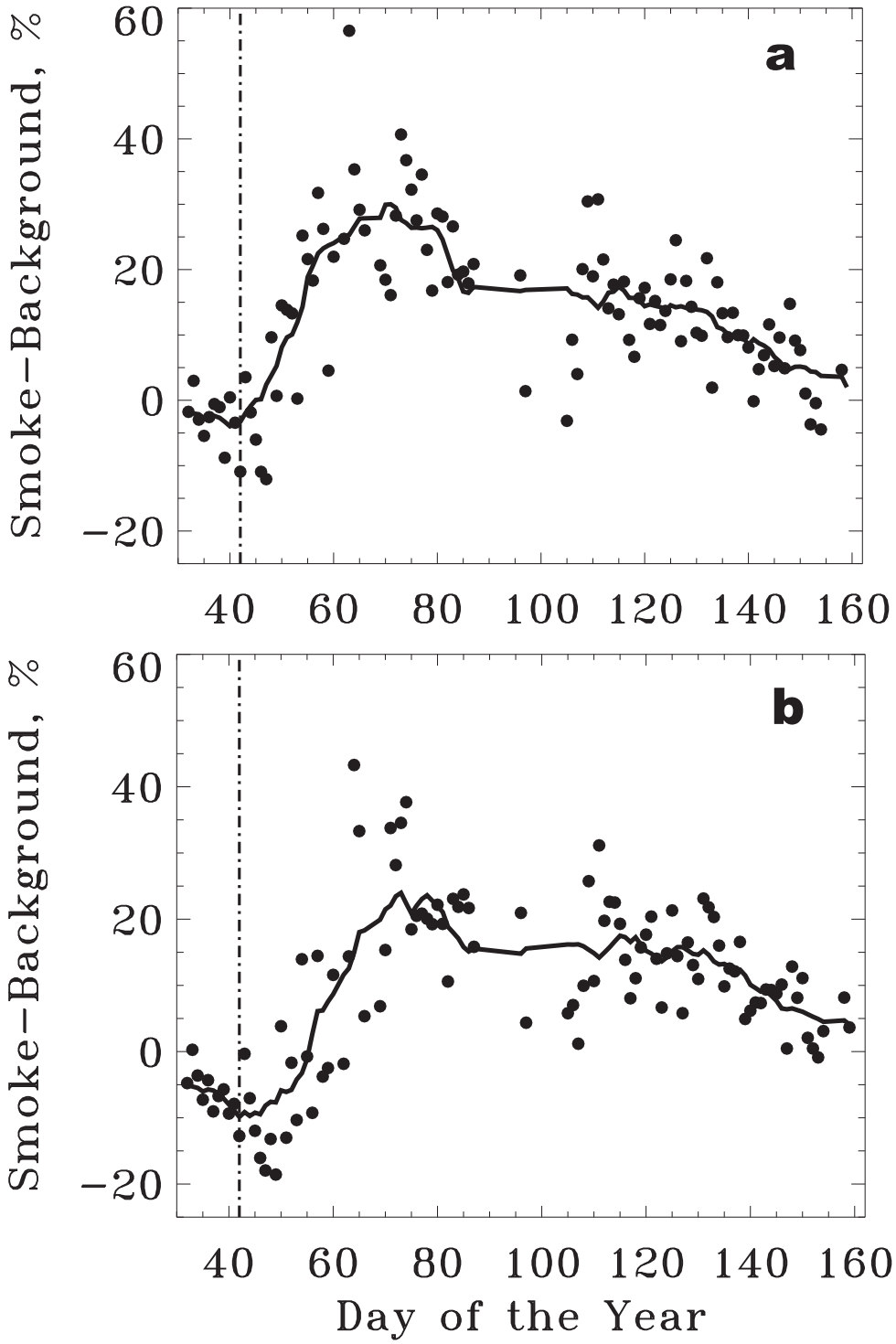

Figure 4.11: Percent difference in OSIRIS daily zonal mean smoke and background L1 radiances in 2009 and 2008 at latitudes 5°-25°S from February to 8 June for (a) 19 km vertical slice and (b) 21 km vertical slice. The thick line indicates the smoothed percentage enhancement averaged over a 14 day running mean. Dash-dotted lines indicate the day when the plume was first observed by OSIRIS in the UTLS region.

The second period in Figure 4.11, shows a maximum radiance enhancement in the 15-day running average of up to 30% at 19 km and up to 25% at 21 km. This enhancement, however, can be about 35% if the above discussed offset of -5% (-10%) at 19 km (21 km) is applied. Maximum radiance enhancement was observed near day 70 (corresponding to March 11, 2009) for both 19 and 21 km altitudes. An increase in the daily zonal mean radiances from day 42 until day 70 is attributed to limitations in the OSIRIS data sampling. On day 42, only a small part of the plume material, which was closely confined in space, was detected in one measurement out of forty that were zonally averaged at 5-25°S. By day 70, smoke aerosols became dispersed well enough to be seen in all daily OSIRIS measurements in this latitude range.

The third period in Figure 4.11 corresponds to a gradual decrease in the elevated stratospheric aerosol loading. This decrease is due to various natural horizontal and vertical transport processes that remove aerosol particles from these latitudes in the lower stratosphere. By the first week of June, the 2009 radiances were close to the 2008 background, over the 4 km altitude range from 18 to 22 km. At this time of year, the spread in the OSIRIS observational geometry parameters for different scans increases. This means that the applied restrictions on SZA and SSA variability for each day, provide fewer data points used to derive daily zonal mean radiances. This is shown in Table 1. The number of data points N, listed for several days evenly spread across the period analysed, gradually decreases from February to June. Examples of daily mean radiance values and corresponding 1σ standard deviations are also shown in Table 1. The latter parameter illustrates the variability in individual data points, which is not shown in Figure 4.11 for clarity purposes. It is noted that the gradual decrease in 2008 radiance values over time in Table 1 is related to the gradual increase in SZA as the Southern Hemisphere approaches its winter season.

	2008			*2009*		
DOY	Rad*	STD*	N	Rad*	STD*	N
45	6.73	0.46	34	6.33	0.64	47
65	5.6	0.65	23	7.23	3.07	19
85	5.16	0.44	28	6.18	1.04	21
105	5.46	0.56	13	5.29	0.61	12
125	4.71	0.36	13	5.58	0.49	6
145	4.54	0.51	3	4.78	0.54	5

Table 4.1: Daily zonal mean radiances at 19 km altitude (Rad), corresponding one sigma standard deviations (STD) and the number of data points N used for the background (2008) and smoke (2009) periods for several randomly selected days of year (DOY).

These results can be compared, to some extent, with changes in stratospheric aerosol extinction caused by the Australian-2003 Canberra bushfire smoke. The latter was measured by the Stratospheric Aerosol and Gas Experiment II (SAGE II) and analysed as zonally averaged values over a narrow 34-46°S latitude range by *Fromm et al.* [2006]. In that study, aerosol extinction decreased by approximately 50% six weeks after the smoke was first detected in the stratosphere. The 50% decrease time for the 2009 Victorian bushfire event shown in Figure 4.11 is about 40 days (from day 70 until day 110). This agrees well with the results of *Fromm et al.* [2006]. At the same time, such straightforward comparison of results could be subject to some uncertainties. Firstly, changes in the OSIRIS limb-scattered radiances represent changes in the aerosol scattering and associated variations in multiple scattering, and thus are not uniquely related to changes in aerosol extinction measured by SAGE II. Secondly, the latitude range for smoke dispersion and 'decay' analysis performed in this work differs from that used by *Fromm et al.* [2006].

Regarding the Pinatubo plume evolution in 1991, continuous aerosol injections into the stratosphere, up to an altitude of 34 km, and over a several month period, resulted in a load peak occurring about 20 weeks after the start date. A 50% decrease in lower stratospheric aerosol levels occurred some 20 weeks later [*Grant et al.*, 1996]. As Pinatubo

continued to erupt and inject aerosols into the UTLS region even after the peak aerosol load had been detected, the direct comparison of temporal evolution of its UTLS pollution with that from the Australian-2009 bushfire is not possible.

Changes in the smoke density during February - March 2009, when the plume peak is clearly seen on global daily L1 radiance maps, can be analysed using a more precise approach. This is described in the next section.

4.4.3 Smoke vertical transport and evolution

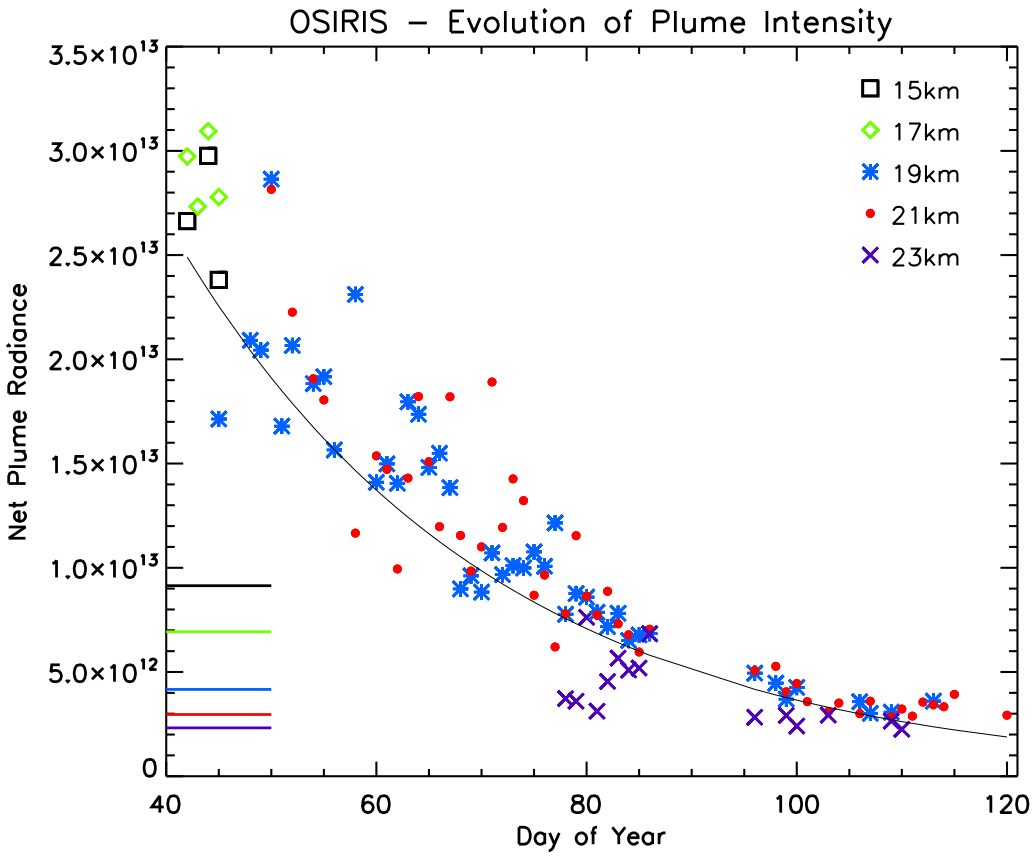

Figure 4.12: Temporal evolution of the net plume radiance at peak over the observation period of 11 February to 30 April 2009. Data points at different tangent altitudes are differentiated by symbols as indicated in the top right corner. The black curve is the best fit to the net plume radiance. 2008 zonal background radiance values for each altitude range are plotted as lines in the lower left corner.

Figure 4.12 shows the temporal evolution in the net plume radiance at its peak from day 42 until day 120. It was during this period that the peak radiance was clearly identifiable in the OSIRIS data. The plume peak altitudes, shown in this Figure by various symbols, allow one to track the smoke vertical transport. They also indicate that the bulk aerosol material remained vertically confined into a 2-6 km range. The maximum plume radiances were observed on day 44 at 15 and 17 km. The best fit curve, also shown in Figure 4.12, suggests that the net plume radiance decreased by 50% every 19 days.

According to OSIRIS, the initial vertical transport rate of the main plume in the lower stratosphere was quite high, about 1.3 km per day, being observed at 15 km on 11 February and at 19 km on 14 February. Subsequent vertical lofting of the main plume from 19 to 21 km took another 5 days. The plume remained in the 18-22 km altitude range until 19 March. After that date, part of the plume was also observed in the 22-24 km region. A nearly exponential decrease in the net plume radiance, reaching background radiance levels by mid-June, is also evident from Figure 4.12.

It is likely that the gradual reduction in radiances shown in Figure 4.12 represents the reduction in both smoke particle size (as larger particles sediment faster) and concentration (due to horizontal and vertical mixing). The smoke evolution is usually considered in terms of chemical reactions of various rates that change particle size, composition, and concentration. In this study, it was not possible to evaluate the chemical ageing of the smoke plume with either measurements, or models, as the plume chemical composition was largely unknown.

4.5 Conclusions

The temporal and spatial evolution, as well as the horizontal and vertical transport of the main smoke plume from the Australian Black Saturday bushfire in February-June 2009 was considered in this work. Odin/OSIRIS limb-scattered solar radiances in the near-IR spectral region were used to retrieve smoke altitudes and analyse its dispersion. The main smoke plume circled the globe in approximately 6 weeks after being first detected in

the lower stratosphere on February 11. Similar to the Mount Pinatubo eruption, smoke aerosols remained in the extra-tropical channel, mostly confined to latitudes of 5-25°S. To examine the lower stratosphere pollution due to the bushfire, the percentage differences in OSIRIS daily zonal mean smoke (2009) and background (2008) radiances at altitudes 18-20 km and 20-22 km were calculated. Maximum zonal pollution was observed around March 11, one month after the smoke was first detected above 18 km. Three months later, by mid-June 2009, OSIRIS radiances at these altitudes and latitudes had returned to their background levels.

OSIRIS limb-scattered radiance at plume peak, governed by number, size, and chemical composition of the smoke particles, decreased by half in about 19 days. This decrease describes the rate of horizontal and vertical dispersion of smoke material from its main peak. The overall smoke pollution of the lower stratosphere at altitudes of 18-22 km and latitudes 5-25°S was up to 35% above the background aerosol level.

The results from this study have implications for direct and indirect aerosol climate forcing, atmospheric circulation and dynamics in the UTLS region, biomass burning, and subsequent aerosol injection events and their impacts on atmospheric properties. It supports the possibility for major bushfire events, via a pyroconvective process, to pollute the austral stratosphere with smoke aerosols. This has ramifications on the radiative budget, locally and globally, and implications for weather and climate [*Fromm et al.*, 2010]. Studying such pyroconvective events also provides the scientific community with information that can be incorporated into global atmospheric climate and chemistry models.

5 Hydration of the lower stratosphere by the 2009 Australian Black Saturday bushfire smoke

5.1 Introduction

Water vapour (H_2O) is a major contributor to the greenhouse effect in the Earth's atmosphere (about 50%) followed by clouds (about 25%) and carbon dioxide (about 20%) [*Schmidt et al.*, 2010]). H_2O in the atmosphere is usually the result of evaporation from the ocean surface, and is predominately located in the lower troposphere. Vertical soundings have shown a decreasing trend in H_2O concentration with altitude, with a minimum H_2O mixing ratio of a few parts per million volume (ppmv) positioned a few km's above the tropopause [*Brasseur and Solomon*, 2005]).

The total content of H_2O in the troposphere does not vary much due to effective recycling processes. Water molecules in the stratosphere, however, are not recycled quickly, and can remain there for a very long time. If the concentration of water molecules in the stratosphere changes over time, this can cause changes in the radiative forcing of the stratosphere and affect climate. In fact, according to *Oltmans and Hofmann* [1995], the trend in stratospheric H_2O concentrations were increasing from 1980 until 1995. They examined vertical profiles of H_2O from balloon measurements, of what is known as the Boulder time series, a continuous dataset of mid-latitude H_2O measurements from the 1960's until the present. A subsequent paper to *Oltmans and Hofmann* [1995], using the

Boulder time series, reported an increasing trend of H_2O concentrations, based on a 35 year dataset (1964-1999) of approximately 1.5% per year [*Oltmans et al.*, 2000].

After 1995, this increase in stratospheric H_2O was reported to have slowed down based on satellite measurements [*Nedoluha et al.*, 2003];[*Nassar et al.*, 2005]. As the Boulder time series is based on measurements that have limited global coverage, it is thought that the observed increase in the stratospheric H_2O concentrations does not represent global trends [*Hegglin et al.*, 2014]. In October 2000, there was a sharp decrease in the amount of H_2O entering the stratosphere which coincided with low tropopause temperatures and anomalously large eddy heat fluxes in the SH [*Fueglistaler*, 2012].

The trend of H_2O in the LS broadly correlates with trends in tropopause temperature [*Fueglistaler and Haynes*, 2005];[*Fueglistaler*, 2012];[*Hegglin et al.*, 2014]. *Fueglistaler and Haynes* [2005] used Lagrangian trajectory calculations to predict the amount of H_2O entering the stratosphere (H_2O_e) and found interannual anomalies of H_2O_e are controlled by anomalies in zonal mean temperature, rather than transport changes and local temperature variations. According to *Fueglistaler* [2012], the satellite record of H_2O_e approximately recovered to pre 2001 levels by 2010. Their results implied that decoupling between trends in tropical tropopause temperatures and H_2O_e can occur on short timescales.

Nedoluha et al. [2003] suggested that an increase in water content observed prior to 1995 was due to changes in the upper stratospheric H_2O rather than because of any increase in water entering the stratosphere from below. They suggested measurements of the H_2O+2CH_4 quantity, is a better indicator of stratospheric water vapour variability, as the major photochemical source of H_2O in the stratosphere is due to methane oxidation.

Methane is a greenhouse gas (GHG), and the observed recent changes in its concentration in the troposphere and stratosphere have been linked to modern climate change [*Rigby et al.*, 2008]; [*Rinsland et al.*, 2009]. A consequence of the observed long-term increase in methane, and the associated increase in the upper stratospheric water vapour concentration, is the increase in brightness and occurrence frequency of ice layers in the summer upper mesosphere [*Thomas et al.*, 1989]; [*Shettle et al.*, 2009] and references therein.

To derive a reliable long term data record of stratospheric H_2O, satellite datasets were merged using a CCM nudged to observed meteorology [*Hegglin et al.*, 2014]. It was found that in the lower stratosphere long term trends are negative from 1988 due to tropical tropopause temperatures and that upper stratosphere long term trends are positive from 1986 due to increased methane oxidation. Increasing methane concentrations did not impact H_2O in the lower stratosphere due to strengthened circulation trends, however, weakened circulation trends were found in the upper stratosphere.

Using water vapour profiles, *Brewer* [1949] was the first to suggest that air parcels enter the stratosphere primarily at tropical latitudes, where the atmosphere is cold enough to dehydrate moist air from the troposphere. This area of transition from a humid and dynamic troposphere to a stable and dry stratosphere, is known as the Tropical Tropopause Layer (TTL) [*Holton et al.*, 1995]; [*Mote et al.*, 1995]. The slow large-scale upwelling of H_2O from the troposphere, through the TTL, is the dominant process by which water enters the stratosphere [*Holton et al.*, 1995].

Another reported process, by which H_2O is transported to the stratosphere, is via rapid dehydration of air via overshooting convection, followed by ascent through the TTL as described by *Sherwood and Dessler* [2000]. *Dessler and Sherwood* [2004] found that deep convective injections in the summer northern extratropics increased H_2O by 40% in the lowermost stratosphere. This convective moisture then travels isentropically to the tropics and ascends into the stratosphere. This observed increase in stratospheric moisture content have been linked to stratospheric cooling [*de F. Forster and Shine*, 1999] which, in turn, can affect the radiative balance and trigger heterogeneous reactions that drive ozone loss cycles [*Oltmans and Hofmann*, 1995]; [*Brasseur and Solomon*, 2005].

More recently, the contribution to stratospheric hydration through overshooting convection has been questioned, with the observed annual mean and seasonal variations in H_2O VMR sufficiently explained by the minimum saturation mixing ratio over ice along calculated trajectory paths in the UTLS [*Fueglistaler et al.*, 2005]. Using saturation mixing ratio calculations at the Lagrangian cold point on both a global and synoptic scale, they found good agreement with observed H_2O VMR values, without including mesoscale

dynamics and cloud microphysics.

In this work, injection of H_2O into the lower stratosphere (LS) by the biomass burning smoke plume that originated from the 2009 Black Saturday bushfires is analysed. To our knowledge, this mechanism for water transport above the tropopause has not been widely reported. As global warming continues, the number of devastating wildfires and resulting smoke loftings into the lower stratosphere may increase. This, in turn, could further increase the H_2O concentration in the UTLS region, further contributing to climate change.

Biomass burning events pollute the atmosphere with a large variety of gaseous and particulate emissions and thus directly affect chemistry and climate. Consequently, knowing their chemical composition and understanding their evolution is important. Young smoke plumes (less than 6 hours after ignition) located in the troposphere, have been extensively studied with laboratory measurements, in-situ measurements, and chemistry transport models [*Crutzen and Andreae*, 1990]; [*Andreae and Merlet*, 2001]; [*Reid et al.*, 2005a]; [*Reid et al.*, 2005b]; [*Alvarado and Prinn*, 2009]. The evolution and transport of aged smoke, especially near and above the tropopause, has not been as well studied. In fact, the ability of biomass smoke aerosols to propagate into the LS via pyrocb events, has been proposed only recently (see Chapter 4). PyroCB events are associated with extreme heat-energy release from large wildfires in a process similar to that following volcanic eruptions.

On a local scale, there is a certain ambiguity about the effect of H_2O released by, or contained within, biomass burning plumes that are transported above the boundary layer (approximately 5 km altitude) [*Potter*, 2005]; [*Trentmann et al.*, 2006]. Ground-based studies of biomass combustion have found that the moisture content from fresh biomass contributes significantly to the level of H_2O emissions transported with the biomass burning smoke plume [*Parmar et al.*, 2008]. There are two sources of H_2O in such plumes: 1) production by chemical reactions during combustion and 2) release of fuel moisture that is not chemically bound to the organic fuel particles. These are known as combustion moisture and fuel moisture, respectively [*Parmar et al.*, 2008]. In addition, the bushfire

smoke plume can entrain moisture as it is moves upward through the atmosphere.

5.2 Methodology

The Optical Spectrograph and Infrared Imager System (OSIRIS) on the Odin satellite [*Llewellyn et al.*, 2004] was the first instrument used in this study. OSIRIS measures limb-scattered spectral solar radiances and was found to be a suitable instrument for tracking the vertical and horizontal locations of smoke particulate matter in the stratosphere during the time period of interest. Daily locations of the smoke plume at altitudes between 14-24 km, have been identified from OSIRIS limb scans using the technique described in the previous chapter. For the plume identification, a spectral region near 800 nm is chosen to ensure the highest contrast between aerosol scattering and Rayleigh scattering (see Chapter 4).

Although unable to measure H_2O concentrations directly, OSIRIS recorded corresponding significant dips in its H_2O absorption band spectra in the visible and near-infrared regions caused by the smoke plume. By analysing these dips with respect to dips in other absorption bands, for plume and plume-free spectra, we can derive the percentage change in H_2O inside the plume with respect to a background H_2O. The details on this are given in the next section.

Similar to the approach used by *Kiedron et al.* [2003], the H_2O band depth measured by OSIRIS was compared to H_2O volume mixing ratio (VMR) data obtained from the Microwave Limb Sounder (MLS) onboard the Aura satellite. The comparison presented here, does not constitute a rigorous validation between the two instruments, but such attribution of certain features in the OSIRIS spectra to MLS H_2O concentrations (as a parameterisation) is considered worthwhile.

In order to obtain MLS H_2O enhancements within the smoke plume, forward trajectories at roughly hourly intervals from OSIRIS plume locations were obtained using an isentropic trajectory model of the Goddard Automailer (http://acdb-ext.gsfc.nasa.gov/Dataservices/automailer/) with NASA GEOS-5 data assimilation system meteorologi-

cal fields [*Rienecker et al.*, 2008]. The Goddard Automailer vertically interpolates daily GEOS-5 potential temperature on pressure levels which are converted to geometric heights via the hypsometric equation.

Using the location of all trajectory points in the 24 hours following the OSIRIS measurement, MLS measurements are searched for coincidences with each trajectory point. MLS data was selected on a spatial criteria of ± 500 km in the horizontal range and ± 1 km in geometric height and a temporal criterion of ± 1 hour, with respect to trajectory locations. Similarly, MLS geometric altitudes were calculated from pressure levels using the hypsometric relation of potential temperature pressure fields extracted from the MLS Derived Meteorological Product (DMP) data. The DMP data also verified at what height the MLS measurement locations were, with respect to the WMO definition of the thermal tropopause and the dynamical tropopause (3.5 P.V.U). It was found that MLS data in the 17 km vertical step were up to 1 km above the tropopause at equatorial latitudes.

MLS H_2O enhancements inside the smoke plume, both percent and absolute, are analysed as daily averages of all MLS measurements that satisfied the coincidence criteria described above.

5.3 Data analysis

Figure 5.1 illustrates OSIRIS spectral radiances at altitudes of 14-30 km, for a typical clean (background) scan and a typical smoke-containing scan. For clarity, only the spectral region from 530 nm to 815 nm is shown. The coloured curves on both panels indicate tangent altitudes within 2 km vertical steps centered at 15, 17, and 19 km. Approximate altitudes for all spectra are given at the right side of each panel.

The smoke layer is observed in bottom panel of Figure 5.1 as a radiance perturbation between 14-19 km when compared with the clean spectra in the top panel. Small differences in the absolute values of spectral radiances at altitudes above the smoke layer (above 21 km), when comparing the two scans, are due to differences in surface albedo, tropospheric clouds, and slight differences in the observation geometry (solar zenith and

scattering angles) between these scans. These two scans were taken at approximately the same latitude of 21°S (but different longitudes) which reduces any latitudinal effect in the observation geometry.

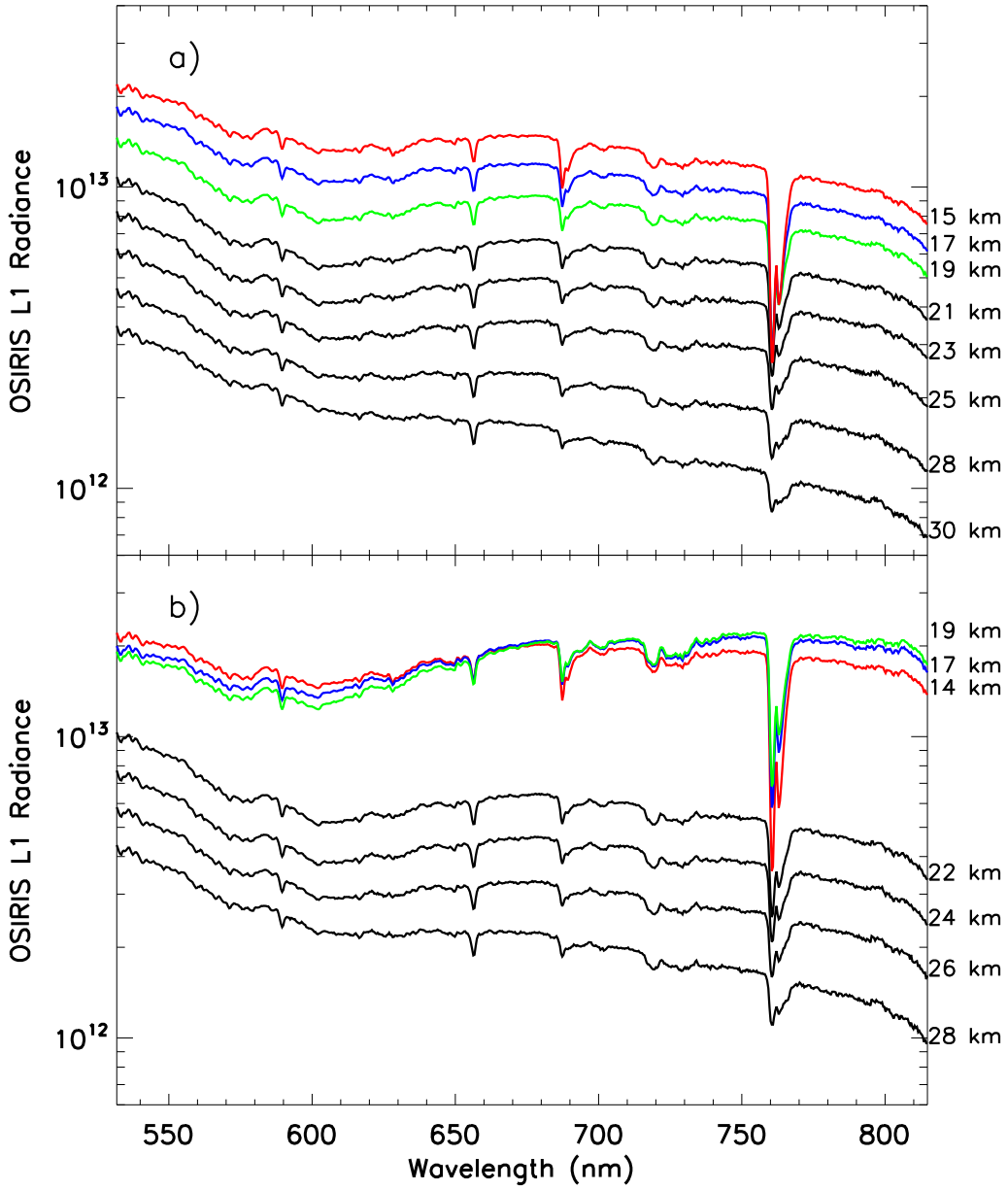

Figure 5.1: OSIRIS spectral radiances [photons/(sterad cm^2 nm sec)] constrained over wavelengths of 530-805 nm; OSIRIS spectral radiances at several altitudes between 14 and 30 km for typical background conditions observed on February 1, 2009, scan 43310020 (top panel) and a smoke-containing scan 43575021 taken on February 18, 2009 (bottom panel). Note the left-hand y-axis is a logarithmic scale.

A significant effect of the smoke presence at altitudes of 14, 17 and 19 km on the OSIRIS limb-scattered radiance spectra in Figure 5.1 (panel b) is apparent. The three spectra are visibly elevated due to additional single and multiple scattering caused by the smoke particles. This scan shows that the largest smoke aerosol particles in the plume were located near 19 km, with the smoke plume having a vertical extent of at least 4 km.

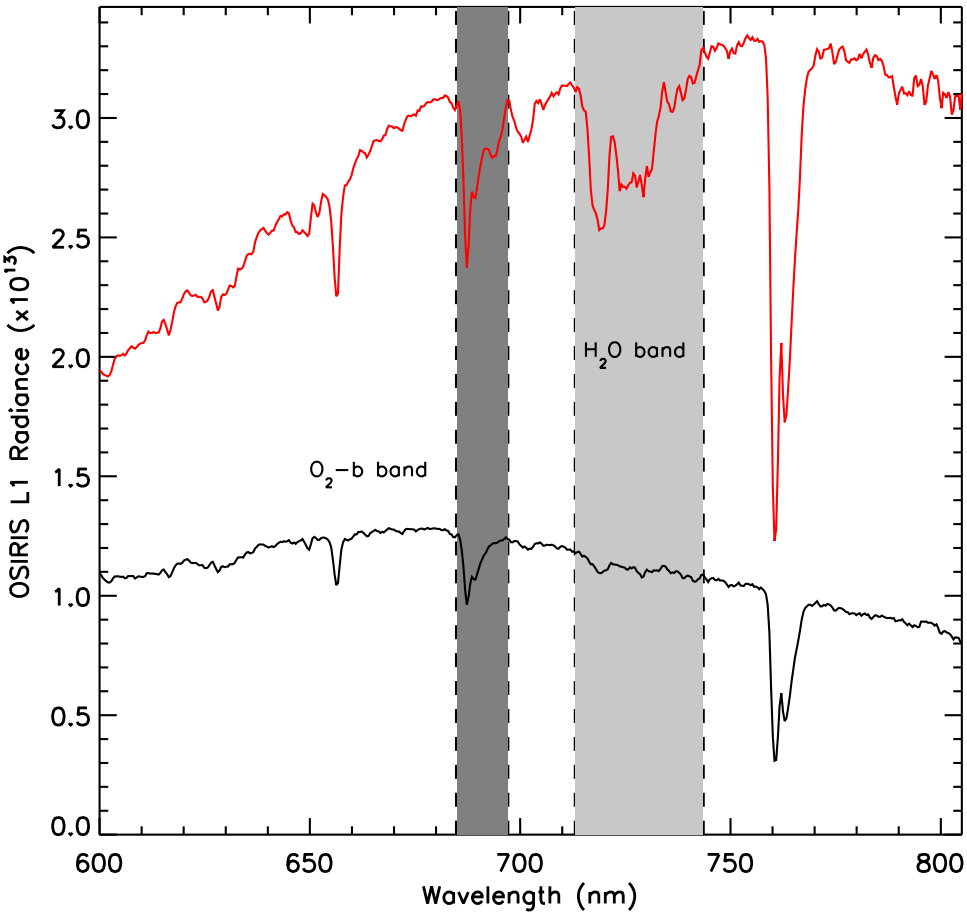

Figure 5.2: OSIRIS spectra taken outside the smoke plumes (black, scan 43470025) and within the smoke plume (red, scan 43470028). A clearly visible H2O absorption band around 725 nm is shown for the smoke plume (light grey). Also for reference is the O_2-B band around 687 nm (dark grey). Both scans were taken at an altitude near 17 km on 11 February 2009 but in seperate locations.

Figure 5.2 illustrates an enhancement in H_2O and other absorption bands measured by OSIRIS inside the smoke plume (upper curve) in comparison with the plume-free (clean) spectrum taken at a different location. Both spectra are measured at an altitude near

17 km on the same day (11 February 2009). Absorption features in the spectral range include the Fraunhofer H-α line near 656 nm, oxygen B-band centred near 687 nm, water vapour band near 725 nm, and oxygen A-band near 760 nm. Clearly, the smoke presence greatly enhances all absorption features in Figure 5.2. A rough quantitative estimation, suggests that the H_2O band depth in the smoke-containing spectrum is around 10 times larger than that in the clean spectrum. In comparison, the depth of the oxygen B-band is only approximately 3 times larger in the smoke-containing spectrum. This suggests that either additional water in the smoke plume is present, or oxygen lines are saturating prior to instrument convolution.

5.3.1 Albedo and single and multiple scattering

To describe the approach to a more accurate quantitative analysis of these features, clarification of factors that contribute to the measured limb-scattered solar radiances is necessary. The signal observed by OSIRIS consists of a single scattering component, and a multiple scattering component, from molecules and aerosol particles along the instrument line-of-sight. According to model simulations for this observation geometry, the relative contribution from single and multiple scattering to the limb signal at altitudes of 20 km (with no albedo effects) is about 80% and 20% respectively [*Griffioen and Oikarinen*, 2000]; [*Bourassa et al.*, 2007]). For an albedo of 1, that contribution changes to about 50% for both single and multiple scattering components (D. Degenstein, private communication). Consequently, the unknown contribution from albedo complicates the direct retrieval of H_2O values from the measured OSIRIS spectra. One way to deal with this is to normalize limb radiances before they are used in the retrieval of geophysical quantities. For example, *von Savigny et al.* [2003] uses the reference altitude of 50 km for normalization before OSIRIS ozone number density profiles are retrieved. The main requirement to the normalization altitude is the absence of any unwanted signal that may be present at lower altitudes due to unknown albedo, or other unknown parameters, for example, absorption features that change with altitude. A clear demonstration of the albedo effect on OSIRIS limb radiances is given in Figure 5.1, for the H_2O absorption band near 725

nm. The actual H_2O concentration at 25-30 km is so low that the simulated OSIRIS spectrum using the SASKTRAN radiative transfer model [*Bourassa et al.*, 2008] does not show any dips in the region around 725 nm (D. Degenstein, private communication). The presence of nearly the same depth in the H_2O band at each altitude for two different scans on both panels of Figure 5.1 illustrates how the water signature from lower altitudes in the troposphere propagates to higher altitudes as part of the signal caused by albedo.

Consequently, one can use the spectrum above 25 km to normalize the plume spectrum and then estimate the albedo-free H_2O band depth, inside and outside the plume. However, this approach will not work in this case, due to the unknown absorption and multiple scattering caused by smoke aerosols. As the microphysics and time evolution of aged smoke plumes in the LS is not well known, a different way of accounting for these unknown effects is required.

5.3.2 Quantifying H_2O enhancement from OSIRIS measurements

Using all the OSIRIS plume scans previously identified in Chapter 4, the limb radiance was integrated from the left shoulder (713 nm) to the right shoulder (743 nm) of the water vapour absorption band, as shown by the light-grey shaded area in Figure 5.2. A line of best fit and the radiance at each pixel beneath the line was integrated within the band as illustrated in Figure 5.3. This integrated quantity, was considered as an initial proxy for water enhancement, since the integrated intensity of the absorption band is proportional to the amount of absorbing water vapour present within the smoke plume. A contour plot of these results over a tangent altitude range of 10-26 km is shown in Figure 5.4. Note that between DOY 87-95, no OSIRIS measurements were available, and the smaller gaps in the time series were days when the smoke plume could not be clearly identified as daily peak radiances [*Siddaway and Petelina*, 2011]. This figure also illustrates how the tropospheric water signature can propagate to higher altitudes due to albedo. From DOY 42, OSIRIS clearly observed the smoke plume at altitudes between 14-16 km as radiance perturbations and a clear spike in the size of the absorption band is clearly seen in this altitude range over the first few days of the OSIRIS observation period in Figure 5.4.

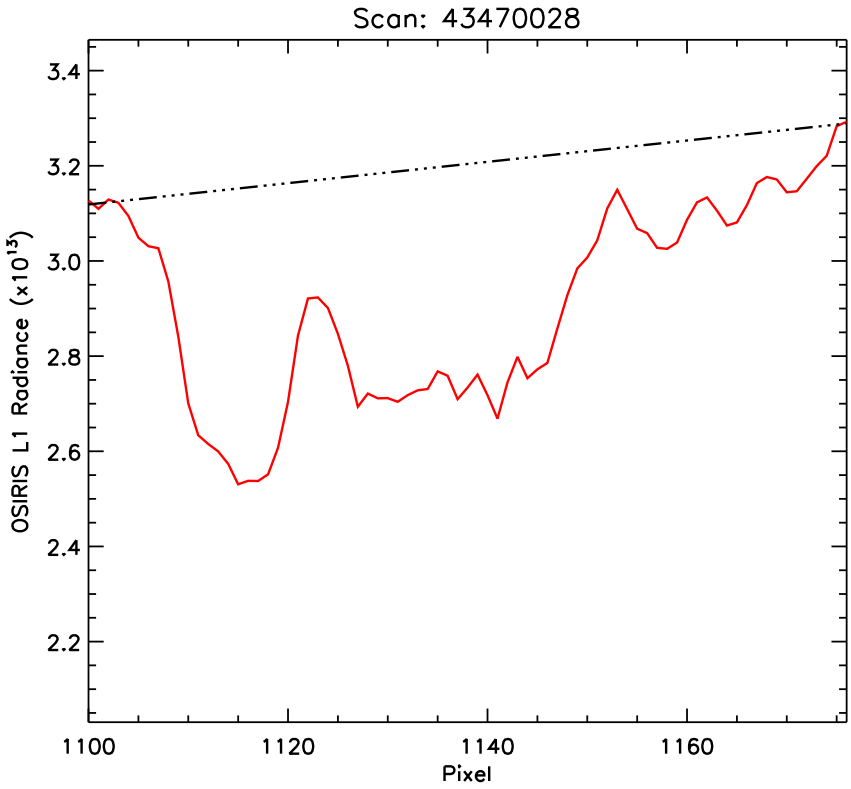

Figure 5.3: The H_2O absorption band from an OSIRIS plume-containing spectra in the 17 km altitude step (scan 43470028) as shown in Figure 5.2 (light-grey shaded area). This illustrates the integrated radiance area within the band that is underneath a linear line fitted across the left and right shoulders. The absorption band in each OSIRIS plume spectra is taken across pixels 1100 to 1176 which corresponds to 713-743 nm.

The plume was located at tangent altitudes that correspond to the lower stratosphere at mid-latitudes. After this time, the smoke plume was transported to more equatorial latitudes as it ascended to higher altitudes. As seen in Figure 5.4, there is an increase in integrated radiance intensity at progressively higher altitudes in the first few weeks. Once the smoke plume is located above 18 km, it is located above the tropical tropopause. However, this integrated radiance intensity could also be affected by the temperature of the smoke plume and microphysical interactions of the absorbing smoke material with incoming solar radiation. This would influence the width of the observed absorption measured by OSIRIS and provide an erroneous proxy H_2O enhancement. It was decided, therefore, that an alternative spectral method was to be used in this study.

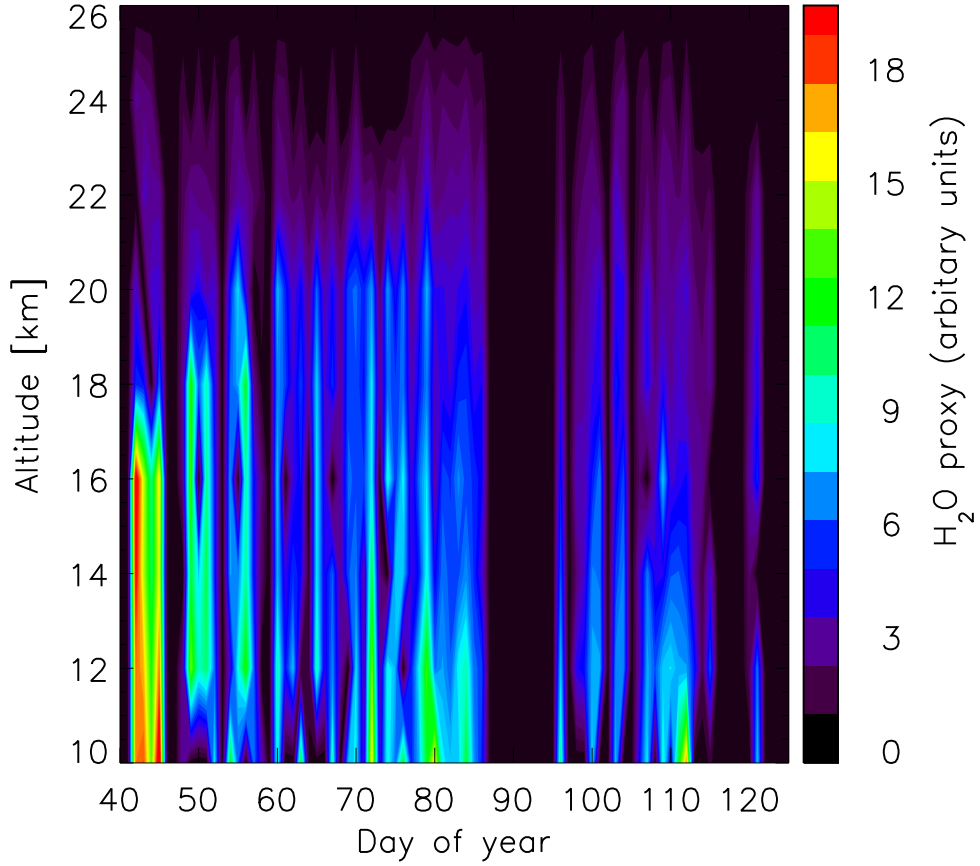

Figure 5.4: Integrated OSIRIS plume scan radiances across the H_2O absorption band centred at 725 nm. Scans from DOY 42 (11 February 2009) until DOY 120 (30 April 2009) at tangent heights of 10-26 km are shown. Missing data is shown as the same colour as the zero value in the displayed scale.

We assume that the effects from smoke absorption and multiple scattering are nearly the same for different absorption features that are close spectrally. In other words, changes in H_2O band near 725 nm should be similar to changes in O_2 B-band near 687 nm. Hence, we analysed all OSIRIS smoke spectra by calculating the ratio of the depth of the H_2O absorption band near 725 nm to the depth of the O_2 B-band, for all smoke spectra and many smoke-free (background) spectra. A plot of raw ratios for OSIRIS plume spectra, taken from DOY 42-86 is shown in Figure 5.5.

All OSIRIS scans measured on 1-6 February 2009 at latitudes of 5°-25°S were used to establish the background ratios for each 2 km altitude step. The percentage difference between plume ratios and these background ratios were interpreted as a percent

enhancement of H_2O in smoke-containing scans. In turn, this percent enhancement acts to normalise the ratios obtained from the smoke spectra from the effects of multiple scattering, and to remove any contribution from tropospheric H_2O in the signal.

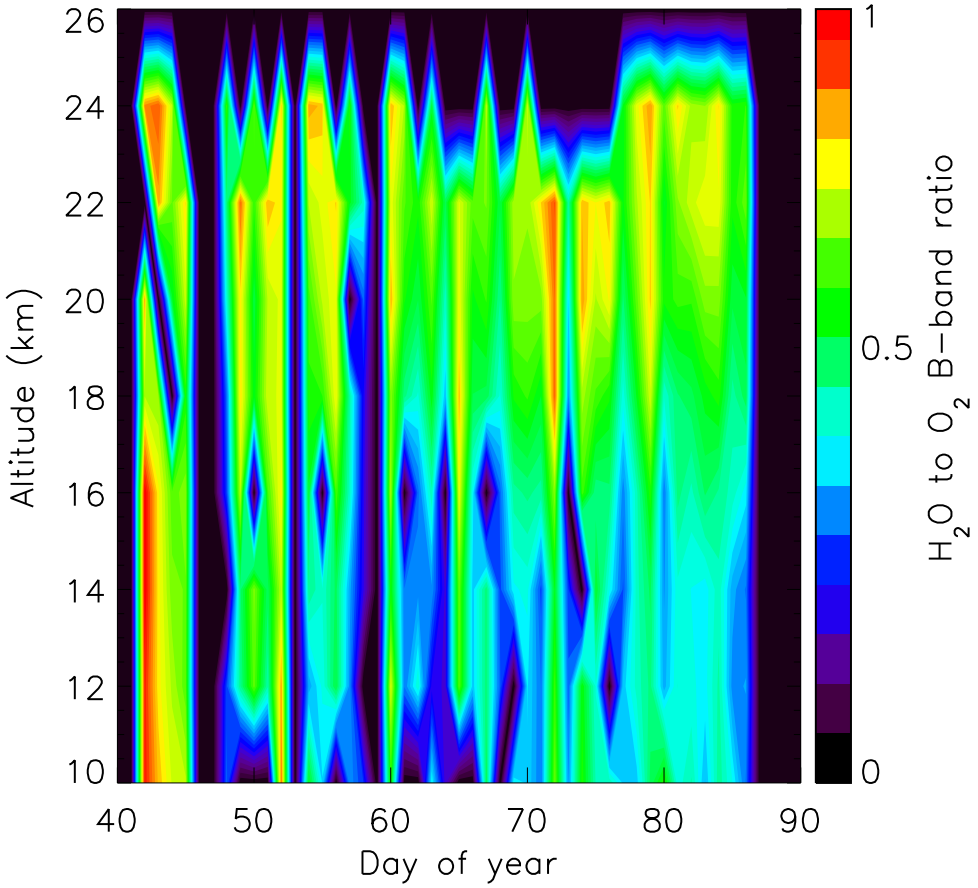

Figure 5.5: A contour plot of H_2O/O_2 B-band ratios from plume containing scans from DOY 42 (11 February 2009) until DOY 86 (26 March 2009) at tangent heights of 10-26 km are shown. Missing data is shown as the same colour as the zero value in the displayed scale.

The H_2O/O_2 B-band background ratios of all OSIRIS scans measured over the latitude range, within each 2km altitude step, during the first week of February, is shown as a time series in Figure 5.6. The mean background ratio values for the 17, 19 and 21 km steps are 0.47, 0.55 and 0.63, respectively. Each of these values have an uncertainty of approximately 0.1 at each level. Data points are clustered around local sunrise/sunset time periods due to the OSIRIS orbital geometry. The variability in spectral ratios il-

lustrates the qualitative variation in pseudo water content that is observed in the lower stratosphere. The mean background values have an approximate variability of 20% within each altitude range.

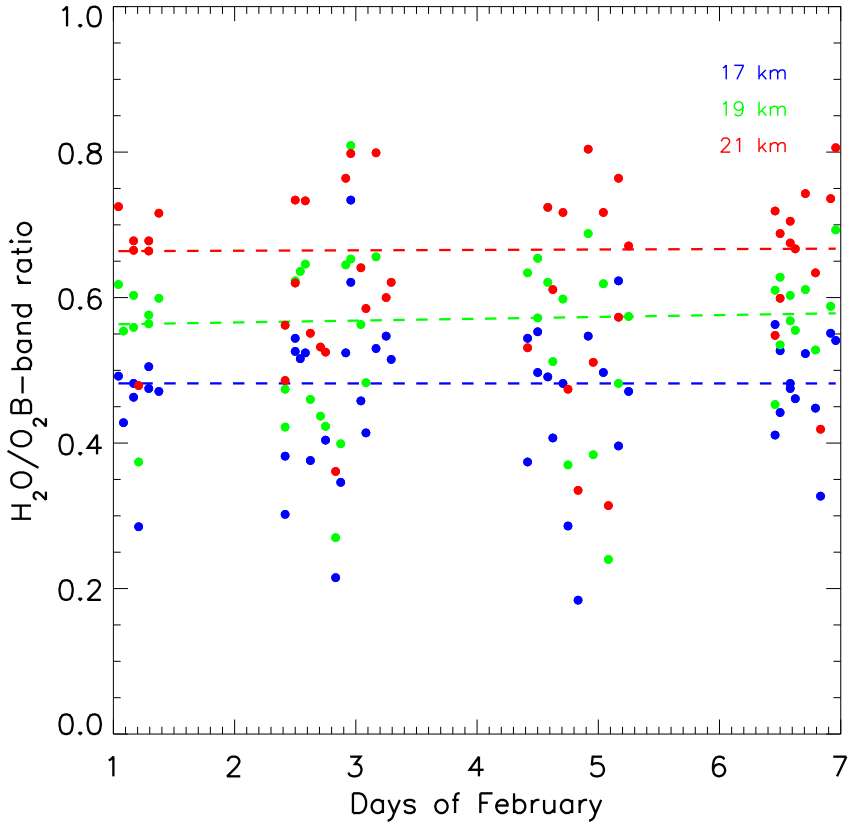

Figure 5.6: All OSIRIS H_2O/O_2 B-band values from 1-6 February 2009 between 5-25°S and 16-22 km altitude. Values are colour-coded by altitude range as shown. Dashed lines indicate the linear trend in ratios.

The analysis of enhancement in OSIRIS ratios is with respect to this early February background and is illustrated in Equation 5.1. ψ is the percentage ratio enhancement and ϕ_p and ϕ_b are the H_2O/O_2-B band ratios of the plume and mean background spectra, respectively.

$$\psi = \left[\frac{\left(\phi_p - \bar{\phi_b}\right)}{\bar{\phi_b}} \right] \times 100\%, \tag{5.1}$$

5.3.3 Quantifying H_2O enhancement from MLS measurements

In order to compare with OSIRIS enhancements, MLS H_2O background values were determined in a similar way to OSIRIS ratios. Using the average of all MLS H_2O VMR measurements within each 2km vertical step, across the 5-25°S latitude range, during the February 1-6, 2009 period. The MLS H_2O trends and variability in February 1-6 and March 1-6 for years between 2008-2010 were considered. Figure 5.7 shows MLS zonal mean values over the 3 different years from 0-60°S. Differences between the February 1-6 and the March 1-6 zonal averages, for a given year, were negligible for all years considered (not shown). The interannual variability in H_2O VMR was somewhat larger. The February 1-6, 2009 period was taken to be a good representative of the H_2O background conditions during February, 2009.

The OSIRIS background values had a percentage variability of around 20%. In comparison, MLS H_2O VMR data across the same spatial and temporal range showed a variability in water content in the plume-free atmosphere, as being around 20% within the 17 km range, but decreasing to around 5% within the 21 km range. One reason for this could be due to the larger sampling volume of measurements from MLS. Another cause could be the larger variability in OSIRIS scans due to a persisting tropospheric contribution to the spectral signal. For comparison with OSIRIS, a percentage enhancement of MLS H_2O VMR values (that had satisfied the spatial and temporal criteria outlined in Section 5.2) with respect to the background, was calculated as per Equation 5.1.

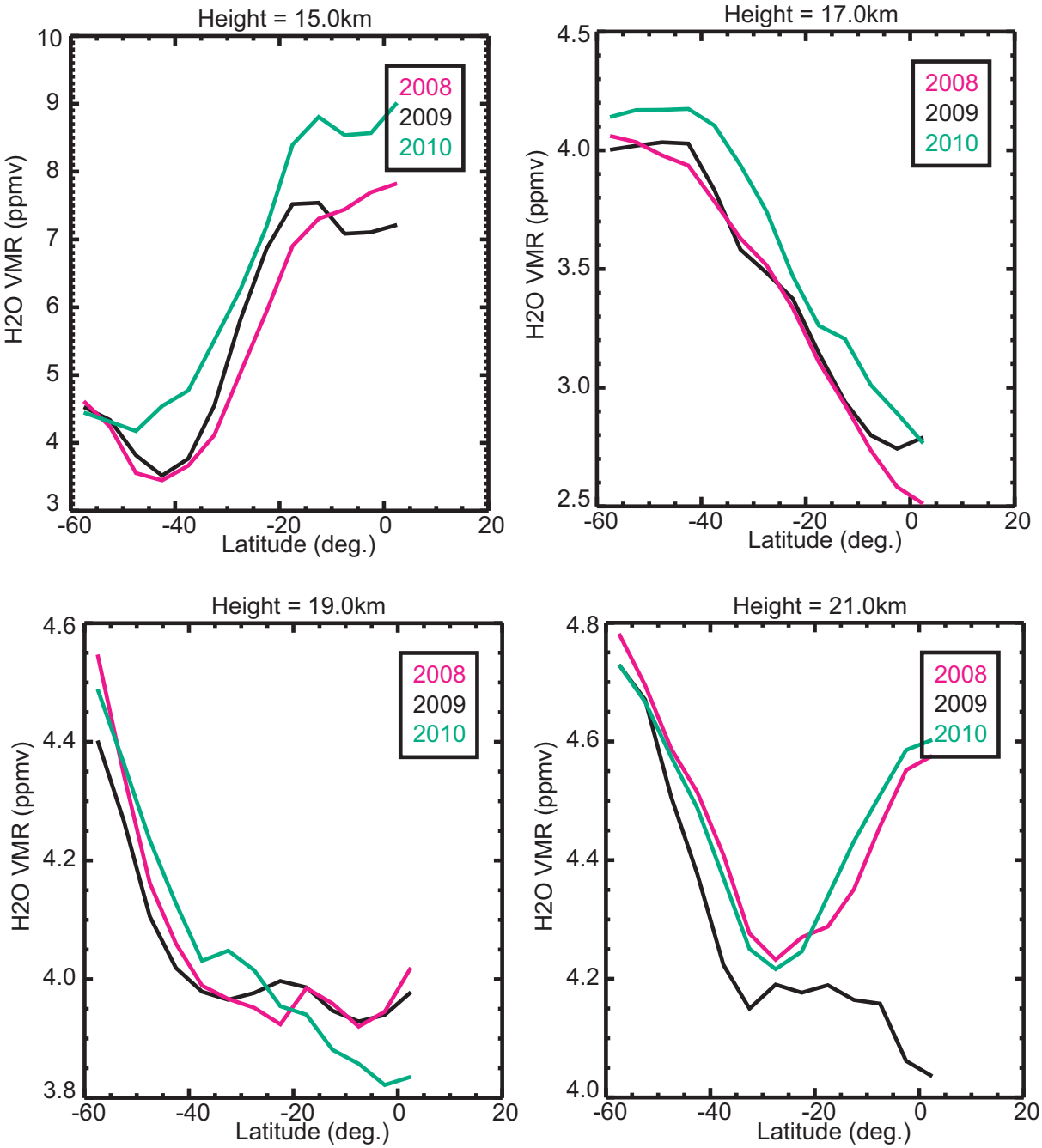

Figure 5.7: MLS zonal mean H_2O VMR within 5° latitude bins between 0-60°S from 1-6 February. Colour coded for years 2008-2010 as shown. Plot courtesy of Andrew Klekociuk, Australian Antarctic Division.

5.4 Results

5.4.1 Comparison of H_2O percentage enhancement from OSIRIS and MLS measurements

The net enhancement of H_2O/O_2 B-band ratios of OSIRIS scans containing the Black Saturday smoke plume, with respect to background ratios, are shown in Figure 5.8 for DOY 42-86. Net ratios are shown for altitude steps centered at 17-23 km.

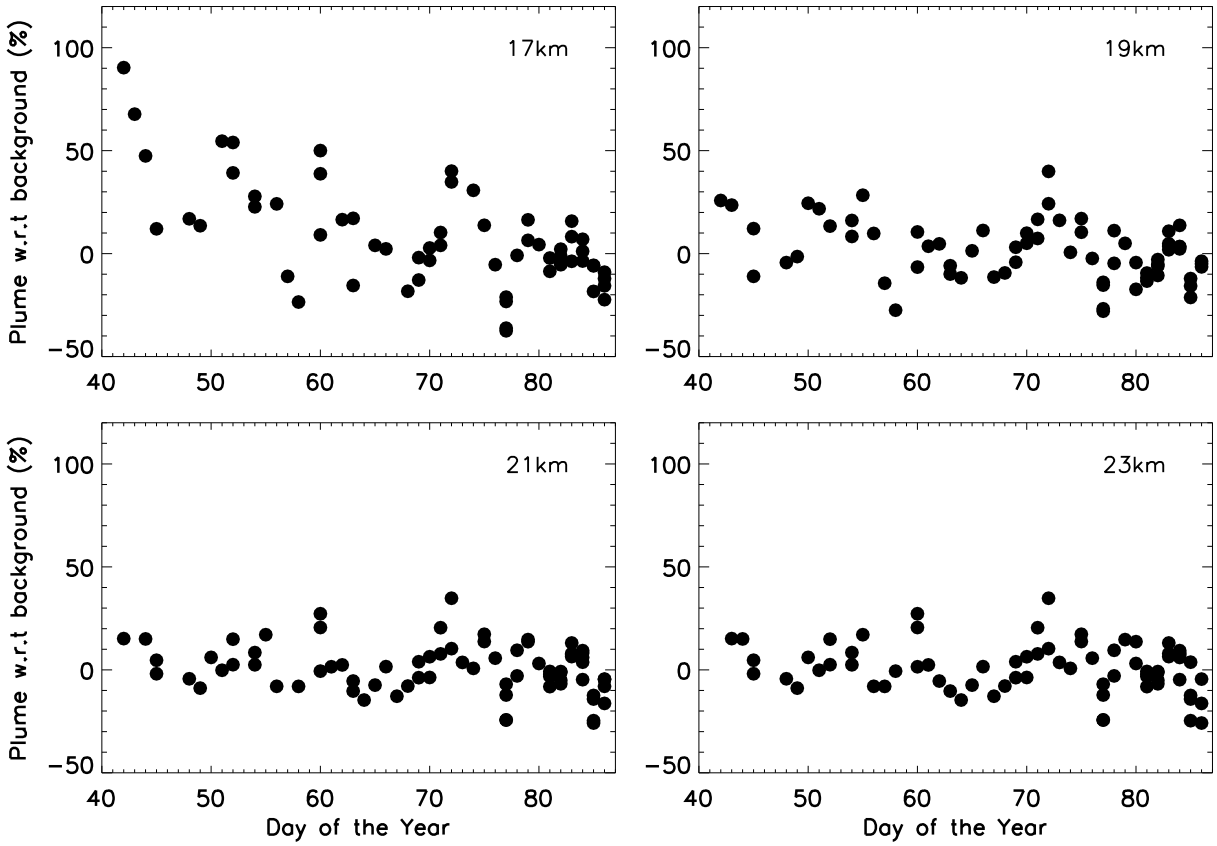

Figure 5.8: Percent enhancement (relative to background) ratios of the H_2O absorption band to the O_2 B-band for all OSIRIS plume-containing scans from 11 February until 26 March 2009. Data points have been smoothed with a 3-day uniformly weighted sliding mean filter.

To reduce the variability in the OSIRIS data, the net enhancement ratios were averaged within the altitude range of 16-22 km, in 7-day periods and compared with MLS

percentage enhancements, as shown in Figure 5.9. The vertically integrated values are shown for the first 4 weeks of the smoke being observed in the stratosphere by OSIRIS, from 11 February to 10 March 2009 (DOY 42-69). Between 16-22 km, OSIRIS percentage H_2O enhancement peaks during week two (February 18-24) at around 23%. MLS H_2O enhancement is highest during the first week (February 11-17) at around 13%, similar to OSIRIS (about 15%). MLS weekly averages decrease to 5% and below in the following two weeks. The water vapour enhancement in the first two weeks for both instruments is statistically significant for the first two weeks only.

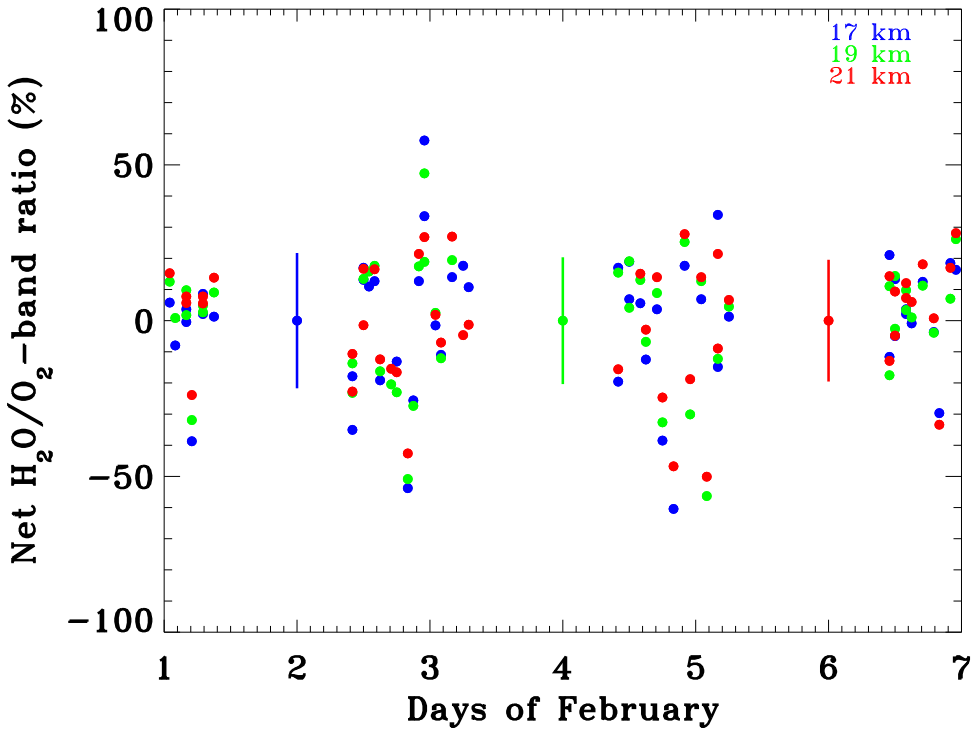

Figure 5.9: Vertically integrated net H_2O percent enhancement between 16-22 km for OSIRIS spectral ratios and MLS VMR. Data are shown on a weekly basis for the February 11 - March 6, 2009 period. Error bars represent the standard error for each instrument within each 7-day period.

As previously mentioned, MLS has greater sampling (more data points) in the spatial and temporal domain with respect to OSIRIS observations of the smoke plume. However, with this increased sampling, there is greater variation in H_2O VMR values. Such a variation means that taking weekly values over an altitude range does not fully convey any

increase in water associated with the smoke plume, with respect to MLS observations. Up until DOY 52, OSIRIS only observes the smoke plume in individual scans, as the smoke plume was limited in horizontal spatial extent with respect to OSIRIS sampling coverage. In the days following, the smoke plume is detected in multiple OSIRIS scans that are located further apart as the smoke pollution spans a larger volume of the stratosphere.

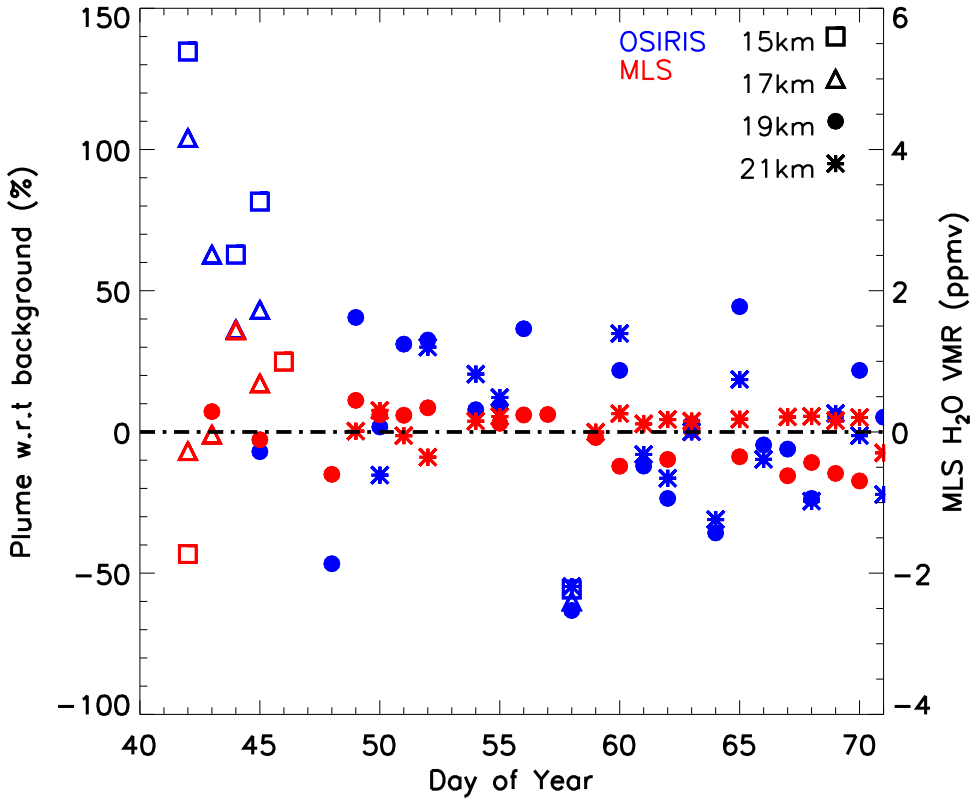

Figure 5.10: Daily averaged H_2O percent enhancement in the smoke plume measured by OSIRIS and MLS from February 11 until March 11, 2009. Corresponding VMR values for MLS H_2O enhancement are indicated on the right y-axis.

Figure 5.10 provides a comparison of both instruments used in this study in relation to daily mean H_2O percentage enhancement. All altitude steps where OSIRIS clearly observes the smoke plume up until 10 March, 2009 (DOY 70), are included. OSIRIS data indicates a very high initial enhancement of over 100% above background H_2O, that quickly decreases in the first few days. The plume is still located at mid-latitudes in the first few days, having ascended to the lower stratosphere corresponding to 14-18 km

altitudes. The first OSIRIS observation in the 19 km altitude range (DOY 45) shows very little perturbation with respect to the atmospheric background, with no enhancement until DOY 49, where there is a 40% enhancement. As the plume undergoes dispersion there is some variation in the OSIRIS ratios, but predominately a positive enhancement until DOY 60 (March 1).

MLS values shown in Figure 5.10, are daily averages of MLS H_2O measurements, which on a day-to day basis are individually quite variable in percentage enhancement values, which averages out to near background values for most days shown. On DOY 42, MLS measurements show negative or no enhancement, possibly due to the discrete spatial extent of the smoke plume. Therefore even with a spatial coincidence criteria, MLS does not provide any observations within the smoke plume. For the following 3 days (DOY 44-46), a reasonably significant enhancement of around 25% in the 15-17 km altitude range is observed, before MLS daily averages seem to relax to background values. The enhancement in water content within the smoke plume can be quantified in terms of MLS VMR values, as shown on the right y-axis in Figure 5.10. During the first 4 days that OSIRIS observes the smoke plume, the enhancement ratios correspond to an increase in H_2O VMR of around 3-5 ppmv at 15 km, and an increase of about 2 ppmv at 17 km with respect to the background. The percentage enhancements for the selected MLS measurements, correspond to an increase of only 1 ppmv, over the same vertical extent.

An increase of 1 ppmv represents a 30% enhancement above zonal mean MLS background values. It is possible that MLS H_2O enhancement is not as significant as what is suggested by OSIRIS measurements, due to a lower sensitivity to water vapour enhancement of this order in the MLS spectral channels. It is noted that *Pumphrey et al.* [2011] observed minimal water vapour enhancement associated with the Black Saturday bushfire plume over the same time period.

5.4.2 MLS H_2O measurements in the UTLS region

To provide a more quantitative analysis of the initial H_2O enhancement associated with the smoke plume, all MLS H_2O data in the 8 days following ignition of the BS bushfire are considered over an expanded latitude range of 25-50°S and a longitudinal range of 140-220°. This includes the spatial domain over which OSIRIS observes the smoke plume from DOY 42-46, together with observations from other satellite instruments that are outlined in Chapter 4. As MLS measurements are provided on pressure levels, and to confine data that lie within the 2 km altitude steps (centered at 15 km and 17 km) a barometric function that converts pressure to geometric heights, based on the US Standard Atmosphere, was used.

Figures 5.11 and 5.12 show daily MLS H_2O VMR measurements along its orbital path, from 8-15 February 2009, confined to the spatial domain described previously. MLS H_2O data that is more than 2-σ above the zonal mean value is shown as a square. For reference, the surface projection of the OSIRIS peak radiance measurement for that day, is also shown. Zonal H_2O VMR average values over the whole latitude range for each day, are used to determine the 2-σ upper uncertainty interval.

In the 15 km altitude step (Figure 5.11), there are large H_2O perturbations at latitudes between 30-40°S, on DOY 39 and 41 to the north-east of New Zealand, of between 8-12 ppmv. These high values are more than 2 standard deviations above the zonal mean and such large localised variations are unlikely to be related to natural atmospheric variability. They represent a percentage enhancement of up to 150-190% above a zonal average of around 4 ppmv. The enhanced water measurements are resolved on DOY 41 in the 17 km altitude step, at the same location, and represent values that are 80% above the zonal mean at that altitude.

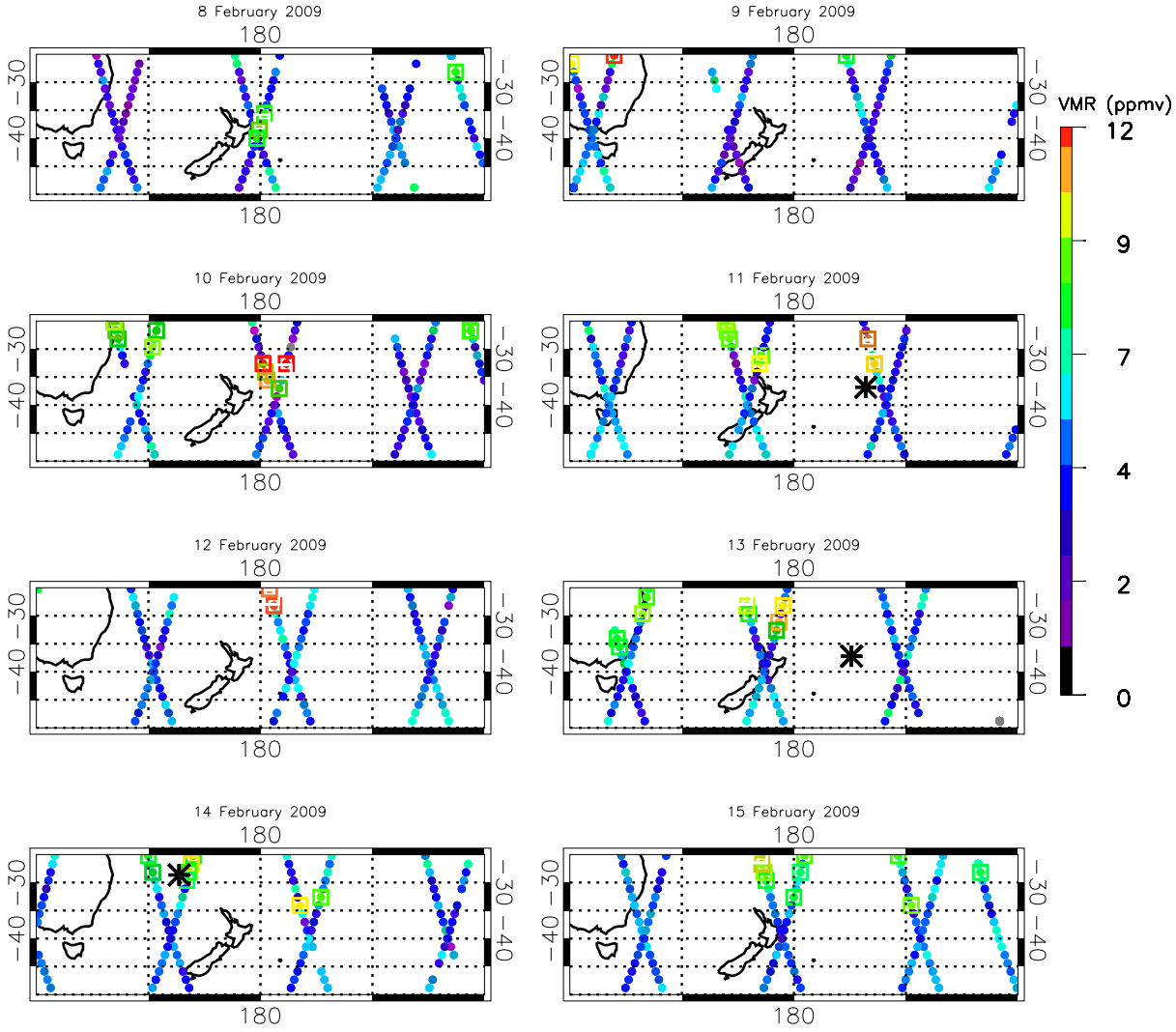

Figure 5.11: Daily MLS water measurements taken in the 15 km altitude step (14-16 km) to the east of Australia (25-50°S latitude and 140-220°E longitude), from 8-15 February 2009 (DOY 39-46). Data is colour coded as shown according to VMR (ppmv). OSIRIS observations, if present for that day at this altitude are shown by a black asterix. Data points that are greater than 2 standard deviations above the zonal mean are shown as squares.

From DOY 43-45, the horizontal distance between high MLS H_2O measurements and OSIRIS peak radiance locations starts to increase. Increased UTLS hydration remains fairly localised at mid-latitudes, whilst the large smoke aerosols are transported both eastward and westward from this location. However, due to the strict temporal criteria imposed on MLS data used previously in this study, these high MLS values, seen in Figures 5.11 and 5.12, were often not included with MLS daily values in Figure 5.10.

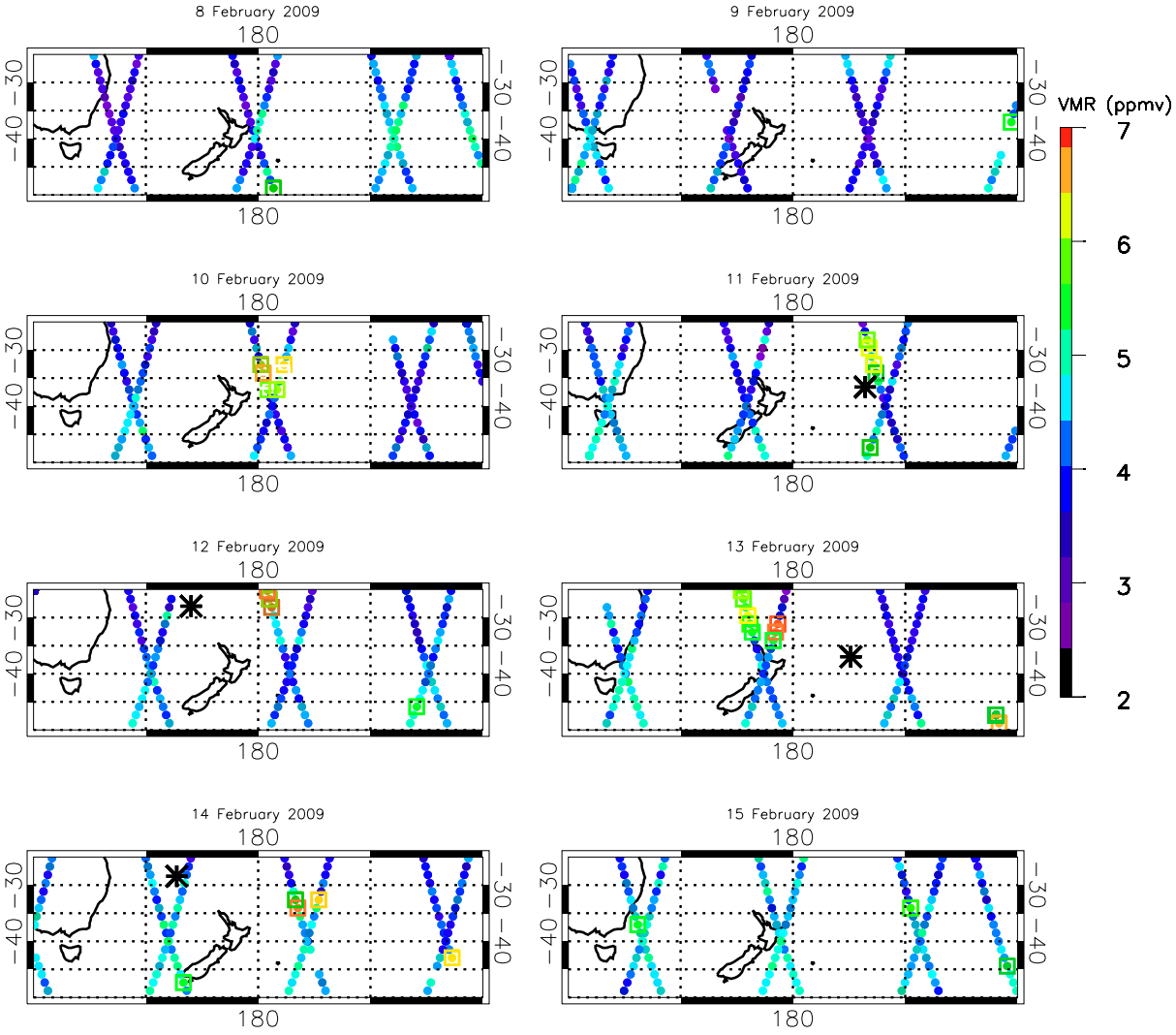

Figure 5.12: As for Figure 5.11 but for the 17 km altitude range.

Peak water enhancements from DOY 42-45 are between 150-200% above the background, within the 15 km step and 50-80% above background at 17 km. From DOY 46 onwards, the main smoke plume had shifted equatorward of 25° and ascended higher in the stratosphere, where it was observed by OSIRIS at approximately 21 km on DOY 48. On 15 February (DOY 46) there is still 100% enhancement above the background at 15 km centered near the international date line and 30°S. This coincides with the plume location in the CALIPSO curtain shown in Figure 4.4. In further agreement with forward trajectories shown in Figure 4.5, there are high H_2O concentrations transported eastward and poleward, perhaps suggesting that some smoke pollution was transported over the

Pacific Ocean towards South America. At latitudes higher than 30°S, the 15 km altitude range is located in the lowermost stratosphere, indicating short term hydration of the LS associated with transport of the smoke plume.

For completeness, daily maps of MLS H_2O measurements for the higher altitudes of 18-22 km were analysed to confirm persistent hydration of the sub-tropical LS associated with the smoke plume. Whilst previous MLS daily averages indicated very little H_2O enhancement at these altitudes, and at locations of OSIRIS peak radiances beyond DOY 46 (see Figure 5.10), expanding the dataset of MLS measurements across the sub-tropics, could illustrate H_2O perturbations in the dry LS, where the plume has dispersed over a wider horizontal domain.

For the 18-22 km altitude range, MLS H_2O residuals were calculated within each altitude step. Zonal mean H_2O VMR values were calculated for each 5° latitude bin from measurements taken from 1-6 February 2009, and subtracted from each MLS measurement within that latitude range. For the 19 km vertical step, residuals are plotted in the 10-30° latitude range, from DOY 45-51 as shown in Figure 5.13. These daily maps show the range of MLS residuals located near the OSIRIS plume locations, with some data points around 0.5 ppmv above the zonal mean. This dry part of the atmosphere, has concentrations of around 3.9 ppmv (see Figure 5.7). Therefore, perturbations above the 2-σ uncertainty range, equate to an increase in H_2O, of between 15-30% (0.5-1.4 ppmv) above the zonal background. Elevated values that spatially coincide with where OSIRIS observes the largest smoke aerosols, are observed between DOY 49-51. However, the variation of surrounding MLS measurements is such, that there are also locations that observe decreased H_2O concentrations.

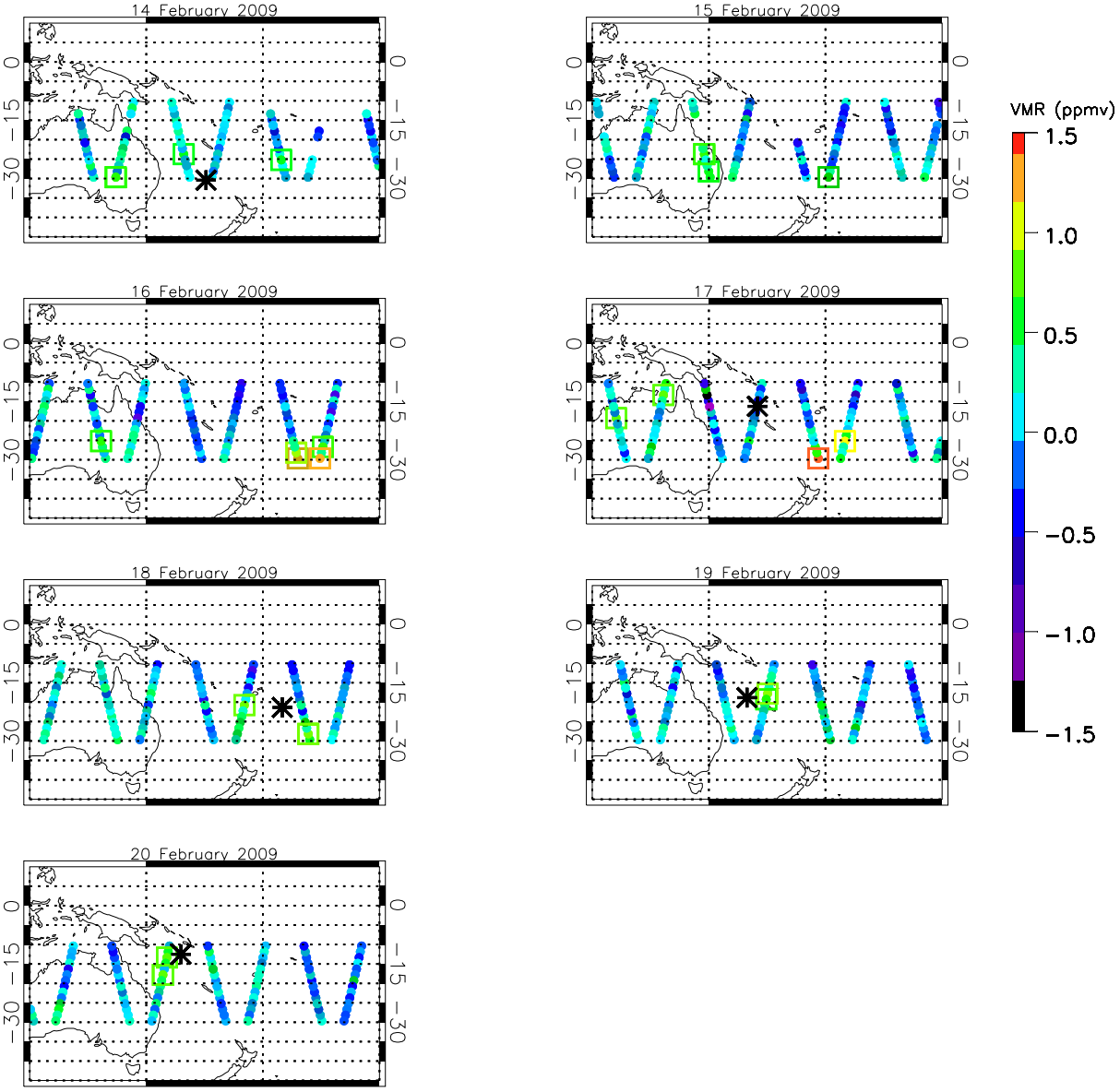

Figure 5.13: Daily MLS H_2O residuals, similar to Figure 5.11 but within the 19 km altitude range. Measurements are restricted to latitudes of 10-30°S and longitudes of 120-210°.

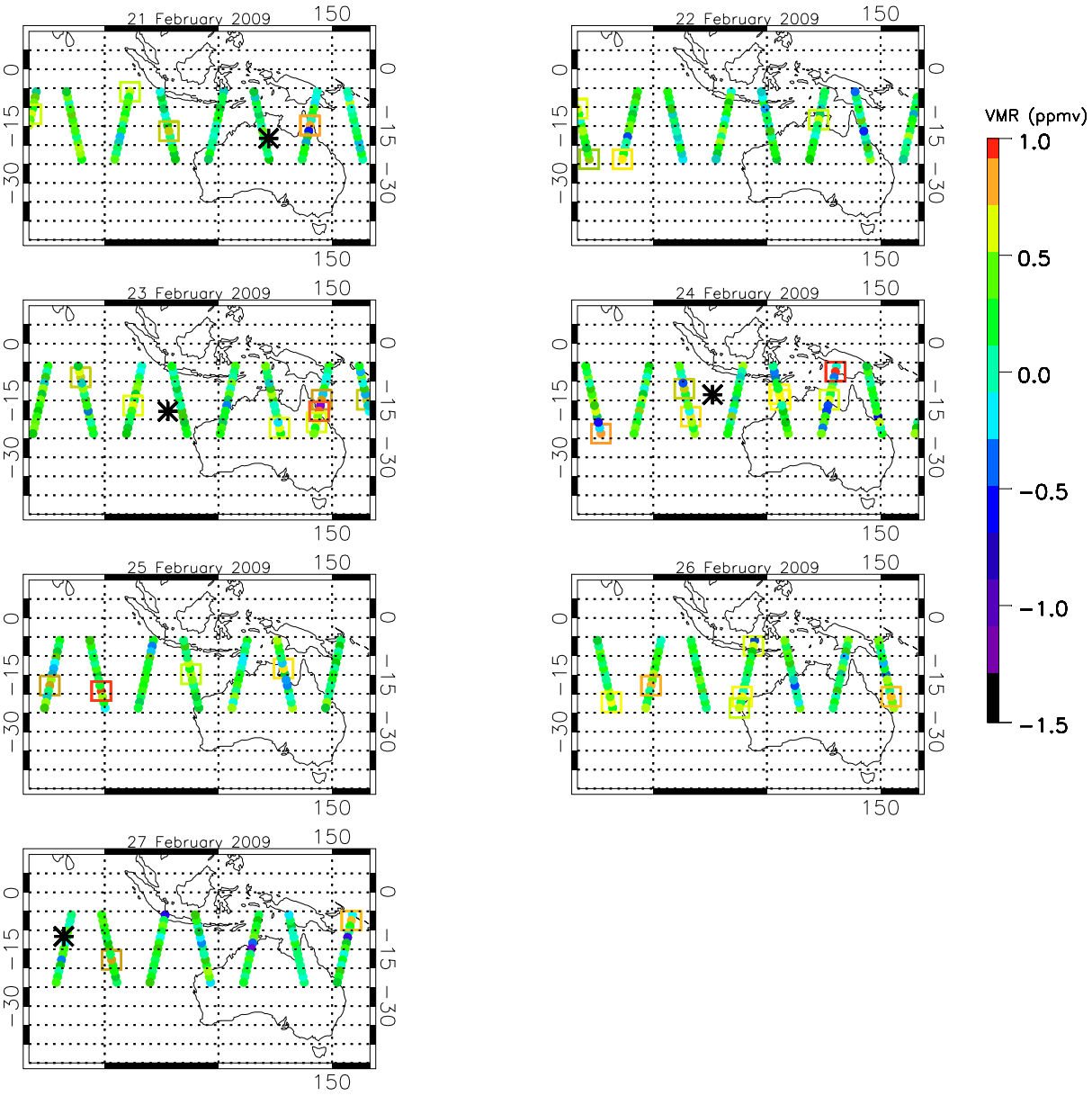

Figure 5.14: As for Figure 5.13 but within the 21 km altitude range. Measurements restricted to latitudes of 5-25°S and longitudes of 70-160°.

In the following week, DOY 52-58, MLS measurements in the 21 km altitude step are shown in Figure 5.14, within the 5-25° latitude range. The locations between OSIRIS peak plume radiances and MLS H_2O perturbations increasingly diverge. In a qualitative sense, this indicates that as the plume continues to age and disperse, the largest smoke aerosols does not necessarily coincide with areas of enhanced hydration, within the bushfire smoke plume.

5.5 Discussion

Using OSIRIS spectra, provides an alternative method to show H_2O enhancement in the smoke plume, using the smoke aerosols as a biomass burning marker. It is noted that water vapour is not a validated product from OSIRIS measurements, whereas, for example, the Microwave Limb Sounder (MLS) onboard the Aura satellite provides a well documented H_2O product and provides greater sampling output [*Read et al.*, 2007]. However, using OSIRIS peak radiance measurements, we were able to clearly track the location of the smoke plume (see Chapter 4) using aerosols, instead of gaseous markers. Smoke affected OSIRIS spectra provides an alternative observation path. Unlike MLS, using OSIRIS spectral indicators of the established water vapour absorption line does not require additional atmospheric parameters to obtain evidence of H_2O enhancement. Further, the MLS H_2O product, to our knowledge, has not been validated in more extreme local conditions, such as within the bushfire smoke plume mass. However, to compare our OSIRIS results, we also utilise MLS H_2O data using a coincidence criteria of plume locations, determined by OSIRIS measurements.

The net enhancement ratios for the 23 km altitude step is shown for completeness in Figure 5.8. However, based on net radiance perturbations shown in Figure 4.12, the smoke plume was not clearly identified at this altitude range until DOY 78. Nor did it show a large enhancement above 2008 values. Correspondingly, the smoke plume was clearly identified between DOY 42-45 as being located at an altitudes between 15-17 km, but from DOY 45 was clearly identified at altitudes above 17 km, as a peak radiance perturbation, once the main smoke plume had reached tropical latitudes.

Therefore, after DOY 45 in the 17 km vertical step, ratio enhancements do not represent where OSIRIS observed the smoke plume clearly. However, as demonstrated in Figure 5.1 the vertical extent of the plume can extend down to this altitude. For scans that are located equatorward of approximately 20°S, this represent tangent altitudes that are located at or just above the tropopause. At altitude steps of 19 km and 21 km higher percentage enhancements are generally seen as the plume vertically ascends into the stratosphere, with peaks at DOY 52 and DOY 60 for increasing altitudes as seen in Figure 5.8. What

is observed at OSIRIS peak radiance locations until DOY 86, is a series of peaks and troughs in net ratio values with peaks seen across the time period at around DOY 52, 60, 73 and 83. There is also a higher density of plume-containing OSIRIS scans over time as the plume increases in spatial extent, therefore across different altitude ranges, peak radiances are found in different scan locations. As the plume locations are flagged peak radiances within each altitude step, and the plume ages and undergoes dispersion, where OSIRIS observes the most optically thick smoke aerosols will not necessarily coincide with the part of the smoke plume that contains the most water vapour associated with it.

In relation to plume dispersion, in the weeks following injection of the smoke into the UTLS region, it is worthwhile to briefly discuss, the OSIRIS enhancement ratio that was obtained on DOY 58 (27 February). The very negative ratio (less than -50%) calculated for this OSIRIS radiance measurement suggests depleted H_2O with respect to the background concentrations. This was located at 11°S latitude over the Indian Ocean, and was observed in both the 19km and 21 km vertical step. On this day, and the previous day (DOY 57-58), there was a high MLS H_2O perturbation (about 15% above zonal mean) located to the southeast, within the same altitude range.

As discussed below in Section 5.5.1, the ACE-FTS instrument did not have many smoke-containing measurements during February. However, a vertical profile of an ACE-Imager scan that did clearly observe the smoke plume is shown in Figure 5.15. Onboard the same satellite as ACE-FTS, the Imager is used for detecting clouds in the field-of-view [*Bernath et al.*, 2005]. This vertical profile of 1020 nm extinction ratio was taken on DOY 57. This scan was taken much closer to the MLS H_2O perturbations observed on that day, and shows a very clear peak extinction ratio at 20 km, due to smoke aerosols. Also shown, is a temperature profile, with a clear temperature inversion at 16 km illustrating the height of the thermal tropopause. This suggests hydration of the lower stratosphere due to the smoke plume some 3 weeks after ignition.

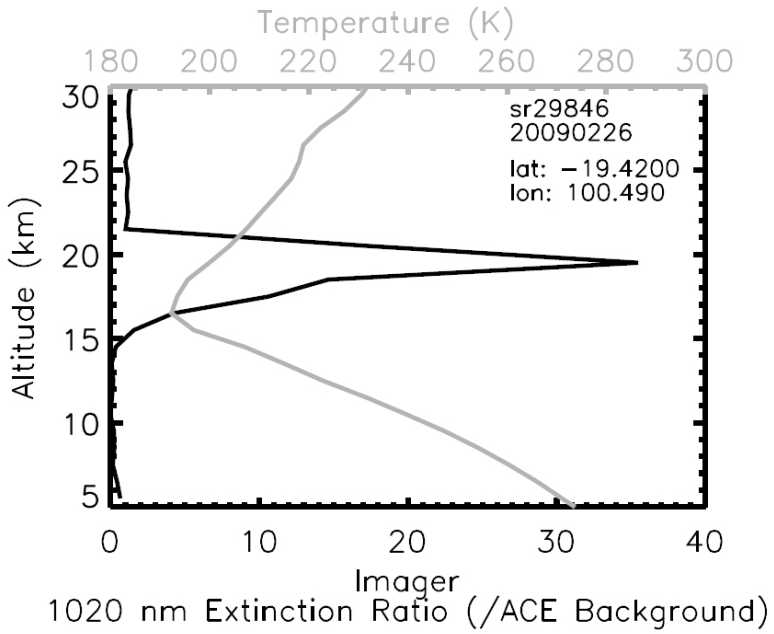

Figure 5.15: ACE-Imager extinction ratio vertical profile from 26 February 2009. Shown in light-grey is the coincident temperature vertical profile. Plot courtesy of Mike Fromm, NRL.

Data from various satellite instruments that are described and validated in peer-reviewed literature, were considered in this study. The OSIRIS method used in this study is a novel one, and in this context, it is worth outlining several datasets that were investigated, and provide justification as to why they were not included in this analysis.

5.5.1 Brief review of satellite instruments that measure H_2O

The SCanning Imaging Absorption spectroMeter for Atmospheric CHartographY (SCIAMACHY) instrument onboard Envisat also measures the limb-scattered solar radiation, but with a lower (compared to OSIRIS) vertical resolution of approximately 3.5 km. SCIAMACHY H_2O data are retrieved for a total column from its nadir measurements and thus can not be used in this work, to resolve water vapour in the LS.

The Sub-Millimetre Radiometer (SMR), another instrument on the Odin satellite [*Murtagh et al.*, 2002], measures the VMR of H_2O and its isotopes at, and above, the UTLS [*Urban*

et al., 2007]. The possible advantage of this instrument is that it's optically co-aligned with OSIRIS and thus observes nearly same volume of air. However, OSIRIS and SMR have slightly different fields-of-view in both the vertical and horizontal dimensions and it was revealed that SMR H_2O VMR retrievals at these altitudes were too noisy to be used in the present analysis (Joachim Urban, private communication).

Atmospheric Chemistry Experiment Fourier-Transform Spectrometer (ACE-FTS) on the Scisat satellite, measures vertical profiles of H_2O VMR and many other trace gases in the solar occultation regime (e.g. *Bernath et al.* [2005]; *Hegglin et al.* [2008]). Its broad infrared extinction spectra include regions where features caused by the presence of solid and liquid water can be seen [*Eremenko et al.*, 2005]. These features were considered to investigate the water droplets (ice particles) concentrations in the LS, at locations behind the main smoke plume. Such information could be important in case the LS temperatures were cold enough for some smoke-injected water molecules to form solid ice particles, or coat the surface of existing aerosol particles. According to several recent studies [*Chepfer and Noel*, 2009]; [*Poole et al.*, 2009], nucleation of some water particles into ice at these LS altitudes and locations is not impossible. However, during much of February 2009 ACE-FTS did not have many smoke-containing measurements, and did not have great temporal and spatial coverage at the latitudes and time of interest. Therefore, data from this instrument was not utilised in this study.

Another instrument on Scisat that also measures the H_2O VMR at UTLS altitudes is Measurements of Aerosol Extinction in the Stratosphere and Troposphere Retrieved by Occultation (MAESTRO) (*McElroy et al.* [2007];*Sioris et al.* [2010]). Water vapour retrievals for all scans during February 2009 were checked, and only 11 scans were available within two weeks of ignition, and they were all located in the tropics. As a result, the tropopause is high in these scans and cannot be restricted to the stratosphere (Chris Sioris, private communication). As reported previously, the smoke plume had reached the stratosphere within a few days at mid-latitudes and was tracked at stratospheric altitudes for the month of February. Therefore to consider any local enhancement in water vapour from the smoke plume, restriction to altitudes above the tropopause is necessary,

to prevent contribution of water enhancement from tropospheric deep convection.

Other satellite instruments that also measure H_2O VMR in the atmosphere are the Atmospheric Infrared Sounder (AIRS) [*Hagan et al.*, 2004], and the Microwave Limb Sounder (MLS) [*VöMel et al.*, 2007] both onboard the Aura satellite . Apart from the above referenced validation papers for AIRS and MLS water vapor retrievals at UTLS altitudes, validation inter-comparison of H_2O VMR for these two instruments is also presented by *Read et al.* [2007]. However, we note that AIRS does not measure H_2O in the stratosphere very well, and that at pressures below 150 hPa, retrievals are not particularly sensitive [*Hagan et al.*, 2004]. As it is a nadir viewing sensor and has a vertical resolution of 3 km, the instrument would not be able to retrieve any variation in water vapour within the smoke plume, when it was located at lower altitudes. The plume was located using OSIRIS radiance data between 15-17 km on the first two days of observations (DOY 41-42), however it is likely that the smoke plume was still quite limited in its spatial extent. AIRS measurements are made along the non-midnight meridian, so would typically be at least 6 hours either side of OSIRIS scans (that are made along the 'terminator'). Therefore, forward or backward trajectories would be necessary to compare with OSIRIS plume locations. As stated in *Read et al.* [2007], AIRS observed radiances are proportional to thermal gradients, and thus require a strong water vapour gradient within its line of sight to measure well, which is only present in the troposphere. The MLS instrument does, however, provide a more appropriate dataset for stratospheric water vapour retrievals in relation to this study, as it does not require a thermal gradient along its line of sight.

5.6 Conclusions

Based on satellite observations, an enhancement of water vapour associated with the smoke plume from the 2009 Black Saturday bushfires was observed in the lower stratosphere, from 8 February (DOY 39, day after ignition) until at least 27 February, 2009 (DOY 58). The plume was clearly wetter than the surrounding atmosphere in the first

few days of observations, in good agreement with *Pumphrey et al.* [2011]. The most significant water enhancement associated with the smoke plume was observed at altitudes of 14-18 km during early February. A smaller, but still statistically significant H_2O enhancement was also seen at higher altitudes of 18-22 km, that persisted in the weeks following bushfire ignition, which has not previously been observed associated with a bushfire smoke plume.

OSIRIS H_2O/O_2 ratios of peak plume radiance measurements, with respect to background ratios taken prior to the bushfire event, were used as a qualitative proxy of H_2O enhancement within the smoke plume. OSIRIS enhancement percentages demonstrated a very clear increase in local stratospheric H_2O (between 50-150%) in the first few days (DOY 42-46). Between DOY 47-60 (16 February - 1 March), OSIRIS spectral ratios demonstrated a variable positive enhancement, between 5-40%, in relation to background values. From DOY 58, some daily OSIRIS ratios showed a negative enhancement, possibly due to plume dispersion. As the plume dispersed, and underwent dilution and mixing, this lead to heterogenous H_2O concentrations within the smoke plume.

MLS H_2O enhancement ratios were used to compare with OSIRIS spectral enhancement ratios. Due to MLS H_2O data sampling differences with OSIRIS radiance measurements, only MLS data within a strict spatial and temporal criteria, were used to compare with OSIRIS observations, and to assist with quantifying any observed enhancement. This MLS restricted dataset, demonstrated a reduced enhancement of H_2O VMR concentrations within the smoke plume of up to 40% (approximately 1 ppmv above the stratospheric background), which was much less than what was observed with OSIRIS. After DOY 46, daily mean MLS H_2O demonstrated little or no enhancement above the calculated background. With a greater MLS sampling dataset, individual daily MLS data points showed a positive enhancement, whilst others showed a depletion with respect to background. By this time, the plume had dispersed over a larger area and any stratospheric hydration due to the smoke plume did not necessarily coincide with the location of the largest smoke aerosols (and therefore the peak OSIRIS radiance locations).

The mechanism by which H_2O, associated with the smoke plume, is transported to

the stratosphere is not directly investigated in this study. However, it is most likely due to vertical advection via entrainment of tropospheric water vapour by the smoke plume, or by in-situ chemical production within the smoke plume, assisted by photolysis as the smoke ascends into the lower stratosphere. The ability for bushfire smoke to penetrate the tropopause is a newly studied phenomenon and this study introduces an alternative method by which the H_2O balance in the stratosphere can be perturbed, at least on a local scale, if not on a larger zonal scale. It is generally accepted, that moisture enters the stratosphere via the tropical tropopause layer through slow diabatic ascent or rapid convection. However, this study shows that a pyroconvective event such as the Black Saturday bushfire can provide enough initial vertical velocity for H_2O to enter the arid stratosphere at mid-latitudes, thus avoiding the 'cold trap' region in the equatorial West Pacific where tropospheric air parcels are dehydrated before entering the dry lower stratosphere [*Holton and Gettelman*, 2001].

In this study, H_2O concentrations were analysed using the absorption band centered at 740 nm; therefore only considering the gaseous phase, rather than H_2O in the ice phase (which has a different absorption window). This analysis is associated with a smoke plume entering the stratosphere at mid-latitudes as a result of pyroconvection, a different convective process to what has been previously observed at mid-latitudes. Overshooting convection is an established mechanism by which ice crystals are injected above the tropopause which then sublimate in the lower stratosphere. These have been observed in the tropics [*Liu et al.*, 2010] and at northern mid-latitudes [*Dessler and Sherwood*, 2004]. While MLS does provide an Ice Water Content data product [*Livesey et al.*, 2011], this was outside the scope of this study.

Stratospheric water vapour trends are still a debated issue, as are the mechanisms which determine its distribution across the UTLS region. It is a vital component of the stratosphere affecting climate and atmospheric chemistry. It is a major source of hydroxyl radicals in the stratosphere, and encourages ozone depletion during winter via PSC formation. MLS also provides CO and O_3 measurements, which are established atmospheric tracers for biomass burning plumes. These MLS tracers are compared against

each other in the next chapter.

6 Effects of the 2009 Australian Black Saturday bushfire smoke on lower stratospheric ozone measured by MLS

6.1 Introduction

An important effect of biomass burning emissions on the atmosphere is that its constituents can significantly affect the number of hydroxyl (OH) radicals present, and thus initiate or impede important chemical reactions [*Seinfeld and Pandis*, 2006]. In particular, ozone (O_3) is often produced within smoke plumes due to carbon monoxide (CO) and volatile organic compounds (VOCs) oxidising by reactions with OH in the presence of sunlight and enhanced levels of nitrogen oxides (NO_x). VOCs is a term often used to represent all vapor-phase atmospheric organics, excluding CO and CO_2 [*Seinfeld and Pandis*, 2006]. Photochemical oxidation of hydrocarbons such as VOCs can lead to additional CO being produced, adding to the amount emitted directly from a fire [*Crutzen and Andreae*, 1990].

The efficiency of O_3 production within smoke plumes is dependent on the proportions of hydrocarbons and NO_x present, along with the transport history of the smoke plume in the atmosphere [*Crutzen and Andreae*, 1990]; [*Andreae*, 1991]. Therefore CO is directly involved in the O_3 chemistry, often increasing the O_3 abundance in the troposphere

[*Forster et al.*, 2001] and influencing stratospheric ozone levels through catalytic reactions [*Fromm et al.*, 2000].

O_3 concentrations within a smoke plume also depend on temperature during smoke transport and the presence of water vapor (H_2O) within the plume and the surrounding troposphere, which can lead to O_3 destruction. Where $O(^1D)$ is produced from photolysis of O_3 as shown in reaction 1.3, catalytic O_3 can be initiated by oxidation of H_2O as shown below

$$H_2O + O(^1D) \longrightarrow 2OH \tag{6.1}$$

$$OH + O_3 \longrightarrow HO_2 + O_2 \tag{6.2}$$

$$HO_2 + O_3 \longrightarrow OH + 2O_2 \tag{6.3}$$

$$Net : 2O_3 \longrightarrow 3O_2 \tag{6.4}$$

Reaction 6.1 is the oxidation of H_2O by the high-energy $O(^1D)$ atoms, followed by the loss of O_3 from both OH and the hydroperoxy radical (HO_2), which together are known as the HO_x radicals. These radicals are efficient catalysts in destroying ozone [*Brasseur and Solomon*, 2005]. Therefore depending on the conditions O_3 can be produced or destroyed within smoke plumes in the presence of HO_x radicals.

Observations of smoke plumes from boreal forest fires have shown low enhancements in O_3 in plumes only a few hours old [*Goode et al.*, 2000]) and significant O_3 production in well-aged plumes (days to weeks after ignition) from Siberian forest fires that were observed over the North Atlantic [*Honrath et al.*, 2004] and over the west coast of the U.S [*Bertschi and Jaffe*, 2005]. *Jaffe et al.* [2004] found that smoke plumes from Siberian fires were transported to western North America, providing an enhancement of background O_3 of between 5-9 ppbv observed in measurements up to 6 km in altitude. *Val Martín et al.* [2006] observed smoke pollution, originating from North America, over the Azore Islands (6-15 days downwind), with significant O_3 production in some parts of the smoke and other parts showing no production. They used a combination of in-situ measurements

and chemistry transport model simulations up to 9 km in altitude.

Val Martín et al. [2006] found that decomposition of peroxyacetyle nitrate (PAN) into NO_x leads to formation of O_3. The role of PAN as a source of NO_x in boreal fire emissions has resulted in increased O_3 over the Arctic [*Leung et al.*, 2007]. Ratios of O_3/CO are used as indicators of ozone production or loss, with negative ratios within aged plumes suggesting ozone loss. *Griffin et al.* [1999] found that ozone destruction by reaction with organic compounds occurred in smoke aerosols. It has also been suggested that night-time chemistry, involving oxidation of NO_x to HNO_3 with simultaneous destruction of O_3 can occur [*Val Martín et al.*, 2006].

Using laboratory data and a chemistry transport model, *Konovalov et al.* [2012] investigated the photo-induced O_3 loss on the surface of biomass burning aerosols during the wildfire season in Russia during 2010. They found that a photo-induced heterogeneous reaction of O_3 on the surface of biomass burning aerosol particles, can decrease the O_3 concentration within a smoke plume. *Konovalov et al.* [2012] also found that the decrease in O_3 was offset by surrounding smoke aerosols, shielding the amount of incident photons available for this reaction. Similarly, aircraft measurements of biomass burning smoke over Indonesia found depleted ozone within the lower portion of the smoke layer and higher ozone concentrations in the middle of the smoke layer [*Tsutsumi et al.*, 1999]. The decrease in O_3 in the lower layer was attributed to a reduction in solar flux from dense smoke aerosols overhead.

Co-located CO and O_3 values measured by the Tropospheric Emission Spectrometer (TES) satellite instrument were used to examine ozone production from a 2006 Siberian fire up to 300 hPa in *Verma et al.* [2009]. They found some ozone enhancement in some parts of the smoke, but also a significantly lower O_3 concentration where aerosols in the smoke plume were optically thick (where aerosol optical depth was >4). By using an air-quality model, *Verma et al.* [2009] found that optically thick aerosols could reduce the photochemical production of ozone, but still could not account for the very low ozone concentrations observed. A large proportion of studies that have considered ozone chemistry in biomass burning smoke pollution within the troposphere, have found ozone production

occurring in smoke plumes in the UTLS region.

In this study, we analyze co-located measurements of CO and O_3 values from the Microwave Limb Sounder (MLS) instrument during February-March 2009, using CO perturbations as a tracer of the Black Saturday smoke plume. The transport and evolution of the main smoke plume using limb-scattered solar radiance perturbations was reported in Chapter 4 and evidence of enhanced H_2O associated with the smoke pollution is presented in Chapter 5. Using CO tracers, the effect on lower stratospheric O_3 due to the smoke plume is analysed.

Pumphrey et al. [2011] reported enhanced CO concentrations originating from combustion products of the Black Saturday bushfire material. This additional CO penetrated the tropopause and reached the pressure level of 46 hPa. Similarly to *Pumphrey et al.* [2011], CO data points are used in this study as tracers for the smoke plume. This provides an alternative pathway to monitoring the transport of smoke pollution rather than through the evolution of limb scattered radiances due to smoke aerosols, as in the previous chapters. The late austral summer period provides a unique window of opportunity, as historically there is minimal SH biomass burning at this time of the year. At this time, CO enhancements in the mid-latitude UTLS region from other biomass burning sources are much less likely [*Duncan et al.*, 2003].

6.2 Data analysis

6.2.1 Instrument description

The Microwave Limb Sounder (MLS) is one of four instruments onboard the Aura platform that was launched in July 2004 [*Waters et al.*, 2006]. MLS continuously measures thermal emissions from 5 spectral bands centered at frequencies between 118 GHz and 2.5 THz. The CO and O_3 VMR data are retrieved from the 240 GHz radiometer measurements. Extensive validation details for the MLS version 2.2 (v2.2) data product are given in *Pumphrey et al.* [2007] and *Livesey et al.* [2008]. In this study, the latest MLS version 3.3 (v3.3) retrievals are used. A full description of the MLS v3.3 data is provided in the

MLS data quality document [*Livesey et al.*, 2011]. The v3.3 MLS CO data is essentially unchanged from v2.2 at the altitudes considered in this study, with O_3 observations generally within 1-2% of v2.2 observations in the stratosphere [*Livesey et al.*, 2013]. There has been no global validation of the MLS v3.3 data product [*Livesey et al.*, 2011]. However, the *Livesey et al.* [2013] paper did analyse v3.3 data for both CO and O_3 between 30°N and 30°S in the upper troposphere (215 hPa), as the v2.2 product had significant bias at this altitude.

Within the 240 GHz region of the spectrum, radiance features measured by MLS are dominated by O_3 emission lines and a CO emission line [*Livesey et al.*, 2011]. The MLS ozone retrievals are provided in the range 261-0.02 hPa. This work focuses on pressures of 147-32 hPa that correspond to the altitudes at which the smoke plume was observed by OSIRIS (see Chapter 4). At the pressure levels considered in this study, MLS O_3 retrievals have a horizontal resolution of approximately 300-400 km and a vertical resolution of about 2.5 km. MLS CO retrievals have a coarser vertical resolution of 3.5 -5 km. This vertical resolution is degraded compared to the v2.2 CO product used in *Pumphrey et al.* [2011], in order to reduce the retrieval uncertainty. However, it also reduces the ability to differentiate between clouds, with scattering from optically thick clouds leading to unrealistic values [*Livesey et al.*, 2011]. Therefore, MLS v3.3 retrievals in the UTLS region at tropical latitudes may exclude measurements at locations where the smoke plume contains very large aerosols or other organic matter. As stated in *Livesey et al.* [2011], future MLS data products will attempt to improve the quality of both CO and O_3 products in the presence of thick clouds.

In the UTLS region, MLS v3.3 O_3 data have uncertainty values of approximately 20-30% (around 0.04 ppmv) at 100 hPa, 3-10% at 68 hPa, and approximately 3% above this altitude [*Livesey et al.*, 2011] very similar to the uncertainties in the MLS v2.2 retrievals [*Livesey et al.*, 2008]. Comparisons of UTLS MLS ozone profiles with other ozone profiles measured by satellite-borne and ground-based techniques suggest a 5-10% agreement [*Livesey et al.*, 2011]. The MLS v3.3 data files contain 2 separate stratospheric ozone columns corresponding to the use of tropopause pressures based either on MLS, or on

GEOS-5 temperatures. The column retrievals based on MLS temperatures are used in this study. All v3.3 quality control criteria of MLS CO and O_3 profiles, as recommended by the MLS team [*Livesey et al.*, 2011] are adhered to here.

6.2.2 Methodology

Based on OSIRIS radiance measurements, as outlined in previous chapters, the largest smoke aerosols were located between 10-40°S during the months of February-March. However, a wider spread of smoke pollution in the Southern Hemisphere is considered. There was some evidence of secondary smoke material that was transported eastward and poleward in the mid-latitude lower stratosphere according to MLS H_2O values in Chapter 5, in conjunction with the forward trajectory analysis presented in Figure 4.5. Therefore to further investigate the latitudinal spread of the smoke plume, MLS CO tracers were analysed over 10-60°S.

To provide atmospheric background values, CO zonal means within 10° latitude bands were calculated across 10-60°. MLS CO perturbations, equal or greater than 4.5 standard deviations above 2008 zonal averages, were flagged as smoke affected measurements. This attempts to exclude any CO measurements associated with natural atmospheric variability, especially at lower stratospheric altitudes, where CO concentrations are reasonably stable all year round. At SH mid-latitudes in February-March, biomass burning emissions are quite low. However, CO perturbations in the upper troposphere at sub-equatorial latitudes (up to 15°S) had been observed during February over Indonesia [*Schoeberl et al.*, 2006]. Using CO data as a bushfire smoke indicator it was possible to analyse MLS O_3 data at the same location, to consider the local effect on ozone concentrations from the smoke plume.

Zonal mean background CO values, from other years (2007, 2010) were also considered in this work, and were found to be very similar to 2008 CO zonal mean values. However, the 2008 CO background values were selected, as 2008 was a relatively quiescent year in relation to the CO maxima values [*Inness et al.*, 2013]. In support of this, the *Torres et al.* [2010] study found a large drop in the SH fire activity during 2008 with a decreased

atmospheric load of carbonaceous aerosols over the main SH source areas of South Africa and South America.

The atmospheric lifetime of CO varies with altitude, dependent on concentrations of other chemical species such as OH. At UTLS altitudes, the lifetime of CO is between 1-2 months [*Liu et al.*, 2007];[*Petrenko et al.*, 2013]. Therefore, a 6 week period from the time of the ignition was considered in this study (up to 25 March 2009; DOY 85). This provides an adequate time period over which to fully consider CO perturbations resulting from the bushfire smoke.

6.3 Results

6.3.1 MLS CO perturbations

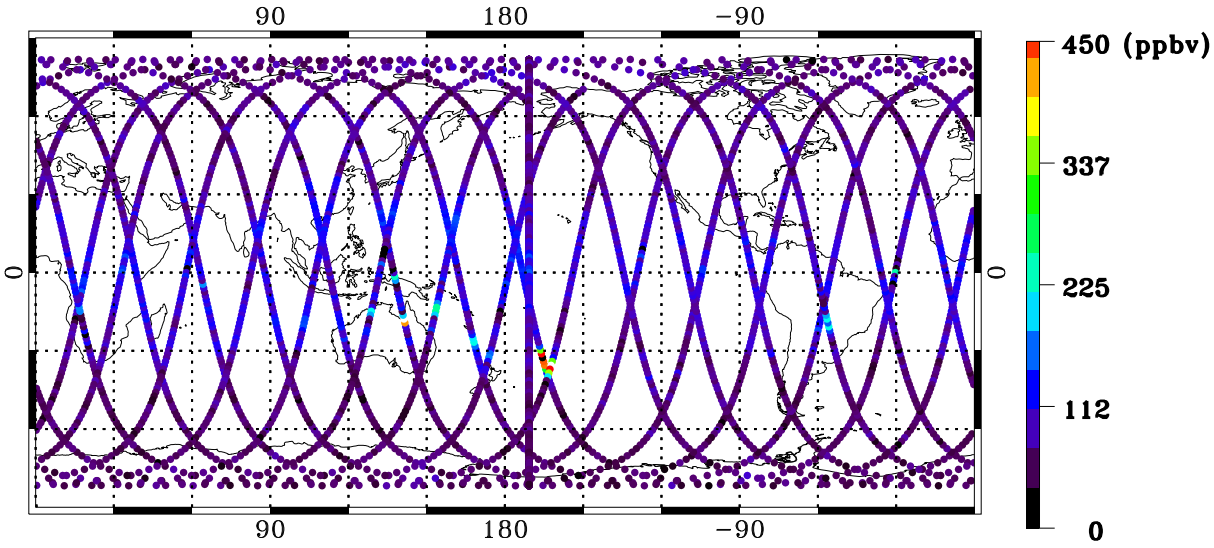

Figure 6.1: Global map of MLS CO VMR on 11 February, 2009 (DOY 42). The scale of CO concentrations is shown on the colour bar at the right of the plot.

Figure 6.1 is a global map of CO VMR measurements taken on 11 February, 2009 at 100 hPa (approximately 16-17 km geometric altitude), and can be compared with the OSIRIS global radiance map taken on the same day (see Figure 4.8). The Black Saturday smoke plume is visible as strong CO perturbations, with respect to the background values. The

enhancements to the north and north-east of New Zealand, coincide well with OSIRIS observations of the the smoke plume, at this approximate altitude. MLS CO perturbations and OSIRIS peak radiances are in good spatial agreement over the whole time period considered.

Figure 6.2 shows all MLS CO measurements taken between 1 February 2009 (DOY 32) and 1 March 2009 (DOY 60) at 147 hPa over a 5° latitude band of 35-40°S. This is a more restricted latitude band than what is considered for the remainder of this study, in order to confirm MLS CO perturbations for the period of time that OSIRIS did not clearly observe the smoke plume (from DOY 39-41). Each CO measurement is centered on the day it was observed, rather than plotting each measurement on an hourly basis, as it was felt that spreading the data points throughout each day did not provide any real advantage in this analysis. Figure 6.2 shows CO VMR concentrations prior to the bushfire and the increase in CO perturbations observed after ignition, on DOY 38. The latitude range in Figure 6.2 includes where the smoke plume originated from in south-eastern Australia, before being transported eastward towards New Zealand. Very high CO values, an order of magnitude higher than the CO background, are seen on DOY 39-41, with some residual enhancement between DOY 42-45. The smoke had lofted to higher altitudes within a few days after ignition. Therefore, little CO enhancement is observed after DOY 45.

MLS CO VMR measurements equal or greater than 4.5 standard deviations above the 2008 zonal mean were extracted, and are shown as a time series in Figure 6.3. The 2008 CO zonal means are calculated over 10° latitude bins, and all data points are colour coded by those 10° latitude ranges. At 147 hPa (and to a lesser extent, 100 hPa), anomalously high CO values are observed prior to the bushfire (DOY 32-36) at latitudes predominately between 10-30°S. This is likely due to seasonal biomass burning emissions that originate from regions such as equatorial Africa [*Galanter et al.*, 2000]. Biomass burning over the Indonesia and South America regions, that are normally the main source of CO enhancement in the austral upper troposphere (UT), are minimal during this time of year [*Gonzi and Palmer*, 2010].

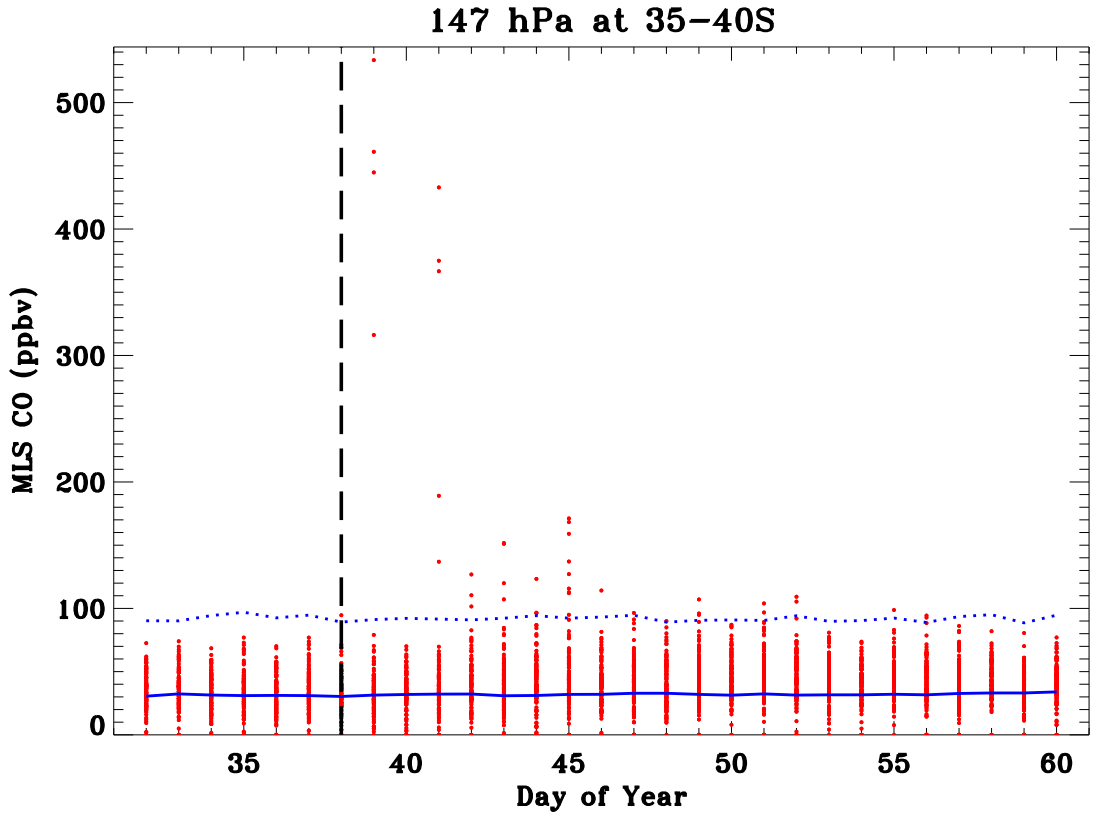

Figure 6.2: MLS CO VMR from 1 February 2009 (DOY 32) to 1 March 2009 (DOY 60) at 147 hPa in the latitude range of 35-40°S. The blue solid line is the 2008 CO background. The blue dotted line represents the 4.5 standard deviation above the 2008 mean. The black dashed line shows the bushfire ignition date; 7 February 2009 (DOY 38).

At lower stratosphere (LS) altitudes (68-32 hPa), the presence of the smoke plume is indicated by very high CO measurements that appear progressively later in the year, with increasing altitude. These high CO values move equatorward over time, in good agreement with previous chapters. Mid-latitude CO perturbations peak at 800 ppbv at 100 hPa on DOY 41. At the pressure altitude of 100hPa, this is over 15 times larger than the 2008 zonal mean (approximately 50 ppbv).

At 68 hPa, CO perturbations maximise between 20-40°S at approximately 450 ppbv. The smoke plume migrates equatorward at this altitude range, with a sharp decrease by DOY 50. CO measurements at DOY 60 peak at around 100 ppbv, in the 10-30°S range, which is still an enhancement of 300% above the zonal mean. By DOY 45, there is significant enhancement observed at 46 hPa, with a peak value of nearly 200 ppbv located

between 10-30°S at DOY 48 and a secondary peak at DOY 60 at around 150 ppbv. At this height, the 2008 CO zonal mean is between 10-20 ppbv. CO enhancements continue to persist towards the end of March at sub-equatorial latitudes.

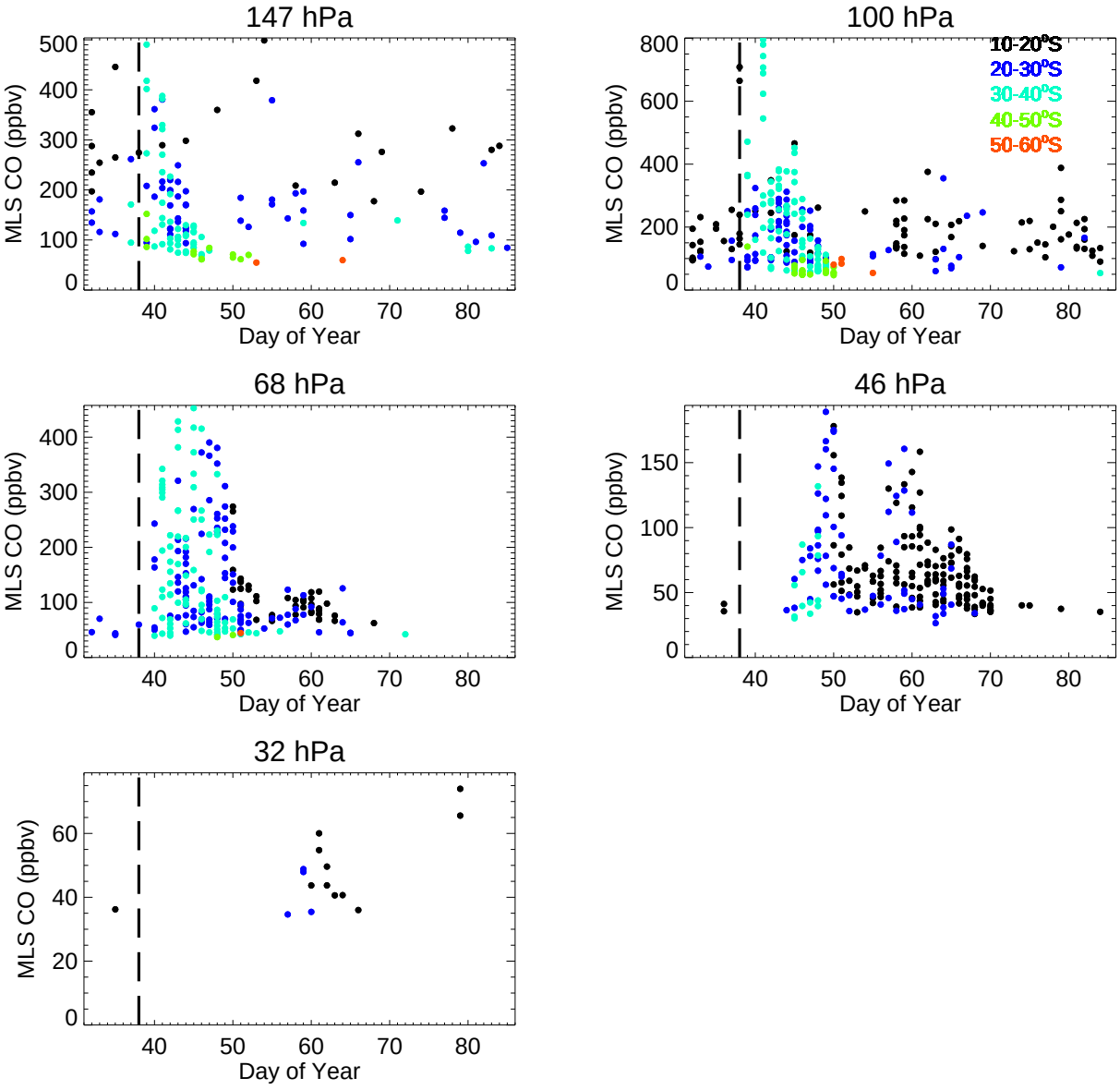

Figure 6.3: Time series of MLS CO perturbations at or above the 4.5-σ uncertainty range of the 2008 CO levels for DOY 32-60. Each latitude band is colour-coded as shown in the top right panel. Note that CO perturbations (y-axis) have differing scales for each pressure level.

The smoke plume even ascends to 32 hPa at sub-equatorial latitudes by March (DOY

60), with some high perturbations observed until DOY 80, in reasonable agreement with OSIRIS net plume radiances at the equivalent 23 km altitude step. This substantiates the extreme height that the smoke plume has ascended to within the LS. However, according to the MLS data quality document, there is a large negative bias of the MLS v2.2 (hence v3.3) CO retrievals at this pressure level, approximately 70%, compared to other satellite measurements [*Livesey et al.*, 2011]. Therefore, in the subsequent analysis, MLS CO perturbations were restricted to the pressure range of 147-46 hPa.

There is an indication of smoke pollution poleward of 40°S, particularly at altitudes corresponding to 147 and 100 hPa. CO perturbations at these latitudes were observed sporadically until DOY 64. At these sub-polar latitudes, such pressure altitudes are located at, or above the tropopause, with tropopause height decreasing at higher latitudes.

6.3.2 MLS CO and O_3 tracer correlations

Figure 6.4 are vertical profiles of MLS O_3 measurements from 265 to 30 hPa, encompassing the UTLS region considered in this study. MLS O_3 data were averaged over February-March, for each individual year (2007-2010) within 10° latitude ranges. O_3 concentrations increase with increasing altitude. There is also a positive latitudinal gradient in O_3, with increasing poleward zonal mean values. This latitudinal gradient from 10-60°S, shows minimal interannual variability, over a 4 year period (2007-2010). This gradient becomes minimal at 30 hPa, where the Brewer-Dobson Circulation dominates O_3 distribution (see Figure 1.1).

Figure 6.4 suggests that any influence from the QBO (as shown in Figure 1.2) on SH O_3 zonal averages is negligible, for the months considered in this study (February-March). Additionally, with bi-monthly mean O_3 trends being quite similar between 2008 and 2010, and each of those years having opposing QBO phases, there appears to be no significant effect on O_3 background trends due to the prevailing QBO phase. This is in agreement with *Kuroda and Yamazaki* [2010], who found for mid latitude (40-60°S) O_3, there was a 0.8% difference between the easterly and westerly QBO phases, as well as a 1.8% difference in O_3 trends between high and low solar activity years.

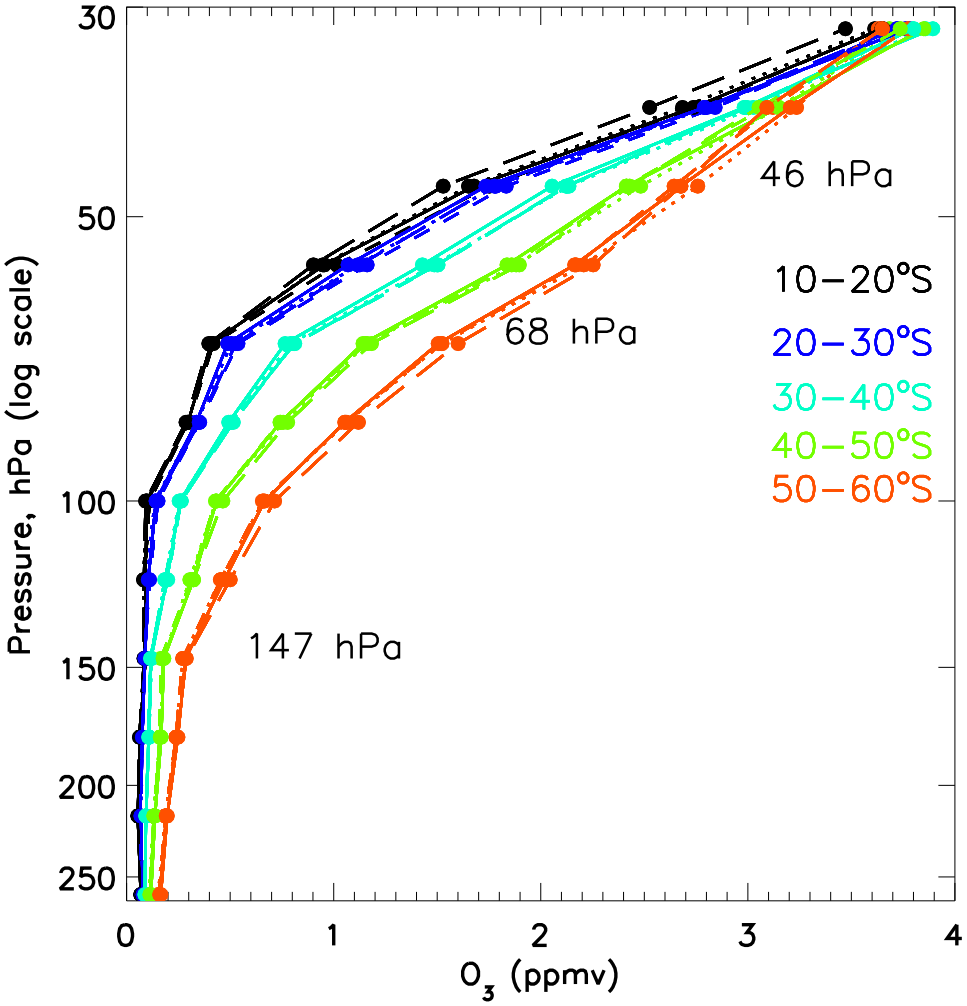

Figure 6.4: MLS O_3 VMR vertical profiles from 260-30 hPa averaged over February-March across 10° latitude bins, colour-coded as shown. The years from 2007-2010, in increasing order are shown as dotted, dashed, solid and long-dashed lines, respectively. The 4 pressure levels considered in this study are displayed for clarity and the y-axis is a log pressure scale.

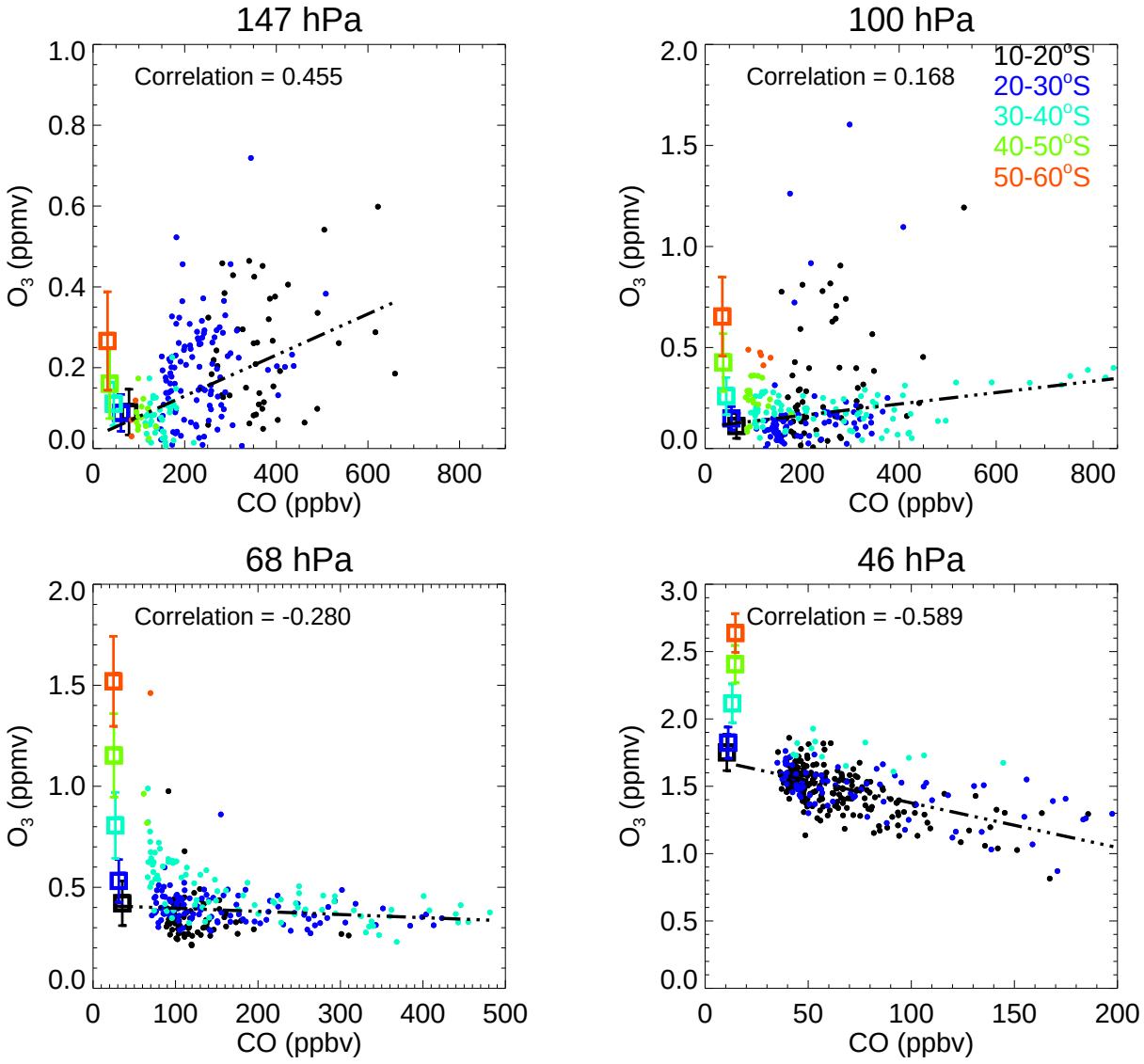

Figure 6.5: Scatter plots of MLS CO perturbations versus co-located O_3 for the four selected pressure levels from 8 February - 25 March, 2009 (DOY 39-85). Data points are colour coded as shown. 2008 zonal background values are shown as squares. Dashed-dotted lines represent a least absolute deviation linear fit across all latitudes. Error bars denote 1-σ uncertainty of 2008 O_3 background values for each 10° latitude band. Note, the axes have different scales for different pressure levels.

Using the anomalously high CO measurements outlined previously as tracers for the bushfire plume, the coincident O_3 measurements were plotted against these CO perturbations. This is shown in Figure 6.5 for all high CO perturbations taken between DOY 39 and DOY 85 (8 February - 25 March 2009), across 10° latitude bands and at pressures of 147-46 hPa. 2008 CO zonal mean values across all latitude bands show relatively stable

values across all latitudes in the SH UTLS region, with CO concentrations decreasing with increasing altitude. Vertical error bars represent a 1-σ uncertainty range of 2008 O_3 background values.

Linear trend lines in Figure 6.5 are obtained using a robust least absolute deviation technique, to reduce the sensitivity to outliers. Positive linear trends are seen between CO and O_3 up to the tropopause (147-100 hPa), implying O_3 production within the smoke plume at these altitudes. However, with increasing height, the trends become negative, suggesting O_3 depletion associated with the smoke plume with respect to the background stratosphere. Even though the CO perturbations are far greater than 2008 background values, data points within the upper troposphere may still include high CO values from external anthropogenic sources, such as industrial emissions. If NO_x is present in these high CO emissions, then tropospheric O_3 can form in photochemical reactions [*Atkinson*, 2000]. Therefore, increases in CO will lead to increased production of O_3.

A comparison of Figure 6.5 and Figure 6.3 shows that the highest CO perturbations at 100 hPa (between 600-800 ppbv), have coincident O_3 values close to 2008 zonal mean variability. The main smoke plume was observed at UT altitudes (147-100 hPa) for only a short period of time, before vertically advecting to the lower stratosphere (see Chapter 4). It is suggested that high O_3 measurements at UT heights between 10-30°S (Figure 6.5), are not related to the BS smoke plume. The few data points poleward of 40°S are likely to be associated with part of the smoke plume that was transported eastward and poleward during February 2009. These poleward O_3 measurements are relatively low (compared to 2008 O_3 zonal means), but usually within the lower 1-σ limit of uncertainty of those 2008 values.

In the LS (68-46 hPa), 2008 O_3 zonal values increase by around 1 ppmv, from 10°S to 60°S, as shown in Figure 6.5. The highest CO perturbations at these altitudes, have decreased O_3 concentrations, suggesting the smoke plume is introducing ozone poor air parcels to the lower stratosphere. As the plume ages, and CO concentrations decrease, O_3 recovers to the 2008 zonal mean within each latitude range. At 68 hPa and above, there are few data points above their respective 2008 zonal mean, particularly at 46 hPa.

Linear correlations between the two tracers are shown at the top of each plot in Figure 6.5. When the 2010 CO zonal mean values were used as a background (not shown), correlations for 147-46 hPa in order of increasing altitude (decreasing pressure), were 0.45, 0.16, -0.29 and -0.6, respectively. The $\delta O_3/\delta CO$ values of the linear fit with respect to the 2008 zonal means, in the same ascending height order were 0.51, 0.28, -0.15 and -3.32, with 2010 zonal means showing very similar values to these.

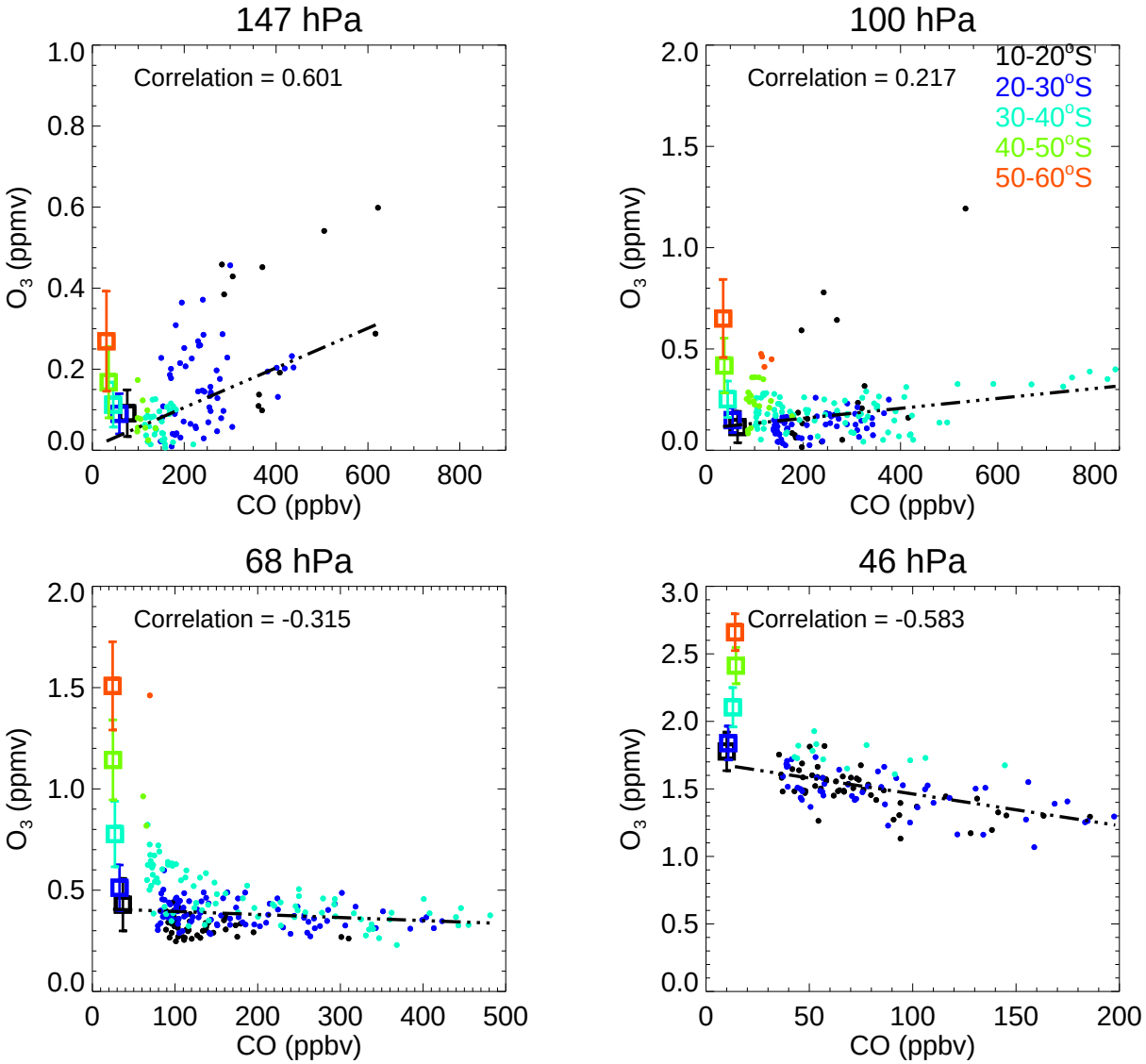

Figure 6.6: As in Figure 6.5 but with MLS data restricted to 60-330° longitude and DOY 39-60.

Table 6.1: Summary of MLS O_3 data as shown in Figure 6.6. The first half of the table lists 2008 background zonal means and corresponding 1-σ values. The second half are 2009 zonal mean and maximum values of O_3 within the smoke plume during February 2009. Bold values are 2009 O_3 zonal plume averages that are at or below the corresponding 2008 1-σ uncertainty range.

Lat Range	*2008 MLS background O_3 averages with 1-σ (ppmv)*			
	147 hPa	*100 hPa*	*68 hPa*	*46 hPa*
10-20°S	0.09±0.06	0.12±0.08	0.43±0.13	1.78±0.14
20-30°S	0.09±0.05	0.15±0.06	0.51±0.11	1.84±0.12
30-40°S	0.11±0.06	0.25±0.09	0.78±0.16	2.1±0.15
40-50°S	0.17±0.09	0.42±0.14	1.14±0.2	2.41±0.13
50-60°S	0.27±0.12	0.65±0.19	1.51±0.22	2.66±0.14
	2009 BS plume O_3 zonal mean/zonal maximum(ppmv)			
	147 hPa	*100 hPa*	*68 hPa*	*46 hPa*
10-20°S	0.34/0.6	0.29/1.19	0.32/0.44	**1.49**/1.82
20-30°S	0.16/0.47	0.12/0.26	**0.38**/0.6	**1.47**/1.74
30-40°S	**0.06**/0.13	0.19/0.4	**0.47**/0.82	**1.75**/1.93
40-50°S	**0.08**/0.17	**0.24**/0.36	**0.89**/0.96	n/a
50-60°S	n/a	**0.45**/0.48	1.46	n/a

To exclude CO pertubations from sources other than the smoke plume, MLS measurements were restricted to 60-330° longitude and to DOY 39-60, according to smoke plume observations presented thus far in this thesis. 2008 zonal mean values were adjusted to the same spatial and temporal range. The restricted MLS CO perturbations and co-located O_3 measurements in Figure 6.6 show a slightly increased positive correlation at 147-100 hPa and a slightly more negative correlation at 68 hPa. In the UT region in particular, this spatial and temporal restriction removes some of the anomolously high O_3 values seen

in Figure 6.5.

The 2008 MLS zonal mean O_3 values, as plotted in Figure 6.6 are listed in Table 6.1, together with the zonal averages and maximum values of the smoke plume O_3 measurements. Shown in bold, are plume zonal averages that are less than the lower limit of the 2008 1-σ uncertainty range. Statistically significant O_3 depletion is observed at most altitudes poleward of 30°S, and at almost all latitude ranges in the lower stratosphere (68-46 hPa). At 46 hPa, O_3 depletion within the smoke plume is statistically significant to a 95% confidence limit. This represents a percentage zonal mean decrease, with respect to the 2008 O_3 zonal mean (and 2009 zonal mean) over latitudes of 10-40°S, of 15-35%.

6.3.3 UTLS O_3 enhancement ratios

To further characterise ozone production or loss in biomass burning smoke plumes an enhancement ratio of $\Delta O_3/\Delta CO$ is often considered, with a positive (negative) value implying production (loss) [*Andreae and Merlet*, 2001];[*Jaffe and Wigder*, 2012]. Enhancement ratios are a ratio of excess concentrations of a chemical tracer (such as O_3), which can change as the plume ages and undergoes dilution or chemical mixing. An example of this, presented in *Glatthor et al.* [2013] in relation to the Black Saturday smoke plume, considered enhancement ratios of $\Delta C_2H_2/\Delta HCN$.

$\Delta O_3/\Delta CO$ ratios are considered up to the lower stratosphere, where ambient O_3 concentrations are much higher than ambient CO concentrations, so the ratios have a large range of values. Therefore, enhancement ratios found in this study are not to be directly compared with enhancement ratios found in tracer studies of tropospheric biomass burning plumes.

Enhancement ratios were obtained, for 3 distinct spatial and temporal periods, in conjunction with what was observed in Figures 6.3 and 6.6. These are shown in Table 6.2. At 46 hPa, ratios were obtained in two separate periods of DOY 48-56 and DOY 57-65. Each enhancement ratio value is an average over each time period within the specified latitude range. Background values for both sets of tracers were obtained from MLS measurements zonally averaged across 10° latitude bins, in the days leading up to the bushfire (DOY

1-37). Enhancement ratios are shown in units of ppbv/ppbv.

Table 6.2: Smoke plume net enhancement ratios ($\Delta O_3/\Delta CO$) zonally averaged over the DOY range listed for each pressure level. For 100 hPa and 68 hPa, the latitude range is 20-40°S and for 46 hPa, the latitude range is restricted to 10-30°S. Also shown are the number of data points used to obtain each mean enhancement ratio and the average background $\Delta O_3/\Delta CO$ values over DOY 1-37 in the specified latitude range. The 1-σ uncertainty range is shown for background and plume enhancement ratios. Ratios are in units of ppbv/ppbv.

Pressure	*Data points*	*DOY*	*Background O_3/CO*	$\Delta O_3/\Delta CO$
100 hPa	55	39-47	5±4.3	-0.25±0.3
68 hPa	66	40-50	25±12	-1.5±0.6
46 hPa	38	48-56	188±10	-4.6±1.7
	38	57-65		-6.6±1.5

These enhancement ratios suggest reduced O_3 loss within the smoke plume in the UTLS region with negative enhancement ratios found at all altitudes. In the unperturbed UTLS region, prior to the bushfire ignition, O_3/CO ratios increase with increasing pressure altitude. By 46 hPa, the ambient ratios are large because the stratospheric O_3 concentrations are almost 3 ppmv, whereas natural CO concentrations are approximately 15 ppbv. These mean ratios are statistically significant, particular in the LS, to at least a 95% confidence limit. Net enhancement ratios of the smoke plume at 100 hPa are negative, suggesting reduced O_3 within the smoke plume soon after ignition. However, this is not statistically significant.

When the smoke plume is located within the LS, statistically significant negative enhancements were found, indicating loss of O_3 within the smoke plume relative to the atmospheric background. At 46 hPa, two separate time periods were considered, with enhancement ratios suggesting continuing loss with respect to the background average. However, this does not necessarily signify further loss over time. CO values will continue to decrease with smoke dispersion, decreased O_3 concentrations within the smoke plume will recover to background stratospheric levels, thus increasing the magnitude of the ratio

calculated.

6.4 Discussion and conclusions

In this study, MLS CO data was used as a tracer to track the Black Saturday smoke plume within the UTLS region. Using these tracers provides a complimentary investigation to using OSIRIS radiance perturbations, outlined in previous chapters. CO perturbations that are 4.5 standard deviations above the 2008 zonal mean values in the UTLS region are used to identify the smoke plume at latitudes between 10-60°S, similar to the method used in *Pumphrey et al.* [2011].

Time series of high CO perturbations clearly illustrates the biomass burning plume ascending to progressively higher altitudes, reaching the mid-latitude lower stratosphere (LS) within a few days of ignition. CO tracers observe the smoke plume reaching 68 hPa by DOY 40 and 46 hPa a few days later. This highlights how quickly the smoke plume was vertically transported to the lower stratosphere after ignition, and that smoke pollution was observed for a sustained period at sub-equatorial latitudes. There is evidence that part of the smoke plume continued travelling eastward across the Pacific Ocean at lower altitudes and higher latitudes. Apart from the radiance perturbations presented in Chapter 4, there was also an indication of a secondary smoke plume reaching 45-55°S latitude in OSIRIS limb radiances, in agreement with MLS CO perturbations (see Figure 6.3). This is shown in the OSIRIS global radiance map for DOY 51 (20 February) at a tangent altitude of 17 km, shown in Figure 6.7. The global limb scattered radiance mean has been subtracted in order to highlight the radiance perturbations.

Radiance perturbations are observed west of South America at mid-latitudes, extending to almost 60°S. For comparison, Figure 6.8 shows MLS CO measurements for the same day and approximate altitude. A CO perturbation is observed near the tip of South America, coinciding with smoke aerosols observed as a radiance perturbation in Figure 6.7.

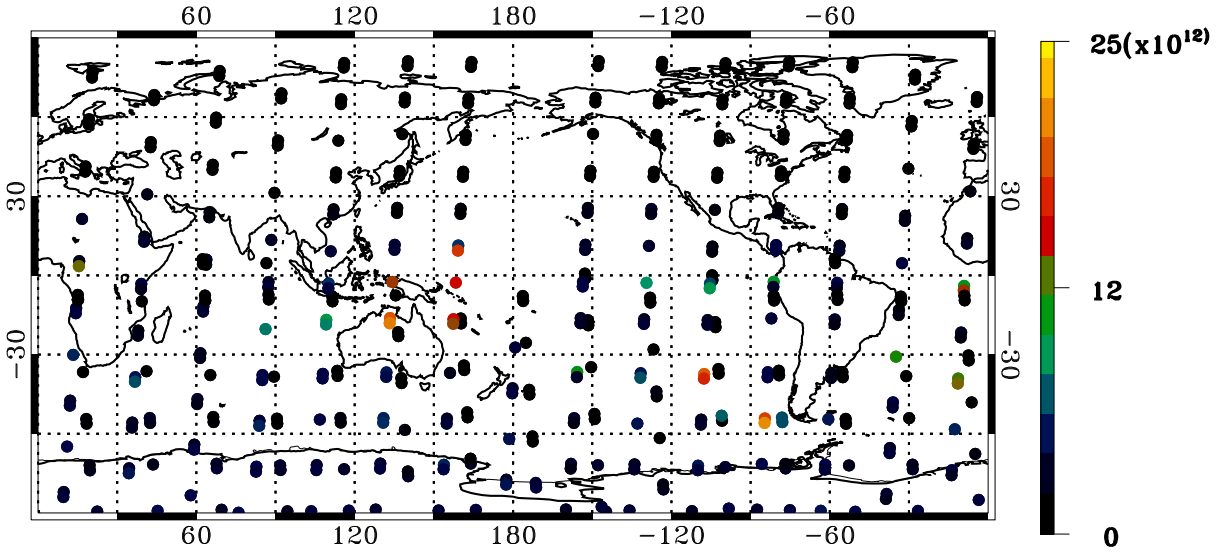

Figure 6.7: Global map of OSIRIS net limb radiances (in units of photons s^{-1} cm^{-2} nm^{-1} sr^{-1}) measured on 20 February 2009 (DOY 51) with global average removed. The scale of radiances is to the right of the plot.

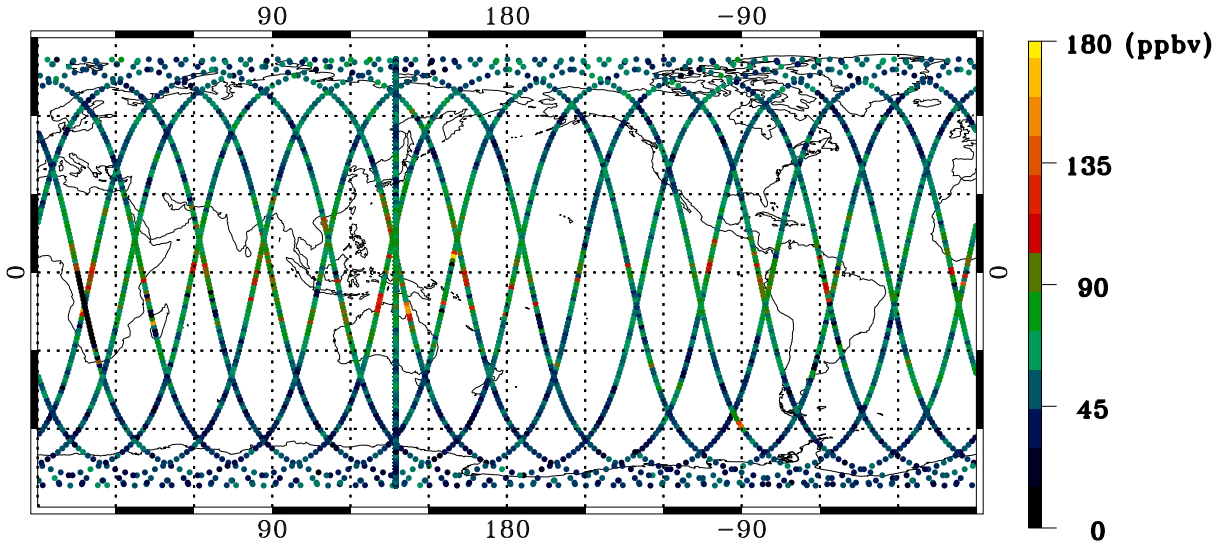

Figure 6.8: Global map of MLS CO measurements for the same day as Figure 6.7 at 100 hPa. The scale is shown on the colour bar at the right of the plot.

The observations presented in this study are supported by observations from the Michelson Interferometer for Passive Atmospheric Sounding (MIPAS) instrument onboard the Envisat platform [*Glatthor et al.*, 2013]. In *Glatthor et al.* [2013], satellite measurements of C_2H_2 and Formic Acid (HCOOH) enhancements were used to investigate the BS smoke

plume. Together with results from a tropospheric chemistry circulation model (GEM-AQ), they found that the lower section (in altitude) of the initial smoke plume had traveled eastward of south-east Australia, and the upper section of the plume had been transported equatorward and westward, in agreement with the observations found in Chapter 4. MIPAS observed the eastward traveling component of the plume had reached South America on 17 February, and the central South Atlantic on 20 February 2009 at around 15 km altitude.

Using high CO perturbations, co-located O_3 measurements were analysed and correlated with CO over pressure altitudes of 147 hPa to 46 hPa. Relative to zonal O_3 mean values from other years, decreased O_3 concentrations were observed. This decrease is statistically significant at LS altitudes (68-46 hPa), which was sustained over a few weeks until the end of February, and beyond. As previously reported, the smoke plume reached heights of at least 18-22 km, between 10-40°S, which means the smoke plume had advected to the lower boundary of the stratospheric ozone layer, located at heights of 20-30 km [*Brasseur and Solomon*, 2005]. With a large vertical gradient in background stratospheric O_3, MLS O_3 values within the smoke plume remain below background values in the LS, within a 1-σ uncertainty range.

At tropospheric altitudes (147-100 hPa), extremely high concentrations of CO are observed betwee 30-40°S, with peak values of 500 ppbv at 147 hPa (DOY 39) and 800 ppbv at 100 hPa (DOY 41). At 147 hPa, corresponding MLS O_3 values do not pass the quality criteria set out in *Livesey et al.* [2011]. This is probably due to MLS data screening procedures treating the optically thick smoke plume as a cloud, Reliable O_3 data becomes available at 147 hPa, once CO concentrations are at around 200 ppbv on DOY 41. The few ozone data points within the smoke plume after DOY 41 at this altitude, are initially lower than 2008 O_3 background concentrations, but quickly return to within the range of natural variability.

When the plume is observed at 100 hPa on 10 February (DOY 41), as seen by the cluster of high CO values (500-800 ppbv) in Figure 6.3, O_3 concentrations are between 0.35-0.4 ppmv, compared with a latitudunal 2008 average of 0.25 ± 0.1 ppmv. The 3-day old smoke

plume is at the upper uncertainty range of background O_3 levels. In the following days (DOY 42-47), O_3 varies considerably within this latitude range, between 0.05-0.3 ppmv, whilst CO concentrations are still above 200 ppbv. Therefore no statistically significant trend in O_3 was found at SH mid-latitudes within the UT region from MLS measurements.

O_3 values within the smoke plume suggest that entrained ozone-poor air parcels have been transported from the UT region into the LS region. In Chapter 5, a combination of OSIRIS radiance measurements and MLS H_2O VMR values suggest there was increased water vapour associated with the smoke plume from DOY 40-44 of more than a 150% and that this hydrated air was transported to the LS in the days following. *Real et al.* [2007], in a study of long-range transport of a smoke plume using aircraft measurements and a photochemistry trajectory model, found that smoke aerosols slowed down photolysis rates within smoke plumes, inhibiting initial O_3 production. Additionally high water vapour content and high temperatures, when introduced into their trajectory model, slowed down O_3 production along the plume path. Based on the very high radiance values from OSIRIS measurements and initial large water concentrations within the smoke plume, this would suggest inhibited O_3 production has occurred within the optically thick smoke plume.

Based on MLS O_3 zonal averages from 2008, O_3 zonal mean values within the smoke plume were within 2 standard deviations of background variability at LS mid-latitudes. These smoke concentrations were averaged between DOY 39-60 as shown in Table 6.1. Whilst there is uncertainty in any reduced O_3 in the troposphere, there is clear evidence of reduced O_3 above the tropopause. However, the smoke did quickly advect up to the stratosphere and did not remain in the UT region for longer than a few days.

Once it had penetrated the tropopause, where ambient O_3 concentrations naturally increase, the smoke plume underwent gradual dispersion and mixing with the surrounding stratosphere. O_3 concentrations within the smoke plume gradually recover to latitudinal background values by the end of the analysis period. MLS CO perturbations associated with smoke pollution from the Black Saturday bushfires were observed over an extended period of time within the sub-equatorial LS, until at least DOY 70, over 4 weeks after ignition.

In conclusion, OSIRIS radiance observations of the Black Saturday pyrocb event found that smoke material penetrated the tropopause within a few days of ignition and was transported around the globe in 6 weeks from ignition, with observable stratospheric radiance perturbations from smoke aerosols lasting for several months. Both MLS and OSIRIS observations found that the smoke plume had reached at least 21 km in altitude, the highest ever recorded for such an event. Such extreme vertical advection of surface emissions was previously thought to have only been possible through the extreme energy release of major volcanic eruptions. Air parcels containing increased water vapour and decreased ozone concentrations were injected into the lower stratosphere at SH mid-latitudes; perturbing atmospheric chemistry for a period of weeks following ignition. This provided a unique opportunity to observe a troposphere-stratosphere exchange that has not been observed in previous studies.

Bibliography

Akiyoshi, H., et al. (2009), A CCM simulation of the breakup of the Antarctic polar vortex in the years 1980-2004 under the CCMVal scenarios, *J. Geophys. Res.*, *114*, D03103, doi:10.1029/2007JD009261.

Alvarado, M., and R. G. Prinn (2009), Formation of ozone and growth of aerosols in young smoke plumes from biomass burning: 1. Langrangian parcel studies, *J. Geophys. Res.*, *114*, D09,306, doi:10.1029/2008JD011144.

Anderson, J. G., D. W. Toohey, and W. H. Brune (1991), Free Radicals Within the Antarctic Vortex: The Role of CFCs in Antarctic Ozone Loss, *Science*, *251*, 39–46, doi:10.1126/science.251.4989.39.

Andersson, S. M., B. G. Martinsson, J. Friberg, C. A. M. Brenninkmeijer, A. Rauthe-Schöch, M. Hermann, P. F. J. van Velthoven, and A. Zahn (2013), Composition and evolution of volcanic aerosol from eruptions of Kasatochi, Sarychev and Eyjafjallajökull in 2008-2010 based on CARIBIC observations, *Atmos. Chem. Phys.*, *13*, 1781–1796, doi:10.5194/acp-13-1781-2013.

Andreae, M. O. (1991), Biomass burning: Its history, use, and distribution and its impact on environmental quality and global climate, in *Global Biomass Burning: Atmospheric, Climatic, and Biospheric implications*, edited by Levine, J. S, pp. 3–21, MIT Press.

Andreae, M. O., and P. Merlet (2001), Emission of trace gases and aerosols from biomass burning, *Global Biogeochem. Cycles*, *15*, 955–966.

Atkinson, R. (2000), Atmospheric chemistry of VOCs and NO_x, *Atmos. Environ.*, *34*, 2063–2101, doi:10.1016/S1352-2310(99)00460-4.

Austin, J., et al. (2010a), Chemistry-climate model simulations of spring Antarctic ozone, *J. Geophys. Res.*, *115*, D00M11, doi:10.1029/2009JD013577.

Austin, J., et al. (2010b), Decline and recovery of total column ozone using a multimodel time series analysis, *J. Geophys. Res.*, *115*, D00M10, doi:10.1029/2010JD013857.

Baldwin, M. P., et al. (2001), The Quasi-Biennial Oscillation, *Rev. Geophys.*, *39*, 179–229, doi:10.1029/1999RG000073.

Bates, D. R., and M. Nicolet (1950), Atmospheric hydrogen, *Astronomical Society of the Pacific*, *62*, 106–110.

Bernath, P. F., et al. (2005), Atmospheric Chemistry Experiment (ACE): Mission overview, *Geophys. Res. Lett*, *32*, L15S01, doi:10.1029/2005GL022386.

Bertschi, I. T., and D. A. Jaffe (2005), Long-range transport of ozone, carbon monoxide, and aerosols to the NE Pacific troposphere during the summer of 2003: Observations of smoke plumes from Asian boreal fires, *J. Geophys. Res*, *110*, D05303, doi: 10.1029/2004JD005135.

Bluth, G. J. S., S. D. Doiron, C. C. Schnetzler, A. J. Krueger, and L. S. Walter (1992), Global tracking of the SO_2 clouds from the June, 1991 Mount Pinatubo eruptions, *Geophys. Res. Lett*, *19*, 151–154, doi:10.1029/91GL02792.

Bourassa, A. E., D. A. Degenstein, and E. J. Llewellyn (2005), Climatology of the subvisual cirrus clouds as seen by OSIRIS on Odin, *Adv. Space. Res.*, *36*, 807–812, doi: 10.1016/j.asr.2005.05.045.

Bourassa, A. E., D. A. Degenstein, R. L. Gattinger, and E. J. Llewellyn (2007), Stratospheric aerosol retrieval with optical spectrograph and infrared imaging system limb scatter measurements, *J. Geophys. Res.*, *112*, D10217, doi:10.1029/2006JD008079.

Bourassa, A. E., D. A. Degenstein, and E. J. Llewellyn (2008), SASKTRAN: A spherical geometry radiative transfer code for efficient estimation of limb scattered sunlight, *J. Quant. Spectrosc. Radiat. Trans.*, *109*, 52–73, doi:10.1016/j.jqsrt.2007.07.007.

Bourassa, A. E., D. A. Degenstein, B. J. Elash, and E. J. Llewellyn (2010), Evolution of the stratospheric aerosol enhancement following the eruptions of Okmok and Kasatochi: Odin-OSIRIS measurements, *J. Geophys. Res.*, *115*, D00L03, doi: 10.1029/2009JD013274.

Bourassa, A. E., A. Robock, J. Randel, W, T. Deshler, L. A. Rieger, N. D. Lloyd, E. J. Llewellyn, and D. A. Degenstein (2012), Large Volcanic Aerosol Load in the Stratosphere Linked to Asian Monsoon Transport, *Science*, *337*(6090), 78–81, doi: 10.1126/science.1219371.

Brasseur, G., and M. H. Hitchman (1988), Stratospheric response to trace gas perturbations: Changes in ozone and temperature distributions, *Science*, *240*, 634–637, doi: 10.1126/science.240.4852.634.

Brasseur, G. P., and S. Solomon (2005), *Aeronomy of the Middle Atmosphere: Chemistry and Physics of the Stratosphere and Mesosphere*, Springer.

Brewer, A. W. (1949), Evidence for a world circulation provided by the measurements of helium and water vapour distribution in the stratosphere, *Q.J.R. Meteorol. Soc.*, *75*, 351–363, doi:10.1002/qj.49707532603.

Brown, A. T., M. P. Chipperfield, N. A. D. Richards, C. Boone, and P. F. Bernath (2014), Global stratospheric fluorine inventory for 2004-2009 from Atmospheric Chemistry Experiment Fourier Transform Spectrometer (ACE-FTS) measurements and SLIMCAT model simulations, *Atmos. Chem. Phys.*, *14*, 267–282, doi:10.5194/acp-14-267-2014.

Butchart, N., and A. A. Scaife (2001), Removal of chlorofluorocarbons by increased mass exchange between the stratosphere and troposphere in a changing climate, *Nature*, *410*, 799–802.

Chapman, S. (1930), On ozone and atomic oxygen in the upper atmosphere, *Philos. Mag*, *10*, 369–383.

Charlton-Perez, A. J., et al. (2010), The potential to narrow uncertainty in projections of stratospheric ozone over the 21st century, *Atmos. Chem. Phys.*, *10*, 9473–9486.

Charney, J. G., and P. G. Drazin (1961), Propagation of planetary-scale disturbances from the lower into the upper atmosphere, *J. Geophys. Res.*, *66*, 83–109, doi: 10.1029/JZ066i001p00083.

Chepfer, H., and V. Noel (2009), A tropical "NAT-like" belt observed from space, *Geophys. Res. Lett*, *36*, L03813, doi:10.1029/2008GL036289.

Choi, W. (1998), Role of the Quasi-Biennial Oscillation in the transport of aerosols from the tropical stratospheric reservoir to midlatitudes, *J. Geophys. Res*, *103*, 6033–6042, doi:10.1029/97JD03118.

Cordero, E., P. A. Newman, C. Weaver, and E. Fleming (2013), The Stratospheric Ozone Electronic Textbook, chapter 11.

Crutzen, P. J. (1970), The influence of nitrogen oxide on the atmospheric ozone content, *Q.J.R. Meteorol. Soc.*, *96*, 320–327.

Crutzen, P. J. (1974), Estimates of possible future ozone reductions from continued use of fluoro-chloro-methanes (CF_2Cl_2, $CFCl_3$), *Geophys. Res. Lett*, *1*, 205–208, doi: 10.1029/GL001i005p00205.

Crutzen, P. J., and M. O. Andreae (1990), Biomass burning in the tropics: Impact on atmospheric chemistry and biogeochemical cycles, *Science*, *250*(4988), 1669–1678.

Daniau, A.-L., et al. (2012), Predictability of biomass burning in response to climate changes, *Global Biogeochem. Cycles*, *26*, GB4007, doi:10.1029/2011GB004249.

de F. Forster, P. M., and K. P. Shine (1999), Stratospheric water vapor changes as a possible contributor to observed stratospheric cooling, *Geophys. Res. Lett*, *26*, 3309–3312, doi:10.1029/1999GL010487.

Dee, D. P., et al. (2011), The ERA-Interim reanalysis: configuration and performance of the data assimilation system, *Q.J.R. Meteorol. Soc.*, *137*, 553–597.

Del Negro, L. A., et al. (1997), Evaluating the role of NAT, NAD, and liquid $H_2SO_4/H_2O/HNO_3$ solutions in Antarctic polar stratospheric cloud aerosol: Observations and implications, *J. Geophys. Res.*, *102*, D11, doi:10.1029/97JD00764.

Deshler, T. (2008), A review of global stratospheric aerosol: Measurements, importance, life cycle, and local stratospheric aerosol, *Atmos. Res.*, *90*, 223–232, doi: 10.1016/j.atmosres.2008.03.016.

Deshler, T., et al. (2006), Trends in the nonvolcanic component of stratospheric aerosol over the period 1971-2004, *J. Geophys. Res.*, *111*, D01201, doi:10.1029/2005JD006089.

Dessler, A. E., and S. C. Sherwood (2004), Effect of convection on the summertime extratropical lower stratosphere, *J. Geophys. Res.*, *109*, D23301, doi:10.1029/2004JD005209.

Deushi, M., and K. Shibata (2011), Impacts of increases in greenhouse gases and ozone recovery on lower stratospheric circulation and the age of air: Chemistry-climate model simulations up to 2100, *J. Geophys. Res*, *116*, D07,107, doi:10.1029/2010JD015024.

Dirksen, R. J., K. Folkert Boersma, J. de Laat, P. Stammes, G. R. van der Werf, M. Val Martin, and H. M. Kelder (2009), An aerosol boomerang: Rapid around-the-world transport of smoke from the December 2006 Australian forest fires observed from space, *J. Geophys. Res.*, *114*, D21201, doi:10.1029/2009JD012360.

Dobson, G. M. B. (1956), Origin and distribution of the polyatomic molecules in the atmosphere, *Royal Society of London Proceedings Series A*, *236*, 187–193, doi: 10.1098/rspa.1956.0127.

Dobson, G. M. B., H. H. Kimball, and E. Kidson (1930), Observations of the amount of ozone in the Earth's atmosphere, and Its relation to other geophysical conditions. Part IV, *Royal Society of London Proceedings Series A*, *129*, 411–433, doi: 10.1098/rspa.1930.0165.

Draxler, R. R., and G. D. Hess (1998), An overview of the HYSPLIT-4 modelling system for trajectories, *Australian Meteorological Magazine*, *47*(4), 295–308.

Duncan, B. N., R. V. Martin, A. C. Staudt, R. Yevich, and J. A. Logan (2003), Interannual and seasonal variability of biomass burning emissions constrained by satellite observations, *J. Geophys. Res.*, *108*, D2, doi:10.1029/2002JD002378.

Dunlap, W. P., and N. C. Silver (1986), Confidence intervals and standard errors for ratios of normal variables, *Behavior Research Methods, Instruments, & Computers*, *18*(5), 469–471, doi:10.3758/BF03201412.

Edwards, D. P., et al. (2006), Satellite-observed pollution from Southern Hemisphere biomass burning, *J. Geophys. Res.*, *111*, D14312, doi:10.1029/2005JD006655.

Eremenko, M. N., S. V. Petelina, A. Y. Zasetsky, B. Karlsson, C. P. Rinsland, E. J. Llewellyn, and J. J. Sloan (2005), Shape and composition of PMC particles derived from satellite remote sensing measurements, *Geophys. Res. Lett*, *32*, L16S06, doi: 10.1029/2005GL023013.

Evtushevsky, O. M., A. V. Grytsai, A. R. Klekociuk, and G. P. Milinevsky (2008), Total ozone and tropopause zonal asymmetry during the Antarctic spring, *J. Geophys. Res.*, *113*, D00B06, doi:10.1029/2008JD009881.

Eyring, V., et al. (2007), Multimodel projections of stratospheric ozone in the 21st century, *J. Geophys. Res.*, *112*, D16303, doi:10.1029/2006JD008332.

Eyring, V., T. G. Shepherd, and D. W. Waugh (Eds.) (2010a), *SPARC CCMVal Report on the Evaluation of Chemistry-Climate Models*, SPARC Report No. 5, WCRP-132, WMO/TD-No. 1526.

Eyring, V., et al. (2010b), Sensitivity of 21st century stratospheric ozone to greenhouse gas scenarios, *Geophys. Res. Lett*, *37*, doi:10.1029/2010GL044443.

Eyring, V., et al. (2010c), Multi-model assessment of stratospheric ozone return dates and ozone recovery in CCMVal-2 models, *Atmos. Chem. Phys.*, *10*, 9451–9472.

Eyring, V., et al. (2013), Long-term ozone changes and associated climate impacts in CMIP5 simulations, *J. Geophys. Res.*, *118*, 5029–5060, doi:10.1002/jgrd.50316.

Farman, J. C., B. G. Gardner, and J. D. Shanklin (1985), Large losses of total ozone in Antarctica reveal seasonal ClO_x/NO_x interaction, *Nature*, *315*, 207–210.

Finger, F. G., R. M. Nagatani, M. E. Gelman, C. S. Long, and A. J. Miller (1995), Consistency between variations of ozone and temperature in the stratosphere, *Geophys. Res. Lett*, *22*, 3477–3480.

Fioletov, V. E., and T. G. Shepherd (2003), Seasonal persistence of midlatitude total ozone anomalies, *Geophys. Res. Lett*, *30*, 1417, doi:10.1029/2002GL016739.

Folkins, I., R. Chatfield, D. Baumgardner, and M. Proffitt (1997), Biomass burning and deep convection in southeastern Asia: Results from ASHOE/MAESA, *J. Geophys. Res.*, *102*, D11, doi:10.1029/96JD03711.

Forster, C., et al. (2001), Transport of boreal forest fire emissions from Canada to Europe, *J. Geophys. Res.*, *106*, 22,887–22,906, doi:10.1029/2001JD900115.

Froidevaux, L., et al. (2006), Temporal decrease in upper atmospheric chlorine, *Geophys. Res. Lett*, *33*, L23812, doi:10.1029/2006GL027600.

Fromm, M., J. Alfred, K. Hoppel, J. Hornstein, R. Bevilacqua, E. Shettle, R. Servranckx, Z. Li, and B. Stocks (2000), Observations of boreal forest fire smoke in the stratosphere by POAM III, SAGE II, and lidar in 1998, *Geophys. Res. Lett*, *27*, 1407–1410, doi: 10.1029/1999GL011200.

Fromm, M., R. Bevilacqua, R. Servranckx, J. Rosen, J. P. Thayer, J. Herman, and D. Larko (2005), Pyro-cumulonimbus injection of smoke to the stratosphere: Observations and impact of a super blowup in northwestern Canada on 3-4 August 1998, *J. Geophys. Res.*, *110*, D08205, doi:10.1029/2004JD005350.

Fromm, M., A. Tupper, D. Rosenfeld, R. Servranckx, and R. McRae (2006), Violent pyroconvective storm devastates Australia's capital and pollutes the stratosphere, *Geophys. Res. Lett*, *33*, L05815, doi:10.1029/2005GL025161.

Fromm, M., O. Torres, D. Diner, D. Lindsey, B. vant Hull, R. Servranckx, E. P. Shettle, and Z. Li (2008a), Stratospheric impact of the Chisholm pyrocumulonimbus eruption: 1. Earth-viewing satellite perspective, *J. Geophys. Res.*, *113*, D08202, doi:10.1029/2007JD009153.

Fromm, M., et al. (2008b), Stratospheric impact of the Chisholm pyrocumulonimbus eruption: 2. Vertical profile perspective, *J. Geophys. Res.*, *113*, D08203, doi:10.1029/2007JD009147.

Fromm, M., D. T. Lindsey, R. Servranckx, G. Yue, T. Trickl, R. Sica, P. Doucet, and S. Godin-Beekmann (2010), The untold Story of Pyrocumulonimbus, *Bulletin of the American Meteorological Society*, *91*, 1193–1209, doi:10.1175/2010BAMS3004.1.

Fromm, M., G. Nedoluha, and Z. Charvát (2013), Comment on "Large Volcanic Aerosol Load in the Stratosphere Linked to Asian Monsoon Transport", *Science*, *339*, 647–647, doi:10.1126/science.1228605.

Fromm, M. D., and R. Servranckx (2003), Transport of forest fire smoke above the tropopause by supercell convection, *Geophys. Res. Lett*, *30*(10), 1542, doi:10.1029/2002GL016820.

Fueglistaler, S. (2012), Stepwise changes in stratospheric water vapor?, *J. Geophys. Res.*, *117*(D16), D13302, doi:10.1029/2012JD017582.

Fueglistaler, S., and P. H. Haynes (2005), Control of interannual and longer-term variability of stratospheric water vapor, *J. Geophys. Res.*, *110*(D9), D24108, doi:10.1029/2005JD006019.

Fueglistaler, S., M. Bonazzola, P. H. Haynes, and T. Peter (2005), Stratospheric water vapor predicted from the Lagrangian temperature history of air entering the stratosphere in the tropics, *J. Geophys. Res.*, *110*, D08107, doi:10.1029/2004JD005516.

Gabriel, A., H. Körnich, S. Lossow, D. H. W. Peters, J. Urban, and D. Murtagh (2011), Zonal asymmetries in middle atmospheric ozone and water vapour derived from Odin satellite data 2001-2010, *Atmos. Chem. Phys.*, *11*, 9865–9885, doi:10.5194/acp-11-9865-2011.

Galanter, M., H. Levy, and G. R. Carmichael (2000), Impacts of biomass burning on tropospheric CO, NO_x, and O_3, *J. Geophys. Res.*, *105*, 6633–6653, doi:10.1029/1999JD901113.

Garcia, R. R., D. E. Kinnison, and D. R. Marsh (2012), "World avoided" simulations with the Whole Atmosphere Community Climate Model, *J. Geophys. Res.*, *117*, D23303, doi:10.1029/2012JD018430.

Garny, H., M. Dameris, W. Randel, G. E. Bodeker, and R. Deckert (2011), Dynamically forced increase of tropical upwelling in the lower stratosphere, *J. Atmos. Sci.*, *68*, 1214–1233, doi:10.1175/2011JAS3701.1.

Gettelman, A., P. H. Lauritzen, M. Park, and J. E. Kay (2009), Processes regulating short-lived species in the tropical tropopause layer, *J. Geophys. Res.*, *114*, D13303, doi:10.1029/2009JD011785.

Gettelman, A., P. Hoor, L. L. Pan, W. J. Randel, M. I. Hegglin, and T. Birner (2011), The extratropical Upper Troposphere and Lower Stratosphere, *Rev. Geophys.*, *49*, RG3003, doi:10.1029/2011RG000355.

Gillett, N. P., J. F. Scinocca, D. A. Plummer, and M. C. Reader (2009), Sensitivity of climate to dynamically-consistent zonal asymmetries in ozone, *Geophys. Res. Lett*, *36*, L10809, doi:10.1029/2009GL037246.

Glatthor, N., et al. (2013), The Australian bushfires of February 2009: MIPAS observations and GEM-AQ model results, *Atmos. Chem. Phys.*, *13*, 1637–1658, doi:10.5194/acp-13-1637-2013.

Gonzi, S., and P. I. Palmer (2010), Vertical transport of surface fire emissions observed from space, *J. Geophys. Res.*, *115*, D02306, doi:10.1029/2009JD012053.

Goode, J. G., R. J. Yokelson, D. E. Ward, R. A. Susott, R. E. Babbitt, M. A. Davies, and W. M. Hao (2000), Measurements of excess O3, CO2, CH4, C2H4, C2H2, HCN, NO, NH3, HCOOH, CH3COOH, HCHO, and CH3H in 1997 Alaskan biomass burning plumes by Airborne Fourier Transform Infrared Spectroscopy (AFTIR) , *J. Geophys. Res.*, *105*, D22,147, doi:10.1029/2000JD900287.

Grant, W. B., E. V. Browell, C. S. Long, L. L. Stowe, R. G. Grainger, and A. Lambert (1996), Use of volcanic aerosols to study the tropical stratospheric reservoir, *J. Geophys. Res*, *101*, 3973–3988, doi:10.1029/95JD03164.

Gray, L. J. (2010), Stratospheric Equatorial Dynamics, *Washington DC American Geophysical Union Geophysical Monograph Series*, *190*, 93–107.

Griffin, R. J., D. R. Cocker, R. C. Flagan, and J. H. Seinfeld (1999), Organic aerosol formation from the oxidation of biogenic hydrocarbons, *J. Geophys. Res*, *104*, 3555–3567, doi:10.1029/1998JD100049.

Griffioen, E., and L. Oikarinen (2000), LIMBTRAN: A pseudo three-dimensional radiative transfer model for the limb-viewing imager OSIRIS on the ODIN satellite, *J. Geophys. Res*, *105*, 29,717–29,730, doi:10.1029/2000JD900566.

Grytsai, A. V., O. M. Evtushevsky, O. V. Agapitov, A. R. Klekociuk, and G. P. Milinevsky (2007), Structure and long-term change in the zonal asymmetry in antarctic total ozone during spring, *Ann. Geophys.*, *25*, 361–374.

Hagan, D. E., C. R. Webster, C. B. Farmer, R. D. May, R. L. Herman, E. M. Weinstock, L. E. Christensen, L. R. Lait, and P. A. Newman (2004), Validating AIRS upper atmosphere water vapor retrievals using aircraft and balloon in situ measurements, *Geophys. Res. Lett*, *31*, L21103, doi:10.1029/2004GL020302.

Hamill, P., E. J. Jensen, P. B. Russell, and J. J. Bauman (1997), The life cycle of stratospheric aerosol particles., *Bulletin of the American Meteorological Society*, *78*, 1395–1410.

Hassler, B., J. S. Daniel, B. J. Johnson, S. Solomon, and S. J. Oltmans (2011), An assessment of changing ozone loss rates at South Pole: Twenty-five years of ozonesonde measurements, *J. Geophys. Res.*, *116*, D22,301, doi:10.1029/2011JD016353.

Haynes, P. H., M. E. McIntyre, T. G. Shepherd, C. J. Marks, and K. P. Shine (1991), On the 'Downward Control' of extratropical diabatic circulations by eddy-induced mean zonal forces., *J. Atmos. Sci.*, *48*, 651–680, doi:10.1175/1520-0469(1991)048¡0651:OTCOED¿2.0.CO;2.

Haywood, J., and O. Boucher (2000), Estimates of the direct and indirect radiative forcing due to tropospheric aerosols: A review, *Rev. Geophys.*, *38*, 513–543, doi:10.1029/1999RG000078.

Hegglin, M. I., C. D. Boone, G. L. Manney, T. G. Shepherd, K. A. Walker, P. F. Bernath, W. H. Daffer, P. Hoor, and C. Schiller (2008), Validation of ACE-FTS satellite data in the upper troposphere/lower stratosphere (UTLS) using non-coincident measurements, *Atmos. Chem. Phys.*, *8*, 1483–1499.

Hegglin, M. I., et al. (2014), Vertical structure of stratospheric water vapour trends derived from merged satellite data, *Nature Geoscience*, *7*, 768–776, doi:10.1038/ngeo2236.

Hitchman, M. H., M. McKay, and C. R. Trepte (1994), A climatology of stratospheric aerosol, *J. Geophys. Res*, *99*, 20,689, doi:10.1029/94JD01525.

Hofmann, D. J., and T. Deshler (1989), Comparison of stratospheric clouds in the Antarctic and the Arctic, *Geophys. Res. Lett*, *16*, 1429–1432, doi:10.1029/GL016i012p01429.

Hofmann, D. J., and S. J. Oltmans (1993), Anomalous Antarctic ozone during 1992: Evidence for Pinatubo volcanic aerosol effects, *J. Geophys. Res*, *98*, 18,555, doi:10.1029/93JD02092.

Hofmann, D. J., S. J. Oltmans, J. M. Harris, B. J. Johnson, and J. A. Lathrop (1997), Ten years of ozonesonde measurements at the south pole: implications for recovery of springtime Antarctic ozone, *J. Geophys. Res*, *102*, 8931–8944.

Holton, J. R., and A. Gettelman (2001), Horizontal transport and the dehydration of the stratosphere, *Geophys. Res. Lett*, *28*, 2799–2802, doi:10.1029/2001GL013148.

Holton, J. R., and H.-C. Tan (1980), The Influence of the equatorial Quasi-Biennial Oscillation on the global circulation at 50 mb., *J. Atmos. Sci.*, *37*, 2200–2208, doi: 10.1175/1520-0469(1980)037¡2200:TIOTEQ¿2.0.CO;2.

Holton, J. R., and H.-C. Tan (1982), The Quasi-Biennial Oscillation in the northern hemisphere lower stratosphere, *J. Meteor. Soc. Jpn.*, *60*(1), 140–148.

Holton, J. R., P. H. Haynes, M. E. McIntyre, A. R. Douglass, R. B. Rood, and L. Pfister (1995), Stratosphere-troposphere exchange, *Rev. Geophys.*, *33*, 403–439.

Honrath, R. E., R. C. Owen, M. Val MartíN, J. S. Reid, K. Lapina, P. Fialho, M. P. Dziobak, J. Kleissl, and D. L. Westphal (2004), Regional and hemispheric impacts of anthropogenic and biomass burning emissions on summertime CO and O_3 in the North Atlantic lower free troposphere, *J. Geophys. Res*, *109*, D24310, doi:10.1029/2004JD005147.

Ialongo, I., V. Sofieva, N. Kalakoski, J. Tamminen, and E. Kyrölä (2012), Ozone zonal asymmetry and planetary wave characterization during Antarctic spring, *Atmos. Chem. Phys.*, *12*, 2603–2614, doi:10.5194/acp-12-2603-2012.

Inness, A., et al. (2013), The MACC reanalysis: an 8 yr data set of atmospheric composition, *Atmos. Chem. Phys.*, *13*, 4073–4109, doi:10.5194/acp-13-4073-2013.

Jaffe, D., I. Bertschi, L. Jaeglé, P. Novelli, J. S. Reid, H. Tanimoto, R. Vingarzan, and D. L. Westphal (2004), Long-range transport of Siberian biomass burning emissions and impact on surface ozone in western North America, *Geophys. Res. Lett*, *31*, L16106, doi: 10.1029/2004GL020093.

Jaffe, D. A., and N. L. Wigder (2012), Ozone production from wildfires: A critical review, *Atmos. Environ.*, *51*, 1–10, doi:10.1016/j.atmosenv.2011.11.063.

Johns, T. C., et al. (2006), The New Hadley Centre Climate Model (HadGEM1): Evaluation of Coupled Simulations, *J. Climate*, *19*(7), 1327–1353.

Jones, A. E., and J. D. Shanklin (1995), Continued decline of total ozone over Halley, Antarctica, since 1985, *Nature*, *376*, 409–411.

Jost, H.-J., et al. (2004), In-situ observations of mid-latitude forest fire plumes deep in the stratosphere, *Geophys. Res. Lett*, *31*, L11101, doi:10.1029/2003GL019253.

Junge, C. E., C. W. Chagnon, and J. E. Manson (1961), Stratospheric aerosols., *J. Atmos. Sci.*, *18*, 81–108, doi:10.1175/1520-0469(1961)018¡0081:SA¿2.0.CO;2.

Kamide, Y., and K. Kusano (2013), Is something wrong with the present Solar Maximum?, *Space Weather*, *11*, 140–141, doi:10.1002/swe.20045.

Kiedron, P., J. Berndt, J. Michalsky, and L. Harrison (2003), Column water vapor from diffuse irradiance, *Geophys. Res. Lett*, *30*(11), 1565, doi:10.1029/2003GL016874.

Klekociuk, A. R., et al. (2011), The Antarctic ozone hole during 2010, *Aust. Met. Ocean. Journal*, *61*, 253–267.

Knight, J. R., J. Austin, R. G. Grainger, and A. Lambert (1998), A three-dimensional model simulation of the impact of Mt. Pinatubo aerosol on the Antarctic ozone hole, *Q.J.R. Meteorol. Soc.*, *124*, 1527–1558, doi:10.1002/qj.49712454909.

Ko, W., M. K, P. A. Newman, S. Reimann, and S. E. Strahan (Eds.) (2013), *Lifetimes of stratospheric ozone-depleting substances, their replacements, and related species*, SPARC Report No.6, WCRP-15/2013.

Konovalov, I. B., M. Beekmann, B. D'Anna, and C. George (2012), Significant light induced ozone loss on biomass burning aerosol: Evidence from chemistry-transport modeling based on new laboratory studies, *Geophys. Res. Lett*, *39*, L17807, doi: 10.1029/2012GL052432.

Kuroda, Y., and K. Yamazaki (2010), Influence of the solar cycle and QBO modulation on the Southern Annular Mode, *Geophys. Res. Lett*, *37*, L12703, doi: 10.1029/2010GL043252.

Lambert, A., R. G. Grainger, J. J. Remedios, C. D. Rodgers, M. Corney, and F. W. Taylor (1993), Measurements of the evolution of the Mt. Pinatubo aerosol cloud by ISAMS, *Geophys. Res. Lett*, *20*, 1287–1290, doi:10.1029/93GL00827.

Langmann, B., B. Duncan, C. Textor, J. Trentmann, and G. R. van der Werf (2009), Vegetation fire emissions and their impact on air pollution and climate, *Atmos. Environ.*, *43*, 107–116, doi:10.1016/j.atmosenv.2008.09.047.

Lary, D. J., D. W. Waugh, A. R. Douglass, R. S. Stolarski, P. A. Newman, and H. Mussa (2007), Variations in stratospheric inorganic chlorine between 1991 and 2006, *Geophys. Res. Lett*, *34*, L21811, doi:10.1029/2007GL030053.

Lavoué, D., C. Liousse, H. Cachier, B. J. Stocks, and J. G. Goldammer (2000), Modeling of carbonaceous particles emitted by boreal and temperature wildfires at northern latitudes, *J. Geophys. Res.*, *105*, D26,871, doi:10.1029/2000JD900180.

Lee, A. M., H. K. Roscoe, A. E. Jones, P. H. Haynes, E. F. Shuckburgh, M. W. Morrey, and H. C. Pumphrey (2001), The impact of the mixing properties within the Antarctic stratospheric vortex on ozone loss in spring, *J. Geophys. Res.*, *106*, 3203–3211.

Leung, F.-Y. T., J. A. Logan, R. Park, E. Hyer, E. Kasischke, D. Streets, and L. Yurganov (2007), Impacts of enhanced biomass burning in the boreal forests in 1998 on tropospheric chemistry and the sensitivity of model results to the injection height of emissions, *J. Geophys. Res.*, *112*, D10313, doi:10.1029/2006JD008132.

Lin, J. C., T. Matsui, R. A. Pielke, and C. Kummerow (2006), Effects of biomass-burning-derived aerosols on precipitation and clouds in the Amazon Basin: a satellite-based empirical study, *J. Geophys. Res.*, *111*, D19204, doi:10.1029/2005JD006884.

Liu, C., E. Zipser, T. Garrett, J. H. Jiang, and H. Su (2007), How do the water vapor and carbon monoxide "tape recorders" start near the tropical tropopause?, *Geophys. Res. Lett*, *34*, L09804, doi:10.1029/2006GL029234.

Liu, X. M., E. D. Rivière, V. Marécal, G. Durry, A. Hamdouni, J. Arteta, and S. Khaykin (2010), Stratospheric water vapour budget and convection overshooting the tropopause: Modelling study from SCOUT-AMMA, *Atmos. Chem. Phys.*, *10*, 8267–8286, doi: 10.5194/acp-10-8267-2010.

Livesey, N. J., M. D. Fromm, J. W. Waters, G. L. Manney, M. L. Santee, and W. G. Read (2004), Enhancements in lower stratospheric CH_3CN observed by the Upper Atmosphere Research Satellite Microwave Limb Sounder following boreal forest fires, *J. Geophys. Res.*, *109*, D06308, doi:10.1029/2003JD004055.

Livesey, N. J., et al. (2008), Validation of Aura Microwave Limb Sounder O_3 and CO observations in the upper troposphere and lower stratosphere, *J. Geophys. Res.*, *113*, D15S02, doi:10.1029/2007JD008805.

Livesey, N. J., et al. (2011), EOS MLS Level 2 Version 3.3 quality document, *Tech. rep.*, Jet Propulsion Laboratory, California Institute of Technology, Pasadena, California, http://mls.jpl.nasa.gov/data/datadocs.php.

Livesey, N. J., J. A. Logan, M. L. Santee, J. W. Waters, R. M. Doherty, W. G. Read, L. Froidevaux, and J. H. Jiang (2013), Interrelated variations of O_3, CO and deep convection in the tropical/subtropical upper troposphere observed by the Aura Microwave Limb Sounder (MLS) during 2004-2011, *Atmos. Chem. Phys.*, *13*, 579–598, doi:10.5194/acp-13-579-2013.

Llewellyn, E., et al. (2004), The OSIRIS instrument on the Odin spacecraft, *Can. J. Phys.*, *82*, 411–422, doi:10.1139/p04-005.

Lu, H., M. P. Baldwin, L. J. Gray, and M. J. Jarvis (2008), Decadal-scale changes in the effect of the QBO on the northern stratospheric polar vortex, *J. Geophys. Res.*, *113*, D10114, doi:10.1029/2007JD009647.

McCormick, M. P., and R. E. Veiga (1992), SAGE II measurements of early Pinatubo aerosols, *Geophys. Res. Lett*, *19*, 155–158, doi:10.1029/91GL02790.

McCormick, M. P., H. M. Steele, P. Hamill, W. P. Chu, and T. J. Swissler (1982), Polar Stratospheric Cloud Sightings by SAM II., *J. Atmos. Sci.*, *39*, 1387–1397, doi: 10.1175/1520-0469(1982)039¡1387:PSCSBS¿2.0.CO;2.

McElroy, C. T., et al. (2007), The ACE-MAESTRO instrument on SCISAT: description, performance, and preliminary results, *Appl. Opt.*, *46*, 4341–4356, doi: 10.1364/AO.46.004341.

McElroy, M. B., R. J. Salawitch, S. C. Wofsy, and J. A. Logan (1986), Reductions of Antarctic ozone due to synergistic interactions of chlorine and bromine, *Nature*, *321*, 759–762, doi:10.1038/321759a0.

McIntyre, M. E., and T. N. Palmer (1983), Breaking planetary waves in the stratosphere, *Nature*, *305*, 593–600, doi:10.1038/305593a0.

Miles, T., W. L. Grose, E. E. Remsberg, and G. Lingenfelser (1994), Evolution of the southern hemisphere subpolar middle atmosphere during summer and autumn., *J. Atmos. Sci.*, *51*, 677–693.

Molina, L. T., and M. J. Molina (1987), Production of Cl_2O_2 from the self-reaction of the ClO radical, *J. Phys. Chem.*, *91*(2), 433–436, doi:10.1021/j100286a035.

Molina, M. J., and F. S. Rowland (1974), Stratospheric sink for chlorofluoromethanes: chlorine atomc-atalysed destruction of ozone, *Nature*, *249*, 810–812, doi:10.1038/249810a0.

Monier, E., and B. C. Weare (2011), Climatology and trends in the forcing of the stratospheric zonal-mean flow, *Atmos. Chem. Phys.*, *11*, 12,751–12,771.

Montzka, S. A., J. H. Butler, R. C. Myers, T. M. Thompson, T. H. Swanson, A. D. Clarke, L. T. Lock, and J. W. Elkins (1996), Decline in the Tropospheric Abundance of Halogen from Halocarbons: Implications for Stratospheric Ozone Depletion, *Science*, *272*, 1318–1322, doi:10.1126/science.272.5266.1318.

Morgenstern, O., P. Braesicke, M. M. Hurwitz, F. M. O'Connor, A. C. Bushell, C. E. Johnson, and J. A. Pyle (2008), The world avoided by the Montreal Protocol, *Geophys. Res. Lett*, *35*, L16811, doi:10.1029/2008GL034590.

Morgenstern, O., et al. (2010), Review of the formulation of present-generation stratospheric chemistry-climate models and associated external forcings, *J. Geophys. Res.*, *115*, D00M02, doi:10.1029/2009JD013728.

Mote, P. W., K. H. Rosenlof, J. R. Holton, R. S. Harwood, and J. W. Waters (1995), Seasonal variations of water vapor in the tropical lower statosphere, *Geophys. Res. Lett*, *22*, 1093–1096, doi:10.1029/95GL01234.

Murtagh, D., et al. (2002), Review: An overview of the Odin atmospheric mission, *Can. J. Phys.*, *80*, 309, doi:10.1139/p01-157.

Nakićenović, N., and R. Swart (Eds.) (2000), *IPCC Special Report on Emissions Scenarios*, Cambridge University Press, UK.

Nash, E. R., P. A. Newman, J. E. Rosenfield, and M. R. Schoeberl (1996), An objective determination of the polar vortex using Ertel's potential vorticity, *J. Geophys. Res*, *101*, 9471–9478.

Nassar, R., P. F. Bernath, C. D. Boone, G. L. Manney, S. D. McLeod, C. P. Rinsland, R. Skelton, and K. A. Walker (2005), Stratospheric abundances of water and methane based on ACE-FTS measurements, *Geophys. Res. Lett*, *32*, L15S04, doi: 10.1029/2005GL022383.

Nedoluha, G. E., R. M. Bevilacqua, R. M. Gomez, B. C. Hicks, J. M. Russell, and B. J. Connor (2003), An evaluation of trends in middle atmospheric water vapor as measured by HALOE, WVMS, and POAM, *J. Geophys. Res.*, *108*, 4391, doi: 10.1029/2002JD003332.

Newland, M. J., C. E. Reeves, D. E. Oram, J. C. Laube, W. T. Sturges, C. Hogan, P. Begley, and P. J. Fraser (2013), Southern hemispheric halon trends and global halon emissions, 1978-2011, *Atmos. Chem. Phys.*, *13*, 5551–5565, doi:10.5194/acp-13-5551-2013.

Newman, P. A., S. R. Kawa, and E. R. Nash (2004), On the size of the Antarctic ozone hole, *Geophys. Res. Lett*, *31, L21104*, 10.1029/2004GL020,596.

Newman, P. A., E. R. Nash, S. R. Kawa, S. A. Montzka, and S. M. Schauffler (2006), When will the Antarctic ozone hole recover?, *Geophys. Res. Lett*, *33, L12814*, 10.1029/2005GL025,232.

Newman, P. A., J. S. Daniel, D. W. Waugh, and E. R. Nash (2007), A new formulation of equivalent effective stratospheric chlorine (EESC), *Atmos. Chem. Phys.*, *7*, 4537–4552.

Newman, P. A., et al. (2009), What would have happened to the ozone layer if chlorofluorocarbons (CFCs) had not been regulated?, *Atmos. Chem. Phys.*, *9*, 2113–2128.

Oltmans, S. J., and D. J. Hofmann (1995), Increase in lower-stratospheric water vapour at a mid-latitude Northern Hemisphere site from 1981 to 1994, *Nature*, *374*, 146–149, doi:10.1038/374146a0.

Oltmans, S. J., H. Vömel, D. J. Hofmann, K. H. Rosenlof, and D. Kley (2000), The increase in stratospheric water vapor from balloonborne, frostpoint hygrometer measurements at Washington, D.C., and Boulder, Colorado, *Geophys. Res. Lett*, *27*, 3453–3456, doi:10.1029/2000GL012133.

Oman, L. D., et al. (2010), Multimodel assessment of the factors driving stratospheric ozone evolution over the 21st century, *J. Geophys. Res.*, *115*, D24306, doi: 10.1029/2010JD014362.

Parmar, R. S., M. Welling, M. O. Andreae, and G. Helas (2008), Water vapor release from biomass combustion, *Atmos. Chem. Phys.*, *8*, 6147–6153.

Pechony, O., and D. T. Shindell (2010), Driving forces of global wildfires over the past millennium and the forthcoming century, *Proceedings of the National Academy of Sciences*, doi:10.1073/pnas.1003669107.

Perlwitz, J., S. Pawson, R. L. Fogt, E. Nielsen, and W. D. Neff (2008), Impact of stratospheric ozone hole recovery on Antarctic climate, *Geophys. Res. Lett*, *35*, doi:10.1029/2008GL033,317.

Peter, T. (1997), Microphysics and Heterogeneous Chemistry of Polar Stratospheric Clouds, *Annu. Rev. Phys. Chem.*, *48*, 785–822, doi:10.1146/annurev.physchem.48.1.785.

Petrenko, V. V., et al. (2013), A 60 yr record of atmospheric carbon monoxide reconstructed from Greenland firn air, *Atmos. Chem. Phys.*, *13*, 7567–7585, doi:10.5194/acp-13-7567-2013.

Plumb, R. A. (2002), Stratospheric transport, *J. Meteor. Soc. Jpn.*, pp. 793–809.

Poole, L. R., and M. P. McCormick (1988), Airborne lidar observations of Arctic polar stratospheric clouds: Indications of two distinct growth stages, *Geophys. Res. Lett*, *15*, 21–23, doi:10.1029/GL015i001p00021.

Poole, L. R., M. C. Pitts, and L. W. Thomason (2009), Comment on "A tropical 'NAT-like' belt observed from space" by H. Chepfer and V. Noel, *Geophys. Res. Lett*, *36*, L20803, doi:10.1029/2009GL038506.

Portmann, R. W., S. Solomon, R. R. Garcia, L. W. Thomason, L. R. Poole, and M. P. McCormick (1996), Role of aerosol variations in anthropogenic ozone depletion in the polar regions, *J. Geophys. Res.*, *101*, 22,991–23,006, doi:10.1029/96JD02608.

Potter, B. E. (2005), The role of released moisture in the atmospheric dynamics associated with wildland fires, *Int. J. Wildland Fire*, *14*(1), 77–84.

Pumphrey, H. C., et al. (2007), Validation of middle-atmosphere carbon monoxide retrievals from the Microwave Limb Sounder on Aura, *J. Geophys. Res.*, *112*, D24S38, doi:10.1029/2007JD008723.

Pumphrey, H. C., M. L. Santee, N. J. Livesey, M. J. Schwartz, and W. G. Read (2011), Microwave Limb Sounder observations of biomass-burning products from the Australian bush fires of February 2009, *Atmos. Chem. Phys.*, *11*, 6285–6296, doi:10.5194/acp-11-6285-2011.

Quintanar, A. I., and C. R. Mechoso (1995), Quasi-Stationary waves in the southern hemisphere. Part I: Observational data., *J. Climate*, *8*, 2659–2672.

Randel, W. J. (1988), The seasonal evolution of planetary waves in the southern hemisphere stratosphere and troposphere, *Q.J.R. Meteorol. Soc.*, *114*, 1385–1409, doi:10.1002/qj.49711448403.

Randel, W. J., and M. Park (2006), Deep convective influence on the Asian summer monsoon anticyclone and associated tracer variability observed with Atmospheric Infrared Sounder (AIRS), *J. Geophys. Res.*, *111*(D10), D12314, doi:10.1029/2005JD006490.

Randel, W. J., F. Wu, J. M. Russell, III, A. Roche, and J. W. Waters (1998), Seasonal Cycles and QBO Variations in Stratospheric CH_4 and H_2O Observed in UARS HALOE Data., *J. Atmos. Sci.*, *55*, 163–185, doi:10.1175/1520-0469(1998)055¡0163:SCAQVI¿2.0.CO;2.

Randel, W. J., et al. (2009), An update of observed stratospheric temperature trends, *J. Geophys. Res.*, *114*, D02107, doi:10.1029/2008JD010421.

Randel, W. J., M. Park, L. Emmons, D. Kinnison, P. Bernath, K. A. Walker, C. Boone, and H. Pumphrey (2010), Asian Monsoon Transport of Pollution to the Stratosphere, *Science*, *328*, 611–, doi:10.1126/science.1182274.

Randerson, J. T., et al. (2006), The impact of boreal forest fire on climate warming, *Science*, *314*, 1130–1132, doi:10.1126/science.1132075.

Raphael, M. N. (1998), Quasi-Stationary waves in the southern hemisphere: An examination of their simulation by the NCAR climate system model, with and without an interactive ocean., *J. Climate*, *11*, 1405–1418.

Rayner, N. A., P. Brohan, D. E. Parker, C. K. Folland, J. J. Kennedy, M. Vanicek, T. J. Ansell, and S. F. B. Tett (2006), Improved analyses of changes and uncertainties in sea surface temperature measured in situ since the mid-nineteenth century: The HadSST2 Dataset, *J. Climate*, *19*(3), 446–469.

Read, W. G., et al. (2007), Aura Microwave Limb Sounder upper tropospheric and lower stratospheric H_2O and relative humidity with respect to ice validation, *J. Geophys. Res.*, *112*, D24S35, doi:10.1029/2007JD008752.

Real, E., et al. (2007), Processes influencing ozone levels in Alaskan forest fire plumes during long-range transport over the North Atlantic, *J. Geophys. Res.*, *112*, D10S41, doi:10.1029/2006JD007576.

Reid, J. S., R. Koppmann, T. F. Eck, and D. P. Eleuterio (2005a), A review of biomass burning emissions part II: intensive physical properties of biomass burning particles, *Atmos. Chem. Phys.*, *5*, 799–825.

Reid, J. S., T. F. Eck, S. A. Christopher, R. Koppmann, O. Dubovik, D. P. Eleuterio, B. N. Holben, E. A. Reid, and J. Zhang (2005b), A review of biomass burning emissions part III: intensive optical properties of biomass burning particles, *Atmos. Chem. Phys.*, *5*, 827–849.

Renard, J.-B., et al. (2008), Vertical distribution of the different types of aerosols in the stratosphere: Detection of solid particles and analysis of their spatial variability, *J. Geophys. Res.*, *113*, D21303, doi:10.1029/2008JD010150.

Rienecker, M. M., et al. (2008), The GEOS-5 Data Assimilation System Documentation of Versions 5.0.1, 5.1.0, and 5.2.0, *Tech. rep.*, NASA Technical report series on global modeling and data assimilation, Volume 27.

Rigby, M., et al. (2008), Renewed growth of atmospheric methane, *Geophys. Res. Lett*, *35*, L22805, doi:10.1029/2008GL036037.

Rigby, M., et al. (2013), Re-evaluation of the lifetimes of the major CFCs and CH_3CCl_3 using atmospheric trends, *Atmos. Chem. Phys.*, *13*, 2691–2702, doi:10.5194/acp-13-2691-2013.

Rinsland, C. P., L. Chiou, C. Boone, P. Bernath, E. Mahieu, and R. Zander (2009), Trend of lower stratospheric methane (CH_4) from atmospheric chemistry experiment (ACE) and atmospheric trace molecule spectroscopy (ATMOS) measurements, *J. Quant. Spectrosc. Radiat. Trans.*, *110*, 1066–1071, doi:10.1016/j.jqsrt.2009.03.024.

Robock, A. (2000), Volcanic eruptions and climate, *Rev. Geophys.*, *38*, 191–219, doi:10.1029/1998RG000054.

Robock, A., T. Adams, M. Moore, L. Oman, and G. Stenchikov (2007), Southern Hemisphere atmospheric circulation effects of the 1991 Mount Pinatubo eruption, *Geophys. Res. Lett*, *34*, L23710, doi:10.1029/2007GL031403.

Rosen, J. M. (1971), The Boiling Point of Stratospheric Aerosols., *J. Appl. Meteor.*, *10*, 1044–1045, doi:10.1175/1520-0450(1971)010¡1044:TBPOSA¿2.0.CO;2.

Rosenfield, J. E., A. R. Douglass, and D. B. Considine (2002), The impact of increasing carbon dioxide on ozone recovery, *J. Geophys. Res.*, *107*, D04049, doi:10.1029/2001JD000824.

Saikawa, E., et al. (2012), Global and regional emission estimates for HCFC-22, *Atmos. Chem. Phys.*, *12*, 10,033–10,050, doi:10.5194/acp-12-10033-2012.

Salby, M. L., and P. F. Callaghan (2006), Influence of the Brewer-Dobson circulation on stratosphere-troposphere exchange, *J. Geophys. Res.*, *111*, D21106, doi:10.1029/2006JD007051.

Sander, S. P., et al. (2011), Chemical kinetics anc photochemical data for use in atmospheric studies- Evaluation No. 17, *Tech. rep.*, JPL Publication 10-6, Jet Propulsion Laboratory, Pasadena.

Sanders, R. W., S. Solomon, J. P. Smith, L. Perliski, H. L. Miller, G. H. Mount, J. G. Keys, and A. L. Schmeltekopf (1993), Visible and near-ultraviolet spectroscopy at McMurdo Station, Antarctica: 9. Observations of OClO from April to October 1991, *J. Geophys. Res.*, *98*, 7219–7228, doi:10.1029/93JD00042.

Sarma, K., and G. M. Bankobeza (Eds.) (2000), *The Montreal Protocol on Substances that Deplete the Ozone Layer*, United Nations Environment Programme.

Schmidt, G. A., R. A. Ruedy, R. L. Miller, and A. A. Lacis (2010), Attribution of the present-day total greenhouse effect, *J. Geophys. Res.*, *115*, D20106, doi:10.1029/2010JD014287.

Schoeberl, M. R., B. N. Duncan, A. R. Douglass, J. Waters, N. Livesey, W. Read, and M. Filipiak (2006), The carbon monoxide tape recorder, *Geophys. Res. Lett*, *33*, L12811, doi:10.1029/2006GL026178.

Schuster, G. L., O. Dubovik, and B. N. Holben (2006), Angstrom exponent and bimodal aerosol size distributions, *J. Geophys. Res.*, *111*, D07207, doi:10.1029/2005JD006328.

Scinocca, J. F., D. B. Stephenson, T. C. Bailey, and J. Austin (2010), Estimates of past and future ozone trends from multimodel simulations using a flexible smoothing spline methodology, *J. Geophys. Res.*, *115*, D00M12, doi:10.1029/2009JD013622.

Seinfeld, J. H., and S. N. Pandis (2006), *Atmospheric chemistry and physics: From air pollution to climate change*, Wiley Interscience.

Shaw, T. A., and T. G. Shepherd (2008), Atmospheric science: Raising the roof, *Nature Geoscience*, *1*, 12–13, doi:10.1038/ngeo.2007.53.

Shepherd, T. G., and A. I. Jonsson (2008), On the attribution of stratospheric ozone and temperature changes to changes in ozone-depleting substances and well-mixed greenhouse gases, *Atmos. Chem. Phys.*, *8*, 1435–1444.

Sherwood, S. C., and A. E. Dessler (2000), On the control of stratospheric humidity, *Geophys. Res. Lett*, *27*, 2513–2516, doi:10.1029/2000GL011438.

Shettle, E. P., M. T. DeLand, G. E. Thomas, and J. J. Olivero (2009), Long term variations in the frequency of polar mesospheric clouds in the Northern Hemisphere from SBUV, *Geophys. Res. Lett*, *36*, L02803, doi:10.1029/2008GL036048.

Shindell, D. T. (2001), Climate and ozone response to increased stratospheric water vapor, *Geophys. Res. Lett*, *28 (8)*, 1551–1554.

Shindell, D. T., and G. A. Schmidt (2004), Southern Hemisphere climate response to ozone changes and greenhouse gas increases, *Geophys. Res. Lett*, *31*, L18209, doi: doi:10.1029/2004GL020724.

Shindell, D. T., D. Rind, and P. Lonergan (1998), Increased polar stratospheric ozone losses and delayed eventual recovery owing to increasing greenhouse-gas concentrations, *Nature*, *392*, 589–592, doi:10.1038/33385.

Siddaway, J. M., and S. V. Petelina (2011), Transport and evolution of the 2009 Australian Black Saturday bushfire smoke in the lower stratosphere observed by OSIRIS on Odin, *J. Geophys. Res.*, *116*, D06203, doi:10.1029/2010JD015162.

Siddaway, J. M., S. V. Petelina, D. J. Karoly, A. R. Klekociuk, and R. J. Dargaville (2013), Evolution of Antarctic ozone in September-December predicted by CCMVal-2 model simulations for the 21st century, *Atmos. Chem. Phys.*, *13*(8), 4413–4427, doi: 10.5194/acp-13-4413-2013.

Sioris, C. E., J. Zou, C. T. McElroy, C. A. McLinden, and H. Vömel (2010), High vertical resolution water vapour profiles in the upper troposphere and lower stratosphere retrieved from MAESTRO solar occultation spectra, *Adv. Space. Res.*, *46*, 642–650, doi:10.1016/j.asr.2010.04.040.

Smith, A. K., R. R. Garcia, D. R. Marsh, D. E. Kinnison, and J. H. Richter (2010), Simulations of the response of mesospheric circulation and temperature to the Antarctic ozone hole., *Geophys. Res. Lett*, *37*, L22,803, doi:10.1029/2010GL045255.

Solomon, S. (1999), Stratospheric ozone depletion: A review of concepts and history, *Rev. Geophys.*, *37(3)*, 275–316.

Solomon, S., R. R. Garcia, F. S. Rowland, and D. J. Wuebbles (1986), On the depletion of Antarctic ozone, *Nature*, *321*, 275–316.

Solomon, S., R. W. Sanders, R. R. Garcia, and J. G. Keys (1993), Increased chlorine dioxide over Antarctica caused by volcanic aerosols from Mount Pinatubo, *Nature*, *363*, 245–248, doi:10.1038/363245a0.

Solomon, S., R. W. Portmann, R. R. Garcia, L. W. Thomason, L. R. Poole, and M. P. McCormick (1996), The role of aerosol variations in anthropogenic ozone depletion at northern midlatitudes, *J. Geophys. Res.*, *101*, 6713–6727, doi:10.1029/95JD03353.

Solomon, S., R. W. Portmann, T. Sasaki, D. J. Hofmann, and D. W. J. Thompson (2005), Four decades of ozonesonde measurements over Antarctica, *J. Geophys. Res.*, *110*, D21311, doi:10.1029/2005JD005917.

Solomon, S., J. S. Daniel, R. R. Neely, J.-P. Vernier, E. G. Dutton, and L. W. Thomason (2011), The persistently variable "Background" Stratospheric Aerosol Layer and global climate change, *Science*, *333*, 866–, doi:10.1126/science.1206027.

Son, S.-W., N. F. Tandon, L. M. Polvani, and D. W. Waugh (2009), Ozone hole and Southern Hemisphere climate change, *Geophys. Res. Lett*, *36*, L15705, doi: 10.1029/2009GL038671.

Son, S.-W., et al. (2010), Impact of stratospheric ozone on Southern Hemisphere circulation change: A multimodel assessment, *J. Geophys. Res.*, *115*, D00M07, doi: doi:10.1029/2010JD01427.

Stephens, G. L., et al. (2002), The Cloudsat Mission and the A-Train, *Bulletin of the American Meteorological Society*, *83*, 1771–1790, doi:10.1175/BAMS-83-12-1771.

Stolarski, R. S., and S. M. Frith (2006), Search for evidence of trend slow-down in the long-term TOMS/SBUV total ozone data record: the importance of instrument drift uncertainty, *Atmos. Chem. Phys.*, *6*, 4057–4065.

Thomas, G. E., E. J. Jensen, J. J. Olivero, W. Schroeder, and O. B. Toon (1989), Relation between increasing methane and the presence of ice clouds at the mesopause, *Nature*, *338*, 490–492, doi:10.1038/338490a0.

Thomas, M. A., M. A. Giorgetta, C. Timmreck, H.-F. Graf, and G. Stenchikov (2009), Simulation of the climate impact of Mt. Pinatubo eruption using ECHAM5 - Part 2: Sensitivity to the phase of the QBO and ENSO, *Atmos. Chem. Phys.*, *9*, 3001–3009.

Thomason, L., and T. H. Peter (Eds.) (2006), *SPARC Assessment of Stratospheric Aerosol Properties*, SPARC Report No. 4, WCRP-124, WMO/TD-No. 1295.

Thompson, D. W. J., and S. Solomon (2002), Interpretation of recent Southern Hemisphere climate change, *Science*, *296*, 895–899.

Toon, O. B., J. Pinto, P. Hamill, and R. P. Turco (1986), Condensation of HNO3 and HCl in the winter polar stratospheres, *Geophys. Res. Lett*, *13*, 1284–1287, doi: 10.1029/GL013i012p01284.

Torres, O., A. Tanskanen, B. Veihelmann, C. Ahn, R. Braak, P. K. Bhartia, P. Veefkind, and P. Levelt (2007), Aerosols and surface UV products from Ozone Monitoring Instrument observations: An overview, *J. Geophys. Res.*, *112*, D24S47, doi: 10.1029/2007JD008809.

Torres, O., Z. Chen, H. Jethva, C. Ahn, S. R. Freitas, and P. K. Bhartia (2010), OMI and MODIS observations of the anomalous 2008-2009 southern hemisphere biomass burning seasons, *Atmos. Chem. Phys.*, *10*, 3505–3513.

Trentmann, J., G. Luderer, T. Winterrath, M. D. Fromm, R. Servranckx, C. Textor, M. Herzog, H.-F. Graf, and M. O. Andreae (2006), Modeling of biomass smoke injection into the lower stratosphere by a large forest fire (Part I): reference simulation, *Atmos. Chem. Phys.*, *6*, 5247–5260.

Trepte, C. R., and M. H. Hitchman (1992), Tropical stratospheric circulation deduced from satellite aerosol data, *Nature*, *355*, 626–628, doi:10.1038/355626a0.

Tsutsumi, Y., Y. Sawa, Y. Makino, J. B. Jensen, J. L. Gras, B. F. Ryan, S. Diharto, and H. Harjanto (1999), Aircraft measurements of ozone, NO_x, CO, and aerosol concentrations in biomass burning smoke over Indonesia and Australia in October 1997: Depleted ozone layer at low altitude over Indonesia, *Geophys. Res. Lett*, *26*, 595–598, doi:10.1029/1999GL900054.

Tupper, A., J. S. Oswalt, and D. Rosenfeld (2005), Satellite and radar analysis of the volcanic-cumulonimbi at Mount Pinatubo, Philippines, 1991, *J. Geophys. Res.*, *110*, D09204, doi:10.1029/2004JD005499.

Urban, J., et al. (2007), Global observations of middle atmospheric water vapour by the Odin satellite: an overview, *Planet. Space. Sci*, *55*, 1093–1102, doi: 10.1016/j.pss.2006.11.021.

Val Martín, M., R. E. Honrath, R. C. Owen, G. Pfister, P. Fialho, and F. Barata (2006), Significant enhancements of nitrogen oxides, black carbon, and ozone in the North

Atlantic lower free troposphere resulting from North American boreal wildfires, *J. Geophys. Res.*, *111*, D23S60, doi:10.1029/2006JD007530.

Verma, S., et al. (2009), Ozone production in boreal fire smoke plumes using observations from the Tropospheric Emission Spectrometer and the Ozone Monitoring Instrument, *J. Geophys. Res.*, *114*, D02303, doi:10.1029/2008JD010108.

Vernier, J.-P., et al. (2011), Major influence of tropical volcanic eruptions on the stratospheric aerosol layer during the last decade, *Geophys. Res. Lett*, *38*, L12807, doi:10.1029/2011GL047563.

Vernier, J.-P., L. W. Thomason, T. D. Fairlie, P. Minnis, R. Palikonda, and K. M. Bedka (2013), Comment on "Large Volcanic Aerosol Load in the Stratosphere Linked to Asian Monsoon Transport", *Science*, *339*, 647–647, doi:10.1126/science.1227817.

Voigt, C., et al. (2000), Nitric Acid Trihydrate (NAT) in Polar Stratospheric Clouds, *Science*, *290*, 1756–1758, doi:10.1126/science.290.5497.1756.

VöMel, H., et al. (2007), Validation of Aura Microwave Limb Sounder water vapor by balloon-borne Cryogenic Frost point Hygrometer measurements, *J. Geophys. Res.*, *112*, D24S37, doi:10.1029/2007JD008698.

von Savigny, C., et al. (2003), Stratospheric ozone profiles retrieved from limb scattered sunlight radiance spectra measured by the OSIRIS instrument on the Odin satellite, *Geophys. Res. Lett*, *30*, 1755, doi:10.1029/2002GL016401.

Wagner, R. E., and K. P. Bowman (2000), Wavebreaking and mixing in the Northern Hemisphere summer stratosphere, *J. Geophys. Res.*, *105*, 24,799, doi:10.1029/2000JD900320.

Waibel, A., H. Fischer, F. Wienhold, P. Siegmund, B. Lee, J. Strm, J. Lelieveld, and P. Crutzen (1999), Highly elevated carbon monoxide concentrations in the upper troposphere and lowermost stratosphere at northern midlatitudes during the STREAM II summer campaign in 1994, *Chemosphere - Global Change Science*, *1*(13), 233 – 248, doi:http://dx.doi.org/10.1016/S1465-9972(99)00027-6.

Waters, J. W., L. Froidevaux, W. G. Read, G. L. Manney, L. S. Elson, D. A. Flower, R. F. Jarnot, and R. S. Harwood (1993), Stratospheric CIO and ozone from the Microwave Limb Sounder on the Upper Atmosphere Research Satellite, *Nature*, *362*, 597–602, doi:10.1038/362597a0.

Waters, J. W., et al. (2006), The Earth Observing System Microwave Limb Sounder (EOS MLS) on the Aura Satellite, *IEEE Trans. Geosci. Remote Sens.*, *44*, 1075–1092, doi:10.1109/TGRS.2006.873771.

Waugh, D. W., and L. M. Polvani (2010), Stratospheric polar vortices, *Washington DC American Geophysical Union Geophysical Monograph Series*, *190*, 43–57, doi:10.1029/2009GM000887.

Waugh, D. W., W. J. Randel, S. Pawson, P. A. Newman, and E. R. Nash (1999), Persistence of the lower stratospheric polar vortices, *J. Geophys. Res.*, *104*, 27,191–27,202.

Waugh, D. W., L. Oman, S. R. Kawa, R. S. Stolarski, S. Pawson, A. R. Douglass, P. A. Newman, and J. E. Nielsen (2009a), Impacts of climate change on stratospheric ozone recovery, *Geophys. Res. Lett*, *36*, L03,805.

Waugh, D. W., L. Oman, P. A. Newman, R. S. Stolarski, S. Pawson, J. E. Nielsen, and J. Perlwitz (2009b), Effect of zonal asymmetries in stratospheric ozone on simulated Southern Hemisphere climate trends, *Geophys. Res. Lett*, *36*, L18701, doi: 10.1029/2009GL040419.

Winker, D. M., W. H. Hunt, and M. J. McGill (2007), Initial performance assessment of CALIOP, *Geophys. Res. Lett*, *34*, L19803, doi:10.1029/2007GL030135.

Wirth, V. (1993), Quasi-stationary planetary waves in total ozone and their correlation with lower stratospheric temperature, *J. Geophys. Res*, *98*, 8873–8882.

WMO (2007), World Meteorological Organisation: Scientific Assessment of Ozone Depletion: 2006, Global Research and Monitoring Project - Report No. 50.

WMO (2011), World Meteorological Organisation: Scientific Assessment of Ozone Depletion: 2010, Global Research and Monitoring Project - Report No. 52.

Young, R. E., H. Houben, and O. B. Toon (1994), Radiatively forced dispersion of the Mt. Pinatubo volcanic cloud and induced temperature perturbations in the stratosphere during the first few months following the eruption, *Geophys. Res. Lett*, *21*, 369–372, doi:10.1029/93GL03302.

Yu, H., et al. (2006), A review of measurement-based assessments of the aerosol direct radiative effect and forcing, *Atmos. Chem. Phys.*, *6*, 613–666.